



HAL
open science

Electrochemiluminescence at different scales : From new fundamental properties to surface-confined microscopy

Silvia Voci

► **To cite this version:**

Silvia Voci. Electrochemiluminescence at different scales: From new fundamental properties to surface-confined microscopy. Chemical engineering. Université de Bordeaux, 2019. English. NNT : 2019BORD0294 . tel-02937886

HAL Id: tel-02937886

<https://theses.hal.science/tel-02937886>

Submitted on 14 Sep 2020

HAL is a multi-disciplinary open access archive for the deposit and dissemination of scientific research documents, whether they are published or not. The documents may come from teaching and research institutions in France or abroad, or from public or private research centers.

L'archive ouverte pluridisciplinaire **HAL**, est destinée au dépôt et à la diffusion de documents scientifiques de niveau recherche, publiés ou non, émanant des établissements d'enseignement et de recherche français ou étrangers, des laboratoires publics ou privés.

Thèse de doctorat de l'Université de Bordeaux
École Doctorale des Sciences Chimiques

Par **Silvia Voci**

Pour obtenir le grade de Docteur

Spécialité : Chimie-Physique

**Electrochemiluminescence at different scales:
From new fundamental properties
to surface-confined microscopy**

Sous la direction de **Professeur Neso Sojic**

Présentée et soutenue publiquement à Bordeaux le 9 Décembre 2019
Devant la commission d'examen composée par :

Anxolabéhère-Mallart Elodie	DR CNRS, Université de Paris	Examinatrice
Kanoufi Frédéric	DR CNRS, Université de Paris	Rapporteur
Miomandre Fabien	PR, École normale supérieure de Cachan	Rapporteur
Paolucci Francesco	PR, Università di Bologna	Examinateur
Sojic Neso	PR, Bordeaux INP	Directeur de thèse

Abstract

Electrogenerated chemiluminescence (ECL) is a light emission phenomenon initiated by electrochemically generated radical species, which then undergo a series of electron transfer reactions. It leads to the final generation of an excited state that radiatively decays to the ground state. In this work, my goal was to develop fundamental aspects of ECL as well as analytical applications at different scales. In the first part, two supramolecular systems are studied. The ECL performances of spirofluorene derivatives based on trigonal truxene-core structure are investigated, focusing on the role of the different functional groups on the ECL properties. Then a bis-pyrene scaffold mounted on a constrained polyether macrocycle displaying intense excimer fluorescence has been selected to study the circularly polarized ECL. We show for the first time that ECL can discriminate enantiomers. In the second part of the thesis, annihilation ECL is enhanced by exploiting nanogap amplification. Furthermore, ECL imaging experiments enabled to demonstrate the increase in the performances of a bipolar electrochemistry system by employing a solid-state micropore configuration. Finally, the first steps in the development of a new ECL-based microscopy are presented. Using a unique ECL mechanism, which involves short-lifetime electrogenerated radicals, surface-confinement of ECL microscopy was demonstrated by cellular membranes' imaging. ECL microscopy applied to cells imaging was further improved by adding a permeabilization step during cells labeling procedure. Disposable transparent carbon nanotube-based electrodes inkjet-printed on classic microscope glass coverslips, were used to image cells in both reflection and transmission configurations.

Résumé

L'électrochimiluminescence (ECL) est un phénomène d'émission de lumière obtenue suite à la génération d'espèces très réactives à l'électrode. Ces dernières vont subir une série de réactions de transfert d'électrons qui conduisent à la formation d'un état excité qui mène à l'émission finale de photons. La première partie de mon travail de thèse a porté sur l'étude de deux systèmes supramoléculaires. Les performances ECL d'un dérivé du spirofluorène et de trois composés modifiés avec un truxène comme partie centrale sont examinées. L'étude d'un deuxième système supramoléculaire, [18]-C-6bispyréne, a permis de démontrer une nouvelle propriété de l'ECL, maintenant capable de distinguer entre deux énantiomères, grâce à la détection du niveau de polarisation de l'émission ECL résultante. La combinaison entre ECL et systèmes confinés est présentée dans la deuxième partie de ma thèse. L'amplification du signal ECL par annihilation a été possible grâce à l'emploi d'un dispositif comprenant deux électrodes séparées par une distance de 100 nm. De plus, l'imagerie ECL a été utilisée pour mettre en évidence l'amélioration des performances de l'ECL bipolaire en utilisant une configuration comprenant un micropore planaire de 20 μm de long. Enfin, une nouvelle microscopie basée sur l'ECL a été développée. En perméabilisant la membrane cellulaire, l'ensemble de la cellule est visualisé par ECL. De plus, en se basant sur la distribution de l'émission ECL dans différents plans focaux, nous avons pu démontrer qu'une des caractéristiques fondamentales de cette nouvelle microscopie ECL est d'être confinée à la surface de l'électrode du fait des temps de vie limités des radicaux électro-générés. L'utilisation

d'électrodes transparentes de nanotubes de carbone imprimés sur une lamelle de microscope a permis de réaliser l'imagerie ECL de cellules marquées aussi bien en réflexion qu'en transmission.

Résumé de thèse

Dans les dernières décennies, le domaine de l'électrochimiluminescence (ECL), également appelée chimiluminescence électrogénérée, a très fortement évolué et est passé du statut de phénomène lumineux restreint aux laboratoires de recherche à une technique analytique puissante employée commercialement pour la bio-analyse. Le succès de l'ECL comme technique analytique peut être attribuée à plusieurs caractéristiques intrinsèques dont une forte résolution spatiale et temporelle, une grande sensibilité et sélectivité.¹ En effet, après une première étape électrochimique se produisant au niveau de la surface de l'électrode, les radicaux électrogénérés vont subir une série de transferts d'électrons aboutissant à la formation de l'état excité du luminophore. La première étape de nature électrochimique permet un contrôle précis du moment, de la durée, de la position et de la zone où l'émission ECL se produit. Il est possible de distinguer deux mécanismes réactionnels ECL principaux : la voie par annihilation et la voie utilisant un coréactif. La première implique la génération des radicaux cations et anions du luminophore par des impulsions alternées entre le potentiel de réduction et d'oxydation du luminophore. Les deux radicaux vont ensuite réagir et produire l'état excité par annihilation. Dans le cas de la seconde voie avec un coréactif, l'émission ECL est produite grâce à l'ajout d'un composé supplémentaire, appelé coréactif, qui, après réduction ou oxydation, peut réagir avec la forme oxydée ou réduite du luminophore. Cela conduit à la formation de l'état excité et donc *in fine* à l'émission ECL. Ce second mécanisme ne nécessite que l'application d'un saut de potentiel.² Le système ECL le plus employé, spécialement en bio-analyse, est formé du complexe $[\text{Ru}(\text{bpy})_3]^{2+}$, utilisé comme luminophore et de la tri-n-propylamine (TPA) comme coréactif. Il permet la génération du signal ECL en solutions aqueuses à pH neutre. Les dernières études ECL visent au développement de nouveaux luminophores ECL présentant des performances plus élevées mais également à la production de systèmes analytiques plus sélectifs et capables de détecter simultanément plusieurs analytes.³

Cette thèse de doctorat est centrée sur l'étude du phénomène ECL à différentes échelles spatiales, depuis l'échelle moléculaire jusqu'à l'échelle micrométrique. Le but est de démontrer de nouvelles propriétés originales de l'ECL. A l'échelle moléculaire, mes recherches ont porté sur l'étude des propriétés ECL de nouveaux luminophores et l'établissement de lien structure/activité. De même, j'ai utilisé un système supramoléculaire chiral pour effectuer la détection de la polarisation de l'émission ECL. Ensuite, la combinaison de l'ECL avec

l'électrochimie a été réalisée dans des espaces confinés, tels que des dispositifs intégrant des électrodes séparées par une distance de 100 nm ou des micropores. Enfin, j'ai contribué au développement d'une microscopie ECL appliquée à l'imagerie de cellules marquées.

Le chapitre I présente les fondements théoriques, les principaux « acteurs » intervenant dans le processus ECL ainsi que les applications (bio)analytiques majeures. Dans la première partie du chapitre II, un dérivé du spirofluorène⁴ (Fig. 1, **1**) et trois composés dans lesquelles le spirofluorène est substitué avec un truxène central (Fig. 1, **2**, **3** and **4**) sont étudiés. La caractérisation électrochimique des composés a permis de montrer que les radicaux électrogénérés sont suffisamment stables pour produire un signal ECL par annihilation. Le luminophore **2**, grâce au groupe donneur d'électrons triphénylamine, montre la meilleure efficacité ECL : 314 % par rapport au complexe $[\text{Ru}(\text{bpy})_3]^{2+}$ pris comme référence.

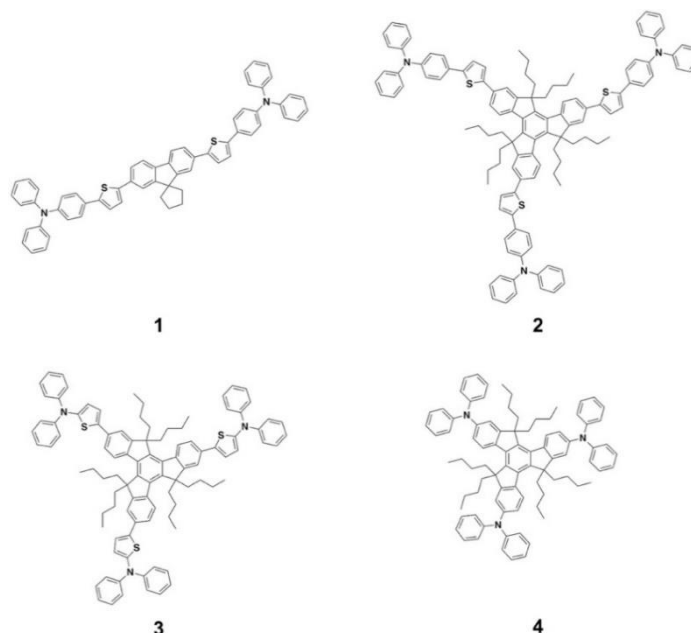


Figure 1. Structures chimiques des luminophores étudiées 1-4.

Pour la série de luminophores **1-4**, le coréactif, peroxyde de benzoyle (en anglais « benzoyl peroxide » ou BPO), a été utilisé pour évaluer l'efficacité ECL. Comme précédemment, **2** montre le signal ECL le plus élevé, plus précisément 4.5 fois plus intense que celui de $[\text{Ru}(\text{bpy})_3]^{2+}$. Les composés **1** et **3** présentent des performances ECL meilleures avec le coréactif que par annihilation.

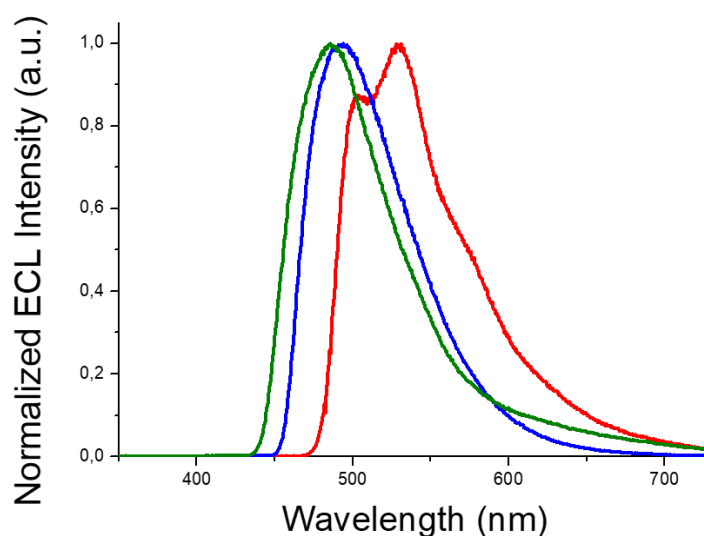


Figure 2. Spectres ECL de **1** (rouge), **2** (bleu), et **3** (vert) en DMF. Les spectres ECL ont été enregistrés dans DMF / 10 mM BPO / 0,1 M TBAPF₆.

Comme illustré par la Figure 2, il a été possible d'enregistrer les spectres ECL avec BPO comme coréactif pour les complexes **1-3**. Par contre, la faible solubilité et les caractéristiques du système **4** n'ont pas permis l'obtention de son spectre ECL. La différence entre les performances ECL peut être interprétée comme dépendant de la meilleure stabilité des radicaux électrogénérés pour le système **2** comparé aux autres systèmes. En particulier, dans le luminophore **3**, la substitution du groupe triphénylamine par la diphenylamine induit probablement une diminution significative de la stabilité des radicaux, tout spécialement du radical cation. La deuxième partie du chapitre II démontre la possibilité de réaliser la détection de la polarisation circulaire de l'émission ECL (CP-ECL) pour un système organique chiral (Fig. 3, a). La stabilité du signal ECL et l'intensité ECL élevée, associée à l'émission de l'excimère des sub-unités pyrène (lequel est favorisé dans la configuration du systèmes supramoléculaire) ont permis la détection du signal CP-ECL (Fig. 3, b) pour les deux énantiomères et pour le mélange racémique.

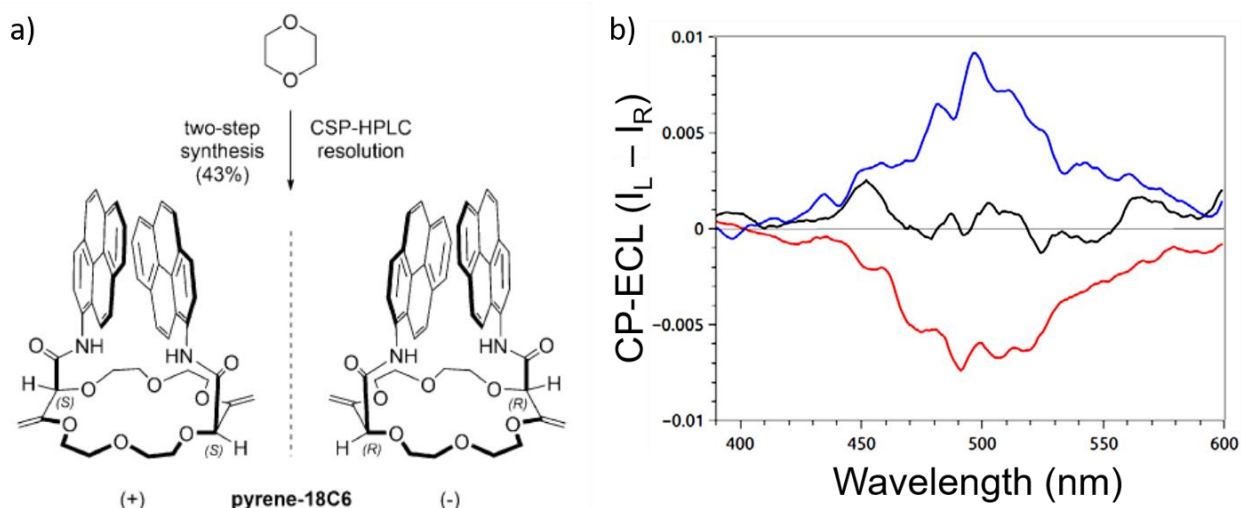


Figure 3. a) Structure moléculaire de [18]-C-6bispyrène; b) Signal CP-ECL pour (+)-[18]-C-6-bispyrène (ligne rouge), (-)-[18]-C-6-bispyrène (ligne bleu) et mélange racémique (ligne noire). Les spectres ont été enregistrés dans une solution dégazée de CH_3CN contenant une concentration de [18]-C-6-bispyrène de 0,7 mM, de BPO de 10 mM, et TBAPF₆ 0,1 M. L'émission ECL a été obtenue en appliquant un potentiel de -2.45 V vs Ag pendant 240 s à l'électrode de travail.

Comme déjà observé pour la polarisation circulaire de photoluminescence (CPL),⁵ l'énantiomère (+)-[18]-C-6-bispyrène donne un signal négatif alors que (-)-[18]-C-6-bispyrène produit un signal positif. Une polarisation proche de zéro est obtenue pour le mélange racémique. Les facteurs de dissymétrie pour l'émission ECL sont respectivement de $+8,4 \times 10^{-3}$ et $-7,3 \times 10^{-3}$ pour (-)-[18]-C-6-bispyrène et (+)-[18]-C-6-bispyrène. Elles sont comparables aux valeurs mesurées pour le facteur de dissymétrie en photoluminescence (CPL).⁵⁻⁶ En conséquence, il est possible de conclure que l'ECL peut distinguer entre l'émission de deux énantiomères, si le signal ECL est assez stable et intense.⁷

La chapitre III de ma thèse combine l'ECL et l'électrochimie dans des espaces confinés. La première étude démontre qu'en utilisant un espacement nanométrique entre les électrodes (« nanogap »), une augmentation du signal ECL du $[\text{Ru}(\text{bpy})_3]^{2+}$ est obtenue par annihilation. Cela a été rendu possible grâce au phénomène de « redox cycling ».⁸ L'espacement était de 100 nm (Fig. 4) entre les deux électrodes de travail en platine (« top » et « bottom »).

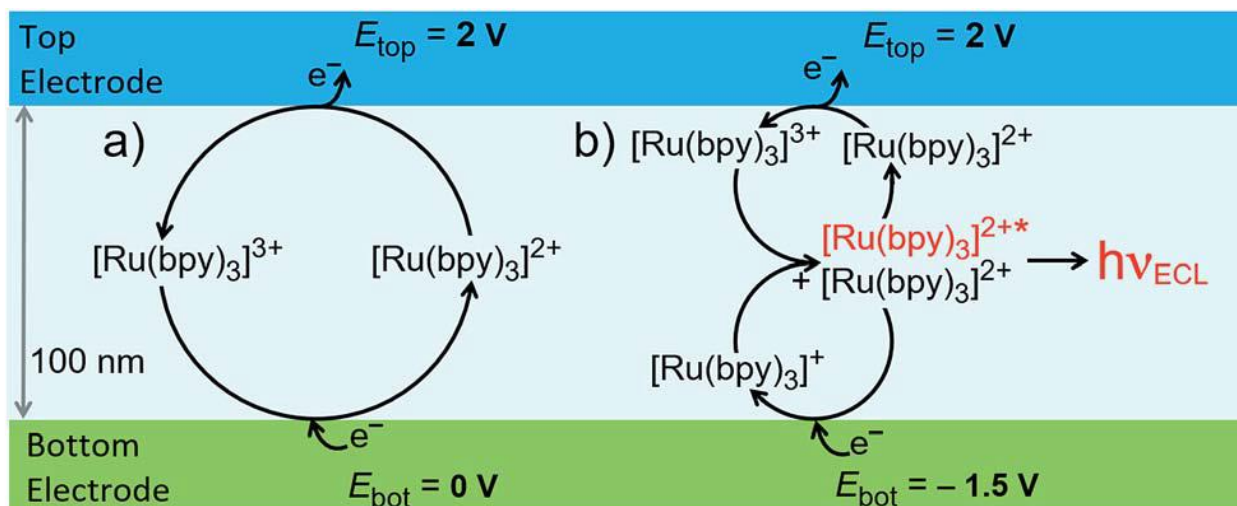


Figure 4. Schéma des deux voies réactionnelles dans le « nanogap »: (a) redox cycling, et (b) annihilation, avec émission ECL.

Le schéma de la Figure 4 montre deux différents modes électrochimiques utilisés dans le système nano-confiné. Dans le mode « redox cycling », le complexe $[\text{Ru}(\text{bpy})_3]^{2+}$ est oxydé à l'électrode « top », en appliquant un potentiel de 2 V et ensuite régénéré à l'électrode « bottom », par l'application d'un potentiel de 0 V vs Ag dans une solution d'acétonitrile. Le chemin diffusif réduit entre les deux électrodes assure une régénération continue du luminophore. Dans le mode « annihilation », une valeur de potentiel de -1,5 V vs Ag est appliquée à l'électrode « bottom », qui est maintenant capable de réduire le complexe $[\text{Ru}(\text{bpy})_3]^{2+}$ en $[\text{Ru}(\text{bpy})_3]^+$. Dans le mode « redox cycling » (Fig. 4, a), la régénération du complexe à l'état $[\text{Ru}(\text{bpy})_3]^{2+}$ a lieu à l'électrode « bottom » alors que, dans le mode « annihilation », $[\text{Ru}(\text{bpy})_3]^{2+}$ est régénéré par annihilation au centre du « nanogap », avec la production de l'état excité qui relaxe à l'état fondamental en émettant l'ECL. Les images ECL et les profils correspondants d'intensité (Fig. 5) confirment que l'émission est confinée dans le canal du nanodispositif.

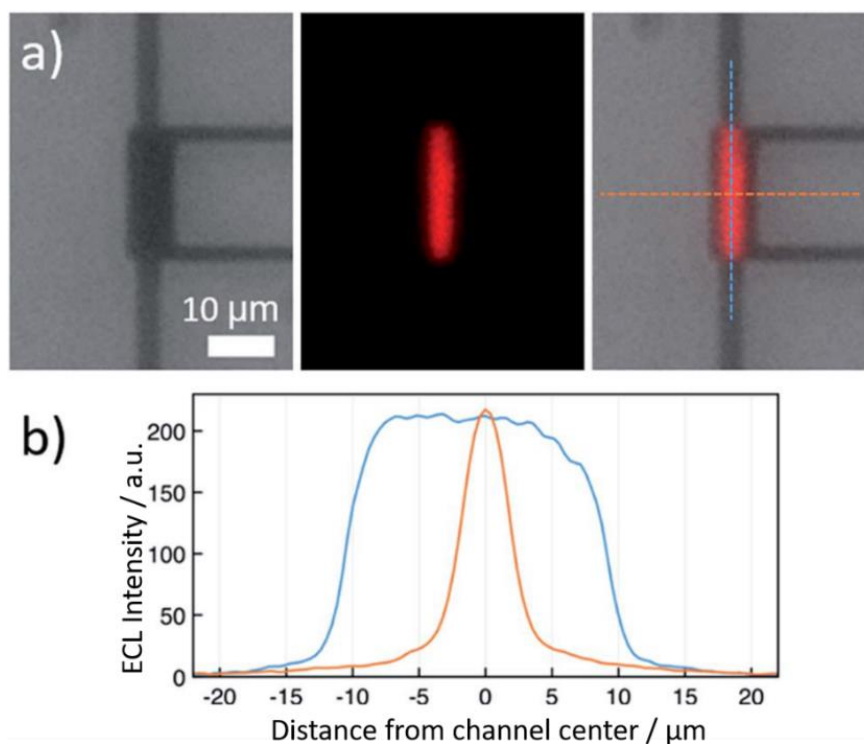


Figure 5. (a) De gauche à droite: Vue des électrodes formant le « nanogap » ; émission ECL enregistré dans l'obscurité, et superposition des deux images (lignes pointillées: direction des profils présentés en (b)). (b) Profils d'intensité ECL parallèlement (bleu) et perpendiculairement (orange) à l'axe longitudinal du canal nanofluidique. Une solution d'acétonitrile contenant 10 mM de $\text{Ru}(\text{bpy})_3(\text{PF}_6)_2$ et 0,1 M TBAPF_6 a été utilisée. Un potentiel de 2 V a été appliqué à la « top » électrode et de 1,5 V vs. Ag à la « bottom » électrode.

L'imagerie ECL a été utilisée aussi pour démontrer l'amélioration des performances de l'électrochimie bipolaire dans un micropore. Un système microfluidique à base de silicium a été développé au Laboratoire d'Analyse et d'Architecture des Systèmes (LAAS, Toulouse) avec deux électrodes source d'or et une restriction spatiale formant un micropore d'une longueur de 20 μm . Seules la base et les parois du micropore ont été désoxydées et étaient donc conductrices. Dans des conditions d'électrochimie bipolaire classique, une électrode bipolaire présentant une longueur de 20 μm nécessiterait l'application d'un potentiel de l'ordre de quelques kV.⁹ Par contre, grâce à la configuration particulière du micropore, la polarisation asymétrique de l'électrode bipolaire a été possible en appliquant un potentiel de 7 V. En introduisant la solution de PBS (pH = 7,4) contenant $[\text{Ru}(\text{bpy})_3]^{2+}$ et TPA dans le système microfluidique, l'imagerie ECL a montré le confinement de la chute de potentiel au niveau du micropore (Fig. 6). En plus,

les profils d'intensité ECL (Fig. 6, d et e) montrent bien que l'émission ECL est confinée au pôle anodique du micropore, démontrant sa polarisation asymétrique.

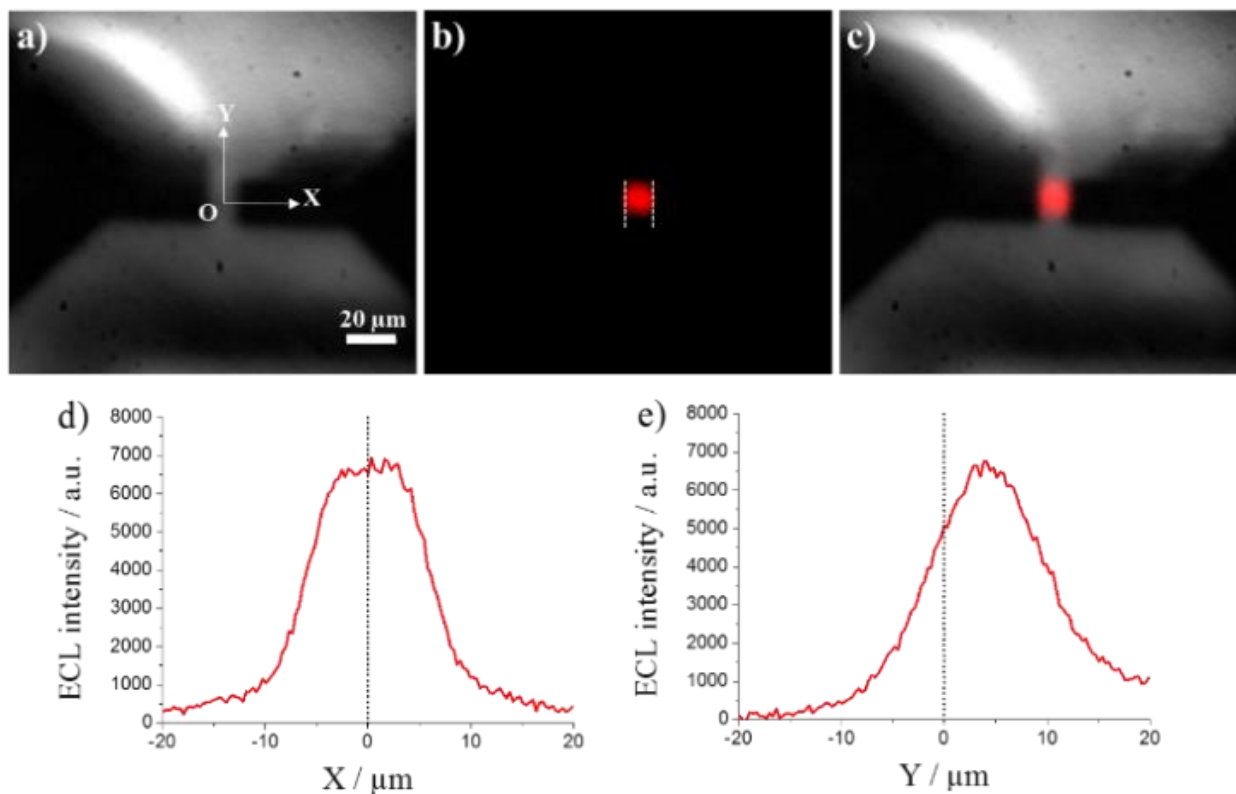


Figure 6. a) PL , b) ECL et c) superposition des deux images de luminescence, de la même région d'intérêt autour du micropore. Les deux axes ont été représentés et l'origine O des axes a été définie au centre du micropore. Les lignes pointillées délimitent les parois du micropore. Les profils d'intensité ECL parallèlement à l'axe X (d) et à l'axe Y (e) ont été enregistrés dans le micropore dans une solution PBS (pH 7,4) contenant 1 mM de $[Ru(bpy)_3]^{2+}$ et 50 mM de TPA, en appliquant un potentiel pulsé de 10 V pendant 0.3 s.

Mon travail a commencé par l'étude de systèmes supramoléculaires (chapitre II) et s'est achevé par l'imagerie ECL, à l'échelle micrométrique, de cellules et de leurs membranes (chapitre IV). Une nouvelle microscopie basée sur l'émission ECL et complémentaire à la microscopie de fluorescence a été développée. La microscopie ECL a été appliquée à l'étude des membranes cellulaires. Des cellules de la lignée « Chinese Hamster Ovary » (CHO) ont été cultivées à la surface d'électrodes de carbone vitreux. Après 48 h, elles étaient incubées avec une solution de biotine X, une protéine capable de réagir avec les protéines de la membrane cellulaire. La forte interaction chimique entre la biotine et la streptavidine a été utilisée pour le

marquage des cellules biotinylées par le luminophore $[\text{Ru}(\text{bpy})_3]^{2+}$. Ce dernier a été modifié par la streptavidine et est noté SAv@Ru.¹⁰ L'image PL (Fig. 7, a) confirme que toute la membrane cellulaire a été marquée avec $[\text{Ru}(\text{bpy})_3]^{2+}$. En éteignant la source d'excitation lumineuse et en appliquant un potentiel de 1.4 V vs Ag/AgCl en présence d'un excès de TPA, l'image ECL (Fig. 7, b) a été enregistrée.

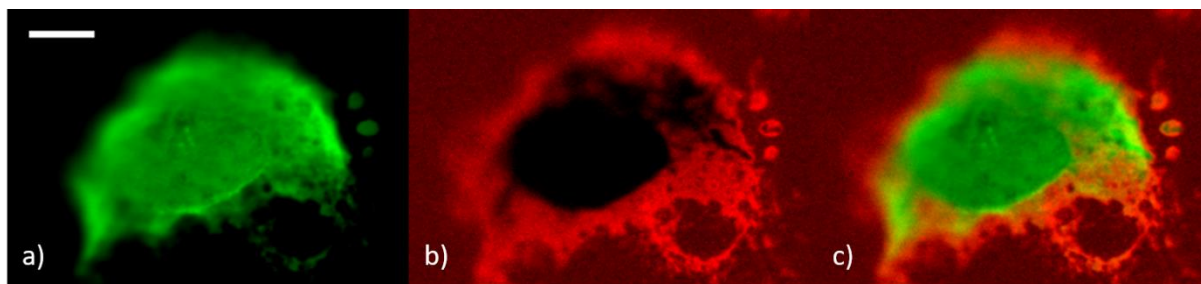


Figure 7. a) PL, b) ECL et c) superposition des deux images de luminescence de cellules CHO marquées par SAv@Ru. Les deux images, PL et ECL, ont été enregistrées en réflexion. L'image ECL a été obtenue dans une solution de PBS (pH = 7,4) contenant 100 mM de TPA et en appliquant un potentiel de 1,4 V vs Ag/AgCl/KCl 3 M. Barre d'échelle : 10 μm .

Contrairement à l'image PL, l'image ECL montre que l'émission est localisée aux bords de la cellule (Fig. 7).¹⁰ Même si l'image ECL permet une meilleure visualisation des pseudopodes de la cellule, aucune émission n'est observée dans la partie centrale de la cellule. Les luminophores localisés à une distance supérieure à 2-3 μm de l'électrode ne peuvent pas réagir avec les radicaux issus de l'oxydation de la TPA, en raison de leurs faibles durées de vie.¹¹ L'oxydation directe à l'électrode du seul coréactif limite l'émission ECL à la région accessible aux radicaux électrogénérés.¹² L'émission ECL est donc confinée à la surface de l'électrode. Pour augmenter l'accessibilité de la TPA et ne pas être limité par la membrane cellulaire qui joue le rôle de barrière diffusionnelle, une étape de perméabilisation des cellules a été ajoutée après leur fixation.¹³ L'image ECL d'une cellule perméabilisée (Fig. 8, b) confirme que l'étape de perméabilisation permet une extension de l'émission ECL à la partie centrale de la membrane cellulaire. Les deux nucléoles visibles dans l'image ECL en Figure 8, b) sont restés sombres, probablement parce que leur membrane n'a pas été perméabilisée par la procédure employée (Triton X). La microscopie ECL peut donc fournir des informations sur le transport passif à travers la membrane cellulaire.¹⁴

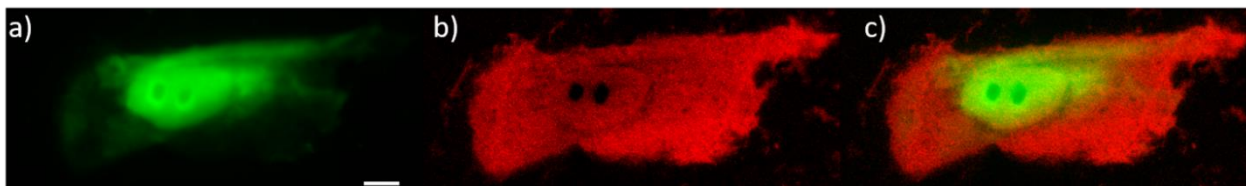


Figure 8. a) PL, b) ECL et c) superposition des deux images de luminescence des cellules CHO perméabilisées et ensuite marquées avec SAv@Ru. Les deux images, PL et ECL, ont été enregistrées en réflexion. L'image ECL a été obtenue dans une solution de PBS (pH = 7,4) contenant 100 mM de TPA et en appliquant un potentiel de 1,4 V vs Ag/AgCl/KCl 3 M. Barre d'échelle : 10 μ m.

Après cette première preuve de concept, les électrodes en carbone vitreux ont été substituées par des électrodes jetables réalisées par impression à jet d'encre par le Dr. Andreas Lesch à l'Ecole Polytechnique Fédérale de Lausanne.¹⁴⁻¹⁵ Les nanotubes de carbone imprimés sur une lamelle de microscope constituent l'électrode de travail. Cette électrode a permis d'obtenir des images ECL pas seulement en réflexion mais aussi en transmission (Fig. 9, ii).

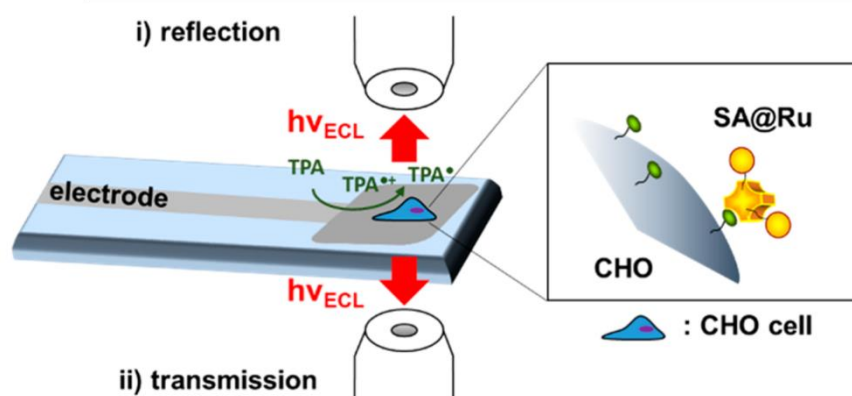


Figure 9. Schéma des deux configurations optiques utilisées pour la microscopie ECL confinée à la surface de l'électrode : i) en mode réflexion avec le carbone vitreux comme matériau d'électrode de travail ; ii) en mode transmission à travers l'électrode transparente composée par les nanotubes de carbone imprimés sur une lamelle de microscope.

La Figure 10 b) montre un exemple d'image ECL de cellules perméabilisées obtenue avec ce dispositif à base de nanotubes de carbone. Il est possible d'observer qu'en PL (Fig. 10, a) les cellules sont bien séparées les unes des autres. Au contraire, dans l'image ECL (Fig. 10, b) les cellules apparaissent plus rapprochées car la partie de la membrane plus proche de la surface d'électrode est plus visible en ECL qu'en PL.

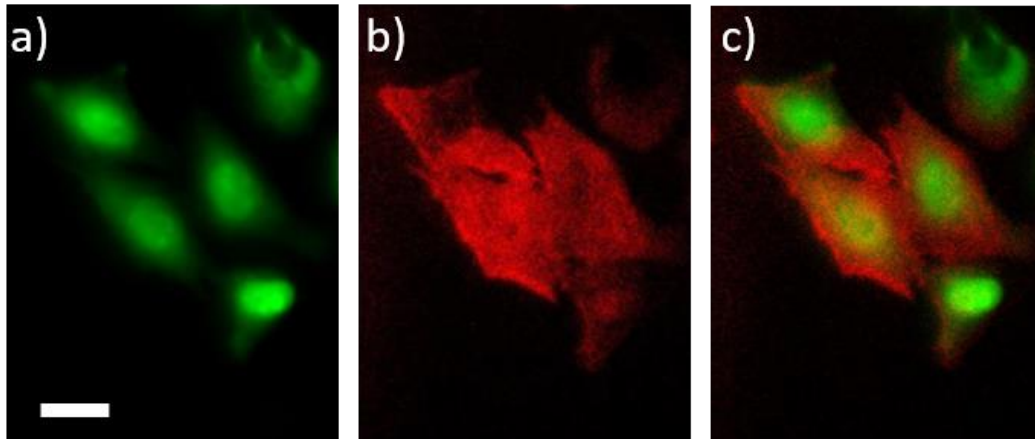


Figure 10. a) PL, b) ECL et c) superposition des deux images de luminescence des cellules CHO, obtenues par transmission en utilisant l'électrode de travail à base de nanotubes de carbone imprimés sur une lamelle de microscope. Les images PL et ECL ont été enregistrées dans la même région d'intérêt. L'image ECL a été obtenue dans une solution de PBS (pH = 7,4) contenant 100 mM de TPA et en appliquant un potentiel de 1,4 V vs Ag/AgCl/KCl 3 M. Barre d'échelle : 20 μ m.

Dans le futur, l'étude de système de marquage plus spécifique, basée sur l'interaction anticorps- antigène pour l'imagerie de composants intracellulaires, ainsi que l'utilisation d'autres systèmes ECL (luminophore/coréactif) sont prévus.

En conclusion, ces travaux de thèse ont porté sur l'étude du phénomène ECL. Des nouveaux luminophores ECL ont été étudiés. Des propriétés originales de l'émission ECL ont été démontrées. Des systèmes confinés aux échelles nanométriques et micrométriques ont permis de mettre en évidence de nouvelles caractéristiques de l'ECL. Enfin, les bases d'une nouvelle microscopie confinée à la surface et basée sur l'ECL ont été posées.

References

- (1) Richter, M. M. *Chemical Reviews* **2004**, *104*, 3003.
- (2) a)Miao, W. *Chemical Reviews* **2008**, *108*, 2506; b)Bard,A.J. *Electrogenerated Chemiluminescence*; M. Dekker: New-York, 2004.
- (3) a)Liu, Z.; Qi, W.; Xu, G. *Chemical Society Reviews* **2015**, *44*, 3117; b)Zhou, J.; Nie, L.; Zhang, B.; Zou, G. *Analytical Chemistry* **2018**, *90*, 12361; c)Guo, W.; Ding, H.; Gu, C.; Liu, Y.; Jiang, X.; Su, B.; Shao, Y. *Journal of the American Chemical Society* **2018**, *140*, 15904; d)Zou, G.; Tan, X.; Long, X.; He, Y.; Miao, W. *Analytical Chemistry* **2017**, *89*, 13024.
- (4) Li, H.; Daniel, J.; Verlhac, J.-B.; Blanchard-Desce, M.; Sojic, N. *Chemistry – A European Journal* **2016**, *22*, 12702.
- (5) Homberg, A.; Brun, E.; Zinna, F.; Pascal, S.; Górecki, M.; Monnier, L.; Besnard, C.; Pescitelli, G.; Di Bari, L.; Lacour, J. *Chemical Science* **2018**, *9*, 7043.
- (6) a)Zinna, F.; Di Bari, L. *Chirality* **2015**, *27*, 1; b)Longhi, G.; Castiglioni, E.; Koshoubu, J.; Mazzeo, G.; Abbate, S. *Chirality* **2016**, *28*, 696.
- (7) Zinna, F.; Voci, S.; Arrico, L.; Brun, E.; Homberg, A.; Bouffier, L.; Funaioli, T.; Lacour, J.; Sojic, N.; Di Bari, L. *Angewandte Chemie International Edition* **2019**, *58*, 6952.
- (8) Al-Kutubi, H.; Voci, S.; Rassaei, L.; Sojic, N.; Mathwig, K. *Chemical Science* **2018**, *9*, 8946.
- (9) Ismail, A.; Voci, S.; Pham, P.; Leroy, L.; Maziz, A.; Descamps, L.; Kuhn, A.; Mailley, P.; Livache, T.; Buhot, A.; Leichlé, T.; Bouchet-Spinelli, A.; Sojic, N. *Analytical Chemistry* **2019**.
- (10) Valenti, G.; Scarabino, S.; Goudeau, B.; Lesch, A.; Jović, M.; Villani, E.; Sentic, M.; Rapino, S.; Arbault, S.; Paolucci, F.; Sojic, N. *Journal of the American Chemical Society* **2017**, *139*, 16830.
- (11) Miao, W.; Choi, J.-P.; Bard, A. J. *Journal of the American Chemical Society* **2002**, *124*, 14478.
- (12) Sentic, M.; Milutinovic, M.; Kanoufi, F.; Manojlovic, D.; Arbault, S.; Sojic, N. *Chemical Science* **2014**, *5*, 2568.
- (13) Bondarenko, A.; Lin, T.-E.; Stupar, P.; Lesch, A.; Cortés-Salazar, F.; Girault, H. H.; Pick, H. *Analytical Chemistry* **2016**, *88*, 11436.
- (14) Voci, S.; Goudeau, B.; Valenti, G.; Lesch, A.; Jović, M.; Rapino, S.; Paolucci, F.; Arbault, S.; Sojic, N. *Journal of the American Chemical Society* **2018**, *140*, 14753.
- (15) Jović, M.; Zhu, Y.; Lesch, A.; Bondarenko, A.; Cortés-Salazar, F.; Gumy, F.; Girault, H. H. *Journal of Electroanalytical Chemistry* **2017**, *786*, 69.

O amazement of things! Even the least particle!
Oh spirituality of things!
I sing the Equalities, modern or old,
I sing the endless finales of things;
I say Nature continues – Glory continues;
I praise with electric voice;
For I do not see one imperfection in the universe;
And I do not see one cause or result lamentable at last in the universe.
I believe a leaf of a grass is no less than the journey-work of the stars,
And the pismire is equally perfect, and a grain of sand, and the egg of the wren.
And the question, o me? O life? So sad, recurring – what good amid these, o me? O life?
Answer:
That you are here – that life exists and identity,
That the powerful play goes on, and you may contribute a verse.

Leaves of Grass, Walt Whitman (1892)

Preface

Light has always attracted the human kind all over the millenniums and it was surely one of the first studied subject. As it happens for other chemical and physical processes, light cannot always be seen with naked eyes. The writer and chemist Primo Levi wrote that a chemist is like a blind assembler or disassembler, which uses many smart tricks to touch and see. What we tried to do in these years could be considered developing tricks, smart enough I hope, for “blinds” to “see” chemical processes related with a very marvelous light phenomenon that is electrogenerated chemiluminescence (ECL).

In this dissertation, ECL phenomenon represents the nucleus of original systems investigated at different scales. The successive experimental chapters are ordered depending on the scale of the systems under investigation: from the supramolecular scale, to the nano-scale, finally reaching the micrometric scale. In addition, since light is the final output of the ECL phenomenon, different potentialities of ECL such as microscopy and circularly polarized luminescence are developed.

In chapter I, an overview of ECL is presented. After a brief historical introduction, ECL will be introduced and distinguished from the other forms of light emission, such as photoluminescence

and chemiluminescence. The fundamentals of ECL will then be discussed, in particular ECL annihilation and coreactant pathways. Both inorganic and organic ECL luminophores and nanomaterials are reported as well as the main analytical applications of ECL in bioanalysis, which represented the main project of my PhD.

Chapter II is devoted to the analysis of two supramolecular systems. Electrochemical characterization and ECL analysis via annihilation and via reductive-oxidative coreactant pathways of new spirofluorene derivatives is reported, evidencing the role of the synthetic design in tuning the ECL performances. In the second part of the chapter, a new property of ECL is disclosed. Circularly polarization of ECL emission, originated from the enantiomers of a supramolecular purely organic system, is reported for the first time.

In chapter III, ECL meets the spreading field of “single-entity” electrochemistry. An enhancement of ECL emission in annihilation mode, thanks to the confinement in a nanofluidic channel, is discussed. ECL imaging permits to demonstrate an enhancement of bipolar electrochemistry performances, by exploiting a solid-state micropore configuration, in the second part of the chapter.

In chapter IV, a new microscopy, based on the ECL phenomenon, is developed and applied to the imaging of single cellular membranes. The surface confinement of ECL microscopy is demonstrated, with important consequences in terms of resolution and monitoring of passive transport properties through cellular membrane. Furthermore, the first steps towards potential analytical applications were moved, by testing the cellular membrane ECL imaging on a disposable analytical device, composed by a microscope coverslip and carbon nanotubes as an electrodic material.

Table of contents

List of Abbreviations.....	1
Symbols.....	5
I. Overview of Electrogenerated Chemiluminescence	7
1.1 Introduction	7
1.2 Light emission phenomena.....	8
1.2.1 Photoluminescence.....	9
1.2.2 Chemiluminescence.....	11
1.2.3 Light in electron transfer reactions.....	11
1.3 ECL mechanisms.....	14
1.3.1 ECL annihilation	14
1.3.2 Coreactant ECL	16
1.3.2.1 Mechanism of the coreactant ECL model system [Ru(bpy) ₃] ²⁺ /TPA.....	17
1.4 ECL luminophores	21
1.4.1 Inorganic systems.....	21
1.4.2 Organic systems	27
1.5 ECL coreactants	32
1.6 ECL analytical applications.....	34
1.6.1 ECL biorelated applications	34
1.7 Conclusions	38
References	39
II. Supramolecular ECL	45
2.1 Introduction	45
2.2 ECL study of trigonal truxene-core spirofluorene dyes	46
2.2.1 Electrochemical characterization.....	48
2.2.2 ECL via annihilation.....	52
2.2.3 ECL via reductive-oxidative coreactant pathway.....	56
2.3 Circularly polarization of ECL from a chiral bispyrene organic macrocycle	59
2.3.1 Synthesis.....	63
2.3.2 Electrochemical characterization.....	65
2.3.3 ECL analysis.....	67
2.3.4 ECL mechanisms.....	68
2.3.5 PL and ECL spectra.....	72
2.3.6 CP-ECL	74
2.3.6.1 Experimental set-up.....	75
2.3.6.2 CP-ECL of [18]-C-6-bispyrene enantiomers.....	76

2.4 Conclusions	80
References	81
III. ECL in Confined Environments	85
3.1 Introduction	85
3.2 ECL by nanofluidic confinement	95
3.2.1 Nanogap device description	95
3.2.2 Enhanced annihilation ECL.....	97
3.2.2.2 Two electrochemical modes	99
3.2.2.3 ECL imaging	102
3.2.3 ECL via coreactant pathway.....	104
3.2.3.1 ECL analysis.....	104
3.2.3.2 ECL imaging	106
3.3 Enhanced bipolar electrochemistry at solid-state micropores	110
3.3.1 Solid-State Micropore Description and Characterization.....	111
3.3.2 ECL analysis.....	113
3.3.3 ECL imaging	116
3.3.4 Simulations	118
3.4 Conclusions	120
References	122
IV. Surface-Confined ECL Microscopy	125
of Cellular Membranes	125
4.1 Introduction	125
4.2 Development of ECL microscopy of cellular membranes	133
4.2.1 Cellular membrane labeling procedure	133
4.2.2 Single cell ECL imaging: proof of concept.....	133
4.2.3 [Ru(bpy) ₃] ²⁺ / TPA mechanisms.....	135
4.2.4 Single cell ECL imaging: permeabilization step	137
4.2.5 [Ru(bpy) ₃] ²⁺ /DBAE ECL system for single cell ECL imaging	140
4.2.6 Comparison between fluorescence and ECL microscopies.....	142
4.3 Towards disposable device-based analysis.....	148
4.3.1 Transparent electrodes for applications in microscopy	148
4.3.2 CNTs-based inkjet-printed electrodes	149
4.3.3 CNTs inkjet-printed electrodes: application to ECL microscopy	151
4.4 Conclusions	152
References	154
Experimental section	157
1. Chapter II – Supramolecular ECL.....	157

1.2	ECL study of trigonal truxene-core spirofluorene dyes	157
1.2.2	Materials.....	157
1.2.2	Electrochemical characterization.....	157
1.2.3	Electrochemiluminescence.....	158
1.3	Circularly polarization of ECL from a chiral bis-pyrene organic macrocycle	158
1.3.1	Materials.....	158
1.3.2	Electrochemical and ECL characterization	158
1.3.3	CP-ECL measurements	159
2.	Chapter III – ECL in confined environments	159
2.1	ECL by nanofluidic confinement	159
2.1.1	Materials.....	160
2.1.2	Device fabrication	160
2.1.3	Electrochemical and ECL characterizations.....	160
2.1.4	ECL Imaging	160
2.2	Enhanced bipolar electrochemistry at solid-state micropores	160
2.2.1	Materials.....	161
2.2.2	Fabrication of silicon with integrated micropore	161
2.2.3	Electrochemical and ECL characterization	161
2.2.4	Imaging.....	161
3.	Chapter IV - Surface-Confined ECL Microscopy of Cellular Membranes	161
3.1	Materials.....	162
3.2	Cell culture, labeling and permeabilization.....	162
3.3	ECL analysis.....	162
3.4	Imaging.....	163
3.5	Atomic force microscopy	163
	References	164
	Conclusions and Perspectives.....	165
	Acknowledgements	169

List of Abbreviations

Abbreviation	Meaning
ABA	<i>p</i> -aminobenzoic acid
AFM	atomic force microscopy
AFP	alpha fetoprotein
APDEA	<i>N</i> -(3-aminopropyl)diethanolamine
a.u.	arbitrary units
BHQ	black hole quencher
BODIPY	boron-dipyrromethene
BPE	bipolar electrode
BPO	benzoyl peroxide
CE	counter electrode
CEA	carcinoembryonic antigen
CD	circular dichroism
CHO	mammalian Chinese hamster ovary cells
CL	chemiluminescence
CNT	carbon nanotube
CP-ECL	circular polarization of electrogenerated chemiluminescence
CPL	circular polarization of luminescence
CSP-HPLC	chiral stationary phase – high-performance liquid chromatography
DAA1	9,10-bis(<i>N</i> -methylimidazolium-3-propoxyphenyl)anthracene
DAA2	9,10-bis(<i>N</i> -methylimidazolium-3-propoxyphenil-2,6 dimethylphenyl)anthracene
DBAE	2-(dibutylamino)ethanol
DMF	dimethylformamide
DNA	deoxyribonucleic acid
DPA	9,10-diphenylanthracene
DSN	doping silica nanoparticle

ECR	enzymatically cyclic release
ECL	electrogenerated chemiluminescence
EGFR	epidermal grow factor receptor
ELISA	enzyme-linked immunosorbent assay
EMCCD	electron multiplying charge coupled device
Eq.	equation
ESR	electron spin resonance
<i>et al.</i>	<i>et altera</i> / and others
Fig.	figure
f-MWCNTs	functionalized multi walled carbon nanotubes
FO	functional oligonucleotide
FTO	fluorine doped tin oxide
GC	glassy carbon
GHD	glucose dehydrogenase
HCR	hybridization chain reaction
HOMO	highest occupied molecular orbital
<i>i.e.</i>	<i>id est</i> / for example
ITO	indium doped tin oxide
L012	8-amino-5-chloro-7-phenylpyrido[3,4-d]-pyridazine-1,4(2H, 3H)-dione]
LC	ligand centered
Luminol	5-amino-2,3-dihydrophthalazine-1,4-dione
LUMO	lowest unoccupied molecular orbital
MC	metal centered
MLCT	metal to ligand charge transfer
NA	numerical aperture
NADH	nicotinamide adenine dinucleotide
NCs	nanocrystals
NHE	normal hydrogen electrode
NHS	<i>N</i> -hydroxysuccinimide
NPs	nanoparticles

NSOM	near-field scanning optical microscopy
NDs	nanodots
OPV	oligo (<i>p</i> -phenylenevinylene)
OTE	optically transparent electrode
PAH	polyaromatic hydrocarbons
PALM	photoactivated localization microscopy
PDMS	polydimethylsiloxane
Pdots	polymer dots
PEEK	polyether ether ketone
PEM	photoelastic modulator
PET	polyethylene
PFA	paraformaldehyde
Ph	phenyl
PITX	palitoxin
PL	photoluminescence
PMT	photomultiplier tube
PSA	prostate specific antigen
PTFE	polytetrafluoroethylene
pt-TOxT-Sq	pyridylthiazole ligand with trioxatridecane chain and squarate amide ethyl ester
QDs	quantum dots
QRE	<i>quasi</i> reference electrode
RE	reference electrode
RNA	ribonucleic acid
ROS	reactive oxygen species
SAv@Ru	[Ru(bpy) ₃] ²⁺ - labeled streptavidin
SCE	saturated calomel electrode
SECM	scanning electrochemical microscopy
SEM	scanning electron microscope
SERS	surface enhanced Raman spectroscopy
SPR	surface plasmon resonance

ssDNA	single stranded deoxyribonucleic acid
STED	stimulated emission depletion
STORM	stochastic optical resolution microscopy
TBA	tetrabutylammonium
TIRF	total internal reflection fluorescence microscopy
TPA	tri-n-propylamine
TTA	triplet-triplet annihilation
UV	ultraviolet
WE	working electrode

Symbols

Symbol	Meaning	Unit
d	distance between feeder electrodes	m
D	diffusion coefficient	cm^2s^{-1}
ΔE_p	peak to peak separation	V
ΔG°	free energy	J or eV
ΔH°	enthalpy	J or eV
ΔI	difference in the luminescence intensity	a.u.
$\Delta \lambda$	difference between wavelengths maxima	nm
ΔS°	entropy	J/K or eV/K
ΔV_{BE}	interfacial potential difference	V
ΔV_{FE}	feeder electrodes potential difference	V
E°	standard potential of a redox couple	V
E_p	peak potential	V
E_s	energy of singlet excited state	eV
E_{exc}	energy of the excimer	eV
F	Faraday constant	96485,3329 s A/mol
Φ_{FL}	fluorescence quantum yield (%)	-
Φ_{ECL}	ECL efficiency (%)	-
g_{LUM}	luminescence dissymmetry factor	-
g_{ECL}	ECL dissymmetry factor	-
h	Planck's constant	Js
I_{L}	left-circularly polarized light intensity	a.u.
I_{R}	right-circularly polarized light intensity	a.u.
L	length of the BPE	m
λ	wavelength	nm

ν	frequency	Hz
$O_{n,n}$	oxidation n potential of compound n	V
pKa	acid dissociation constant	-
r	resolution	m
$R_{n,n}$	reduction n potential of compound n	V
§	paragraph	-
h	Planck's constant	$6.62607015 \times 10^{-34}$ Js
T	temperature	K
\varnothing	disk electrode diameter	m
$\tau_{1/2}$	half-life time	s

I. Overview of Electrogenerated Chemiluminescence

1.1 Introduction

Electrogenerated chemiluminescence (or electrochemiluminescence, ECL) is the emission of light from excited states produced by reactive intermediates generated at an electrode surface.¹ The first studies of chemiluminescence resulting from electrogenerated species were reported in 1920s.² In 1927, Dufford et al.³ published a study of the phenomenon with Grignard compounds in anhydrous ether applying between 500 V and 1500 V at cathode or anode. In 1929, Harvey⁴ observed luminescence during electrolysis from a solution of 5-amino-2,3-dihydrophthalazine-1,4-dione (luminol) at basic pH at the interface with anode surface (by applying about 2.8 V). He suggested to apply the phenomenon as a test for active oxygen detection. After few studies,^{2,5} more detailed investigations followed in 1960s, due to the introduction of the use of aprotic solvents.⁶ These first ECL experiments involved the generation of the oxidized and reduced form of the luminophore, generating the excited state via annihilation reaction. The wider potential range availability of aprotic solvents allowed ECL analysis of several organic molecules (*vide* § 1.4).¹ ECL emission from aromatic hydrocarbons (such as diphenylanthracene, anthracene and rubrene) was described by Hercules⁷ in 1964, by cycling the electrode potential and by applying a dc current to two closely spaced Pt electrodes. In the same years, other studies permitted a deeper understanding of ECL on aromatic hydrocarbons.⁸ First ECL observations for the complex $[\text{Ru}(\text{bpy})_3]^{2+}$ were reported by Lytle

and Hercules in 1966⁹ and by Tokel and Bard in 1972,¹⁰ respectively in water and acetonitrile. In 1977, for the first time ECL generation with the use of coreactants was proposed.¹¹ The concomitant oxidation of oxalate and various ECL luminophores (diphenylanthracene, rubrene, Ru(bpy)₃(ClO₄)₂ and Os(bpy)₃(ClO₄)₂) at the electrode surface produced ECL emission. Other reducing agents were studied in the successive years, to react with the ECL luminophores, for potential analytical applications.¹² Tri-n-propylamine (TPA) and other aliphatic amines became in the successive years the most studied and utilized coreactants, thanks to the high ECL efficiencies correlated with the use of those systems.¹³ The first ECL instrument for the detection of ECL labels ([Ru(bpy)₃]²⁺) on the surface of magnetic beads in presence of TPA was commercialized by Roche in 1994.¹⁴ In parallel with the development of new ECL luminophores, coreactants and analytical applications, fundamentals of ECL were investigated and rate constants for several annihilation reactions were calculated.^{1,15} Moreover, ECL provided the first evidence of the Marcus inverted region. The generation of very reactive intermediates directly at the electrode surface has permitted to observe experimentally that the formation of the excited states results kinetically (very low activation energy barrier) more favored than the thermodynamically (highly negative free energy) more favored back electron transfer to the ground state.¹⁶ To date, ECL immunoassay systems for the sensitive and selective detection of several types of biomolecules are commercialized, for example, by Roche Diagnostic Corporation and Mesoscale Diagnostics.¹⁴

1.2 Light emission phenomena

The phenomenon of radiative deactivation of a species at the electronically excited state is called luminescence. Different types of luminescence are known, depending on the pathway followed for the generation of the emitting state. In photoluminescence (PL), light emission is caused by an initial photoexcitation step, while in chemiluminescence (CL) the excitation occurs following chemical reactions. This latter is called electrogenerated chemiluminescence when the reactants are electrochemically generated.¹⁴ Electroluminescence is instead correlated with the radiative recombination of holes and electrons in a material, after the application of a strong electric field or current flow.¹ Other light emission phenomena are bioluminescence¹⁷ (chemiluminescence from living organisms), sonoluminescence¹⁸ (excitation from nonlinear motion of gas bubble, i.e. by ultrasonication or by energy transfer), and radiochemiluminescence¹⁹ (radiation-induced chemical excitation). In this paragraph,

photoluminescence and chemiluminescence are described. In addition, the role of light in electron-transfer reactions is briefly discussed.

1.2.1 Photoluminescence

The interaction between light and molecular systems is generally an interaction between one photon and one molecule:



Where A represents the molecule at the electronically ground state, $h\nu$ the absorbed photon and A^* the molecule in the electronically excited state. After light absorption, A^* can undergo different deactivation pathways: chemical reaction (with the generation of other species), non-radiative deactivation (degradation to heat) and radiative deactivation. This latter is defined as photoluminescence.²⁰ The processes of light absorption and emission can be conveniently discussed by the Jablonski diagram (Fig. 1.1).

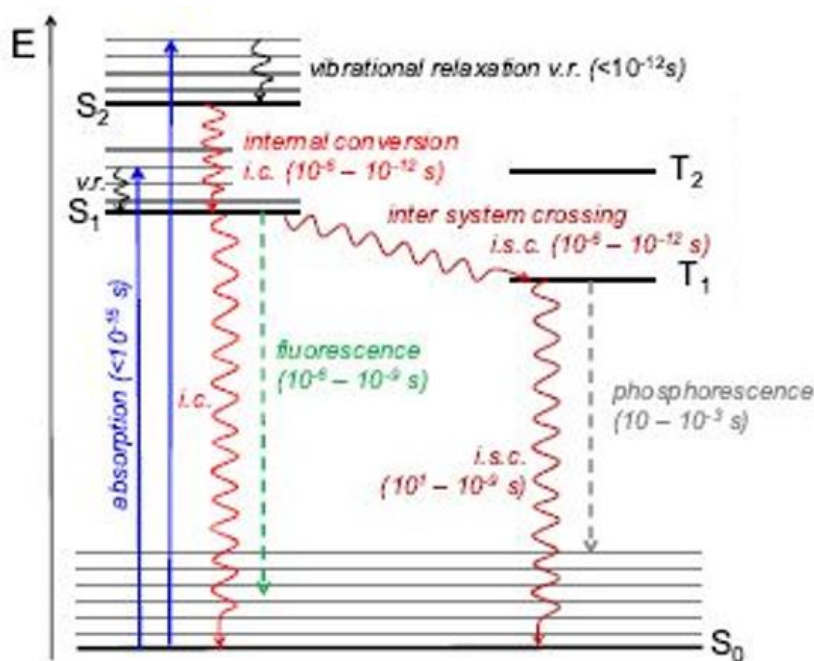


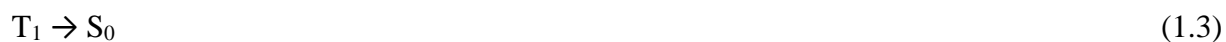
Figure 1.1 A representation of Jablonski diagram.²¹

The electronic states are represented as thick horizontal lines. The vertical ones indicate the state of higher energies. S₀ represents the electronically ground state (singlet as usual for organic compounds), S₁ the first excited singlet state, S₂ the second excited state. Excited states

with higher energies are not considered in the scheme. The triplet excited state T_1 is represented on the right, horizontally separated to distinguish the multiplicity. Vibrational levels of each electronic state are represented as thin lines, the lowest one indicates $v = 0$. Absorption is indicated with solid arrows, radiative deactivations with dot arrows and radiationless transitions with wavy arrows.²⁰ Photoexcitation permits the population of electronic states with higher energy than the ground state. Following absorption, molecules relax usually to the lowest vibrational level ($v = 0$) of the populated state (vibrational relaxation) in a very short time ($< 10^{-12}$ s). According to Kasha's rule, emission can usually be observed only from the lowest excited state of any multiplicity. A radiation less transition occurs, called internal conversion, in a lower range of time than relaxation to the ground state (Fig. 1.1). Several pathways can lead to the deactivation of the molecule at the state S_1 . Radiationless transitions to the ground state (internal conversion) can occur. Otherwise, a spin-forbidden non-radiative transition, called inter system crossing, allows the population of T_1 and from this latter to the ground state S_0 . Photoluminescence can be divided in fluorescence and phosphorescence. Fluorescence indicates light emission from a spin-allowed electronic transition, where the multiplicity of the states is the same. Therefore, an example of fluorescence can be related to the electronic transition:



from the first excited singlet state to different vibrational levels of the singlet ground state, which then rapidly relax to $v = 0$. A spin-forbidden transition is called phosphorescence and it is generally shifted to longer wavelengths than fluorescence, for example:



The lowest probability of this latter transition, caused by a change in multiplicity, results in rate constants several orders of magnitude lower than those for fluorescence.²⁰⁻²¹ Phosphorescence is extended on a longer time interval (from milliseconds to seconds) and it is usually shifted to longer wavelengths than fluorescence. In presence of heavy atoms, spin-orbit coupling becomes high enough to facilitate intersystem crossing and therefore enhance phosphorescence quantum yields. Generally, the energy of emission transitions are lower than absorption ones. Consequently, radiative deactivation transitions occur at longer wavelengths than absorption

transitions. This phenomenon is called Stokes shift and is caused by the rapid vibrational relaxation to the lowest vibrational level of S_1 . On the other hand, further decay to higher vibrational levels of S_0 could also result in loss of excitation energy by thermalization of the excess vibrational energy. Effects correlated with the solvent, excited-state reactions and bimolecular processes like complex formation account for the Stokes shifts.²⁰⁻²¹

1.2.2 Chemiluminescence

In chemiluminescence, light emission results from an electronically excited state produced by a chemical reaction in a homogeneous phase. Such chemical reaction generates sufficient energy to induce the promotion of an electron from the ground state to an excited electronic state. Even if the process to reach the excited state is different, the radiative deactivation process is the same as photoluminescence. A chemiluminescent reaction can follow two mechanisms. In a direct route, a part of the product or intermediate can be generated at the electronic excited state, which then relaxes via light emission. Otherwise, chemiluminescence can occur from the excited state of a species that is not directly involved in the chemical reaction. An energy transfer from a product or intermediate of the reaction at the excited state to a fluorophore can occur, resulting in chemiluminescent emission from the sensitized species.²² The most studied chemiluminescent system is luminol, thanks to its analytical applications, in particular for the detection of oxidants or metal ions (due to their use as catalysts) or products of enzymatic activities. By reaction with a strong oxidizing agent (i.e. H_2O_2), and in presence of a catalyst (such as a metal, a metal-containing compound or an enzyme) in strong basic conditions, luminol can produce 3-aminophthalate in an excited electronic state, which then can emit chemiluminescent light.

1.2.3 Light in electron transfer reactions

Electron transfer reactions are particularly important in the connection between light and chemistry.²³ Light can act as a catalyst (photocatalysis) or as a reactant (photochemical reactions):



By contrast, in chemiluminescent reactions light is generated as a product:



The generation of the electronically excited state of a molecule involves usually the promotion of an electron from a low energy (bonding) orbital to a high energy (antibonding) orbital. Therefore, a species at the excited state will be a better electron donor and a better electron acceptor than at the corresponding ground state. When the Stokes shift is small, it is possible to approximate the reduction and the oxidation potentials of a molecule (A) at the excited state as:

$$E^\circ (A^*/A^-) = E^\circ (A/A^-) + E (A^*) \quad (1.6)$$

$$E^\circ (A^*/A^+) = E^\circ (A/A^+) + E (A^*) \quad (1.7)$$

Where $E^\circ (A/A^-)$ and $E^\circ (A/A^+)$ are respectively the reduction and the oxidation potentials of A at the ground state and $E (A^*)$ is the electronic spectroscopic energy, equal to the difference between the first ($\nu = 0$) vibrational level of the ground state and the first ($\nu' = 0$) vibrational level of the excited state, which can be approximated as¹⁴:

$$E (A^*) = h c / \lambda \quad (1.8)$$

Where h is the Plank constant (4.13×10^{-15} eV), c is light speed (3.00×10^8 ms⁻¹) and λ is the emission wavelength. Figure 1.2 reports three different electron transfer processes involving light for the reaction:



In the first scheme (Fig. 1.2, a), the electron transfer process is exoergonic and a high activation energy is needed. The excited state A^* is generated by photoexcitation of A. A^* acts as a stronger oxidant than A, and the electron transfer reaction between A^* and B presents a decreased activation energy barrier due to the increase in reaction exoergonicity. In this case, light plays the role of a catalyst (photocatalysis), by modifying the kinetic barrier of the reaction.

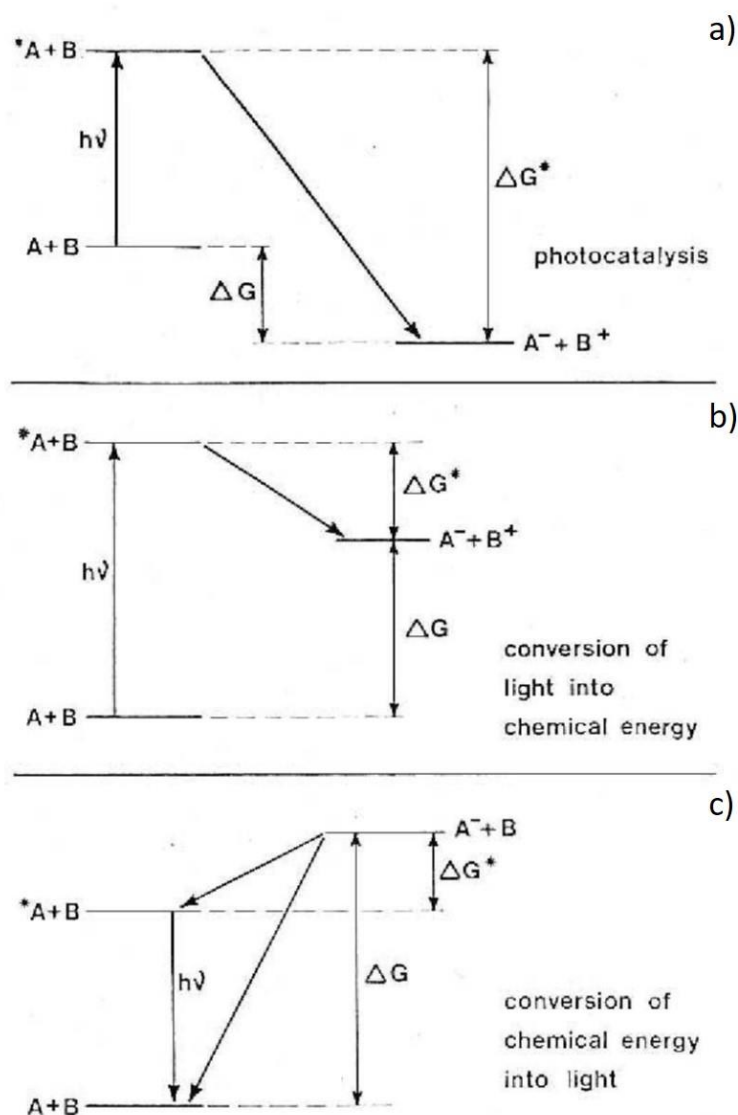


Figure 1.2 Schematic representations of three possible ways in which light can be involved in electron transfer processes. (Reported with modifications from [23])

The case shown in Figure 1.2 b) corresponds to a highly endoergonic reaction. The generation of A* by photoexcitation allows the electron transfer process. A fraction of the light energy can be converted in chemical energy of the products. In the third reported situation (Fig. 1.2, c), the reaction from A + B to A⁻ + B⁺ cannot be driven neither thermally or photochemically. The generation of A⁻ + B⁺ at the electrode surface by an alternate pulsing at appropriate potential values would allow the back electron transfer to A + B to occur with complete dissipation of the excess of free energy into heat or via the intermediate formation of A* + B. The preferential pathway can be estimated by the Marcus theory of electron transfer.²⁴ The deactivation of A* to A converts a fraction of the free energy in light energy by radiative emission. This particular

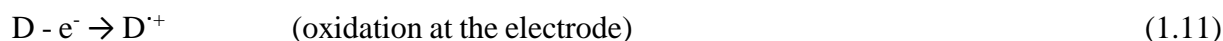
case of chemiluminescence emission is denominated electrogenerated chemiluminescence (ECL).^{20,23-24}

1.3 ECL mechanisms

In this section, fundamentals of ECL generation are treated, describing the two main pathways for the excited states production: ion annihilation and coreactant ECL.

1.3.1 ECL annihilation

The first reported ECL pathway concerned the generation of the excited state by annihilation reaction between an oxidized and a reduced species, of the same molecule or of two different species. The general mechanisms can be represented by the following equations (Eq. 1.10-1.15):



or



Where the acceptor, A, and the donor, D, can be the same species, ${}^1A^*$ is the singlet excited state and ${}^3A^*$ is the triplet excited state. The corresponding enthalpy for the reaction can be approximated as:¹⁴

$$\Delta H_{ann}^\circ = \Delta G_{ann}^\circ + T\Delta S = E_{p,A^+/A} - E_{p,A/A^-} - 0.16 \text{ eV} \quad (1.16)$$

Where ΔH_{ann}° is the enthalpy for the annihilation (in eV), $E_{p,A^+/A}$ and $E_{p,A/A^-}$ are the peak potentials for respectively the electrochemical oxidation and reduction (in V), and 0.16 eV corresponds to the entropic contribution ($T\Delta S$) at 25°C (0.10 eV) with an addition of 0.057 eV, due to the difference between the reversible potential and the peak potential of each reaction.¹⁴

When ΔH_{ann}° presents a higher value than the energy necessary to populate the lowest excited state (singlet E_{A^*} , Eq.1.8) from the ground state, the system is called “energy-sufficient” and $^1A^*$ can be directly populated (Eq. 1.12, “S-route”). By contrast, when ΔH_{ann}° is lower than the singlet excited state ($^1A^*$) energy but higher than the triplet excited state ($^3A^*$) energy, the system will follow the “T-route” (or “energy-deficient” way) as reported in equations 1.13 and 1.14. Annihilation reactions permit not only the population of singlet and triplet excited states but also the direct generation of excimers and exciplexes (called “E-route”), particularly in the case of polyaromatic hydrocarbons, following the reported mechanism (Eq. 1.17-18):²⁵



Triplet-triplet annihilation (TTA) can also lead to the generation of excimers or exciplexes (Eq. 1.19):¹⁴



In the range 400-689 nm, ECL emissions are associated with a singlet excited state energy (singlet E_{A^*} , Eq. 1.8) between 3.1 and 1.8 eV. Consequently, the potential window of the electrochemical system should be wide enough (from -2 V to about 3.3 V) to allow the production of stable cation and anion radicals. Anhydrous organic solvents represent the preferential environment for ECL via annihilation. The potential of the working electrode can be pulsed alternatively at the appropriate potentials to generate the oxidized (1.10) and the reduced (1.11) species of the luminophore. During the two potential steps, both radical species exist in the diffusion layer near the electrode and can react via annihilation (1.12). The generation of the oxidized and reduced species can occur also concomitantly by employing two different working electrodes at a distance short enough to permit the reaction between the two intermediates.^{15c,26} Different methods can be actuated, such as the use of a ring disk electrode^{15c} or of interdigitated microelectrodes arrays.²⁷ Scanning electrochemical microscopy (SECM), a generation/collection mode, has been recently applied to the investigation of ECL via annihilation.²⁸ In last decades, the development of lithographically microfabricated nanogap devices has permitted to decrease the distance between two independently biased working

electrodes and to obtain an enhancement in ECL via annihilation thanks to the nanoconfinement ($< 2 \mu\text{m}$).²⁹ Independently on the electrochemical mode applied for the generation of the two radicals, their lifetime must be long enough to allow the annihilation reaction and then ECL emission. Cyclic voltammetry represents an excellent probe to determine the best potential values for the generation of the oxidized and reduced species and to test their stability.^{26a,30}

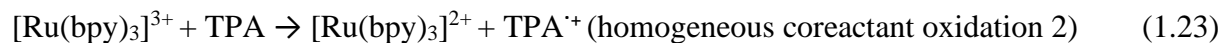
1.3.2 Coreactant ECL

ECL emission can occur also in one directional potential scanning at an electrode, in a solution containing an ECL luminophore and a coreactant. This latter generates, upon oxidation or reduction, an intermediate that can react with the ECL luminophore, producing excited states.^{1,26a,31} It is possible to distinguish two coreactant ECL pathways, “oxidative-reductive” ECL and “reductive-oxidative” ECL. When the electrochemical oxidation of the coreactant generates a strong reducing intermediate the corresponding ECL reactions are defined as “oxidative-reductive” ECL.³² While “reductive-oxidative” ECL occurs when the electrochemical reduction of the coreactant generates a strong oxidizing species.^{31,33} Typical “oxidative-reductive” coreactants are oxalate, amino-acids, TPA and NADH.¹⁴ $\text{S}_2\text{O}_8^{2-}$ and H_2O_2 are examples of “reductive-oxidative” coreactants. “Oxidative-reductive” ECL is considered a more usable pathway. More coreactants following this route are known and the narrow cathodic electrochemical window in aqueous solutions limits the “reductive-oxidative” ECL. The generation of ECL emission in a single potential step can be a significant advantage in several ECL studies. It allows to generate ECL emission from luminophores that present only an electrochemically reversible reduction or oxidation.¹ In addition, in solvents with a narrow potential window, such as water, ECL can still occur by adding a coreactant, generating only the reduced or oxidized form of the luminophore. A good coreactant candidate should combine a high solubility in the reaction medium and good electrochemical properties (easily reduced or oxidized, in the same potential region of the luminophore). The electrochemically generated intermediate of the coreactant must be stable enough to permit the reaction with the ECL luminophore with a good reaction rate. Finally, the coreactant should not act as an ECL emission quencher or give an ECL signal itself, increasing the background of the emission. Coreactant ECL has been used in a wide range of analytical applications. ECL can be applied to the analysis of various species.¹ The comprehension of coreactant ECL mechanism is fundamental for improving coreactant ECL performances, for the design of new potential coreactant ECL systems and in the development of ECL analytical applications. The vast

majority of coreactant ECL and their related analytical applications are based on the ECL system involving tris(2,2'-bipyridine)ruthenium(II), $[\text{Ru}(\text{bpy})_3]^{2+}$, and TPA as coreactant, because of the excellent ECL properties, even in aqueous media and in presence of oxygen.¹ Such an ECL system forms the basis of commercial ECL immunoassays and DNA analyses.³⁴

1.3.2.1 Mechanism of the coreactant ECL model system $[\text{Ru}(\text{bpy})_3]^{2+}/\text{TPA}$

In 1990,^{13b} Leland and Powell reported the first study on ECL emission from the system $[\text{Ru}(\text{bpy})_3]^{2+}/\text{TPA}$ on a gold electrode in buffered aqueous solution. An overwhelming number of publications followed, in order to clarify the related ECL emission mechanism.³⁵ Several pathways are possible and the most probable one depends on the experimental conditions, in particular on the relative concentrations of $[\text{Ru}(\text{bpy})_3]^{2+}$ and TPA.



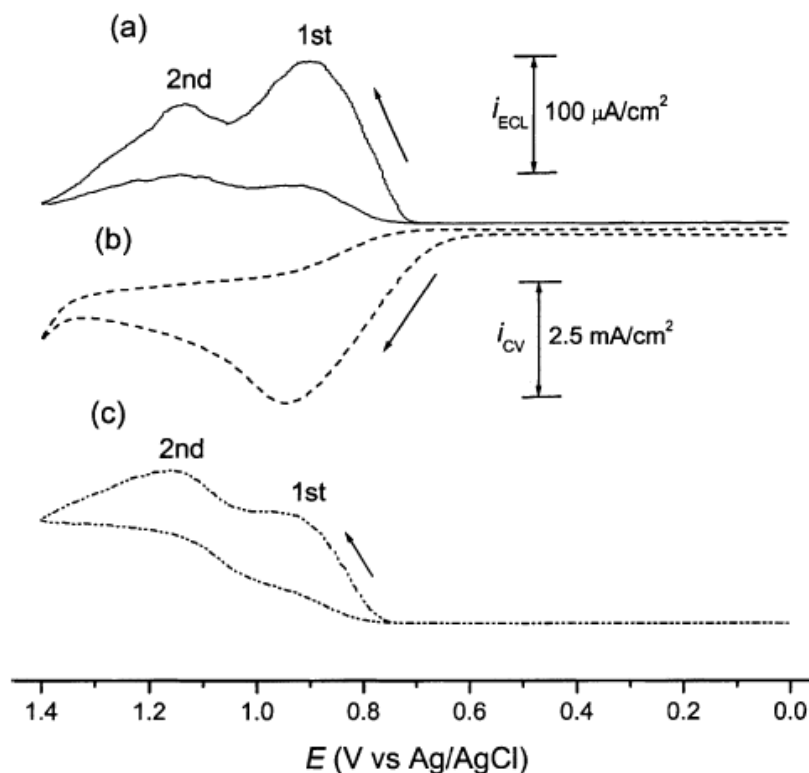


Figure 1.3 a) ECL and b) cyclic voltammogram of 1.0 nM of $[\text{Ru}(\text{bpy})_3]^{2+}$ in the presence of 0.10 M of TPA with 0.1 M Tris/0.10 M of LiClO_4 buffer (pH = 8) at a GC electrode (d = 3mm). Scan rate = 50 mV/s. c) As a) but with 1.0 μM $[\text{Ru}(\text{bpy})_3]^{2+}$. The ECL intensity scale is given for c) and should be multiplied by 100 for a).³⁶

By imposing a sufficiently anodic potential, the luminophore and TPA are both oxidized (Eq. 1.21-22). The acid-base equilibrium of TPA ($\text{pK}_a \sim 10.4$) is correlated with the oxidation peak potential of the coreactant (~ 0.86 V vs NHE)^{35c}. By decreasing the pH (no variation above pH = 11), a concomitant shift towards more positive potentials of the oxidation peak potential occurs. TPA can also be homogeneously oxidized by the electrochemically oxidized form of the luminophore (Eq. 1.23). This “catalytic route” resulted more probable at high $[\text{Ru}(\text{bpy})_3]^{2+}$ concentrations.^{35a} The route following the direct electrochemical oxidation of TPA (Eq. 1.22), becomes significant in low concentrations of $[\text{Ru}(\text{bpy})_3]^{2+}$ ($< \mu\text{M}$) or at high TPA concentrations. Two ECL waves, associated with $[\text{Ru}(\text{bpy})_3]^{2+*}$ emission, were experimentally observed on both glassy carbon (GC) and Au electrodes.³⁶ The first ECL wave occurs at a less positive potential than $[\text{Ru}(\text{bpy})_3]^{2+}$ oxidation potential, while the second ECL emission is observed at potentials where $[\text{Ru}(\text{bpy})_3]^{2+}$ is electrochemically oxidized (Fig. 1.3). In Figure 1.3, ECL emission intensities are reported for the system $[\text{Ru}(\text{bpy})_3]^{2+}/\text{TPA}$ at concentrations of 1 nM and 1 μM respectively. The first ECL peak at low potentials decreased with the increasing of $[\text{Ru}(\text{bpy})_3]^{2+}$ concentration. No ECL signal was recorded in the absence of $[\text{Ru}(\text{bpy})_3]^{2+}$ or TPA. As experimentally demonstrated, the first ECL peak is associated with an

ECL mechanism different from the second peak. SECM experiments were applied to such ECL system to clarify the predominant mechanism in this case. A modified $[\text{Ru}(\text{bpy})_3]^{2+}$ complex was immobilized on an indium tin oxide (ITO) electrode surface, as substrate. The reaction medium was composed by a buffered ($\text{pH} = 8$) solution 0.1 M of TPA. The ECL signal could be detected only at a very short distance between the SECM tip and the ITO surface. The experiments demonstrated that it is possible to obtain ECL emission only by direct oxidation of TPA at the electrode surface (Eq. 1.27-28).³⁶ The reducing radical TPA^\cdot (~ -1.7 V vs Ag/AgCl)³⁷, generated from TPA oxidation, can diffuse to ITO substrate and react with the immobilized $[\text{Ru}(\text{bpy})_3]^{2+}$ with the generation of the excited state. Thanks to SECM and digital simulations, a half-life time ($\tau_{1/2}$) of about 0.2 ms was estimated for the radical cation $\text{TPA}^{\cdot+}$. The recording of the electron spin resonance (ESR) spectrum of this latter permitted to confirm the presence of such intermediate in this alternative route. Studies on $[\text{Ru}(\text{bpy})_3]^{2+}$ -labeled microbeads permitted to confirm the role of the direct oxidation of TPA and of the radical cation $\text{TPA}^{\cdot+}$ in experimental conditions in which only a very low concentration of $[\text{Ru}(\text{bpy})_3]^{2+}$ molecules can be directly oxidized at the electrode.³⁸ The anodic oxidation of TPA is strongly dependent on the electrode material.^{35a,39} At a GC electrode, TPA oxidation starts at about 0.6 V vs SCE and is characterized by a broad irreversible anodic peak. The production of surface oxides on Au and Pt electrodes limits drastically TPA oxidation, decreasing ECL intensity. Nonionic surfactants⁴⁰ (i.e. Triton X-100, Nonidet P40, or Thesit) can adsorb on the surface of the metallic electrode and increase the hydrophobicity of the surface. At surfactants concentrations below the critical micelle concentrations, ECL increases. The use of the nonionic fluorosurfactants⁴¹ allows also to retard the growth of the surface oxide layer. The fluorinated chains close to the electrode surface (Fig. 1.4) limits the access of H_2O at the electrode, leading to a more efficient ECL emission, more than with a simple nonionic surfactant.

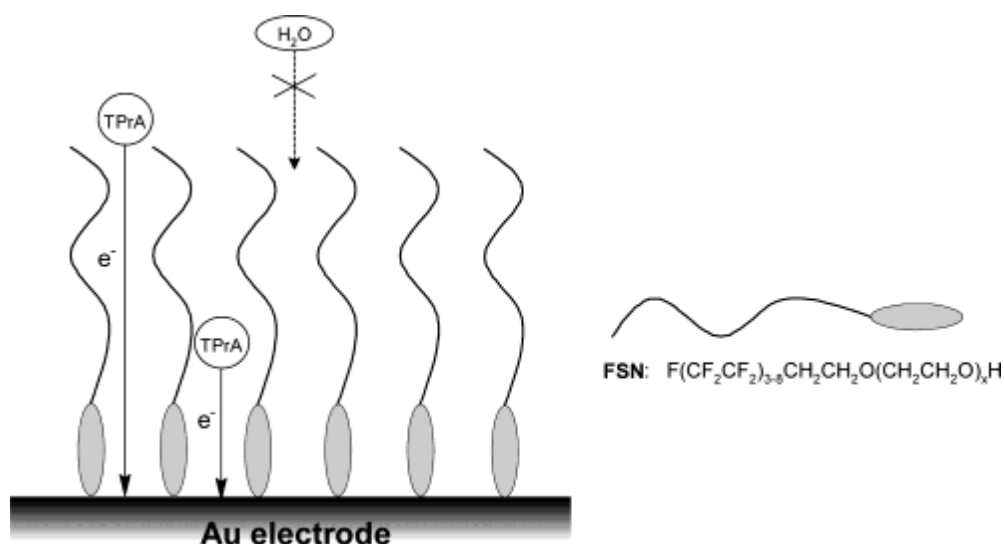


Figure 1.4 Adsorption of a nonionic fluorosurfactant (FSN) at a gold electrode. The adsorption precludes the access of H_2O to the electrode surface while it facilitates the oxidation of TPA.⁴¹

The addition of a small amount of halide species was also found to inhibit the formation of surface oxide on Pt and Au electrodes, with a maximum enhancement of TPA oxidation by using a bromide-containing solution at Au electrode.^{35a} The strong dependence of ECL performances on electrode materials and on the presence of surfactants confirm the importance of the direct oxidation TPA pathway in the ECL generation.³⁶ The ECL intensity is also strongly related to the solution pH.^{13b,42} It drastically increases at $\text{pH} > 5.5$, with a maximum at $\text{pH} = 7.4$. TPA^{*+} deprotonation reaction (Eq. 1.25), intermediates stability as well as the reduced TPA solubility at high pH values present the main reasons of this behavior. At $\text{pH} > 9$, $[\text{Ru}(\text{bpy})_3]^{3+}$ can produce ECL emission also by reaction with the hydroxide ions, generating an ECL background and decreasing the selectivity of the system in analytical applications.¹⁴ Finally, O_2 influences the ECL intensity in the coreactant ECL system $[\text{Ru}(\text{bpy})_3]^{2+}/\text{TPA}$.⁴³ At high $[\text{TPA}]$, oxygen molecules are completely reduced by the strong amount of reducing intermediate radicals, and no quenching effect occurs. By contrast, at low $[\text{TPA}]$ the amount of reducing intermediated radicals generated by TPA oxidation is relatively low. Therefore, O_2 can act as interceptor, reacting with such intermediates before these latter meet $[\text{Ru}(\text{bpy})_3]^{2+}$ molecules. Consequently, in those experimental conditions oxygen results as an ECL quencher, in particular of the low-potential route (Eq. 1.27-28), where only TPA is directly oxidized at the electrode.

1.4 ECL luminophores

ECL luminophores can be separated in three categories: inorganic systems, in particular organometallic complexes; organic systems and nanomaterials (semiconductor nanoparticles, carbon dots, etc.).

1.4.1 Inorganic systems

The complex $[\text{Ru}(\text{bpy})_3]^{2+}$ (Fig. 1.5, a) was the first studied and still the most utilized. Indeed, the unique combination of chemical stability, redox properties, excited state reactivity, luminescence emission and excited state lifetime has permitted the intensive use of this complex for fundamental studies as well as for several applications over the years.^{1,14,26a,44} Its solubility extends from water to a variety of organic solvents and can undergo reversible one-electron transfer reactions at easily achievable potentials (Fig. 1.5, b).

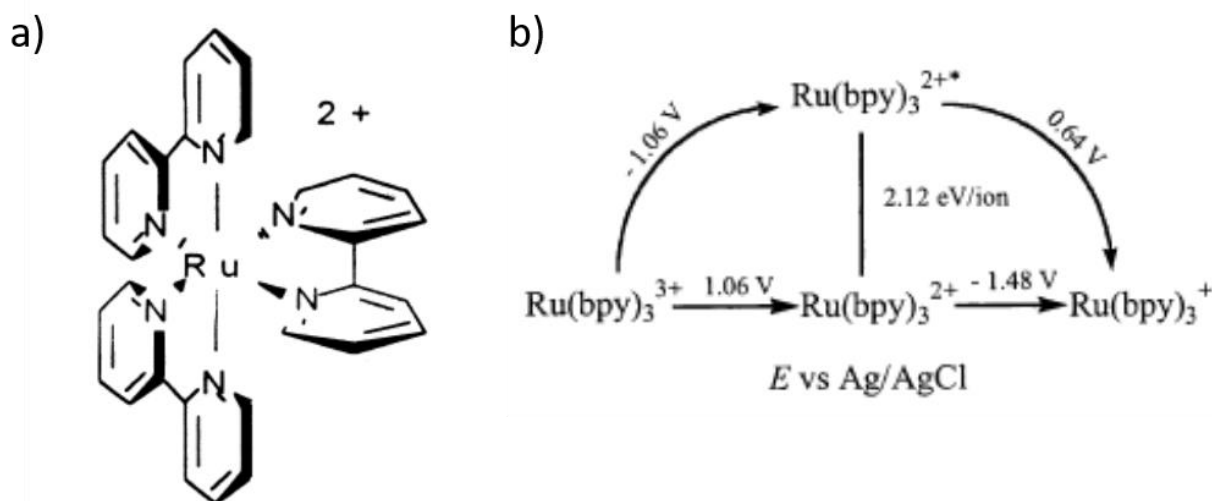


Figure 1.5 a) Chemical structure of $[\text{Ru}(\text{bpy})_3]^{2+}$;¹ b) scheme of the complex in different electronic states.³⁶

The structure is composed by a Ru(II) atom surrounded by coordination bonding with three bidentate polypyridine ligands (bpy). Ru(II) presents a d^6 configuration and its polypyridine ligands possess σ -donor orbitals, localized on the nitrogen atoms and π donor and π^* acceptor orbitals, delocalized on the aromatic rings. The promotion of an electron from a π_M metal orbital to the π_L^* ligand orbitals leads to a metal-to-ligand charge transfer (MLCT) excited states. The promotion of an electron from π_M to σ_M^* orbitals generates metal centered (MC) excited states.

Finally, a ligand centered transition occurs by promoting an electron from π_L to π_L^* (Fig. 1.6, a).⁴⁵

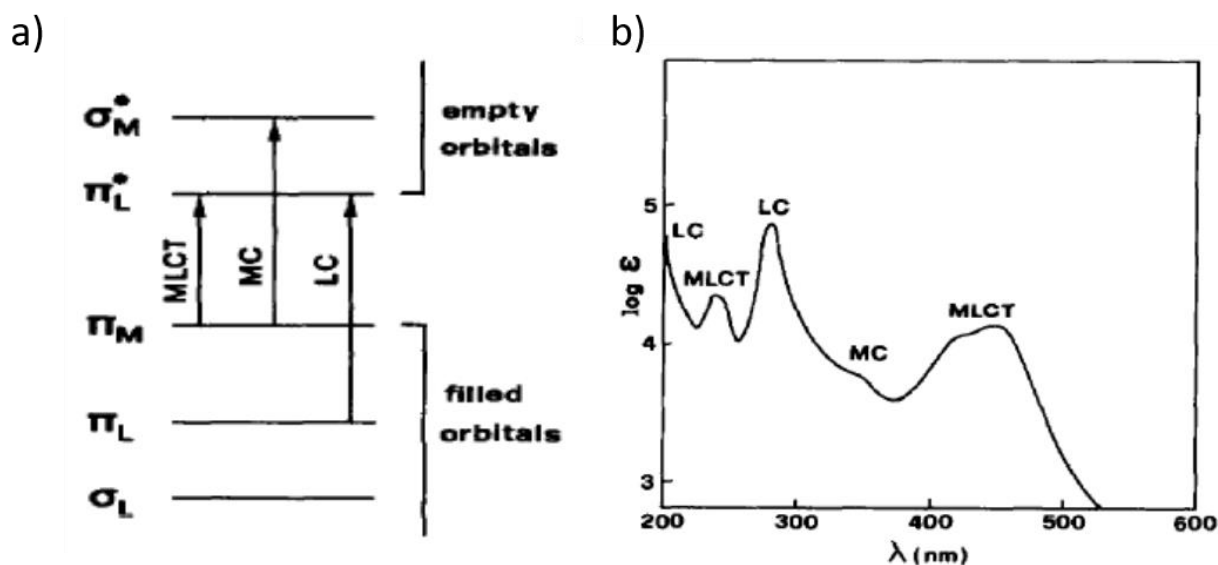


Figure 1.6 a) Simplified molecular orbital diagram for a system $[Ru(LL)_3]^{2+}$; b) electronic absorption spectrum of $[Ru(bpy)_3]^{2+}$.

The lowest excited state (Fig. 1.6, b) is a MLCT state, which undergoes slow non-radiative deactivation, because it is not strongly displaced compared to the ground state. It can be considered a triplet as multiplicity, even if, as for other heavy metals based complexes, a strong spin-orbit coupling is present.²⁰ Excitation of $[Ru(bpy)_3]^{2+}$, by exciting at the relative maximum absorption wavelength (λ_{abs}) of 454 nm, generates an emission spectrum dominated by MLCT transitions, whose energy position, lifetime and intensity is temperature dependent (Fig. 1.7). At room temperature, the maximum emission wavelength is located at about 610 nm.⁴⁶

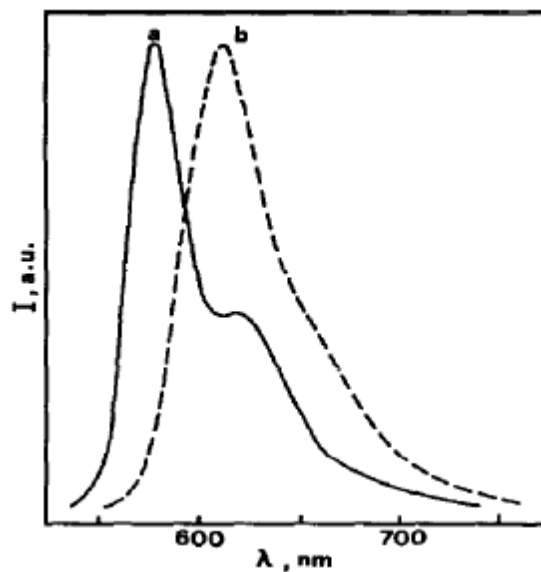


Figure 1.7 emission spectrum of $[\text{Ru}(\text{bpy})_3]^{2+}$ in EtOH: a) at 77 K; b) at room temperature.⁴⁵

Other Ru(II) complexes present similar emission wavelengths (between 600 and 650 nm), but the limited ligand-field splitting energies of Ru(II) ion leads to a difficulty in tuning the photophysical properties of Ru-based complexes. By functionalization of bipyridine moieties with suitable groups (Fig. 1.8), $[\text{Ru}(\text{bpy})_3]^{2+}$ can be covalently bonded with biological molecules or antibodies and act as label for biodiagnostic applications.^{26a}

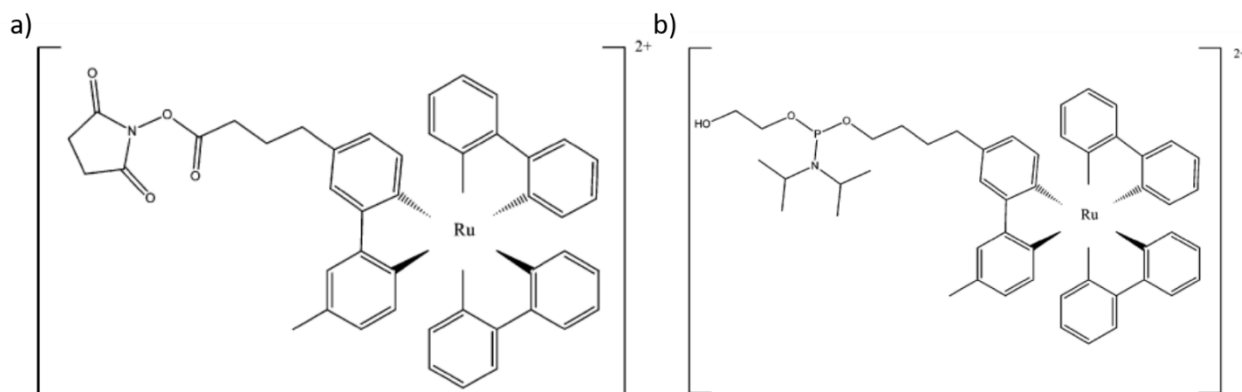


Figure 1.8 a) $[\text{Ru}(\text{bpy})_3]^{2+}$ -NHS ester for ECL labeling of biological molecules; b) $[\text{Ru}(\text{bpy})_3]^{2+}$ -phosphorimidate linker for ECL labeling of DNA and RNA.^{26a}

A number of $[\text{Ru}(\text{bpy})_3]^{2+}$ derivatives and other ruthenium(II) N,N-chelating complexes have been synthesized and their ECL properties were deeply investigated.⁴⁷ An example is represented by the functionalization of a bipyridine ligand with different types of crown ethers (Fig. 1.9).^{47a}

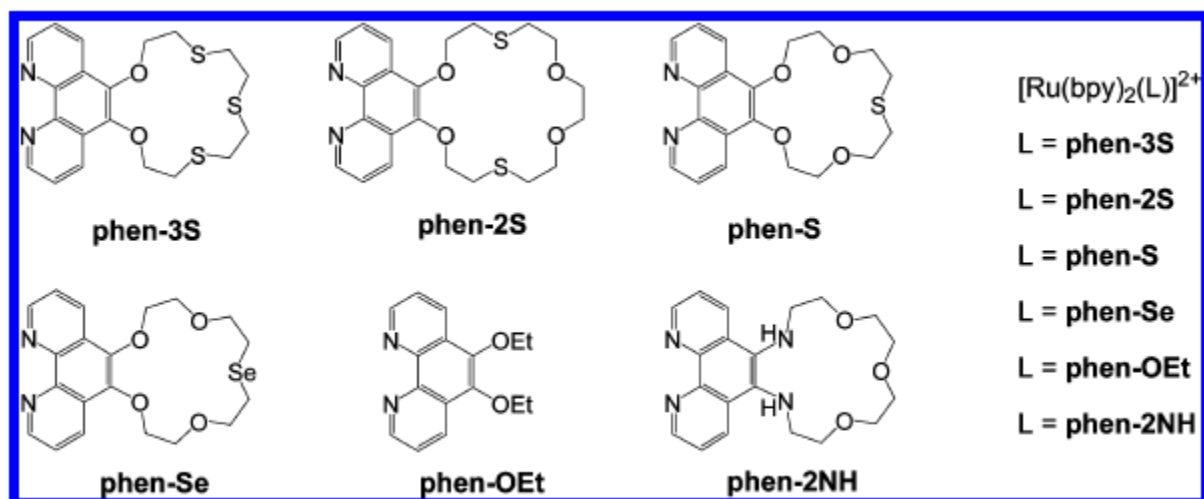


Figure 1.9 Ruthenium(II) diimine complexes with appended crown ethers derived from 1,10-phenanthroline.^{47a}

The effect of the binding of metal ions with crown ethers on ECL efficiencies was investigated via both annihilation and coreactant ECL. Some compounds result insensitive to the cation binding (such as $[\text{Ru}(\text{bpy})_2(\text{phen-2NH})]^{2+}$, Fig. 1.10) by using TPA as coreactant (the “oxidative-reductive” ECL coreactant pathway) but present a strong enhancement of the ECL intensity by performing experiments at a negative potential (via “reductive-oxidative” ECL coreactant pathway). TPA probably competes with the crown ethers for the interaction with the cations. Following the annihilation pathway, a strong enhancement of ECL intensity was found by addition of cations, such as Ca^{2+} , Mg^{2+} , Ba^{2+} and Zn^{2+} . Potential applications of those compounds are in the determination of electrolytes and metal ions in clinical and environmental analyses.

Cyclometallated iridium(III) complexes have emerged as new candidates for replacing the standard ECL luminophore $[\text{Ru}(\text{bpy})_3]^{2+}$ in several ECL applications and studies.⁴⁸ The higher ligand-field splitting energies of iridium(III) ion compared to Ru(II) complexes facilitates the tuning of the photophysical features, with new opportunities for multiplexed ECL detection systems.⁴⁹ In last decades, the development of blue-emitting (high-energy) complexes for ECL applications represented a great challenge. Several blue-emitting Ir(III) complexes were investigated.⁴⁹⁻⁵⁰ Following the wide development of iridium complexes for photonic applications,⁵¹ a useful strategy to create luminophores with high energy emission is to incorporate in the ligands electro-withdrawing fluorine substituents. The HOMO level results stabilized to a much greater extent than the LUMO level. For example, the green emitter $[\text{Ir}(\text{ppy})_3]^{3+}$ (ppy = 2-phenylpyridine) with a λ_{max} of emission at about 520 nm can be tuned to

a blue emission ($\lambda_{em} = 495 \text{ nm}$) by functionalization of the cyclometallating ring of ppy with fluorine groups (Fig. 1.10, a).⁵⁰ However, the stability of the fluorinated ECL luminophores decreases in the operating devices. To overcome this difficulty, an alternative strategy was investigated by using methoxy- and methyl-substituted 2,3'-bipyridine as ligands. The new complexes (an example is shown in Figure 1.10, b) emits in the blue-green wavelengths region, at about 450 nm.^{49,52}

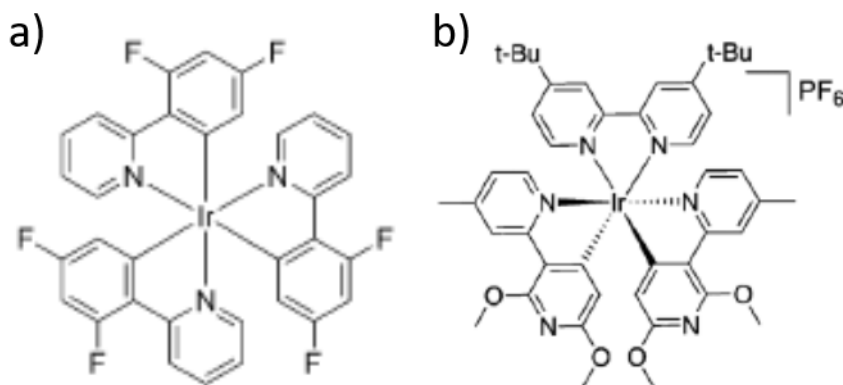


Figure 1.10 Chemical structures of a) $[\text{Ir}(\text{df-ppy})_3]^{3+}$ (df-ppy = difluorophenylpyridine)⁵⁰ and b) $[\text{Ir}(4,4'\text{-tBu-bipyridine})(2',6'\text{-dimethoxy-4-methyl-2,3'-bipyridine})_2][\text{PF}_6]_3$.⁵²

Another challenge is the design of Ir(III) complexes with UV emission. In 2012,⁵³ by using carbene-base N^+C^- as ligand, a series of charged iridium complexes, emitting from red to near-UV, was reported. The emitting excited state is mainly localized on the N^+C^- ligands, which present high-energy LUMO. In the UV-visible absorption spectra, strong bands in the UV up to 300 nm were attributed to intraligand $\pi-\pi^*$ transitions.⁵³ Ir(III) complexes present usually a low solubility in water. By adding disulfonated bathophenanthroline as ligand, water solubility could be improved.^{49,54} Recently, a new class of ECL label⁴⁸, $[\text{Ir}(\text{C}^+\text{N})_2(\text{pt-TOxT-Sq})]^+$ (where C^+N is a range of possible cyclometalating ligands and pt-TOxT-Sq is a pyridyltriazole ligand with trioxatridecane chain and squarate amide ethyl ester, Fig. 1.11, b).

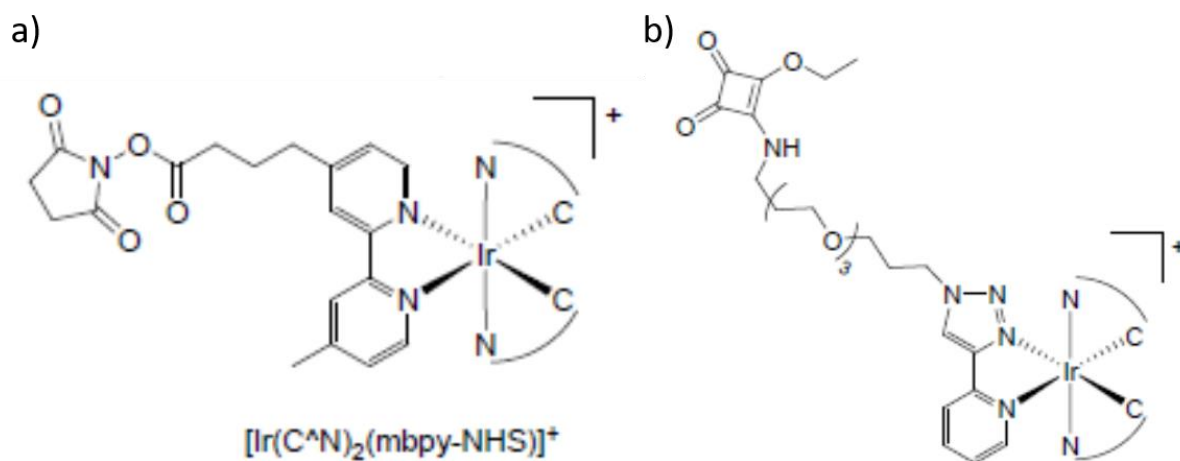


Figure 1.11 General chemical structure for the systems a) $[\text{Ir}(\text{C}^{\wedge}\text{N})_2(\text{mbpy-NHS})]^+$ and b) $[\text{Ir}(\text{C}^{\wedge}\text{N})_2(\text{pt-TOxT-Sq})]^+$.⁴⁸

Previously, other Ir(III) complexes (Fig. 1.11, a) were synthesized with specific groups, able to bind molecules of biological interest and act as labels for ECL bioanalysis.⁵⁵ However, these latter could generate coreactant ECL emission only with the direct oxidation of the ECL luminophore at the electrode surface. When the ECL luminophore is immobilized as a label on the surface of an object (as it happens in the most part of ECL bioassays), it cannot diffuse to the electrode. Therefore, the application as ECL labels requires the possibility to follow the coreactant ECL route, described by equations 1.26 and 1.27 for the ECL system $[\text{Ru}(\text{bpy})_3]^{2+}/\text{TPA}$. The new Ir(II) complexes (Fig. 1.11, b) satisfied such a requirement, with a higher versatility in ECL applications. Transition metal species as $[\text{Ru}(\text{bpy})_3]^{2+}$ and $\text{Ir}(\text{ppy})_3$ present broad emission spectra that cover a wavelength range of about ~ 200 nm. In ECL multianalytes analyses and as for ECL internal standard, ECL luminophore with a narrower emission spectrum could be an advantage. Europium chelates, cryptates and mixed chelates/cryptates systems were studied by Bard and coworkers via “reductive-oxidative” coreactant ECL.⁵⁶ Although the peculiar electronic transitions of lanthanide complexes permit to obtain very narrow emission spectra, the ECL efficiencies of such systems remained very low. Recently, Hogan et al.⁵⁷ reported an ECL sensitization via energy transfer of the europium emission by development of a heterobimetallic array. The donor species consist of Ir(III) 1,2,4-triazole complexes, conjugated to the macrocyclic ligand, 1,4,7-tris(carboxymethyl)-1,4,7,10-tetraazacyclododecane into which Eu(II) ions are bound (Fig. 1.12, b).

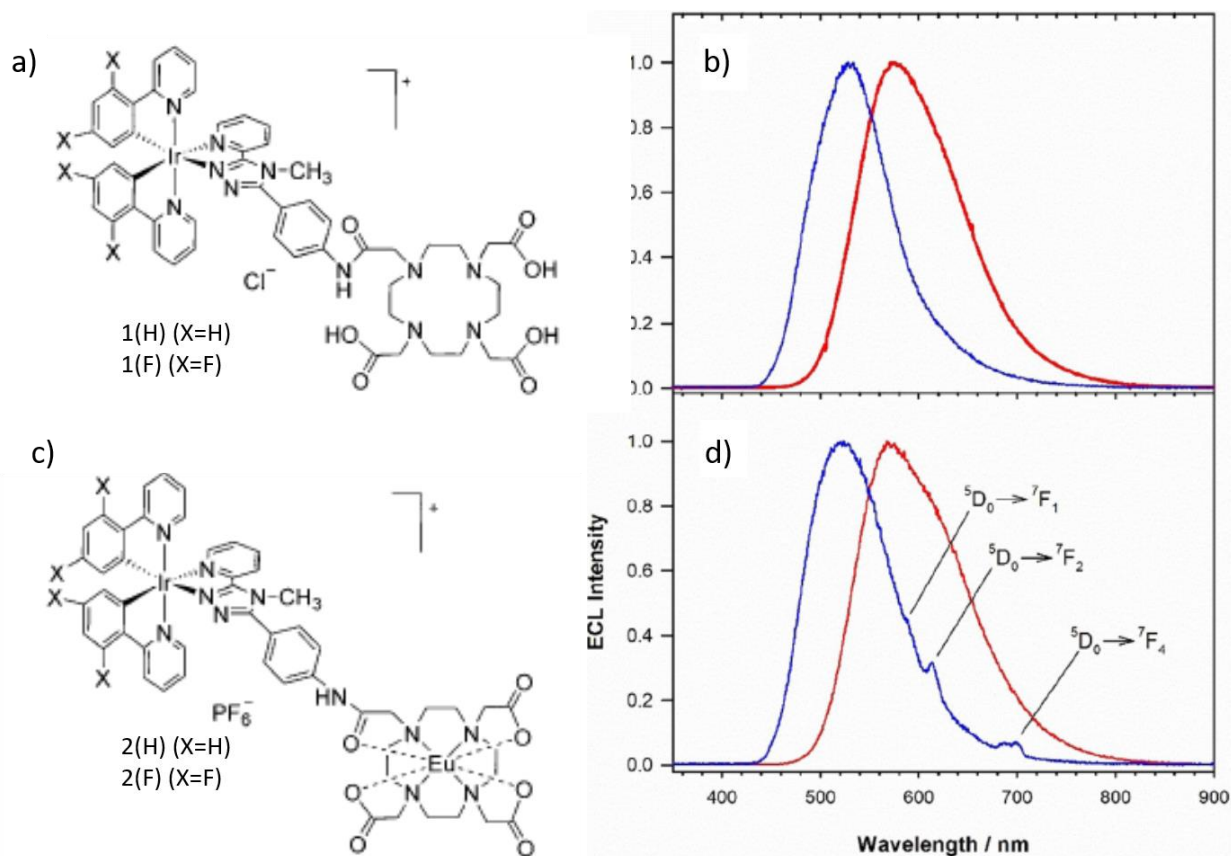


Figure 1.12 a) Chemical structure of dyads Ir(III) (1,2,4-triazole) (1,4,7-tris(carboxymethyl)-1,4,7,10-tetraazacyclododecane; b) normalized ECL spectra produced via TPA coreactant mechanism in 0.5 mM solutions of a) 1(H) red and 1(F) blue, in acetonitrile ([Bu4N][PF6]) 0.1 M and TPA 10 mM); b) Chemical structure of dyads Ir(III) (1,2,4-triazole) (1,4,7-tris(carboxymethyl)-1,4,7,10-tetraazacyclododecane Eu(II); d) normalized ECL spectra produced via TPA coreactant mechanism in 0.5 mM solutions of b) 2(H) red and 2(F) blue, in acetonitrile ([Bu4N][PF6]) 0.1 M and TPA 10 mM).⁵⁷

ECL emission of Ir(III) complex triggers via energy transfer Eu(II) PL emission, whose main transitions are highlighted in Figure 1.12, d). The normalized ECL spectra of the dyads without the acceptor Eu(II) confirm the energy transfer phenomenon (Fig. 1.12, b).

1.4.2 Organic systems

The first studied ECL system was the polyaromatic hydrocarbon (PAH) 9,10-diphenylanthracene (DPA).^{1,26a} PAHs (i.e. DPA, pyrene, rubrene) present generally highly stable radical cations and anions. Their excited states can be easily energetically accessible via annihilation reaction between the oxidized and reduced intermediates. Consequently, the ECL efficiencies of such compounds are quite high.¹ One important limitation of PAHs for ECL applications is their low solubility in water. ECL analysis must be performed in rigorously

purified and deoxygenated organic solvents. To improve the water solubility, hydrophilic substituents, as sulphonate groups, have been added on the systems.⁵⁸ Recently, Natarajan and Schmittel⁵⁹ could obtain stable ECL emission in water from hydrophilic diarylanthracene, 9,10-bis(N-methylimidazolium-3-propoxyphenyl)anthracene (DAA1) and 9,10-bis(N-methylimidazolium-3-propoxy-2,6-dimethylphenyl)anthracene (DAA2) (Fig. 1.13).

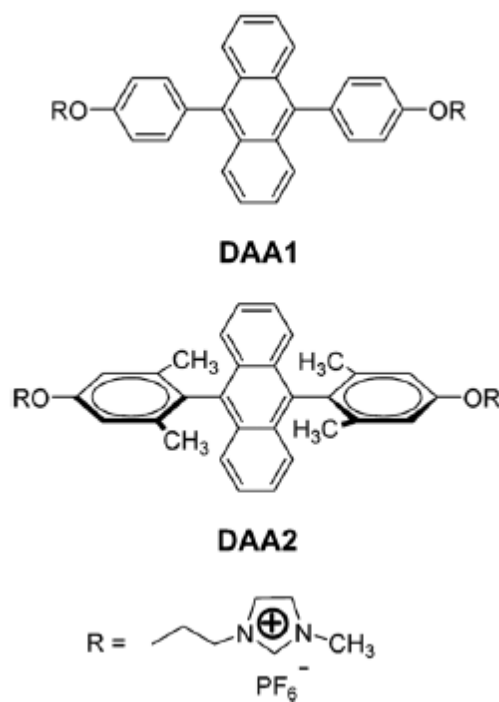


Figure 1.13 Chemical structure of aqueous soluble DAA1 and DAA2.⁵⁹

Omer et al.⁶⁰ combined anthracene, pyrene and rubrene derivatives with two spirobifluorene derivatives. Spirobifluorene is composed by two fluorene units, connected through the spiro-carbon atom. Blue ECL emission was obtained by the new compounds, whose spirobifluorene functionalization permits to stabilize PAHs core and shift the emission to longer wavelengths (higher energies). In the last decade, many spirobifluorene derivatives with donor and acceptor moieties, for a fine tuning of the electrochemical and photophysical properties, were reported.⁶¹ For example, the addition of triphenylamine groups as donors connected with fluorenes stabilizes the electrogenerated radical cation (Fig. 1.14, a).^{61c} In a recent study, triphenylamines were modified at the *para*-position by electro-withdrawing and electro-donating groups (Fig. 1.14, b).

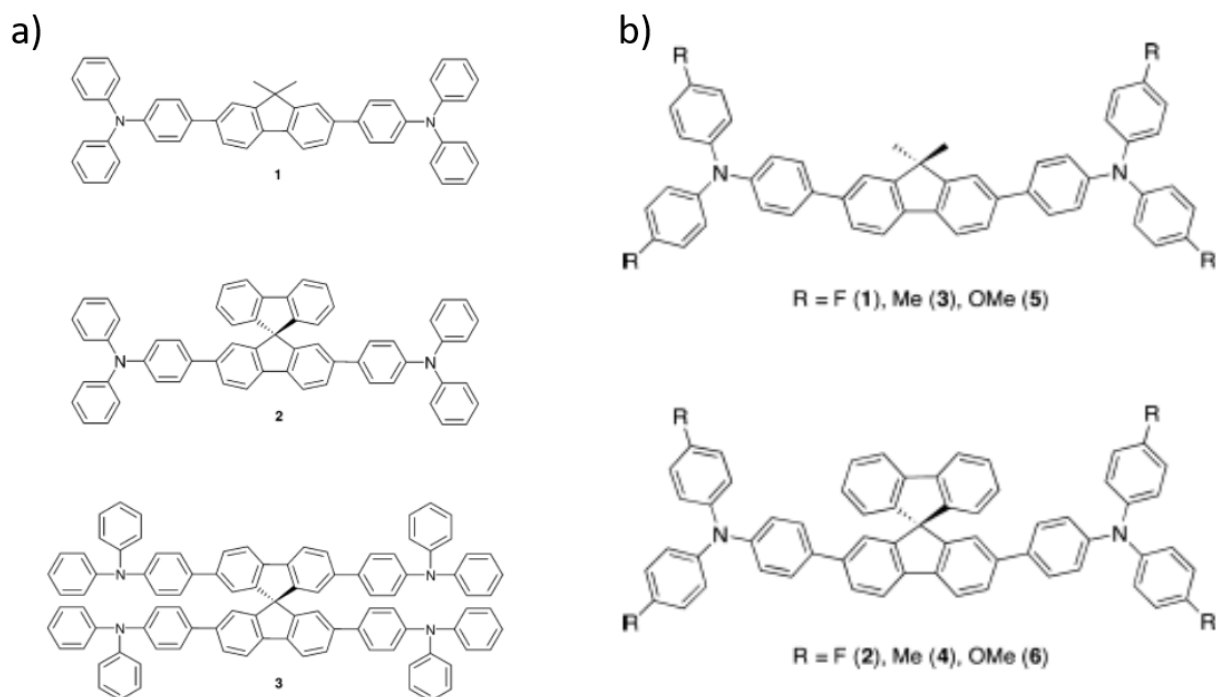


Figure 1.14 a) Examples of spirobifluorene derivatives modified with triphenylamine moieties;^{61c} b) Modified spirobifluorene derivatives a) 1 and 2 with electro-withdrawing groups (-F or -OMe) and an electro-donating group (-Me).^{61a}

An effective fine-tuning of the ECL via annihilation properties was achieved, with a bathochromic shift of the ECL emission going from fluorine to methoxy with a $\Delta\lambda$ of 67 nm. In 2018,⁶² the modification of an ITO substrate using single assembled monolayers of a spirobifluorene was reported for the first time, opening new possibilities in multicolour ECL applications at the solid state.

Boron dipyrromethene (BODIPY, Fig. 1.15, a) and its derivatives present photochemical and electrochemical properties comparable to aromatic hydrocarbons.⁶³ The electronic state of BODIPY can be tuned by the introduction of electron donating/accepting groups and the extension of π conjugation. Alkyl substituted⁶⁴ BODIPYs show a good radicals stability that allows to perform efficiently ECL via annihilation.⁶⁵ Polyethylene glycol-BODIPYs were reported as the first water soluble BODIPY derivatives in 2013, with potential interesting ECL analytical applications.⁶⁶ Recently, ECL analysis of a BODIPY derivative with extended conjugation (Fig. 1.15, b) was reported, with ECL emission via TPA coreactant pathway in the range of 650-800 nm..⁶⁷

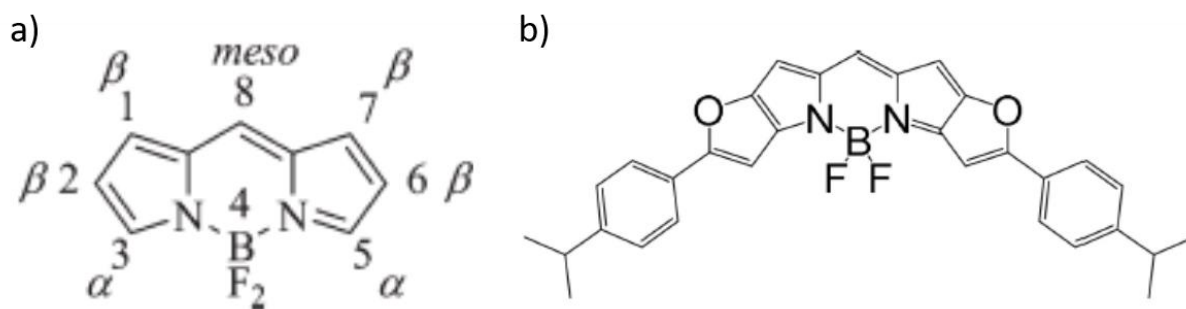


Figure 1.15 Chemical structures of a) the BODIPY core⁶⁵ and b) 2,8-bis(4-isopropylphenyl)-difuro[2,3-b][3,2-g]-5,5-difluoro-5-bora-3a,4a-diaza-s-indacene.⁶⁷

1.4.3 Nanomaterials

In the last decade, silica nanoparticles doped with organic and inorganic luminophores were used as labels in ECL analyses, in order to improve emission detection limit for biomolecules.⁶⁸ They are characterized by an intrinsic hydrophilicity and they can be easily bioconjugated, thanks to silica chemistry.⁶⁹ The tuning of the emission wavelength can be achieved by exploiting Forster resonance energy transfer.⁷⁰ Beyond passive nanomaterials such as silica nanoparticles, active semiconductor nanocrystals (or quantum dots, QDs) are receiving increasing attention as ECL luminophores, because of the capability to tune their properties with shape, size, composition and for the advanced surface modifications and conjugation technologies.⁷¹ To date, various types of QDs are reported, such as classical chalcogenide QDs (CdSe, CdTe, CdS, etc.), graphene QDs, carbon nanodots and carbon nitride QDs. Chalcogenide QDs are composed by the element of groups II-VI or IV-VI. Their emission can vary from UV to infrared regions, depending on the size and the composition. In addition, ECL emission is usually significantly red-shifted compared to PL.⁷² As schematically shown in Figure 1.16, electronic transitions triggered by photoexcitation occurs from the interior of particles, while ECL emission is produced starting from electron transfers at the particles' surfaces, much more dependent on the experimental conditions.

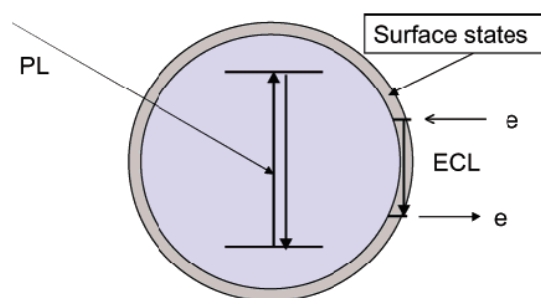


Figure 1.16 Schematic representation of PL and ECL in a QD.⁷²

Carbon-based QDs, including carbon nanodots (NDs) and graphene QDs are non-toxic and their size can reach respectively less than 10 nm and 100 nm. Qu et al.⁷³ demonstrated the amplified detection of cancer cells by using NDs@Ag nanocomposites as ECL probes and graphene nanosheets as amplifying agent. PAH functionalized reduced graphene oxide was exploited to increase the surface area of the electrode, facilitating the electron transfer. NDs@Ag nanocomposites were functionalized with folic acid, which can specifically target folate receptors (over-expressed in several cancer cells). For the first time, ECL cytosensor was designed with NDs as ECL luminophore. The excellent conductivity, the surface passivation of NDs with Ag and the graphene nanosheets on the electrode surface were responsible of the superior cell-capture ability and of the detection limit for cancer cells. Stimuli-responsive microgels can expand or contract, following an external stimulus (i.e., temperature, light, pH, bimolecular recognition). By introduction of a luminescent probe during the microgels' synthesis, the swelling variations can be correlated with a change in the light emission intensity. This strategy was used to design new ECL nanomaterials, in particular for bioanalytical applications. In 2013, Sojic et al.⁷⁴ discovered an amplification of the ECL signal associated with thermoresponsive 100-nm microgels. The collapse of the microgels, due to a temperature increase, is related with a decrease in the average distance between adjacent $[\text{Ru}(\text{bpy})_3]^{2+}$ derivative sites (Fig. 1.17).

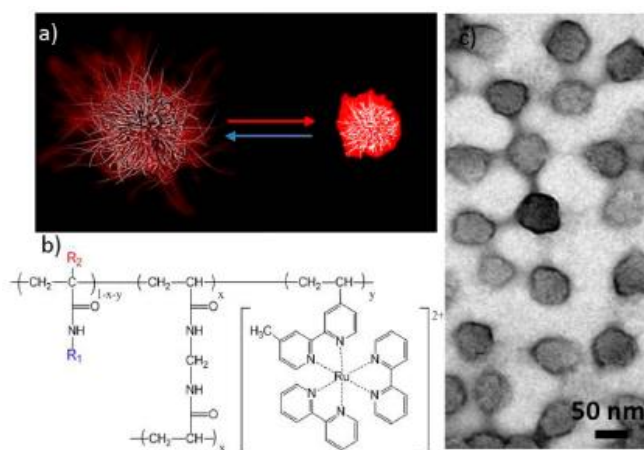


Figure 1.17 a) Schematic representation of the swell-collapse transition of the thermoresponsive ECL microgel; b) chemical structure of the cross-linked microgels with different chemical groups R_1 and R_2 ; c) transmission electron microscopy image of dried microgels.⁷⁴

ECL signal was enhanced of two orders of magnitude, with potential developments of tunable ECL energy-transfer nanomaterials for multicolor systems.

1.5 ECL coreactants

The first reported coreactant was the oxalate ion $C_2O_4^{2-}$,¹¹ whose oxidation leads to the generation of the strong reductant species $CO_2^{\cdot-}$. This electrogenerated radical reacts with the oxidized form of the luminophore, via “oxidative-reductive” coreactant ECL. Another important class of “oxidative-reductive” ECL is represented by the alkylamines. Generally, ECL intensity increases in the order: primary amines < secondary amines < tertiary amines.¹ Aromatic amines and amines having a double bond C=C that can conjugate the radical intermediates are associated with a very low ECL signal. Probably, the stability of the radical intermediates hinders the ECL reaction. The most important amine coreactant is TPA, whose mechanism was discussed in § 1.4.2.1. The high toxicity of TPA as well as the limitation related with the narrow available pH range and the strong dependence from the electrodic surface have driven the studies of valuable alternative coreactants.⁷⁵ The less toxic coreactant 2-(dibutylamino)ethanol (DBAE) was tested with $[Ru(bpy)_3]^{2+}$ as luminophore. The system $[Ru(bpy)_3]^{2+}/DBAE$ was found to work at a coreactant concentration 5 times lower than the system $[Ru(bpy)_3]^{2+}/TPA$, with a lower buffer concentration. The sensitivity of the alternative system with DBAE was also an order of magnitude higher than for the standard ECL coreactant system. DBAE present the electro-withdrawing hydroxyethyl group as substituent. Such group

promotes the oxidation of amines and is probably responsible of the enhanced ECL performances of $[\text{Ru}(\text{bpy})_3]^{2+}/\text{DBAE}$ system compared with the standard $[\text{Ru}(\text{bpy})_3]^{2+}/\text{TPA}$ system. Successively, another coreactant, *N*-butyldiethanolamine, was investigated.⁷⁶ An ECL efficiency higher than DBAE was obtained at Au and Pt electrodes. While DBAE presents a single hydroxyethyl group, two groups are reported for *N*-butyldiethanolamine. In 2016, Xu et al.⁷⁷ compared the standard ECL system $[\text{Ru}(\text{bpy})_3]^{2+}/\text{TPA}$ with *N*-(3-aminopropyl)diethanolamine (APDEA) as coreactant. The presence of an amine group and a hydroxyl group in APDEA compared to TPA (Fig. 1.18) leads to an increase in oxidation amine's rates with an enhancement in ECL intensity 10 and 36 times stronger respectively at Au and Pt electrodes, stronger than the system *N*-butyldiethanolamine too.

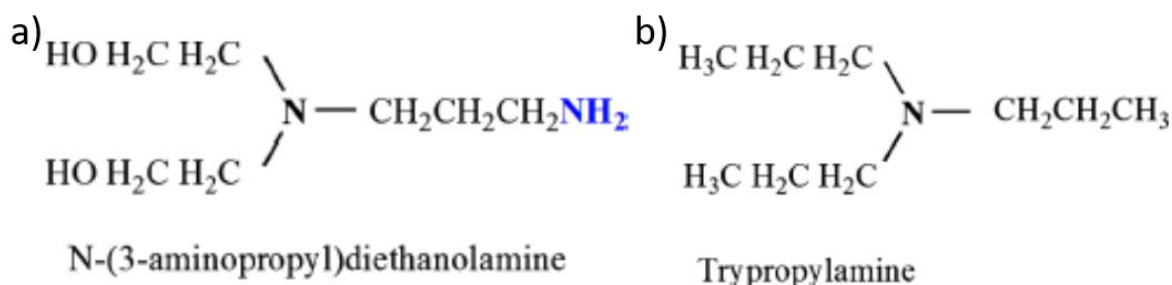


Figure 1.18 Chemical structures of a) APDEA and b) TPA.⁷⁷

Peroxidisulfate (or persulfate, $\text{S}_2\text{O}_8^{2-}$) was reported as the first example of “reductive-oxidative” ECL coreactant.^{33,78} The strongly oxidizing electrogenerated species $\text{SO}_4^{\cdot -}$ ($E^\circ \geq 3.15$ vs SCE)⁷⁸ reacts with the luminophore (i.e. with $[\text{Ru}(\text{bpy})_3]^+$) for ECL generation. Another example of “reductive-oxidative” ECL is represented by hydrogen peroxide and related systems.¹ Highly reactive oxidizing reagents are produced upon peroxides’ reduction. For H_2O_2 , ECL mechanism appears to involve the peroxide anion HOO^- and the electrochemically formed superoxide $\text{O}_2^{\cdot -}$. Many biological activities are correlated with the generation of hydrogen peroxide, which can be selectively detected via ECL, with luminol as commonly used luminophore, with powerful bioanalytical applications.⁷⁹ The reduced form of the cofactor β -nicotinamide adenine dinucleotide (NADH) acts as an amine coreactant.⁸⁰ The possibility to perform ECL by using an enzyme cofactor presents a special importance, because of the possibility to monitor via ECL the enzymatic activity of dehydrogenase.⁸¹ NAD^{\cdot} is generated upon oxidation of NADH to $\text{NADH}^{+\cdot}$ and successive deprotonation. In the form NAD^{\cdot} , the cofactor can no more act as coreactant.⁸²

1.6 ECL analytical applications

ECL phenomenon offers significant advantages compare to other light emission phenomena (PL, CL). The first electrochemical step allows to easily control the time and position of the light-emitting reaction, giving high temporal and spatial resolutions.¹⁴ ECL presents also a high selectivity, because ECL generation is driven by controlling the electrode potentials. The absence of photoexcitation can avoid sample degradation and a high background. ECL intensity is proportional to the concentration of the ECL luminophore or of the coreactant. If ECL is generated in presence of a constant concentration of the luminophore, ECL intensity will linearly depend on the concentration of the coreactant in a wide dynamic interval. Alternately, if ECL experiments are carried out in an excess or constant concentration of coreactant, the signal will be proportional to the emitting species. In this way, the concentration of an analyte can be determined by measuring the ECL intensity of a label. Such outstanding features are the reason for the rapid diffusion of ECL as analytical technique, for the detection of a wide range of analytes in several types of systems.^{26a}

1.6.1 ECL biorelated applications

The most common and commercially available ECL applications are related with the analysis of biological entities (biomolecules, cells, mitochondria, nucleic acids, etc.).⁴⁹ One of the most important ECL applications is in immunoassay. ECL related immunoassays have proven to hold excellent reproducibility, sensitivity and limit of detection compared to other assays, such as enzyme-linked immunosorbent assays (ELISA), CL, PL, and surface plasmon resonance-based immunosensors.⁸³ Therefore, ECL immunoassay represents a powerful analytical technique for ultrasensitive detection of biomarkers.⁸⁴ The main part of such ECL diagnostic assays is based on the coreactant ECL system $[\text{Ru}(\text{bpy})_3]^{2+}/\text{TPA}$, in which $[\text{Ru}(\text{bpy})_3]^{2+}$ derivatives are used as label, interacting with the analyte via strong biological bonds, such as antigen-antibody or biotin-streptavidin links. TPA is used as coreactant to generate the ECL signal. In the last decades, many studies have been performed to improve ECL immunoassay selectivity and sensitivity and extend its applications.⁷⁹ Recently, a sandwich immunoassay system was combined with an optically transparent electrode (OTE) with functionalized multiwalled carbon nanotubes (f-MWCNTs, Fig. 1.19).⁸⁵

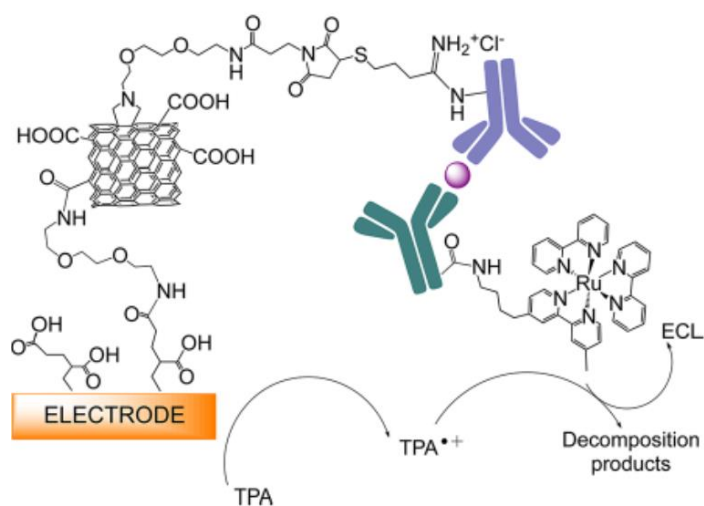


Figure 1.19 Schematic representation of the nano-biosensor and of its ECL development.⁸⁵

The composed nano-biosensor was applied to detection of palytoxin (PITX), one of the most potent marine toxin. The derivatized amino group functionalization of the f-MWCNTs covalently bound the antibody (PITX), whereas other groups anchored the OTE surface. The antigen PITX detection was completed by an anti-PITX antibody labeled with a $[Ru(bpy)_3]^{2+}$ derivative. The reaction of this latter with the electrogenerated radical $TPA^{\bullet+}$ generates the ECL signal. The system was tested in complex biological systems (i.e., mussels and microalgae) and a detection limit 1 to 2 orders of magnitude lower than the previous reported PITX sensors was obtained. In recent years, multiplexed immunoassays, able to detect multiple analytes in a single-run experiment and/or in a single volume, have been the subject of various studies.⁸⁶ Multiplexing analysis minimizes the sample volume and the experimental time and increases the amount of information detectable for each sample.⁸³ In 2018, Zou et al.⁸⁷ reported the spectral ECL responses of three antigens, carcinoembryonic antigen (CEA), prostate specific antigen (PSA) and alpha fetoprotein (AFP), simultaneously acquired by an ECL multiplex immunoassay strategy. Nanocrystals (NCs) CdSe (550 nm), CdTe (650 nm) and CdTe (776 nm) were utilized as labels on specific antibodies ($Ab_2|NCs$) respectively for CEA, PSA and AFP, whose specific antibodies (Ab_1) were immobilized on the surface of a glassy carbon electrode via the linker molecule *p*-aminobenzoic acid (ABA)(Fig. 1.20).

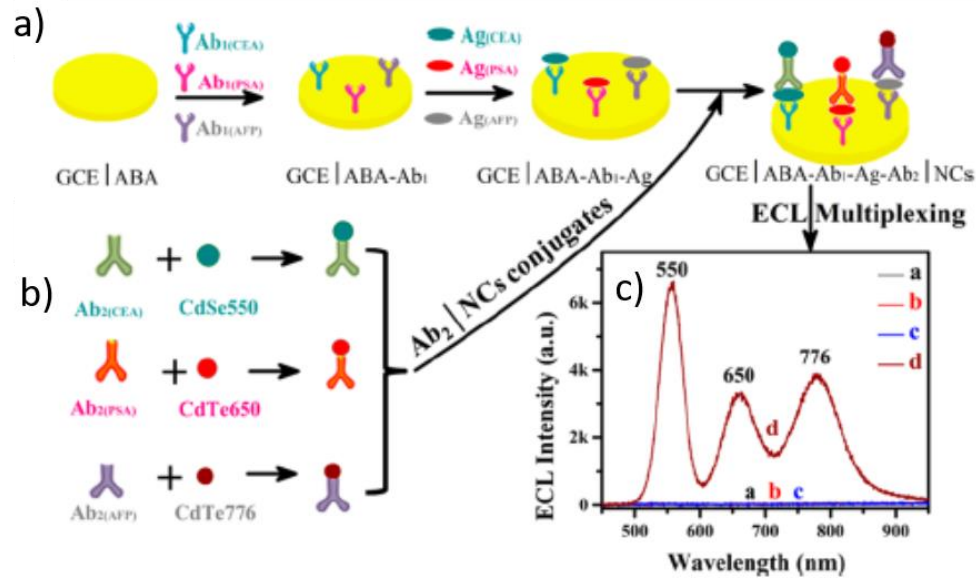


Figure 1.20 a) Fabricating procedure of the ECL multiplex immunoassay; b) fabricating Ab₂|NCs conjugates; c) accumulated ECL spectra of a) GC; b) GC|ABA; c) GC|ABA-Ab₁(CEA, PSA, AFP) < antigens (CEA, PSA, AFP) > Ab₂(CEA, PSA, AFP); d) GC|ABA-Ab₁(CEA, PSA, AFP) < antigens (CEA, PSA, AFP) > Ab₂(CEA, PSA, AFP)|NCs (550, 650, 776) in 0.10 M pH 7.4 PBS, 0.10 M (NH₄)₂S₂O₈.⁸⁷

They could successfully develop a spectrum-resolved triplex-color ECL multiplexing in a waveband-resolved way, as it occurs in fluorescent multiplexing. ECL immunoassay has been recently applied also to the detection of membrane proteins and over-expressing proteins cancer cells.⁸⁸ The biosensor was composed of single stranded DNAs blocked on the surface of Au electrode via a thiolated capture. Target protein (AFP) was simultaneously bound by two antibodies tagged with two other single stranded DNAs. Successively, the three single stranded DNAs could hybridize. When the luminophore [Ru(phen)₃]²⁺ was intercalated into the hybridized double stranded DNAs, ECL analysis was performed via coreactant pathway. This work showed for the first time “signal-on” proximity hybridization-regulated ECL immunoassay for the selective detection of membrane over-expressed protein, directly on a cancer living cell surface. ECL was also applied for the sensitive detection of DNA. ECL DNA assays can be distinguished in label and label-free techniques. A good reproducibility, timesaving, low cost and simple manipulation are the main advantages of the label-free ECL DNA assays.⁴⁹ In 2012, Chai et al.⁸⁹ reported a new strategy for the detection of a specific DNA sequence at the femtomolar level through *in situ* hybridization chain reaction (HCR) signal amplification. The DNA capture probe was self-assembled on the surface of a Au electrode (Fig. 1.21). The presence of the target DNA analyte permits, with two hairpin helpers DNAs stranded, the formation of long double-stranded DNAs polymer chains. HCR allows the

intercalation of a numerous $[\text{Ru}(\text{phen})_3]^{2+}$ molecules, which produces ECL signal by reaction with TPA coreactant.

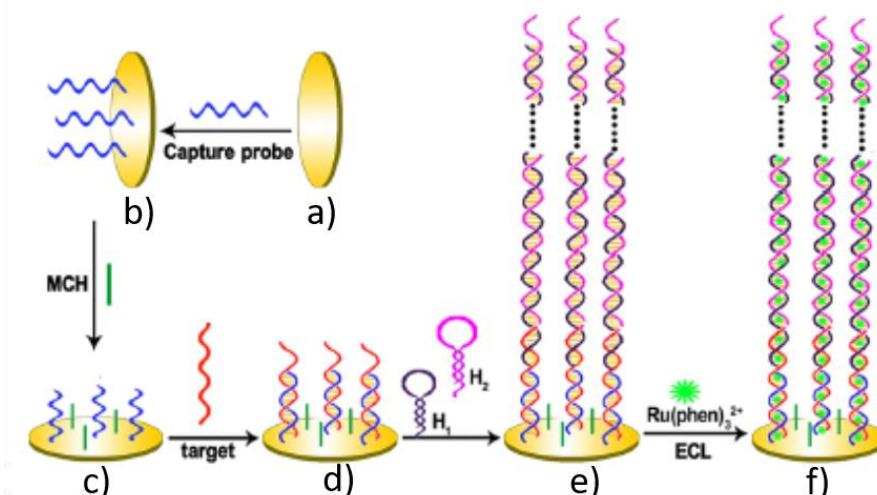


Figure 1.21 Illustration of the HCR-based strategy for ECL detection of DNA.⁸⁹

An alternative amplification technique was reported for the label-free detection of DNA methylation and assay of methyltransferase activity.⁹⁰ $[\text{Ru}(\text{phen})_3]^{2+}$ intercalated into double-stranded DNAs of a supersandwich immunoassay. Each capture probe can capture multiple signal probes, reaching an excellent sensitivity with a detection limit of 3×10^{-6} U mL⁻¹. $[\text{Ru}(\text{bpy})_3]^{2+}$ can also be directly labeled with DNA to form an ECL probe.⁴⁹ Based on the quenching of the ECL $[\text{Ru}(\text{bpy})_3]^{2+}$ /TPA signal by oxygen-containing groups at the surface of MWCNTs, a new “signal-on” hybridization DNA assay was developed.⁹¹ A single-stranded DNA labeled with $[\text{Ru}(\text{bpy})_3]^{2+}$ (ssDNA-Ru) was covalently linked at the distal end with a MWCNTs electrode. ECL signal was quenched where ssDNA-Ru was self-organized on the surface of MWCNTs, whereas the ECL signal increased again in presence of the complementary single-stranded DNA.

Aptamers are single-stranded DNA or RNA with high recognition ability to a wide range of molecular targets, included ions, proteins and even whole cells.⁹² Due to their unique properties, great progress has been accomplished in the development of ECL assays having aptamers as recognition element. For example, quenching ECL of $[\text{Ru}(\text{bpy})_3]^{2+}$ labeled-silica nanoparticles by ferrocene represented the basis for the development of ECL aptasensors for the determination of adenosine.⁹³ DNA-based enzymes, also called deoxyribozymes or DNAzymes, are single-stranded DNA molecules with catalytic activity towards many chemical and biological reactions.⁹⁴ They can be produced by *in vitro* selection of random-sequence DNA

pools and isolated. As many reactions require metal ions as cofactors, DNA-zymes are mostly used in ECL sensors system for the amplified detection of metal ions, but also of DNA, aptamer-substrate complexes, etc.⁴⁹ For example, an ECL sensing platform was developed by Yin and coworkers⁹⁵ based on DNA-zymes, for the detection of Ag^+ , cysteine and for the study of their interaction. A functional oligonucleotide (FO) was designed with an intermolecular duplex, permitting $[\text{Ru}(\text{phen})_3]^{2+}$ intercalation, with a multi-cytosine section for Ag^+ recognition. A thiolated C_5 oligonucleotide was also immobilized on the surface of a Au electrode and a C- Ag^+ -C complex was formed between FO and C_5 in presence of Ag^+ ions. ECL emission via TPA coreactant ECL was correlated with the concentration of Ag^+ . Moreover, when metal ions interacted with cytosine, the complex C- Ag^+ -C dissociates, with corresponding decrease in ECL signal. This latter was used to quantify the cytosine content. In 2018, a new ECL-based strategy, called ECL-therapeutics, was developed for killing pathogenic bacteria.⁹⁶ The coreactant ECL system luminol/ H_2O_2 was used for the excitation (via energy transfer) of the photosensitizer cationic oligo(*p*-phenylenevinylene) (OPV). This latter forms excited states, followed by sensitizing surrounding oxygen molecules to generate reactive oxygen species (ROS) in a hydrogel substrate containing various pathogens (i.e. *Escherichia Coli*, *Candida Albicans*) (Fig. 1.22).

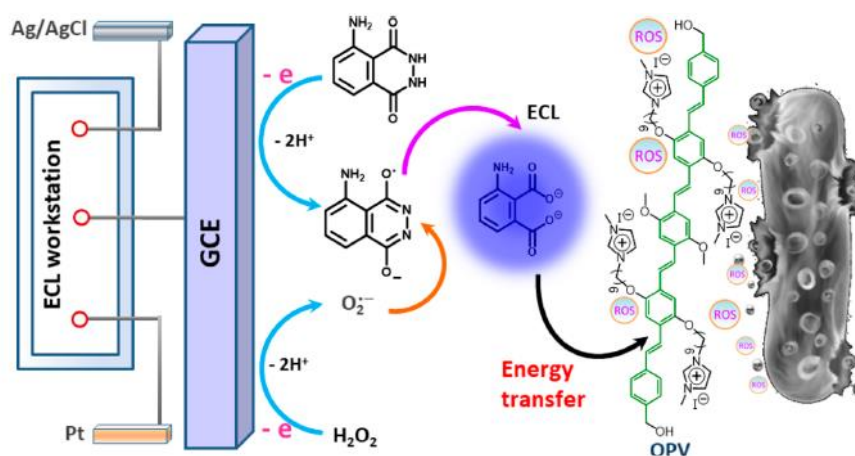


Figure 1.22 Electric driven mechanism for ECL-therapeutics to produce ROS and kill pathogenic bacteria.⁹⁶

The bactericidal efficiency of the system towards *Candida Albicans* was nearly about 80 %.

1.7 Conclusions

Although great advances in the understanding of ECL mechanisms and principles and the wide spread of ECL applications have been achieved, many studies are still in progress. First, the

replacement of the standard ECL system $[\text{Ru}(\text{bpy})_3]^{2+}/\text{TPA}$ with a less toxic alternative system, capable to produce ECL emission in aqueous solutions in a wider dynamic range.⁷⁵ The development of new ECL emitting species and new coreactants with improved ECL performances is still under investigation.⁹⁷ The combination of ECL with innovative electrochemical systems, such as nano- and micro-confined ones, can potentially result in an enhancement of ECL signal, decreasing the limit of detection in several ECL analytical applications.²⁹ Finally, ECL remains a powerful tool for clarifying fundamental principles inside many physical, chemical and biological systems.

References

- (1) Bard, A. J. *Electrogenerated Chemiluminescence*; M. Dekker: New-York, 2004.
- (2) Knight, A. W.; Greenway, G. M. *Analyst* **1994**, 119, 879.
- (3) Dufford, R. T.; Nightingale, D.; Gaddum, L. W. *Journal of the American Chemical Society* **1927**, 49, 1858.
- (4) Harvey, N. *The Journal of Physical Chemistry* **1928**, 33, 1456.
- (5) Kuwana, T.; Epstein, B.; Seo, E. T. *The Journal of Physical Chemistry* **1963**, 67, 2243.
- (6) a) Kolthoff, I. M.; Coetzee, J. F. *Journal of the American Chemical Society* **1957**, 79, 1852; b) Popov, A. I.; Geske, D. H. *Journal of the American Chemical Society* **1958**, 80, 1340.
- (7) Hercules, D. M. *Science* **1964**, 145, 808.
- (8) a) Santhanam, K. S. V.; Bard, A. J. *Journal of the American Chemical Society* **1965**, 87, 139; b) Visco, R. E.; Chandross, E. A. *Journal of the American Chemical Society* **1964**, 86, 5350.
- (9) Hercules, D. M.; Lytle, F. E. *Journal of the American Chemical Society* **1966**, 88, 4745.
- (10) Tokel, N. E.; Bard, A. J. *Journal of the American Chemical Society* **1972**, 94, 2862.

- (11) Chang, M.-M.; Saji, T.; Bard, A. J. *Journal of the American Chemical Society* **1977**, 99, 5399.
- (12) a) Miller, D.; McLendon, G. *Inorganic Chemistry* **1981**, 20, 950; b) Nonidez, W. K.; Leyden, D. E. *Analytica Chimica Acta* **1978**, 96, 401; c) Rubinstein, I.; Martin, C. R.; Bard, A. J. *Analytical Chemistry* **1983**, 55, 1580.
- (13) a) Noffsinger, J. B.; Danielson, N. D. *Analytical Chemistry* **1987**, 59, 865; b) Leland, J. K.; Powell, M. J. *Journal of the Electrochemical Society* **1990**, 137, 3127.
- (14) Miao, W. *Chemical Reviews* **2008**, 108, 2506.
- (15) a) Feldberg, S. W. *Journal of the American Chemical Society* **1966**, 88, 390; b) Feldberg, S. W. *The Journal of Physical Chemistry* **1966**, 70, 3928; c) Maloy, J. T.; Prater, K. B.; Bard, A. J. *Journal of the American Chemical Society* **1971**, 93, 5959.
- (16) Marcus, R. A. *The Journal of Chemical Physics* **1965**, 43, 679.
- (17) Harvey, E. N. *Bioluminescence*; Academic Press: New York, 1952.
- (18) Arakeri, V. H. *Current Science* **2003**, 85, 911.
- (19) Papadopoulos, K.; Triantis, T.; Dimotikali, D.; Nikokavouras, J. *Journal of Photochemistry and Photobiology A: Chemistry* **2000**, 131, 55.
- (20) Balzani, V. C., Paola; Juris, Alberto *Photochemistry and Photophysics: Concepts, Research and Applications*; Wiley-VCH, 2014.
- (21) Lakowicz, J. R. *Principles of fluorescence spectroscopy*; Second edition. New York : Kluwer Academic/Plenum, [1999] ©1999, 1999.
- (22) Fereja, T.; Hymete, A.; Gunasekaran, T. *A Recent Review on Chemiluminescence Reaction, Principle and Application on Pharmaceutical Analysis*, 2013; Vol. 2013.
- (23) Balzani, V.; Bolletta, F.; Ciano, M.; Maestri, M. *Journal of Chemical Education* **1983**, 60, 447.
- (24) a) Hercules, D. M. *Accounts of Chemical Research* **1969**, 2, 301; b) Marcus, R. A. *Angewandte Chemie International Edition in English* **1993**, 32, 1111.
- (25) a) Fleet, B.; Kirkbright, G. F.; Pickford, C. J. *Journal of Electroanalytical Chemistry and Interfacial Electrochemistry* **1971**, 30, 115; b) Weller, A.; Zachariasse, K. *Chemical Physics Letters* **1971**, 10, 197.
- (26) a) Richter, M. M. *Chemical Reviews* **2004**, 104, 3003; b) Brilmyer, G. H.; Bard, A. J. *Journal of the Electrochemical Society* **1980**, 127, 104.
- (27) Fiaccabrino, G. C.; Koudelka-Hep, M.; Hsueh, Y.-T.; Collins, S. D.; Smith, R. L. *Analytical Chemistry* **1998**, 70, 4157.
- (28) Rodríguez-López, J.; Shen, M.; Nepomnyashchii, A. B.; Bard, A. J. *Journal of the American Chemical Society* **2012**, 134, 9240.
- (29) Al-Kutubi, H.; Voci, S.; Rassaei, L.; Sojic, N.; Mathwig, K. *Chemical Science* **2018**, 9, 8946.
- (30) Bard, A. J.; Faulkner, L. R. *Electrochemical methods*; Wiley: New York, 2001.
- (31) Yuan, Y.; Han, S.; Hu, L.; Parveen, S.; Xu, G. *Electrochimica Acta* **2012**, 82, 484.
- (32) Rubinstein, I.; Bard, A. J. *Journal of the American Chemical Society* **1981**, 103, 512.
- (33) White, H. S.; Bard, A. J. *Journal of the American Chemical Society* **1982**, 104, 6891.
- (34) Forster, R. J.; Bertocello, P.; Keyes, T. E. *Annual Review of Analytical Chemistry* **2009**, 2, 359.
- (35) a) Zu, Y.; Bard, A. J. *Analytical Chemistry* **2000**, 72, 3223; b) Gross, E. M.; Pastore, P.; Wightman, R. M. *The Journal of Physical Chemistry B* **2001**, 105, 8732;

- c) Kanoufi, F.; Zu, Y.; Bard, A. J. *The Journal of Physical Chemistry B* **2001**, 105, 210; d) Collinson, M. M.; Taussig, J.; Martin, S. A. *Chemistry of Materials* **1999**, 11, 2594.
- (36) Miao, W.; Choi, J.-P.; Bard, A. J. *Journal of the American Chemical Society* **2002**, 124, 14478.
- (37) Lai, R. Y.; Bard, A. J. *The Journal of Physical Chemistry A* **2003**, 107, 3335.
- (38) Sentic, M.; Milutinovic, M.; Kanoufi, F.; Manojlovic, D.; Arbault, S.; Sojic, N. *Chemical Science* **2014**, 5, 2568.
- (39) Valenti, G.; Fiorani, A.; Li, H.; Sojic, N.; Paolucci, F. *ChemElectroChem* **2016**, 3, 1990.
- (40) Workman, S.; Richter, M. M. *Analytical Chemistry* **2000**, 72, 5556.
- (41) Li, F.; Zu, Y. *Analytical Chemistry* **2004**, 76, 1768.
- (42) a) Knight, A. W.; Greenway, G. M. *Analyst* **1996**, 121, 101R; b) Pastore, P.; Badocco, D.; Zanon, F. *Electrochimica Acta* **2006**, 51, 5394.
- (43) Zheng, H.; Zu, Y. *The Journal of Physical Chemistry B* **2005**, 109, 12049.
- (44) Balzani, V.; Barigelletti, F.; De Cola, L. *Topics in current chemistry*. **1990**, 158, 31.
- (45) Juris, A.; Balzani, V.; Barigelletti, F.; Campagna, S.; Belser, P.; von Zelewsky, A. *Coordination Chemistry Reviews* **1988**, 84, 85.
- (46) Factor, B.; Muegge, B.; Workman, S.; Bolton, E.; Bos, J.; Richter, M. M. *Analytical Chemistry* **2001**, 73, 4621.
- (47) a) Li, M.-J.; Chen, Z.; Zhu, N.; Yam, V. W.-W.; Zu, Y. *Inorganic Chemistry* **2008**, 47, 1218; b) Bruce, D.; McCall, J.; Richter, M. M. *Analyst* **2002**, 127, 125; c) Zhou, M.; Roovers, J. *Macromolecules* **2001**, 34, 244; d) Zhou, M.; Roovers, J.; Robertson, G. P.; Grover, C. P. *Analytical Chemistry* **2003**, 75, 6708.
- (48) Chen, L.; Hayne, D.; Doeven, E.; Agugiaro, J.; Wilson, D.; Henderson, L.; Connell, T.; Heng Nai, Y.; Alexander, R.; Carrara, S.; Francis Hogan, C.; Stephen Donnelly, P.; Francis, P. *Chemical Science* **2019**.
- (49) Liu, Z.; Qi, W.; Xu, G. *Chemical Society Reviews* **2015**, 44, 3117.
- (50) Barbante, G. J.; Doeven, E. H.; Kerr, E.; Connell, T. U.; Donnelly, P. S.; White, J. M.; Lópes, T.; Laird, S.; Wilson, D. J. D.; Barnard, P. J.; Hogan, C. F.; Francis, P. S. *Chemistry – A European Journal* **2014**, 20, 3322.
- (51) a) You, Y.; Nam, W. *Chemical Society Reviews* **2012**, 41, 7061; b) Lowry, M. S.; Bernhard, S. *Chemistry – A European Journal* **2006**, 12, 7970; c) Flamigni, L.; Barbieri, A.; Sabatini, C.; Ventura, B.; Barigelletti, F. *In Photochemistry and Photophysics of Coordination Compounds II*; Balzani, V., Campagna, S., Eds.; Springer Berlin Heidelberg: Berlin, Heidelberg, 2007, p 143.
- (52) Evariste, S.; Sandroni, M.; Rees, T. W.; Roldán-Carmona, C.; Gil-Escrig, L.; Bolink, H. J.; Baranoff, E.; Zysman-Colman, E. *Journal of Materials Chemistry C* **2014**, 2, 5793.
- (53) Kessler, F.; Costa, R. D.; Di Censo, D.; Scopelliti, R.; Ortí, E.; Bolink, H. J.; Meier, S.; Sarfert, W.; Grätzel, M.; Nazeeruddin, M. K.; Baranoff, E. *Dalton Transactions* **2012**, 41, 180.
- (54) Yu, L.; Huang, Z.; Liu, Y.; Zhou, M. *Journal of Organometallic Chemistry* **2012**, 718, 14.
- (55) a) Gao, H.; Dang, Q.; Xia, S.; Zhao, Y.; Qi, H.; Gao, Q.; Zhang, C. *Sensors and Actuators B: Chemical* **2017**, 253, 69; b) Li, C.; Lin, J.; Guo, Y.; Zhang, S. *Chemical Communications* **2011**, 47, 4442; c) Zhou, Y.; Xie, K.; Leng, R.; Kong, L.; Liu, C.; Zhang, Q.; Wang, X. *Dalton Transactions* **2017**, 46, 355.
- (56) Richter, M. M.; Bard, A. J. *Analytical Chemistry* **1996**, 68, 2641.

- (57) Stringer, B. D.; Quan, L. M.; Barnard, P. J.; Hogan, C. F. *ChemPhotoChem* **2018**, 2, 27.
- (58) Richards, T. C.; Bard, A. J. *Analytical Chemistry* **1995**, 67, 3140.
- (59) Natarajan, P.; Schmittl, M. *The Journal of Organic Chemistry* **2012**, 77, 8669.
- (60) Omer, K. M.; Ku, S.-Y.; Wong, K.-T.; Bard, A. J. *Angewandte Chemie International Edition* **2009**, 48, 9300.
- (61) a)Rizzo, F.; Polo, F.; Bottaro, G.; Fantacci, S.; Antonello, S.; Armelao, L.; Quici, S.; Maran, F. *Journal of the American Chemical Society* **2017**, 139, 2060; b)Li, H.; Daniel, J.; Verlhac, J.-B.; Blanchard-Desce, M.; Sojic, N. *Chemistry - A European Journal* **2016**, 22, 12702; c)Polo, F.; Rizzo, F.; Veiga-Gutierrez, M.; De Cola, L.; Quici, S. *Journal of the American Chemical Society* **2012**, 134, 15402; d)Omer, K. M.; Ku, S.-Y.; Cheng, J.-Z.; Chou, S.-H.; Wong, K.-T.; Bard, A. J. *Journal of the American Chemical Society* **2011**, 133, 5492; e)Rashidnadimi, S.; Hung, T. H.; Wong, K.-T.; Bard, A. J. *Journal of the American Chemical Society* **2008**, 130, 634.
- (62) Kudruk, S.; Villani, E.; Polo, F.; Lamping, S.; Körsgen, M.; Arlinghaus, H. F.; Paolucci, F.; Ravoo, B. J.; Valenti, G.; Rizzo, F. *Chemical Communications* **2018**, 54, 4999.
- (63) Loudet, A.; Burgess, K. *Chemical Reviews* **2007**, 107, 4891.
- (64) a)Lai, R. Y.; Bard, A. J. *The Journal of Physical Chemistry B* **2003**, 107, 5036; b)Nepomnyashchii, A. B.; Cho, S.; Rossky, P. J.; Bard, A. J. *Journal of the American Chemical Society* **2010**, 132, 17550.
- (65) Nepomnyashchii, A. B.; Bard, A. J. *Accounts of Chemical Research* **2012**, 45, 1844.
- (66) Nepomnyashchii, A. B.; Pistner, A. J.; Bard, A. J.; Rosenthal, J. *The Journal of Physical Chemistry C* **2013**, 117, 5599.
- (67) Ishimatsu, R.; Shintaku, H.; Adachi, C.; Nakano, K.; Imato, T. *ChemistrySelect* **2017**, 2, 10531.
- (68) Zanarini, S.; Rampazzo, E.; Ciana, L. D.; Marcaccio, M.; Marzocchi, E.; Montalti, M.; Paolucci, F.; Prodi, L. *Journal of the American Chemical Society* **2009**, 131, 2260.
- (69) Valenti, G.; Rampazzo, E.; Bonacchi, S.; Petrizza, L.; Marcaccio, M.; Montalti, M.; Prodi, L.; Paolucci, F. *Journal of the American Chemical Society* **2016**, 138, 15935.
- (70) a)Valenti, G.; Rampazzo, E.; Bonacchi, S.; Khajvand, T.; Juris, R.; Montalti, M.; Marcaccio, M.; Paolucci, F.; Prodi, L. *Chemical Communications* **2012**, 48, 4187; b)Qi, W.; Wu, D.; Zhao, J.; Liu, Z.; Zhang, W.; Zhang, L.; Xu, G. *Analytical Chemistry* **2013**, 85, 3207.
- (71) Chen, X.; Liu, Y.; Ma, Q. *Journal of Materials Chemistry C* **2018**, 6, 942.
- (72) Myung, N.; Bae, Y.; Bard, A. J. *Nano Letters* **2003**, 3, 1053.
- (73) Wu, L.; Wang, J.; Ren, J.; Li, W.; Qu, X. *Chemical Communications* **2013**, 49, 5675.
- (74) Pinaud, F.; Russo, L.; Pinet, S.; Gosse, I.; Ravaine, V.; Sojic, N. *Journal of the American Chemical Society* **2013**, 135, 5517.
- (75) Liu, X.; Shi, L.; Niu, W.; Li, H.; Xu, G. *Angewandte Chemie International Edition* **2007**, 46, 421.
- (76) Han, S.; Niu, W.; Li, H.; Hu, L.; Yuan, Y.; Xu, G. *Talanta* **2010**, 81, 44.
- (77) Kitte, S. A.; Wang, C.; Li, S.; Zholudov, Y.; Qi, L.; Li, J.; Xu, G. *Analytical and Bioanalytical Chemistry* **2016**, 408, 7059.
- (78) Bolleta, F.; Ciano, M.; Balzani, V.; Serpone, N. *Inorganica Chimica Acta* **1982**, 62, 207.
- (79) Hu, L.; Xu, G. *Chemical Society Reviews* **2010**, 39, 3275.

- (80) Downey, T. M.; Nieman, T. A. *Analytical Chemistry* **1992**, 64, 261.
- (81) Sentic, M.; Arbault, S.; Goudeau, B.; Manojlovic, D.; Kuhn, A.; Bouffier, L.; Sojic, N. *Chemical Communication* **2014**, 50, 10202.
- (82) Milutinovic, M.; Sallard, S.; Manojlovic, D.; Mano, N.; Sojic, N. *Bioelectrochemistry* **2011**, 82, 63.
- (83) Zou, G.; Tan, X.; Long, X.; He, Y.; Miao, W. *Analytical Chemistry* **2017**, 89, 13024.
- (84) Kurita, R.; Arai, K.; Nakamoto, K.; Kato, D.; Niwa, O. *Analytical Chemistry* **2010**, 82, 1692.
- (85) Zamolo, V. A.; Valenti, G.; Venturelli, E.; Chaloin, O.; Marcaccio, M.; Boscolo, S.; Castagnola, V.; Sosa, S.; Berti, F.; Fontanive, G.; Poli, M.; Tubaro, A.; Bianco, A.; Paolucci, F.; Prato, M. *ACS Nano* **2012**, 6, 7989.
- (86) Guo, W.; Ding, H.; Gu, C.; Liu, Y.; Jiang, X.; Su, B.; Shao, Y. *Journal of the American Chemical Society* **2018**, 140, 15904.
- (87) Zhou, J.; Nie, L.; Zhang, B.; Zou, G. *Analytical Chemistry* **2018**, 90, 12361.
- (88) Wang, X.; Gao, H.; Qi, H.; Gao, Q.; Zhang, C. *Analytical Chemistry* **2018**, 90, 3013.
- (89) Chen, Y.; Xu, J.; Su, J.; Xiang, Y.; Yuan, R.; Chai, Y. *Analytical Chemistry* **2012**, 84, 7750.
- (90) Li, Y.; Luo, X.; Yan, Z.; Zheng, J.; Qi, H. *Chemical Communications* **2013**, 49, 3869.
- (91) Tang, X.; Zhao, D.; He, J.; Li, F.; Peng, J.; Zhang, M. *Analytical Chemistry* **2013**, 85, 1711.
- (92) Nasiri Khonsari, Y.; Sun, S. *Chemical Communications* **2017**, 53, 9042.
- (93) Chen, L.; Cai, Q.; Luo, F.; Chen, X.; Zhu, X.; Qiu, B.; Lin, Z.; Chen, G. *Chemical Communications* **2010**, 46, 7751.
- (94) Morrison, D.; Rothenbrocker, M.; Li, Y. *Small Methods* **2018**, 2, 1700319.
- (95) Tang, C.-X.; Bu, N.-N.; He, X.-W.; Yin, X.-B. *Chemical Communications* **2011**, 47, 12304.
- (96) Liu, S.; Yuan, H.; Bai, H.; Zhang, P.; Lv, F.; Liu, L.; Dai, Z.; Bao, J.; Wang, S. *Journal of the American Chemical Society* **2018**, 140, 2284.
- (97) Soulsby, L. C.; Hayne, D. J.; Doeven, E. H.; Wilson, D. J. D.; Agugiaro, J.; Connell, T. U.; Chen, L.; Hogan, C. F.; Kerr, E.; Adcock, J. L.; Donnelly, P. S.; White, J. M.; Francis, P. S. *Physical Chemistry Chemical Physics* **2018**, 20, 18995.

II. Supramolecular ECL

2.1 Introduction

Supramolecular chemistry originated from the pioneering works of Paul Ehrlich, Alfred Werner, Emil Fischer and Jean-Marie Lehn and was consecrated by the 1987 Nobel Prize in Chemistry awarded to Charles Pedersen, Donald Cram and Jean-Marie Lehn.¹ With supramolecular chemistry, the focus moved from molecular to multimolecular or multicomponent systems, driven by the emergence of new chemical functions. The interaction between the components composing the supramolecular system enables not only to tune the chemical properties of the single component but also to observe new interesting features, not detectable in each isolated component. In the last decades, the necessity to develop new ECL luminophores with higher ECL performances and original properties in ECL applications extended the studies in this field from molecular to supramolecular systems.² For example, Prodi and coworkers³ reported in 2015 a new ECL biosensor for the selective detection of prostate cancer-biomarker sarcosine in urine, based on a supramolecular approach instead of classic immunoassay.⁴ The unique complexation properties of the tetrakisphosphate cavitands toward sarcosine in specific pH conditions were applied to the capture of the analyte in a complex matrix. The supramolecular structure of these cavitands, chemically bonded to microbeads' surface, permitted the controlled release of sarcosine by variation of pH condition in a solution containing $[\text{Ru}(\text{bpy})_3]^{2+}$ as ECL

luminophore. Sarcosine was quantitatively detected by using it as ECL coreactant, with an efficiency of 30 % compared with the standard $[\text{Ru}(\text{bpy})_3]^{2+}$ / TPA system. In this context, ECL studies were conducted on two supramolecular systems and the results will be discussed in this chapter. In the first part of the chapter, an ECL investigation on trigonal truxene-core spirofluorene dyes is discussed. A previous reported ECL-active luminophore⁵ was further modified by substitution of spirofluorene with a truxene core and by adding new components, in order to improve the ECL efficiency and tune the ECL features. The comparison of the new derivatives with the unmodified luminophore, containing only part of the components, allowed studying the contribution of the newly introduced groups to the ECL performances. In the second part of the chapter, a new supramolecular system featuring pyrene moieties mounted on a rigid scaffold is presented. Such molecule has permitted to disclose a new property of ECL emission, where the optical characteristics of the light emitted can now distinguish between two enantiomers. In fact, ECL activity of pyrene was previously reported as weak, due to the generation of by-products.⁶ By rigidly positioning two pyrene units on a chiral polyether macrocycle, the generation of pyrene excimer is favored and a strong ECL emission has been observed. The stable and high ECL intensity of the supramolecular system permitted to detect for the first time the circular polarization of the ECL emission for both enantiomers of an organic compound.⁷

2.2 ECL study of trigonal truxene-core spirofluorene dyes

Among organic ECL emitters, PAHs represent the first studied luminophores for ECL.⁸ Spirofluorene derivatives, a class of PAHs, are the subject of numerous ECL studies because of the high fluorescent quantum yields and the stability of radical cations and anions in aprotic environment.⁹ They are extensively employed in organic light-emitting diodes,¹⁰ solar cells,¹¹ organic lasers.¹² Moreover, the ECL emission of spirofluorene derivatives and the stability of their radicals can be easily tuned by chemically modifying the main backbone structure with electron donor and acceptor moieties. The presence of both donor and acceptor moieties in a single supramolecular system permits the generation of the excited state *via* annihilation between the radical cation of the donor and the radical anion of the acceptor moieties, respectively. In the last years, many publications described the design and ECL characterization of new spirofluorene-based systems in which the stability of the radical cation was increased by adding donor groups like di- and tri-phenylamines.¹³ Moreover, donor-acceptor systems were investigated in which spirofluorene and spirobifluorene served as π -bridge to connect

other acceptor groups, such as 2,1,3 benzothiadiazole or oxadiazoles. Moreover, the emission wavelength of spirobifluorene can also be tuned by intercalation of a π -bridge like N-phenylcarbazole.¹⁴ Star-shaped structures conjugated with fluorine have been reported as novel ECL dyes.¹⁵ Donor and acceptor components can also be further functionalized with electron withdrawing or electron donating groups to achieve a fine-tuning of ECL emission wavelength.¹⁶ Spirobifluorene molecules have been patterned as monolayers for solid-state ECL applications.¹⁷ In a previous work, a spirofluorene-based system with triphenylamine end groups and a thiophene bridge was investigated.¹⁸ The ECL performances of this system were evaluated using TPA as coreactant in dichloromethane, while exploring only the oxidation process due to the limited potential window of the solvent. An ECL efficiency of about 4.5 times larger than that of the standard $[\text{Ru}(\text{bpy})_3]^{2+}$ luminophore was achieved. In the present study, the same spirofluorene-based system (Figure 2.1, **1**) was first further investigated *via* annihilation reaction in a different solvent (*i.e.* N,N-dimethylformamide, DMF), which shows a wider potential window.

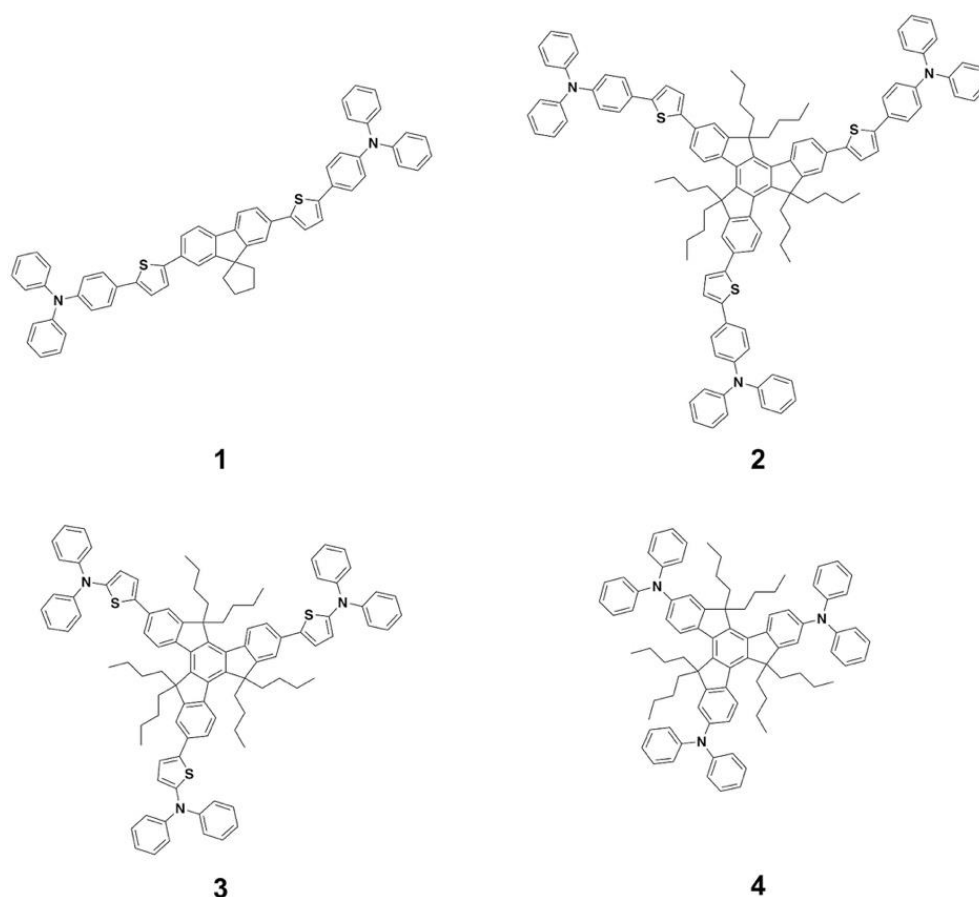


Figure 2.4 Chemical structures of the investigated spirofluorene dyes **1-4**.

Therefore, it provides a deeper evaluation of the stability of both radical cations and anions. Thanks to the wider potential window of DMF in reduction, BPO was selected as a “reductive-oxidative” coreactant. **1** can be considered as a building block for the design and preparation of more complex ECL dyes. The electrochemical and photochemical characterizations, and ECL performances of two more complex ECL emitters are also described and confronted to **1**, which gave the brightest ECL emission.¹⁸ The synthesis of dyes **1-4** was developed in the group of Prof. Blanchard-Desce and molecule **1** was already published at the time of this study.¹⁸ The new luminophores consist of a truxene core, which can be regarded as three fused fluorine units, that is further functionalized with three triphenylamine (**2**) and three diphenylamine (**3**) end groups, respectively, linked to the central core by thiophene moieties. Another simpler ECL emitter, consisting of a truxene core bearing only three diphenylamine moieties without the thiophene spacer (**4**), was also investigated as a model system for the backbone of **2** and **3**. By comparison, **4** can give insights on the role of the thiophene bridge on the electrochemical and ECL properties.

2.2.1 Electrochemical characterization

Cyclic voltammetry experiments were performed for all dyes in a degassed DMF solution with 0.1 M tetra-*n*-butylammonium hexafluorophosphate (TBAPF₆) as supporting electrolyte. Overall, the cyclic voltammograms feature a single redox process in the positive potential region ($O_{1,n}$ with *n* referred to the luminophore under investigation) and several redox processes in the negative potential region (from $R_{1,n}$ to $R_{3,n}$), as reported in Figure 2.2.

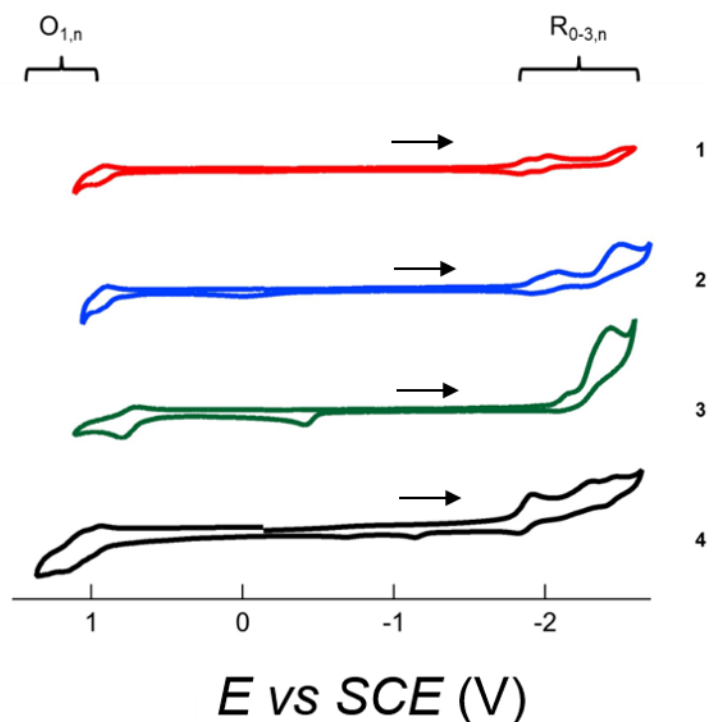


Figure 2.2 Cyclic voltammograms of **1-4** (subscript n) in DMF with 0.1 M TBAPF₆. A glassy carbon (GC) disk ($\varnothing = 2$ mm) was used as working electrode. Scan rate: 200 mVs⁻¹.

Table 1 summarizes all the electrochemical data obtained for the luminophores **1-4**.

Table 2.1 Electrochemical data of luminophores **1-4** extracted from CV in 0.1 M TBAPF₆/DMF.

n	$E^{\circ}_{O,n}$ ^a (V)	$\Delta E_{p,O}$ (mV)	$E_p - E_{p/2} (O_{1,n})$ (mV)	$E^{\circ}_{R1,n}$ (V)	$\Delta E_{p,R1}$ (mV)	$i_{p,O}/i_{p,R1,n}$ ^b	$E^{\circ}_{R2,n}$ (V)	$E_{R3,n}$ ^c (V)
1	0.935	68	69	-1.858	61	1.38	-1.984	-2.548 ^{ir}
2	0.931	80	71	-1.947	64	1.65	-2.028	-2.499 ^{ir}
3	0.764	93	81	–	–	–	-2.136	-2.407 ^{ir}
4	0.964 ^d	51	–	-1.873	97	–	-2.201	-2.435
	1.108 ^d	115	–					

^a This is an apparent E°_O because the peak is caused by the oxidation on all the triphenylamine/diarylamine units (*vide text*); n is referring to the molecular system investigated (**1-3**). ^b Absolute ratio at 0.2 V s⁻¹, where $i_{p,R1}$ corresponds to a one-electron process. ^c Superscript “*ir*” refers to an irreversible process, and the reported values correspond to the peak potentials, E_p . ^d **4** showed two distinct redox processes in the positive-going scan, see text for details.

Figure 2.3 illustrates the cyclic voltammograms of luminophores **1** to **3** in the positive potential region (Fig. 2.3, a) and in the negative potential region (Fig. 2.3, b), respectively.

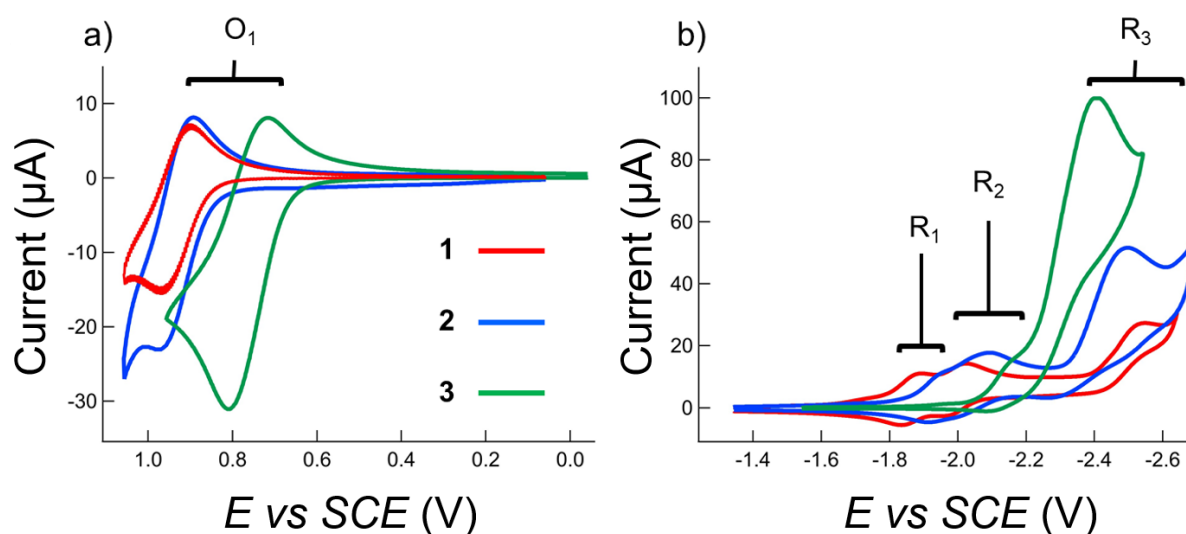


Figure 2.3 Cyclic voltammograms of **1-3**, in DMF containing 0.1 M TBAPF₆ displaying a) the positive potential region; b) the negative potential region. A GC disk ($\varnothing = 2$ mm) was used as working electrode. Scan rate: 200 mVs⁻¹.

In the forward scan (Fig. 2.3, a), a reversible oxidation process is associated with all three luminophores and it can be related with the oxidation of terminal triphenylamine and diphenylamine donor groups of these systems.^{13,18} The reversibility of the oxidation processes reveals the good stability of the cations generated from these neutral dyes. For **2**, the oxidation potential value ($O_{1,2} = 0.931$ V vs SCE, Table 1) is comparable with the reference compound **1** ($O_{1,1} = 0.935$ V vs SCE, Table 1), whereas the oxidation of **3** occurs at a significantly lower potential of 0.764 V vs SCE. This shift results from the substitution of the triphenylamine with a diphenylamine group that favors the generation of the cation. As reported in Table 1, the estimated peak-to-peak separations for the three compounds, calculated as $E_p - E_{p/2}$ ($O_{1,n}$, Table 1), present higher values than the one predicted for one-electron reversible process (where $\Delta E_p = 57$ mV at 298 K)¹⁹. It is likely that the single oxidation peaks accounts for the simultaneous oxidation of the three diphenylamines or triphenylamine moieties. In this case, it can be concluded that no electronic communication occurs between these single donor groups. Considering the negative potential region (Fig. 2.2, b), several redox processes occur for the three luminophores (data summarized in Table 1). The cyclic voltammogram of **1** (red line, Fig. 2.2, b) shows two consecutive reversible mono-electronic reduction peaks (at -1.858 V vs SCE

and -1.984 V vs SCE), probably related to the reduction of the spirofluorene component.^{15a} A third irreversible peak follows at -2.548 V vs SCE. In Figure 2.2 b, the blue curve corresponds to the cyclic voltammogram of the derivative **2**. Two reversible peaks are observed, at -1.947 V vs SCE and -2.028 V vs SCE and an irreversible one at the more negative potential of -2.499 V vs SCE, which can be assigned to the reduction of the truxene core.^{15b} In this second compound, a truxene core replaces the spirofluorene of **1**. Such a chemical modification probably decreases the stabilization of the negative charge, which can explain the slight difference observed in the electro-reduction behavior. Unlike compounds **1** and **2**, the cyclic voltammogram of luminophore **3** features two close irreversible reduction peaks at -2.136 V vs SCE and -2.407 V vs SCE. The influence of the scan rate on both reduction and oxidation waves was investigated in the range 100 mVs⁻¹ to 500 mVs⁻¹, as reported in Figure 2.4.

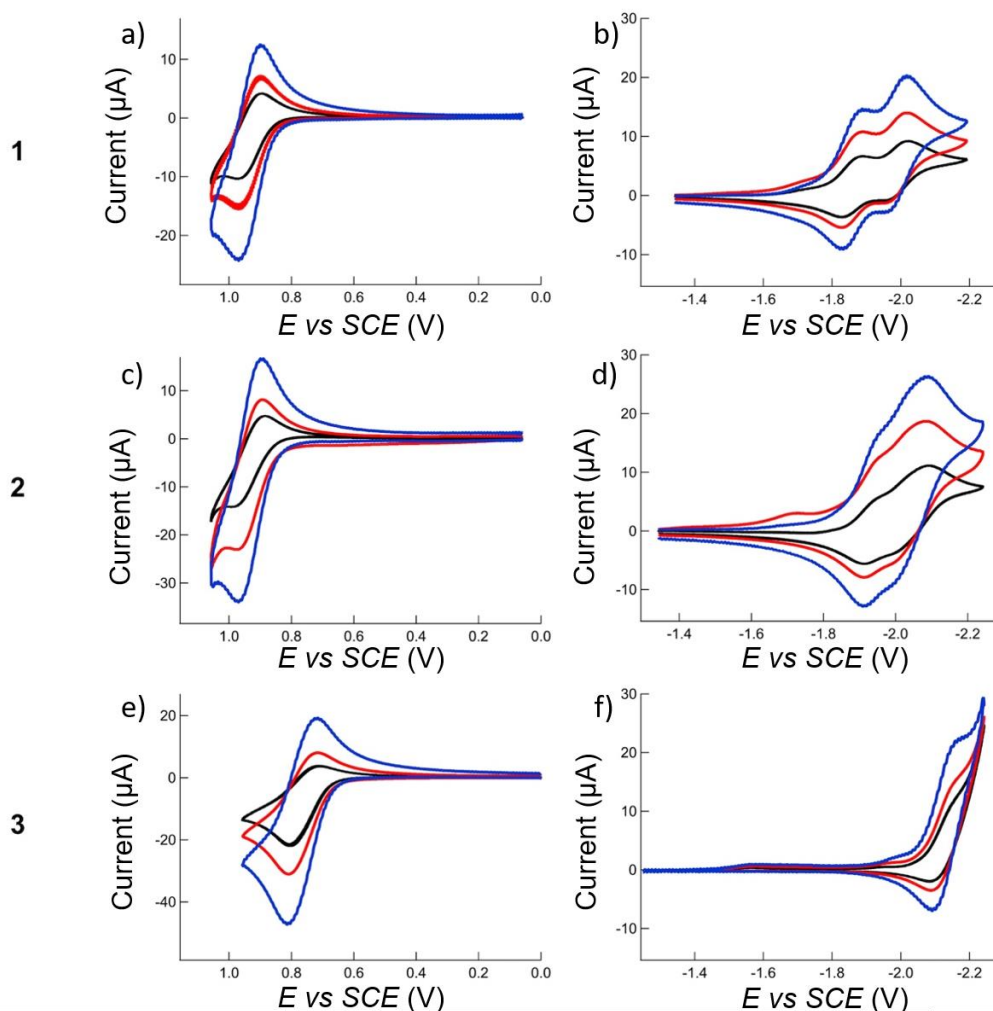


Figure 5.4 Cyclic voltammograms of **1-3** in DMF solution with 0.1 M TBAPF₆ in the positive (a, c and e) and negative-going (b, d and f) scan. A GC disk ($\varnothing = 2$ mm) was used as working electrode. Scan rates varied in the range 100 mVs⁻¹ (black line), 200 mVs⁻¹ (red line) and 500 mVs⁻¹ (blue line).

Overall, as expected for diffusion-controlled processes, at higher scan rate an improvement in the reversibility can be detected. In particular, considering the variation in the reduction peak of compound **3**, it can be stated that a full reversibility can be achieved for scan rates higher than 500 mVs^{-1} . The less efficient reduction process of **3** compared to **2** can be assigned to the presence of a following chemical reaction. The substitution of the triphenylamine with diphenylamine groups probably causes a decrease in the stability of the thiophene unit. Further calculations are necessary to investigate the role of the specific components in the electrochemical processes and to clarify the HOMO and LUMO localizations for the different compounds. Due to the low solubility in DMF with 0.1 M TBAPF_6 , the concentration of **4** could not be absolutely determined and only a qualitative analysis was possible. As reported in Figure 2.2 (black line), the electrochemical reduction behavior is consistent with the other compounds. Three reduction peaks can be observed at -1.873 V vs SCE , -2.201 V vs SCE and -2.435 V vs SCE . By contrast, two distinct and not completely resolved oxidation peaks are identified, at about $+0.964 \text{ V vs SCE}$ and $+1.108 \text{ V vs SCE}$. The electrochemical characterization verified the formation of stable radical cations (corresponding to the first oxidation processes) and stable radical anions for the first two reduction reactions. The stability of the electrogenerated radicals represent the first required condition for producing ECL emission with high intensity.²⁰

2.2.2 ECL via annihilation

Firstly, ECL emission was investigated via annihilation pathway. The potential of the working electrode was alternatively pulsed between a sufficient anodic and cathodic potentials, in order to simultaneously generate anion and cation radicals of the luminophores in the reaction layer adjacent to the electrode surface. A potential of 100 mV higher than the first oxidation peak potential ($O_{1,n} + 100 \text{ mV}$) was applied in the positive potential pulse for all dyes and a potential of 100 mV more negative than the first reduction potential ($R_{1,n} - 100 \text{ mV}$) was applied during the cathodic potential pulse for compounds **1**, **2** and **4**. For compound **3**, a potential value of 100 mV more negative than the second reduction potential ($R_{2,3} - 100 \text{ mV}$) was used for the generation of the anion radicals.²¹ Figure 2.5 shows an example of transient ECL signal as well as the corresponding chronoamperometric curve for compound **2**.

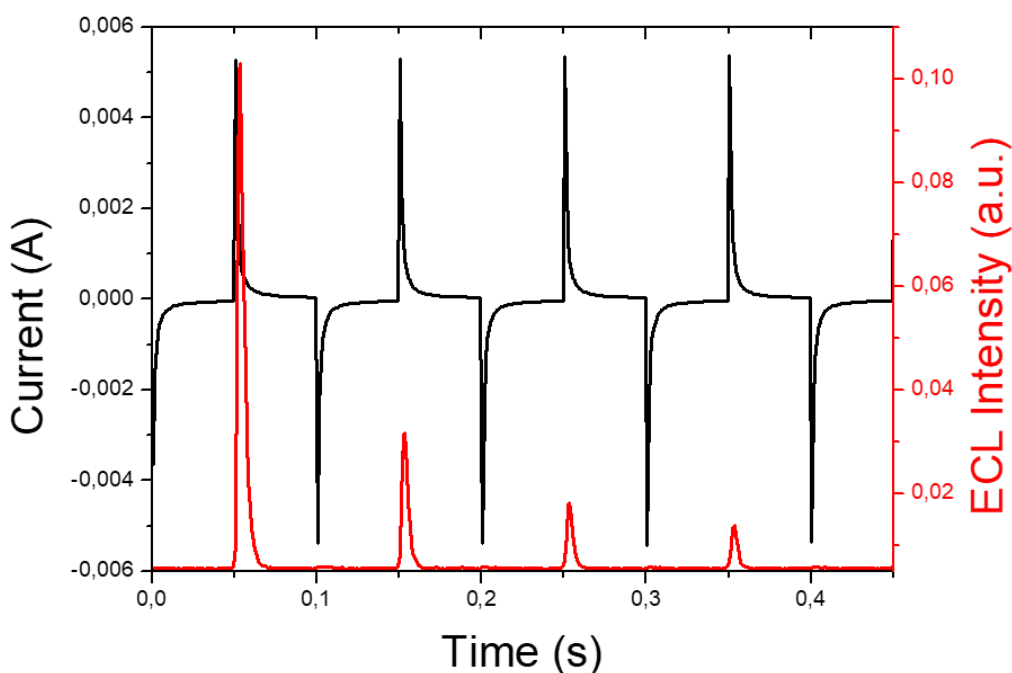


Figure 2.5 Chronoamperometric curve and ECL transient of 0.05 mM of **2** in deoxygenated DMF solution containing 0.1M TBAPF₆. The potential was pulsed between the first oxidation peak potential ($O_{1,2}$) + 100 mV and the first reduction peak potential ($R_{1,2}$) + 100 mV for **2**. A GC disk ($\varnothing = 2$ mm) was used as working electrode. Pulse duration: 0.05s.

ECL emission occurs concomitantly with the potential switching from the negative to the positive potential pulse. It is reasonable to consider that the stability of the radical anions is higher than that of radical cations, whose lifetime is insufficient to maintain a proper concentration in the reaction layer before the next negative pulse. Also, it can be noticed that the ECL intensity decreases after the first emission at $t = 0.05$ s. The regular decrease of ECL emission after repetitive pulses could be ascribed to the passivation of the electrode surface, due to the generation of a polymer film, as previously reported for other luminophores containing triphenylamine moieties unprotected at the *para* position.^{13b} The same trend was found for compounds **1** and **3**, as reported in Figure 2.6.

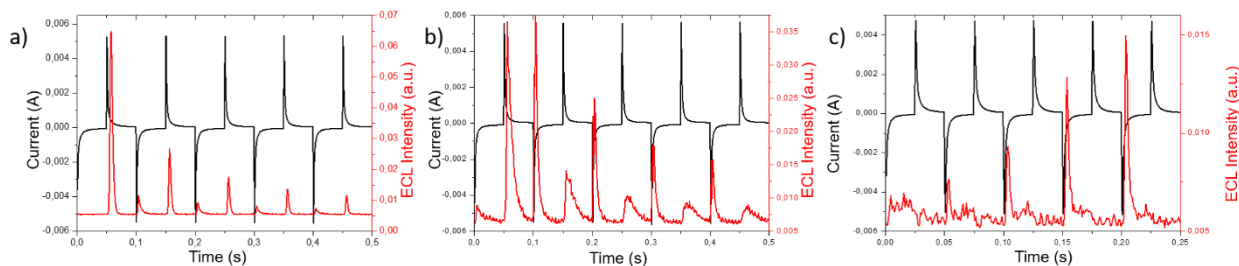


Figure 2.6 Chronoamperometric curve and ECL photocurrent transient in deoxygenated DMF/0.1M TBAPF₆ solutions. (a) 0.05mM of **1**, potential pulsed between (0.05 s, PMT scale: 0.000 mA). Pulse duration: 0.05s.; b) 0.05mM of **3** in deoxygenated DMF solution containing 0.1M TBAPF₆. Pulse duration: 0.025s. PMT scale: 0.000 μ A; c) 0.025mM of **4** in deoxygenated DMF solution containing 0.1M TBAPF₆. Pulse duration: 0.1s. PMT scale: 0.000 μ A. The potentials were pulsed between the first oxidation peak potential ($O_{1,n}$) + 100 mV and the first reduction peak potential ($R_{1,n}$) - 100 mV for **1** and **4** and the second reduction ($R_{2,2}$) - 100 mV potential for **3**.

It is possible to distinguish two general routes for the generation of ECL emitting state. In a first case, called “S route”, the energy provided by the annihilation reaction is large enough to directly populate the emitting state and the following criteria must be satisfied: $-\Delta G^{\circ}_{ann,n} > E_{S,n}$. A second possibility, so-called “T route”, concerns the initial population of the triplet excited state that is non-emissive. However, the singlet excited state can be populated by triplet-triplet annihilation reaction. In this second case, $-\Delta G^{\circ}_{ann} < E_{S,n}$. The term ΔG°_{ann} (eV) is defined as the annihilation enthalpy (as the entropic term, $T\Delta S^{\circ}$, of about 0.1 eV is neglected) and it can be calculated by the following equation^{8a,8c,22}:

$$-\Delta G^{\circ}_{ann,n} \text{ (eV)} = E^{\circ}_{O_{1,n}} \text{ (V)} - E^{\circ}_{R_{1,n}} \text{ (V)} \quad (2.1)$$

For compound **3**, $E^{\circ}_{R_{2,n}}$ was used. The term $E_{S,n}$ is the energy of the excited state for a compound n, extracted from the PL spectrum (*vide* Chapter I). For all studied compounds, the values of the enthalpy of the annihilation reaction are very similar, ranging between 2.79 eV and 2.9 eV. Table 2.2 summarizes the data concerning the spectroscopic properties and annihilation ECL for dyes **1-4**.

Table 2.2 Data concerning the spectroscopic properties and annihilation ECL for **1-4** in DMF with 0.1 M TBAPF₆.

<i>N</i>	$\lambda_{max,n}^{Abs}$ (nm) ^a	$\lambda_{max,n}^{FL}$ (nm) ^a	$\lambda_{max,n}^{Ann/ECL}$ (nm)	$E_{S,n}$ (eV) ^b	$-\Delta G^{\circ}_{Ann,n}$ (eV)	$\Phi_{FL,n}$ ^a	$\Phi_{Ann,n}$ ^c
1	417	501	530	2.47	2.79	0.71	159
2	402	483	494	2.57	2.88	0.60	314
3	381	465	485	2.67	2.9	0.45	16
4	362	393	-	3.15	2.84	0.29 ^b	19

^a PL data obtained in DMF. ^b Value measured in dichloromethane only for **4**. ^c The ECL quantum efficiencies were calculated relative to the reference [Ru(bpy)₃]²⁺ ($\Phi_{Ann} = 100\%$).

For compounds **1**, **2** and **3**, $-\Delta G^{\circ}_{ann,n} > E_{S,n}$. Consequently, they are considered as “energy-sufficient” systems, following the “S-route”. By contrast, for compound **4** $-\Delta G^{\circ}_{ann} < E_{S,n}$, meaning that is an “energy-deficient” system, which may only follow the “T-route”. This explains why **4** gives a very low ECL efficiency (Table 2.2). The ECL efficiencies (Table 2.2) were calculated relatively to the ECL efficiency of the reference standard compound $[\text{Ru}(\text{bpy})_3]^{2+}$ ($\Phi = 100\%$). All data were collected in the same experimental conditions, and same concentrations and sensitivity range, for both the investigated luminophores **1-4** and for the reference standard. The following equation was used^{5,23}:

$$\Phi_{(x)} = 100 \times \left[\frac{\int_0^t I_{ECL} dt}{\int_0^t i dt} \right]_n / \left[\frac{\int_0^t I_{ECL} dt}{\int_0^t i dt} \right]_{st} \quad (2.2)$$

Although the enthalpy of the annihilation for **2**, $-\Delta G^{\circ}_{ann,2}$, is the lowest of the series, the ECL efficiency is the highest. Indeed, it is twice larger than that of **1** and more than three times larger than $[\text{Ru}(\text{bpy})_3]^{2+}$. The thermodynamic driving force and the quantum yields are not the only contributions to consider for reaching a high ECL efficiency. One hypothesis is that the electrogenerated radicals (in particular the anion radical) of **2** exhibit a more elevated stability than the radicals of the other compounds. Figure 2.7 illustrated the ECL spectra (a) for compounds **1-3**, and the absorption spectra (b, dot lines) and the PL spectra (b, solid line) for all compounds. ECL signal associated with **4** was too low to record successfully an ECL spectrum.

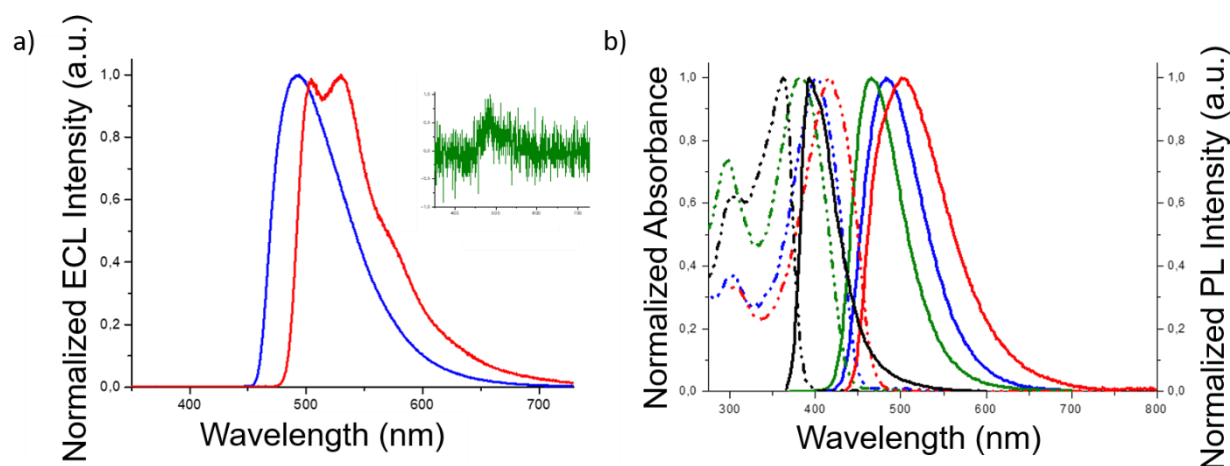


Figure 2.7 a) Normalized ECL spectra obtained by annihilation mechanism for **1** (red curve), **2** (blue curve) and **3** (inset, green curve) in DMF. ECL spectra were recorded in DMF containing 0.1M TBAPF₆; b) Normalized absorption (dot lines) and PL spectra (solid lines), for **1** (red line), **2** (blue line), **3** (green line), and **4** (black line) in DMF.

The potential was pulsed between 100 mV higher than the oxidation peak ($O_{1,1-3}$) and 100 mV lower than the second reduction peak ($R_{2,1-3}$), each step lasting 25 ms. ECL emission signal was integrated for 1 s, using a 1 nm slit width. The emission-wavelength maxima ($\lambda_{max,n}^{Ann/ECL}$) are gathered in Table 2.2. Whereas compound **3** shows a very weak ECL emission, compounds **1** and **2** are much brighter ECL dyes according to the annihilation process, as a short exposition time is needed to collect their ECL spectra. By comparing the ECL and PL spectra of compounds **2** and **3**, similar emission-wavelength maxima can be observed. By contrast, the annihilation ECL spectrum of luminophore **1** shows two maxima, which were not observed in the ECL spectrum recorded with TPA as coreactant.⁵ The different ECL spectrum in annihilation might be related to by-products generated during the negative potential pulse. The small Stokes shift (*vide* Chapter I) between the absorption and PL can cause inner filter effects, which are favored at higher concentrations of the luminophore.²⁴ Moreover, considering compounds **1** to **3**, a remarkable $\Delta\lambda$ of 35 nm in ECL and PL has been obtained, even though no electron-donating or withdrawing groups other than thiophene and truxene moieties were introduced to modulate the energy levels of HOMO and LUMO, as it was previously reported in other studies.^{13b,16}

2.2.3 ECL via reductive-oxidative coreactant pathway

The ECL performances of the spirofluorene derivatives **1-4** were also investigated via the reductive-oxidative coreactant pathway, by employing benzoyl peroxide (BPO) as sacrificial coreactant. Figure 2.8 reports the ECL emission from compounds **1-4** when scanning the potential towards the cathodic potential region until -2.6 V vs SCE, in presence of an excess of BPO. The ECL response of the reference compound $[\text{Ru}(\text{bpy})_3]^{2+}$ is also reported for comparison in the same experimental conditions.

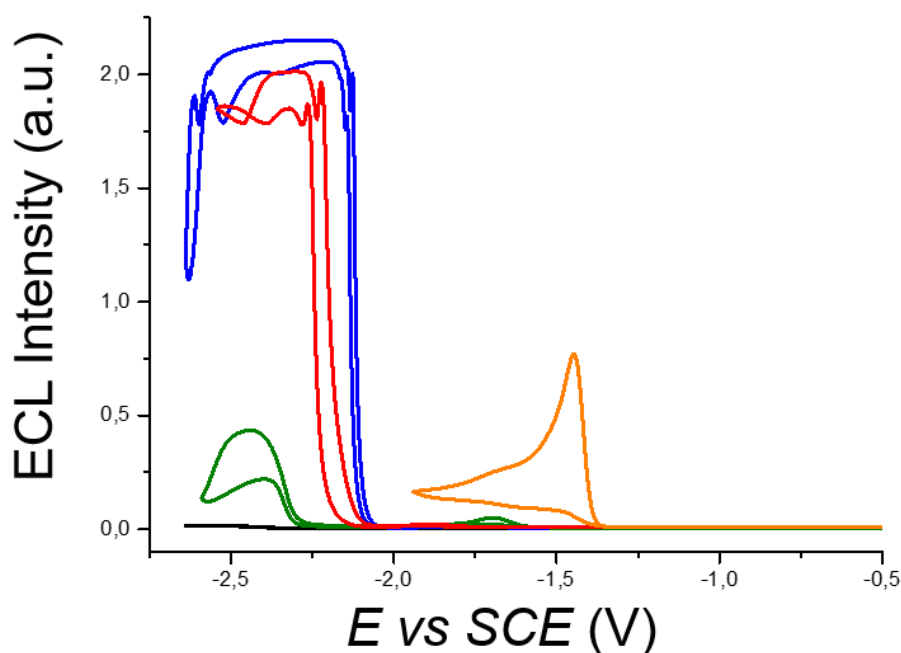
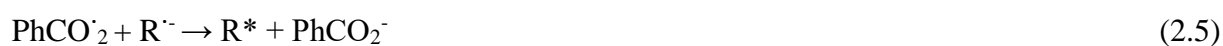
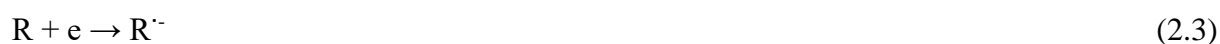


Figure 2.8 Comparison of the ECL responses for 0.5 mM of **1** (red line), **2** (blue line), **3** (green line), 25 μM of **4** (black line) and 0.5 mM $[\text{Ru}(\text{bpy})_3]^{2+}$ (orange line), as the standard reference, in DMF solution containing 10 mM BPO and 0.1M TBAPF₆. The ECL signals were generated at a GC electrode while scanning the potential at 0.1 Vs^{-1} .

The ECL emissions of dyes **1** and **2** occur at potential values slightly more negative than -2 V vs SCE. A rapid increase is then observed and the intensity maximum is maintained for a wide potential range, covering all the reduction ($R_{1-3,n}$) processes. Therefore, ECL emission is only obtained at potentials where the luminophores are reduced. BPO is an efficient and widely-used coreactant, which follows the “reductive-oxidative” mechanism.^{22b} A very strong oxidizing species (PhCO_2^\bullet) is produced upon concerted reductive cleavage of the O-O bond.²⁵ The so-generated radical, which shows an $E^0 = 1.5 \text{ V vs SCE}$,²⁵⁻²⁶ reacts with the reduced form of the dye, thus generating the exciting state, as described by the following sequence of reactions, where R represents the compounds under study (Eq. 2.3-2.6):



The shift of **3** towards more negative reduction potentials is reflected also in the ECL behavior. The ECL response for **3** occurs at a potential value of around -2.25 V vs SCE. Its ECL intensity is lower than that of compounds **1** and **2**, probably due to the lower stability of the radical anion, as observed in cyclic voltammetric studies. The low solubility of **4** in the solution DMF/TBAPF₆ 0.1 M is responsible for a very low ECL intensity, as the effective concentration was much lower than for the other compounds (*i.e.*, 20 times). Recording the ECL emission of the reference standard [Ru(bpy)₃]²⁺ allowed calculating the ECL efficiencies of all compounds, following Eq. 2.2. Table 2.3 reports ECL efficiencies and the calculated thermodynamic quantities describing the energetics of the ECL processes.

Table 2.3 ECL data for **1-4** in DMF solution containing 0.1 M TBAPF₆ and 10 mM BPO.

<i>n</i>	$\lambda_{max,n}^{Coreac/ECL}$ (nm)	$-\Delta G_{Coreac,n}^0$ (eV) ^a	$\Phi_{ECL,n}$ (%) ^b
1	528	3.36	230
2	493	3.45	450
3	485	3.63	75
4	-	3.37	7

^a $-\Delta G_{Coreac,n}^0$ was calculated using Eq. 10 with $E_{R1,n}^\circ$, except for **3** where we used $E_{R2,n}^\circ$. ^b The ECL quantum efficiency values are relative to the standard [Ru(bpy)₃]²⁺ ($\Phi_{ECL} = 100\%$) with BPO in the same experimental conditions.

In the reductive-oxidative coreactant pathway (*vide* Chapter I) with BPO, the energy available to populate the electronic excited states results from the exergonic electron-transfer reaction between the benzoate radical and the reduced dye (Eq. 2.5). The enthalpy of the process (named $-\Delta G_{Coreac,n}^\circ$ as the entropic contribution is neglected) is approximated by using the following equation:

$$-\Delta G_{Coreac,n}^0(\text{eV}) = E_{Ox_{PhCO_2}^{\cdot-}/PhCO_2^-}_{1,n} (V) - E_{R_{1,n}}^\circ (V) \quad (2.7)$$

Where $E_{R1,n}^\circ$ is the first reduction potential of the luminophore *n* (for **3** $E_{R2,3}^\circ$ was used) and $E_{Ox_{PhCO_2}^{\cdot-}/PhCO_2^-}_{1,n}^\circ$ is the oxidation potential of the benzoate radical (1.5 V vs SCE).²⁵⁻²⁶

$-\Delta G_{Coreac,n}^0$ is higher than the energy required for the direct formation of the excited state ($E_{s,n}$ data in Table 2.2) for **1-3**, whereas for **4** it is very close. In fact, a low ECL intensity is observed for compound **4**. As in the annihilation pathway, dye **2** reported an ECL efficiency twice greater than that of **1**. Indeed, the ECL efficiency of **2** is particularly high in comparison to those

reported for similar systems.^{9a,13b,15a,15b,15d,16,27} Apart from the dye **4**, ECL spectra (Fig. 2.9) were recorded for luminophores, thanks to the high intensities of the ECL emission using BPO.

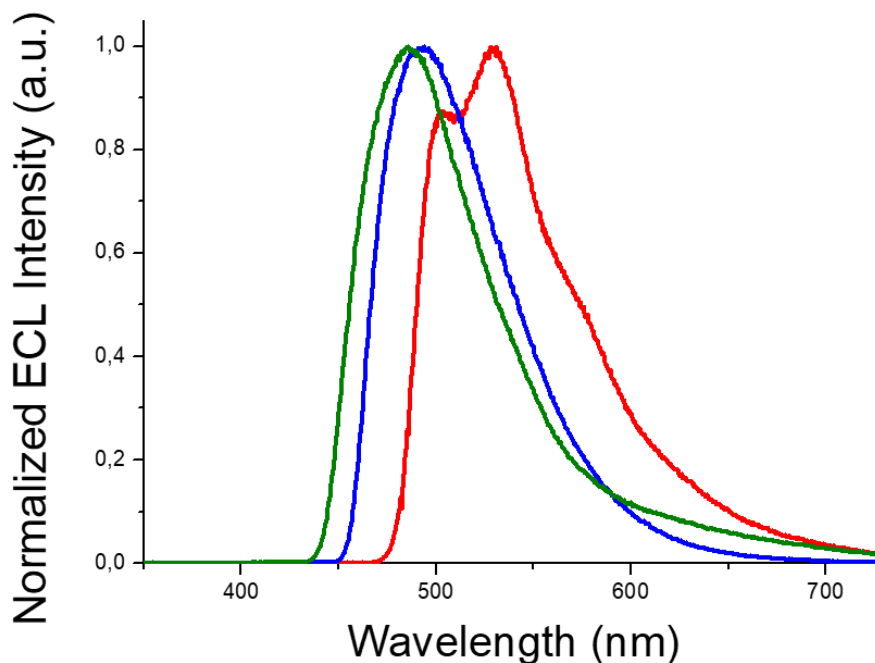


Figure 2.9 ECL spectra for **1** (red), **2** (blue), and **3** (green) in DMF. ECL spectra were recorded in DMF solution containing 10 mM BPO and 0.1 M TBAPF₆.

It can be observed that ECL spectra via annihilation (Fig. 2.7, a) of **1** and **2** are similar to those obtained by using BPO as coreactant. ECL spectrum of compound **1** shows a bathochromic shift of about 30 nm, when compared to the corresponding PL spectrum. As in the annihilation mode, two maxima are observed. As in the former case, by-products from collateral reactions or inner filter effects related with the low Stokes shift and the higher concentration could be responsible of the difference between the ECL and PL spectra. On the other hand, **2** and **3** showed ECL maxima with a blue-shift of respectively 35 nm and 43 nm, in good agreement with PL spectra (Fig. 2.7, b). It could be concluded that the same excited state is populated for ECL and PL emissions.

2.3 Circularly polarization of ECL from a chiral bispyrene organic macrocycle

Circularly polarized luminescence (CPL) spectroscopy is based on the differential spontaneous emission of left- and right-circularly polarized radiation by chiral luminescent systems.²⁸ It can be considered the emission analogue of circular dichroism (CD), which measures the

differential absorption of left- and right-circularly polarized light by chiral systems. CD is therefore related with the chirality of the molecule at the ground state, while CPL reflects the chirality of the electronic excited states.²⁹ The first observation of circular polarization in luminescence was reported by Samoilov and coworkers in 1948, from a chiral crystal of sodium uranyl acetate $\text{Na}[\text{UO}_2(\text{CH}_3\text{COO})_3]$.³⁰ Comparing to solid-state measurements, CPL from chiral luminescent systems in solution is more difficult, and usually smaller. The first pioneering studies of this latter were published by Oosterhof's group in 1960s for organic molecules³¹ and for biomolecular systems in the early 1970s by Steinberg's group.³⁰ In 1974, Luk and Richardson published for the first time a CPL study on chiral luminescent lanthanide(III) complexes that until now represent the most investigated CPL systems, due to their excellent CPL performances.³² CPL was also recently observed in QDs, by adoption of a chiral structure.³³ In 2010, the structural distortion of ferrihydrite (in ferritin), generating a chiral nano-sphere, was exploited for the production of QDs within the ferritin, with high left-CPL signal.³⁴ An alternative strategy for building chiral QDs was shown by Balaz *et al.*³⁵ through functionalization of achiral CdSe QDs with chiral thiol-capping ligands, namely L- and D-cysteine. CPL can also be applied as a probe of configurational and conformational structure in the emitting states of molecular systems.³³ For example, Swager *et al.*³⁶ reported circularly polarized fluorescence with opposite polarization from films of the same chiral polymer poly(*p*-phenylene-vinylene). The difference of solvents' polarity used for the spin-casting of the film caused a modification in polymer's structural organization, detectable by CPL spectroscopy.³⁶ In CPL spectroscopy, the difference in the luminescence intensity (ΔI) of left-circularly polarized light intensity (I_L) versus right-circularly polarized light intensity (I_R) can be defined as:

$$\Delta I = I_L - I_R \quad (2.8)$$

However, the determination of the absolute emission intensities is hardly achievable. The estimation of the degree of polarization of the emission is consequently represented by the luminescence dissymmetry factor g_{lum} , which can be defined by the following equation³³:

$$g_{\text{lum}} = \frac{I_L - I_R}{\frac{1}{2}(I_L + I_R)} \quad (2.9)$$

Where ΔI is divided by the average total luminescence intensity. Ideally, when the emission is completely polarized, $g_{lum} = \pm 2$. By contrast, the value 0 corresponds to an unpolarized light. Isolated chiral molecules and macromolecules present typically g_{lum} values of 10^{-3} - 10^{-2} .^{33,37} Lanthanide complexes display the highest range of g_{lum} values (between 0.1 and 1), with a maximum of 1.38 for the complex Cs(heptafluoro-butylryl-(+)camphorato) Eu(III) in chloroform.³⁸ High g_{lum} values are related with electric dipole forbidden/magnetic dipole-allowed transitions, like Ln-centered f-f transitions.³⁷ Luminescent lanthanide complexes are commonly applied as probes to analytical and biological applications, due to their narrow emission bands and long lifetimes.³⁸ The intensity and shape of their CPL signal can be modified upon interaction with the target molecule.³⁷ Whereas CD commercially available instruments have reached an advanced level of development and construction, CPL instrumentation has only become commercially available recently³⁹ and most studies are performed with custom-built systems, which are designed and constructed in research groups.^{28,33} Figure 2.10 illustrates a scheme of the different parts of a CPL apparatus.

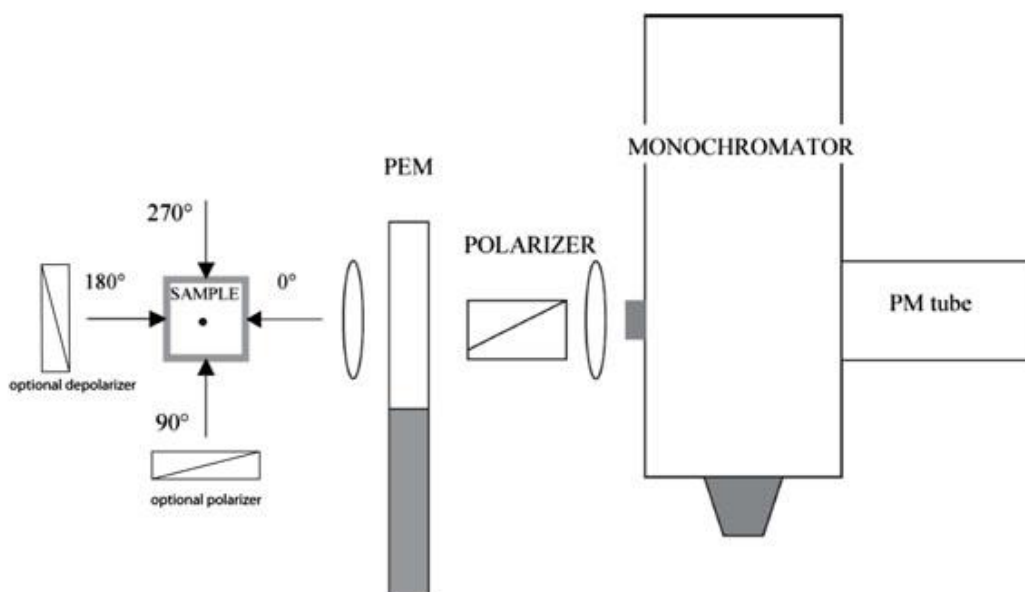


Figure 2.10 Schematic representation of a CPL apparatus.³³

A continuous wave light source is utilized for sample excitation. The choice of the excitation light source depends on the chiral system under investigation. Lasers are usually employed when selective excitation is necessary, such as for the excitation of lanthanide ions (III). Alternately, the excitation of organic based systems or organic ligands that exhibit a much broader absorption is obtained with xenon arc lamps. The excitation light source is generally

located at 180° , aligned with the direction of the emission, to avoid artifacts. Other causes of artifacts can be found in sample irradiation with linearly polarized light. In this case, the excitation of more molecules with an electric dipole transition moment parallel to the polarization direction results in selective photoexcitation. However, a linearly polarized excitation light source can be utilized for CPL measurements of racemic mixture, for a quantification of enantiomeric proportion.^{30,33} Between the sample and emission monochromator, a circular analyzer is positioned. It is composed by a photoelastic modulator (PEM), followed by a linear polarizer. In CPL measurement, the PEM acts as a quarter-wave plate. Left- and right-circularly polarized components of the light emission coming from the sample are anticipated one with respect to the other by shifting the phase usually of 90° (corresponding to a 50 kHz shift, Fig. 2.11).

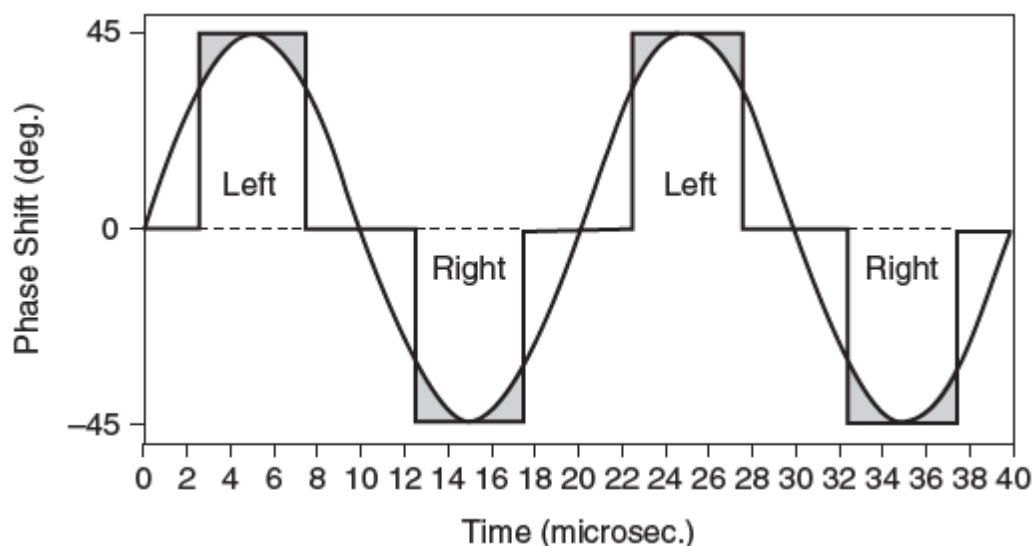


Figure 2.11 Plot of the phase modulation versus time for a 50 kHz PEM.³⁰

In this way, both emission components can alternatively be converted from circular to linear polarized light by the linear polarizer, positioned at 45° of the PEM. The last part of the apparatus is composed by a monochromator and a photomultiplier tube (PM tube) for the collection of a wavelength-resolved light emission.

The peculiar characteristics of chiral lanthanide complexes spectra, combined with their strong CPL signal, led to a multidisciplinary interest. In particular, the selectivity of the CPL response can be employed in bioanalysis for biomarkers detection with a spectroscopic or microscopic approach.³⁷ Changes in the coordination environment of the lanthanide ions in complexes can cause significant variations on CPL signals. For example, Eu and Tb chiral complexes are able to switch the sign of the CPL signal upon selective interaction with serum albumin.⁴⁰ Chiral

lanthanide complexes-based optical probes can also track variations in living cells metabolites. In the last decades, the high temporal and spatial resolution, high sensitivity and low background of ECL imaging allowed its implementation in biomolecules detection and single cell imaging (*vide* Chapter IV).⁴¹ The opportunity to detect the degree of polarization of ECL emission will add further advantages in ECL-bioassays, in terms of selectivity and specific response in a chiral environment. A new level of information would be accessible, not only ECL intensity and its temporal and spatial locations but also the degree of polarization, which can vary with the change in the biological environment. Consequently, new and original information would be afforded by combination of CPL phenomenon with ECL microscopy.⁷ To the best of our knowledge, the only previous example of circularly polarized electrogenerated chemiluminescence (CP-ECL) was published by Blok and coworkers in 1987.⁴² They estimated an ECL dissymmetry factor (g_{ECL}) for the system (+)-[Ru(phen)₃](ClO₄)₂ · 6 H₂O of $+12(\pm 2) \times 10^{-4}$ at 550 nm, in good agreement with the g_{lum} value of $+14(\pm 1) \times 10^{-4}$ at the same wavelength. However, no experimental data related to the CPL signal was reported in this communication. Also, the authors only tested one enantiomer of the Ru complex. In the next paragraphs, the electrochemical, photochemical and ECL investigations of the supramolecular system [18]-C-6-bispyrene and its CP-ECL signal are discussed. This work represents the first observation of the circular polarization of ECL from a purely organic molecule.⁷

2.3.1 Synthesis

[18]-C-6-bispyrene compound was designed and synthesized in Prof. Lacour's group in Geneva University.⁴³ The crown ether [18]-C-6 was chosen as building block and synthesized by using Rh(II) as catalyst (0.001 mol %) for the decomposition of α -diaza- β -keto ester (Fig. 2.12, 1) in 1,4-dioxane, used as solvent and reactant ([3+6+3+6] condensation, Fig. 2.12).⁴⁴

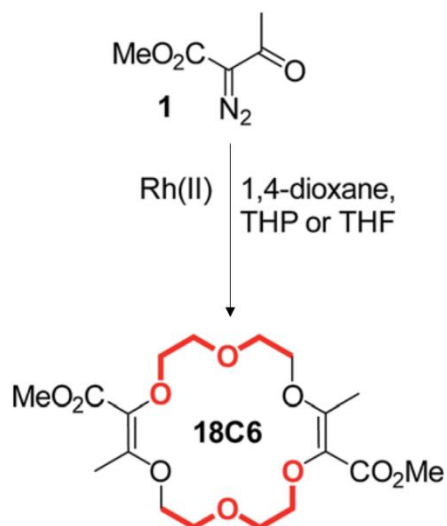


Figure 2.12 Synthesis of the unsaturated macrocycle [18]-C-6-bispyrene (Reproduced with modifications from [17]).

The successive introduction of 1-aminopyrene could be possible under strong basic conditions (*t*-BuOK, 4.0 equivalents) by amidation-olefin transpositions. The separation of the two enantiomers was achieved by chiral stationary phase high-performance liquid chromatography (CSP-HPLC).

Therefore, the supramolecular system under investigation (Fig. 2.13) comprises a constrained polyether ring ([18]-C-6bispyrene) and two pyrene subunits rigidly positioned on top of it.

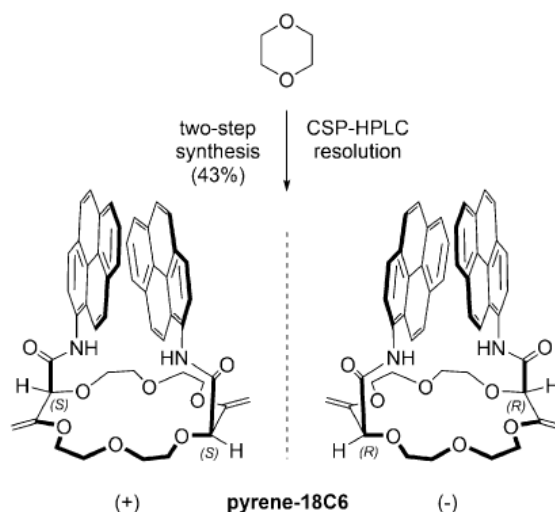


Figure 2.13 Molecular structure of [18]-C-6bispyrene.⁷

2.3.2 Electrochemical characterization

Firstly, the electrochemical properties of the supramolecular system were investigated, to determine the appropriate conditions for ECL generation on glassy carbon as working electrode. The system was studied by cyclic voltammetry and compared with isolated pyrene used as a model system. Figure 2.14 shows the cyclic voltammogram of the system [18]-C-6bispyrene, at a concentration of 0.5 mM in acetonitrile/TBAPF₆ 0.1 M on GC electrode.

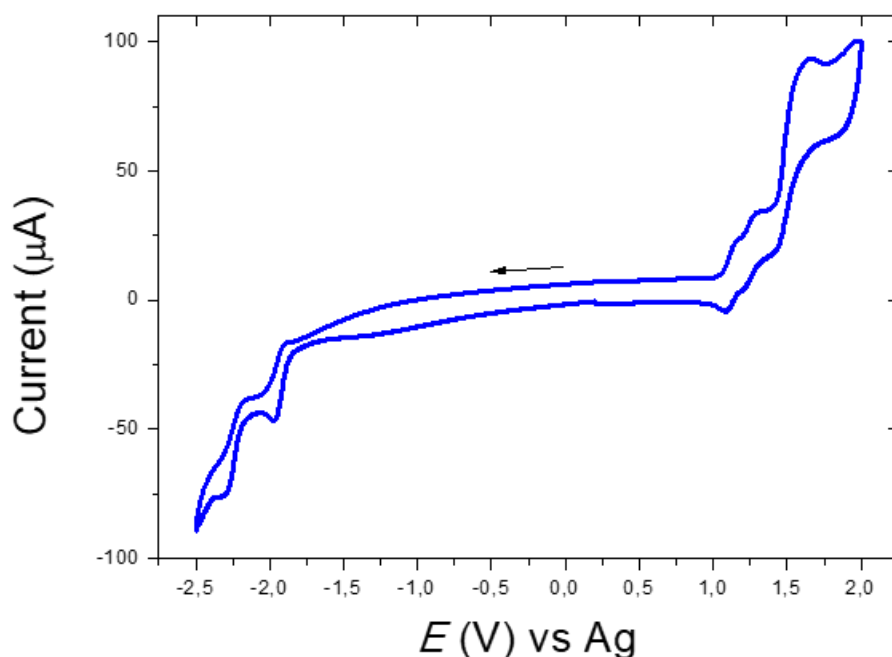


Figure 2.14 Cyclic voltammogram of 0.5 mM of [18]-C-6bispyrene, in in degassed CH₃CN solution with 0.1 M of TBAPF₆ as supporting electrolyte. A GC disk ($\varnothing=3\text{mm}$) was used as working electrode. Scan rate: 100 mVs⁻¹.

Regarding the positive potential region, two superimposed fairly reversible oxidations are observed. Half-peak potentials of respectively 1.12 V *vs* Ag and 1.27 V *vs* Ag pseudo-reference were measured for the first and second oxidations, respectively. A third oxidation, with an estimated half-peak potential of 1.55 V *vs* Ag, occurs with a lower degree of reversibility. It might be supposed that the electrogenerated cations of pyrene subunits react with each other generating covalently bonded dimers or oligomers, upon successive oxidation.⁴⁵ In the cathodic region, two stepwise reversible reduction waves are observed (Fig. 2.14). The first reduction occurs at a potential of -1.92 V *vs* Ag, while the second reduction at the more negative potential of -2.24 V *vs* Ag. The peak currents for the two reduction waves are comparable. Figure 2.15

compares the supramolecular system's behavior at negative potentials with the cyclic voltammogram of an isolated pyrene molecule.

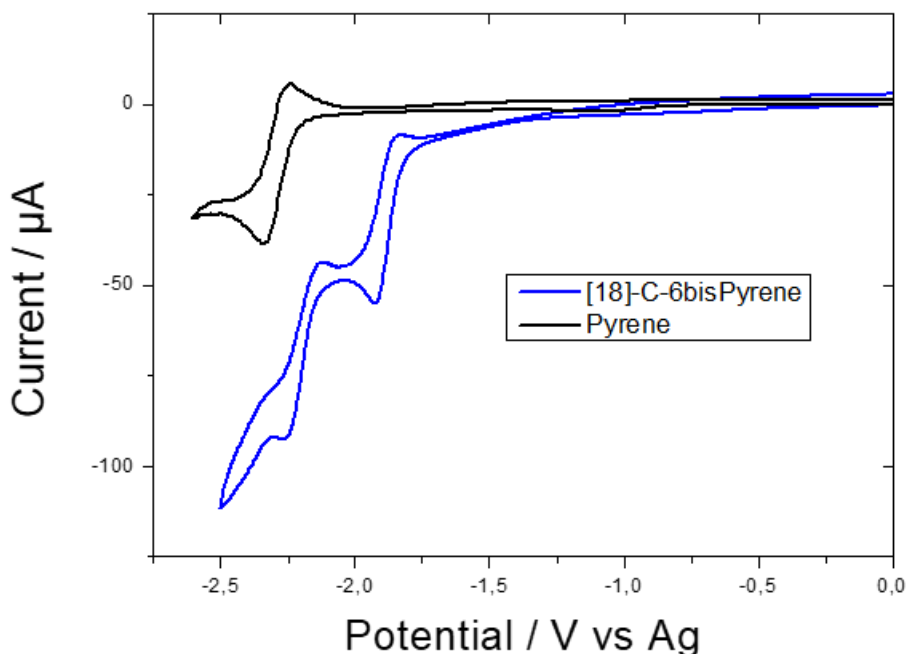


Figure 2.15 Cyclic voltammogram of 1 mM of [18]-C-6-bispyrene (blue curve) and pyrene (black curve) in degassed CH_3CN solution with 0.1 M of TBAPF_6 as supporting electrolyte. A GC disk ($\varnothing=3\text{mm}$) was used as working electrode. Scan rate: 100 mVs^{-1} .

An isolated pyrene molecule shows one peak reduction at -2.1 V vs Ag , corresponding with the generation of the monoanion, as reported in previous publications.^{6,46} In the macrocycle, the first pyrene reduction occurs at a more positive potential. Therefore, it can be concluded that the first pyrene molecule can be more easily reduced into the supramolecular system. The second reduction recorded for the macrocycle can be accounted for the reduction of the second pyrene to the corresponding monoanion. Indeed, the generation of the dianion (Py^{2-}) was reported by Heinze and Meerholz^{46b} at a much more negative potential of -2.86 V vs SCE . The stepwise monoelectronic reduction of both pyrenes in [18]-C-6-bispyrene allows to conclude that the two pyrene subunits of the supramolecular system present an electronic communication between each other. As already reported,^{6,20b,47} pyrene cation radicals, resulting from electrochemical oxidation, show a high instability. By contrast, both the mono-anion and the di-anion of [18]-C-6-bispyrene are stable at least during the time-scale of the cyclic

voltammetry experiment. The observed reversible reduction behavior suggest investigating the generation of ECL via reductive-oxidative coreactant pathway.

2.3.3 ECL analysis

ECL emission of the system [18]-C-6-bispyrene was tested by adding BPO as sacrificial coreactant^{8a,8c,22b,48} and by scanning the potential of the working electrode between 0 V and -2.75 V *vs* Ag. As previously reported, the oxidation of pyrene subunits generates unstable cations, which do not allow the production of ECL via oxidative-reductive ECL coreactant. Bard and coworkers⁶ reported the generation of a very weak ECL via annihilation for pyrene and derivative compounds, due to cations instability and collateral reactions. Figure 2.16 shows the cyclic voltammogram (black curve) and the corresponding ECL intensity (blue curve) for a solution of 0.5 M of [18]-C-6-bispyrene and 50 mM of BPO in acetonitrile with 0.1 M TBAPF₆ as supporting electrolyte. The potential of the GC electrode was scanned between 0 V *vs* Ag and -2.75 V *vs* Ag.

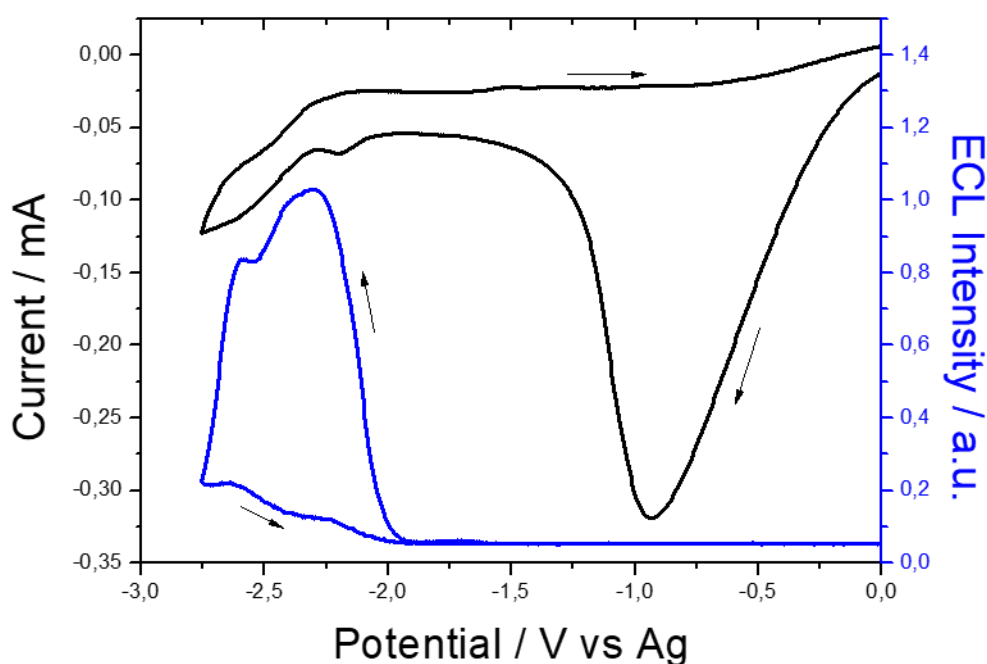


Figure 2.16 Cyclic voltammogram (black curve) and ECL intensity (blue curve) of 0.5 mM of [18]-C-6-bispyrene, 50 mM of BPO as sacrificial coreactant and 0.1 M of TBAPF₆ as supporting electrolyte in CH₃CN solution. A GC disk ($\varnothing=3\text{mm}$) was used as working electrode. Scan rate: 100 mVs⁻¹.

A broad irreversible peak at -0.9 V vs Ag is observed, corresponding to BPO reduction. BPO is irreversibly reduced in acetonitrile with a peak potential, E_p , of -0.9 V vs Ag (*i.e.*, -1.23 V vs SCE)⁴⁹, because of the successive generation of the strongly oxidizing benzoate radical species (PhCOO^\cdot , with $E^\circ_{\text{PhCOO}^\cdot/\text{PhCOO}^-} = 1.5 \text{ V vs SCE}$)^{25,48}. ECL emission starts only at potentials where the two pyrene subunits of the macrocycle are reduced, at about -1.9 V vs Ag. Moreover, the ECL intensity peak is composed of two overlapping peaks, probably related with the two successive reduction. The maximum of ECL intensity occurs at -2.3 V vs Ag, with a rapid decrease at more negative potentials.

2.3.4 ECL mechanisms

BPO is involved as reductive-oxidative coreactant for ECL generation. The reduction of BPO at the electrode surface generates a strong oxidizing species that can react with the reduced form of the luminophore, with the production of its excited state. Different mechanisms have been proposed for the system pyrene/BPO.^{6,48,50} An energy-sufficient ECL mechanistic pathway involves the reduction of the two pyrene subunits of the supramolecular system, upon the following equations:



Where Py-Py is [18]-C-6-bispyrene. In addition, BPO can be heterogeneously reduced monoelectronically (2.13) or by the reduced form of [18]-C-6-bispyrene ($\text{Py-Py}^{\cdot-}$, 2.14):



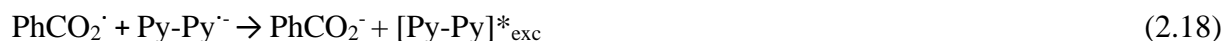
Successively, $\text{BPO}^{\cdot-}$ dissociates (2.15), by breaking of the O-O bond, affording benzoate anion PhCO_2^- and benzoate radical PhCO_2^\cdot . This latter can be reduced into the benzoate anion (2.16):



Furthermore, BPO can be directly reduced by two electrons, generating two benzoate anions, upon the following reaction:



The electron transfer reaction between the benzoate radical and Py-Py \cdot produces the excimer [Py-Py] \cdot^* _{exc} (2.18), which deactivates by ECL emission (2.19):



An excimer is a short-lived dimer, composed by two units of the same molecule, one being in the excited state and the other one in the ground state. When the interacting molecules are from two different chemical species, the excimer is called exciplex.²⁴ Excimers and exciplexes exist only in the excited state, and the potential energy curve of the corresponding ground state is dissociative. Therefore, they are different from excited complexes and dimers, which are stable also at their ground state. Moreover, excimer and exciplex emissions occur at lower energy (higher wavelength) of the emission of the isolated species. Experimentally, the excimer emission can be distinguished from the emission of the isolated species from several evidences. Firstly, the emission band of an excimer does not present a vibrational resolution, as it exists only when one of the two species is at the excited state, the corresponding ground state for the excimer being dissociative. Another key point is the bimolecular nature of the excimer generation. The production of the excimer is favored at high concentrations and it is not observable at very low concentrations of the luminophore. Since the excimer generation is a bimolecular process, it depends on the diffusion of the two species. Therefore, in time-resolved fluorescence measurements with pulsed excitation, emission from an excimer is characterized by a rise time before emission decay, corresponding to the excimer generation. By contrast, the emission of an isolated molecule is associated with an immediate maximum after the excitation pulse before observing the emission decay. If the two interacting molecules are components of the same supramolecular system, as it occurs for [18]-C-6-bispyrene, the excimer has been defined by Birks⁵¹ as “static excimer”. In this case, the excimer generation is favored, it has a weaker dependence on the luminophore concentration and no rise-time is observed in time-resolved intensity measurements. Alternately, if the two molecules are sufficiently separated when light is absorbed, the excimer is called “dynamic”.⁵² The generation of excimers is commonly observed for PAHs, because of their strong π - π^* interactions. In particular, the first

example of excimer emission was published in 1955 by Förster and Kasper^{24,53} for pyrene molecules in degassed solution. Excimer formation was obtained at the relatively low concentration of 10^{-3} M. In fact, pyrene presents an unusual long life-time for singlet excited state⁵² (650 ns), which increases the probability of bimolecular interactions.

The redox reaction that produces the excimer $[\text{Py-Py}]^*_{\text{exc}}$ (Eq. 2.18) is exergonic enough to populate spontaneously the excimer state, who finally relaxes to the ground state by photon emission ($\lambda = 490$ nm, equivalent to $E = 2.5$ eV, *vide* Chapter I). Figure 2.17 summarizes the different potential values, experimentally found or reported in literature, involved in the ECL mechanism.⁷

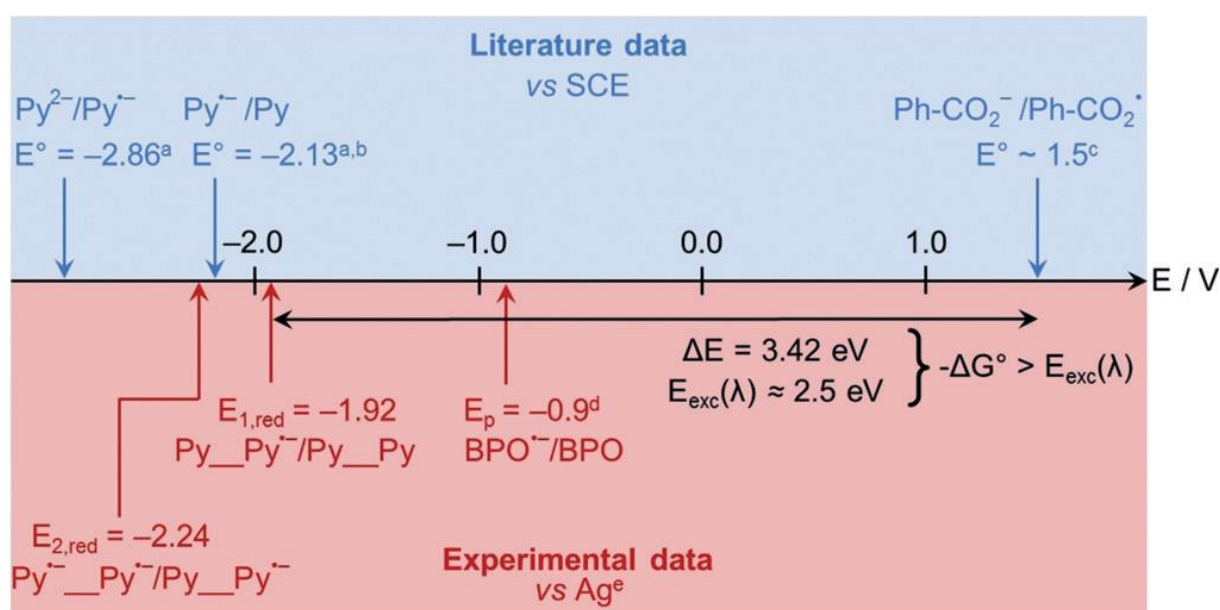


Figure 2.17 Potential scale of the redox species involved in the ECL mechanism. The top part refers to literature data whereas the bottom part shows the experimental data under discussion. Py₂Py represents [18]-C-6-bispyrene. a) reduction potential of pyrene (noted Py) reported by Heinze and Meerlhoz^{46b}; b) data in good agreement with with the reported results and with Bard and coworkers^{6,46a}; c) value estimated from the irreversible oxidation of PhCO₂⁻ by Maran and coworkers^{25,54}; d) peak potential of the irreversible reduction of BPO, which is a slow redox couple and its position depends on the BPO concentration, scan rate and electrode material; e) difference of potential between a SCE reference and a Ag pseudo-reference is negligible^{7,55}

The energy to produce the excited state results from the electron transfer reaction between the benzoate radical and the reduced form of the luminophore, in accordance with the equation^{8c,22b}:

$$\Delta G^\circ \text{ (eV)} \approx - [E^\circ (\text{PhCO}_2^\cdot/\text{PhCO}_2^-) \text{ (V)} - E^\circ_{1,\text{red}} \text{ (V)}] = - \Delta E \text{ (V)} \quad (2.20)$$

Where E° ($\text{PhCO}_2^-/\text{PhCO}_2^\cdot$) was previously reported (*vide* § 2.3.4) as 1.5 V *vs* SCE and $E_{1,\text{red}}$ was estimated as -1.92 V *vs* Ag (Fig. 2.17). The entropic term (estimated as 0.1 ± 0.1 eV)^{8c} can be neglected. Therefore, ΔG° corresponds to the enthalpy, calculated from Eq. 2.20 as about 3.4 eV ($-\Delta G^\circ$). As mentioned above, the energy required for the excimer generation is 2.5 eV ($E_{FL}(\lambda) = 1239.8 / \lambda$, λ in nm, *vide* Chapter I). In conclusion, the enthalpy of the electron transfer reaction is much larger than the energy required for the generation of the excimer. The mechanism discussed above corresponds to an energy sufficient pathway.

Alternative mechanistic pathways involving aromatic ECL dyes with BPO as coreactant have been reported by Akins and Birke^{50a} via triplet-triplet annihilation, triplet quenching reaction and anion-cation annihilation. The pathway involving triplet-triplet annihilation is described by the following equations:



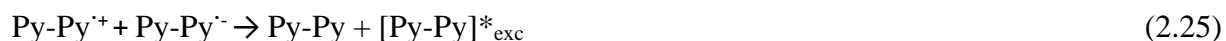
It is also possible to generate the cation radical $\text{Py-Py}^{\cdot+}$ by reaction with the benzoate radical:



Another possibility to generate the cation radical of the two pyrene subunits is by triplet quenching reaction:



Finally, the generated $\text{Py-Py}^{\cdot+}$ reacts with the radical anion, for the production of the excimer via cation-anion annihilation:



The enthalpy for the cation-anion annihilation can be estimated, by neglecting the entropic contribution, as:

$$-\Delta G^\circ = (E^\circ_{1,ox} - E^\circ_{1,red}) = 2.97 \text{ eV} \quad (2.26)$$

Where $E^\circ_{1,ox}$ value is about 1.28 V vs SCE^{47,56} and $E^\circ_{1,red}$ is -1.92 V vs Ag. According to Eq. 2.26, the cation-anion annihilation reaction is associated with an energy high enough to permit the generation of the excimer ($E_{exc}(490) = 2.5 \text{ eV}$). In conditions of large excess of BPO compared to the supramolecular system, the rate of triplet quenching reaction (Eq. 2.24) is higher. Consequently, the cation-anion annihilation is more probable than triplet-triplet annihilation (Eq. 2.21-2.22).

Overall, the bimolecular nature of the redox reaction between instable radicals that characterize these alternative mechanistic pathways (Eq. 2.23-2.25) comforts that the main mechanism for excimer generation involves more probably the energy-sufficient pathway discussed previously (Eq. 2.10-2.19).

2.3.5 PL and ECL spectra

Figure 2.18 shows a superposition of the PL (black curve), ECL via annihilation (blue curve) and ECL with BPO as sacrificial coreactant (red curve) spectra.

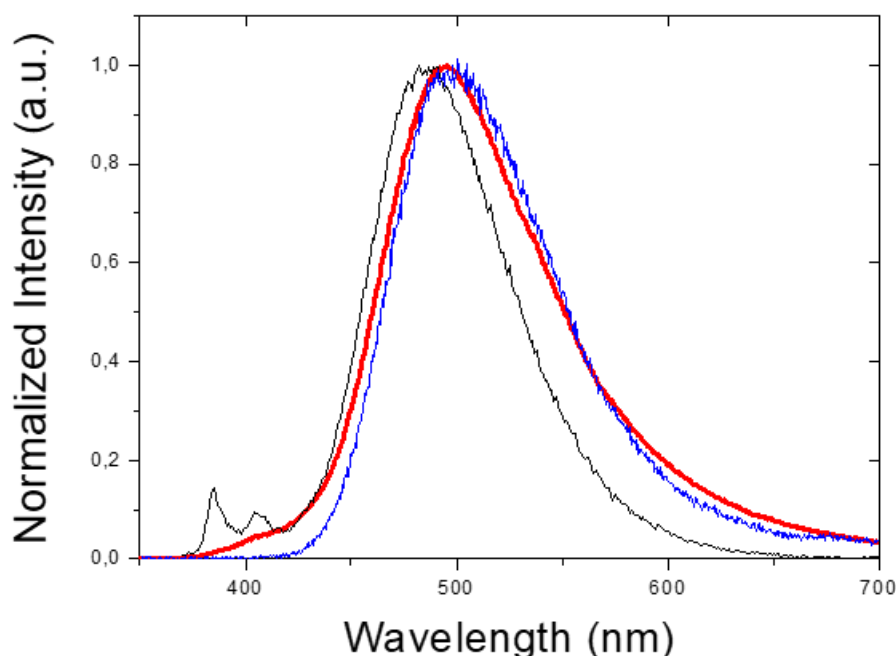


Figure 2.18 Superimposition of PL (black curve), annihilation ECL (blue curve) and BPO/ECL (red curve) normalized spectra of [18]-C-6-bispyrene, recorded in degassed CH_3CN solution. PL spectrum was recorded for a solution of 10 μM of [18]-C-6-bispyrene, with a $\lambda_{exc} = 366 \text{ nm}$. Annihilation ECL spectrum of a solution of 1 mM

of [18]-C-6-bispyrene and 0.1 M of TBAPF₆ was obtained by pulsing the GC working electrode potential between -2.45 V vs Ag and +1.2 V vs Ag. Coreactant ECL spectrum of a solution of 0.5 mM of [18]-C-6-bispyrene and 0.1 M of TBAPF₆ was obtained by applying constantly -2.1 V vs Ag at the GC working electrode.

A low concentration of 10 μM of the supramolecular system was enough to collect the PL spectrum in a degassed acetonitrile solution. At around 400 nm two emission bands are observed, with two maxima at $\lambda = 385$ nm and $\lambda = 405$ nm. These emissions are attributed to PL of pyrene monomer.⁵⁷ Depending on the solvent in which the PL spectrum of pyrene is recorded, the monomer emission counts up to five bands (with well-defined peaks at around 375, 379, 385, 395 and 410 nm). The intensity of the band III at 385 nm (corresponding to the third vibronic band with 0-2 transition) depends on the polarity of the solvent, with an enhancement in hydrophobic environments. By contrast, the band I (not visible in Fig. 2.18) increases with the polarity of the solvent. The possibility to identify the polarity of the surrounding media by the relative intensities of bands I and III was applied to the detection of changes in probe microenvironment as a result of protein conformational changes.⁵⁸

At lower energies ($\lambda_{\text{max}} = 485$ nm), the PL spectrum shows the most intense band, related with the emission of the excimer. The high intensity of the excimer emission, even at a low concentration of [18]-C-6-bispyrene of 10 μM, is caused by the short distance between the two pyrene moieties that is imposed by the supramolecular system. The generation of the excimer moves from a bimolecular process to an intramolecular one where the pyrene-pyrene close proximity is ensured. In Figure 2.18, two ECL spectra are reported in acetonitrile solution, with TBAPF₆ as supporting electrolyte. The ECL spectrum via coreactant pathway was obtained with a concentration of 0.5 mM of [18]-C-6-bispyrene and 10 mM of the coreactant BPO. A red-shift of the excimer emission of 10 nm occurs compared to the PL spectrum. A slight intensity, hidden under the broad excimer band, is associated with the monomer emission at around 400 nm. As reported in previous publications,^{6,47} the monomeric ECL emission of pyrene is weak and rarely resolved. A higher concentration of 1 mM of [18]-C-6-bispyrene was required to collect a rather noisy ECL spectrum via annihilation, by alternate pulsing of the electrode potential between -2.45 V vs Ag and +1.2 V vs Ag. A red-shift ($\lambda_{\text{max}} = 497$ nm), comparable with the ECL spectrum via coreactant pathway, is reported for ECL spectrum via annihilation. The difference in concentration and in the experimental set-up can explain the slight bathochromic shift of the ECL spectra compared to the PL spectrum. The good agreement between the PL and ECL spectra allows supposing that the same excited state is responsible of the emission in both cases.

2.3.6 CP-ECL

CPL spectroscopy of the system [18]-C-6-bispyrene was previously reported by Prof. Di Bari's group at Pisa University.⁴³ The stability of the ECL intensity for the system [18]-C-6-bispyrene/BPO was good enough to obtain a reasonable constant strength for more than 300 seconds. Such time interval was necessary to perform the full scanning of the wavelength range by a monochromator. Such a condition is required to record a whole ECL spectrum of [18]-C-6-bispyrene. In Figure 2.19, a typical ECL intensity signal for a solution of 1mM of [18]-C-6-bispyrene and 10 mM of BPO in degassed acetonitrile with 0.1 M of TBAPF₆, is shown, monitored over time at 490 nm by applying -2.45 V vs Ag at GC working electrode.

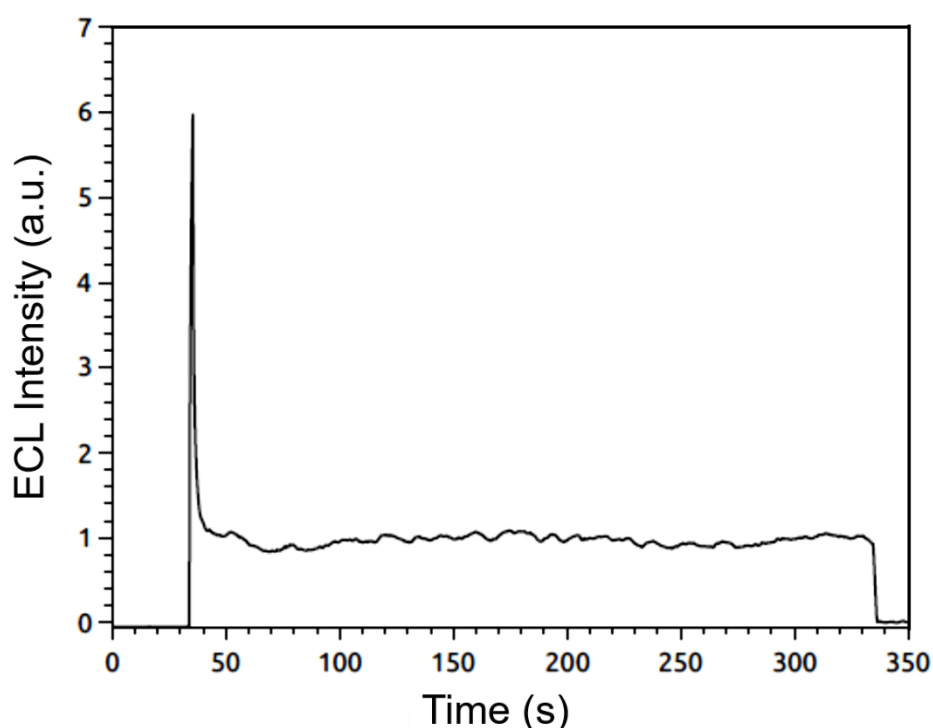


Figure 2.19 ECL intensity of [18]-C-6-bispyrene 1 mM, BPO 10 mM as sacrificial coreactant, TBAPF₆ 0.1 M as supporting electrolyte in degassed CH₃CN solution. ECL emission was obtained by pulsing the GC working electrode at -2.45 V vs Ag for 294 s (GC electrode was biased at 0 V vs Ag for the first 42 s).

Figure 2.19 illustrates that the ECL intensity was stable at least during the time of acquisition of a spectrum (about 240 s). The spectrum was recorded after 10 s from the beginning of the pulse of -2.45 V vs Ag, to allow the ECL intensity to reach a plateau after the initial transient (Fig. 2.19).

2.3.6.1 Experimental set-up

The experimental set-up applied to CP-ECL analysis was composed by a spectrofluoropolarimeter built in Prof. Di Bari's group in Pisa University, where the measurements of CP-ECL were performed, coupled with a potentiostat. Figure 2.20 schematizes the whole CP-ECL instrumentation. The light source, normally used for sample's excitation, was replaced by a potentiostat. The cuvette containing the sample was substituted with a modified-one, enabling *in situ* electrochemical measurements. ECL emission was collected at 180° of the sample. A PEM was able to collect alternatively the left and right circularly polarized components of the emission, which were then transformed from circularly to linearly polarized radiations by the linear polarizer. A diffraction grating was used to disperse the light, which was then detected by the PMT.

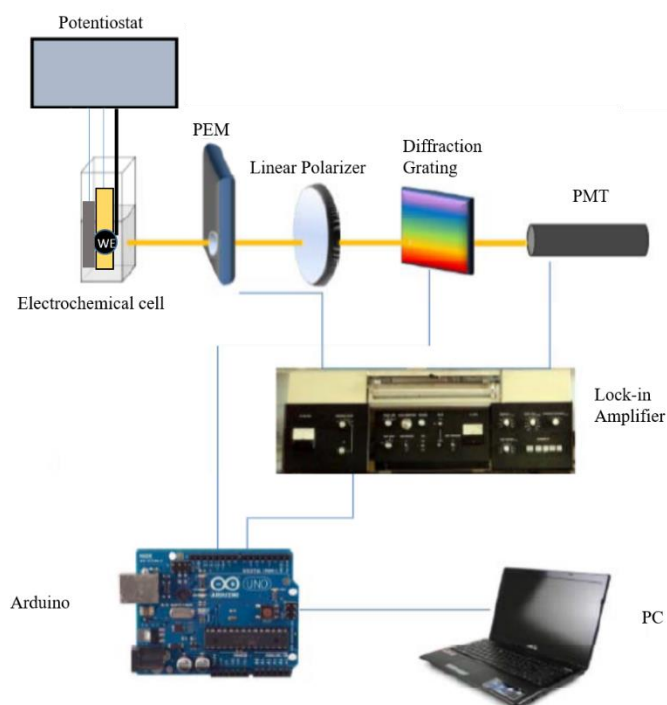


Figure 2.20 Scheme of the home-built spectrofluoropolarimeter, modified with an electrochemical apparatus. (Reproduced with modifications from [35]).⁵⁹

Subsequently, it is wavelength-resolved by the diffraction grating and detected by the PMT. A lock-in amplifier is used to reduce the noise and extract the ECL signal by selectively amplifying only the circularly polarized parts and provide an output proportional to the CP-ECL.⁶⁰ An Arduino (hardware and software) controller was used to interface the apparatus.

2.3.6.2 CP-ECL of [18]-C-6-bispyrene enantiomers

Figure 2.21 reports the CP-ECL signal of the two enantiomers of the investigated supramolecular system [18]-C-6-bispyrene as well as the corresponding racemic mixture. These following set of results is the first CP-ECL chiral discrimination of a purely organic molecule. Moreover, this is the first time that the two enantiomers are distinguished by CP-ECL.

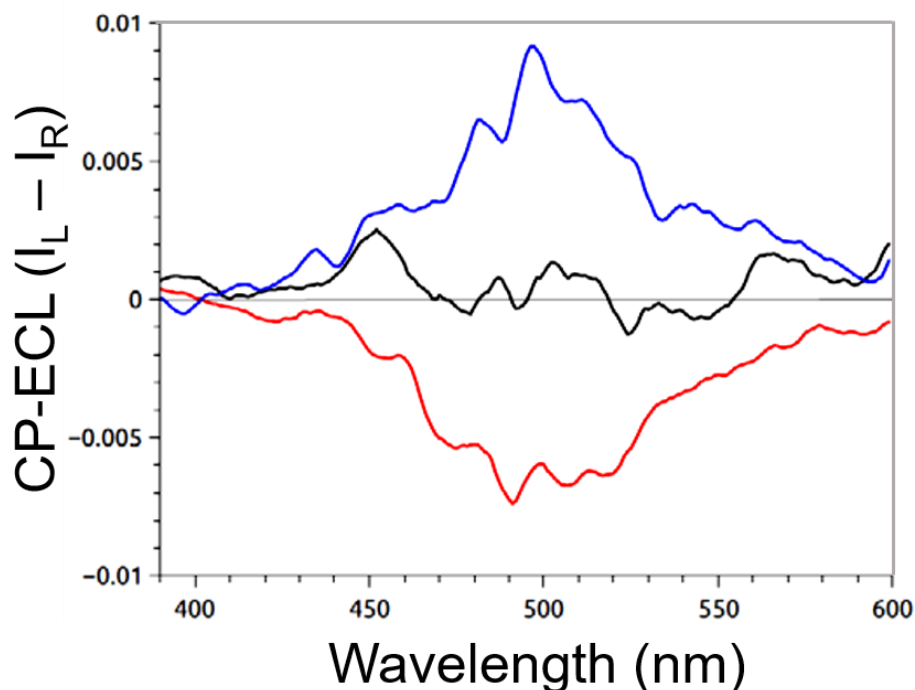


Figure 2.21 CP-ECL signal for (+)-[18]-C-6-bispyrene (red line), (-)-[18]-C-6-bispyrene (blue line) and racemic mixture (black line). The spectra were recorded at a [18]-C-6-bispyrene concentration of 0.7 mM, a BPO concentration of 10 mM, TBAPF₆ 0.1 M as supporting electrolyte in degassed CH₃CN solution. ECL emission was obtained by pulsing the GC working electrode at -2.45 V vs Ag for 240 s.

A positive CP-ECL signal (corresponding to the difference between the left and right linearly polarized components) was recorded for the enantiomer (-)-[18]-C-6-bispyrene (Fig. 2.21, blue curve), at the emission wavelength region of the excimer ($\lambda_{\text{max}} \approx 500$ nm), whereas a negative CP-ECL signal is accounted for the enantiomer (+)-[18]-C-6-bispyrene (Fig. 2.21, red curve). The reproducibility was confirmed by performing at least six measurements for each enantiomer. As expected, CP-ECL signals of the two enantiomers are mirror images. The racemic mixture (Fig. 2.21, black curve) was also analyzed as control measurement and a degree of polarization close to zero was observed in the entire wavelength range. Figure 2.22 shows the corresponding ECL spectra for the enantiomers and the racemic mixture.

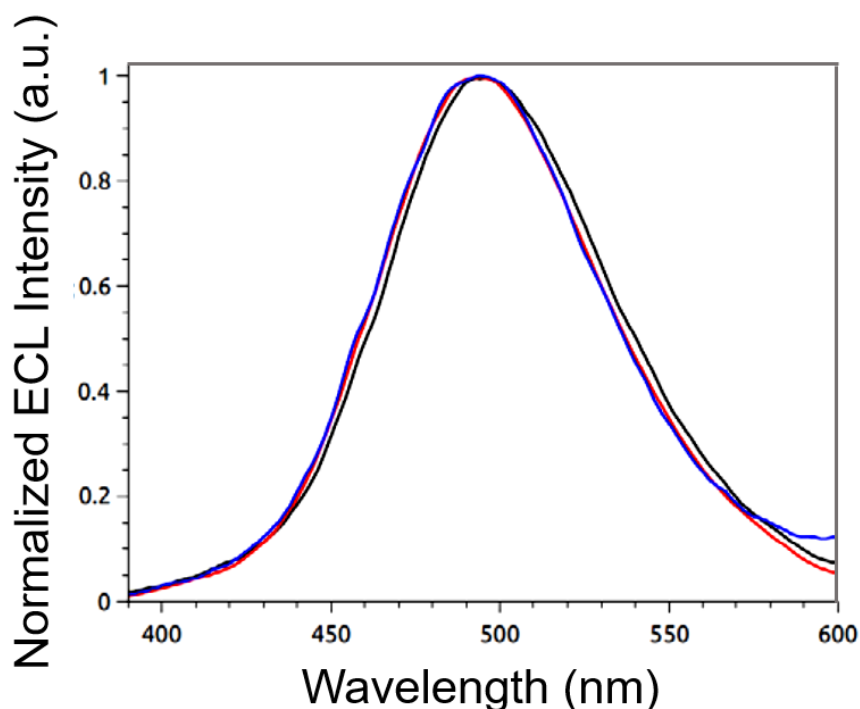


Figure 2.22 ECL spectra for (+)-[18]-C-6-bispyrene (red line), (-)-[18]-C-6-bispyrene (blue line) and racemic mixture (black line). The spectra were recorded at a [18]-C-6-bispyrene concentration of 0.7 mM, a BPO concentration of 10 mM, TBAPF₆ 0.1 M as supporting electrolyte in degassed CH₃CN solution. ECL emission was obtained by pulsing the GC working electrode at -2.45 V vs Ag for 240 s.

ECL spectra are perfectly superimposable for both enantiomers as well as for the racemic mixture. It confirms that conventional ECL emission alone is not sufficient and the chirality can only be highlighted through a CP-ECL analysis, as expected. Lacour *et al.*⁴³ previously reported the CPL study of [18]-C-6-bispyrene. Figure 2.23 shows the CPL signal for the two enantiomers. Despite of the less noisy CPL signal compared to CP-ECL signals, probably due to the higher intensity related with the PL emission, the sign (positive or negative) of the CPL signal is in accordance with the CP-ECL one. It is therefore possible to conclude that a CP-ECL measurement is able to distinguish between the two enantiomers just like a classic CPL analysis. Moreover, PL and ECL emission of the two enantiomers show the same sign of the polarization, confirming that the same polar excited state is involved in both measurements.

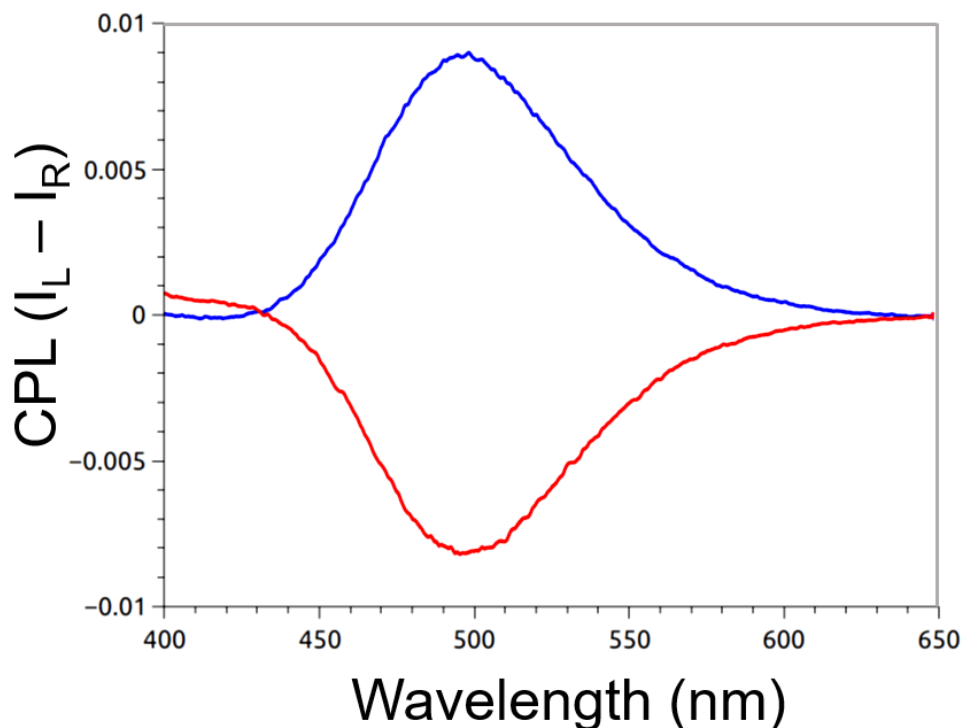


Figure 2.23 Circularly polarized photoluminescence (CPL) of (-)- and (+)-[18]-C-6-bispyrene (blue and red curve, respectively) under 366 nm irradiation.⁴³

By analogy to CPL spectroscopy, it is possible to define an ECL dissymmetry factor g_{ECL} to quantify the preferential CP-ECL polarization (*vide* § 2.3.1):

$$g_{ECL} = \frac{I_L - I_R}{\frac{1}{2}(I_L + I_R)} \quad (2.27)$$

Where I_L and I_R are the left- and right-circularly polarized components of the ECL emission. ECL dissymmetry factor's values of $+8.4 \times 10^{-3} (\pm 1.4 \times 10^{-3})$ and $-7.3 \times 10^{-3} (\pm 2.0 \times 10^{-3})$ were calculated respectively for (-)- and (+)-[18]-C-6-bispyrene at around 490 nm. Figure 2.24 illustrates the g_{ECL} values for the whole wavelength range analyzed. At smaller ECL intensity values, g_{ECL} error bars becomes significantly higher (Fig. 2.24).

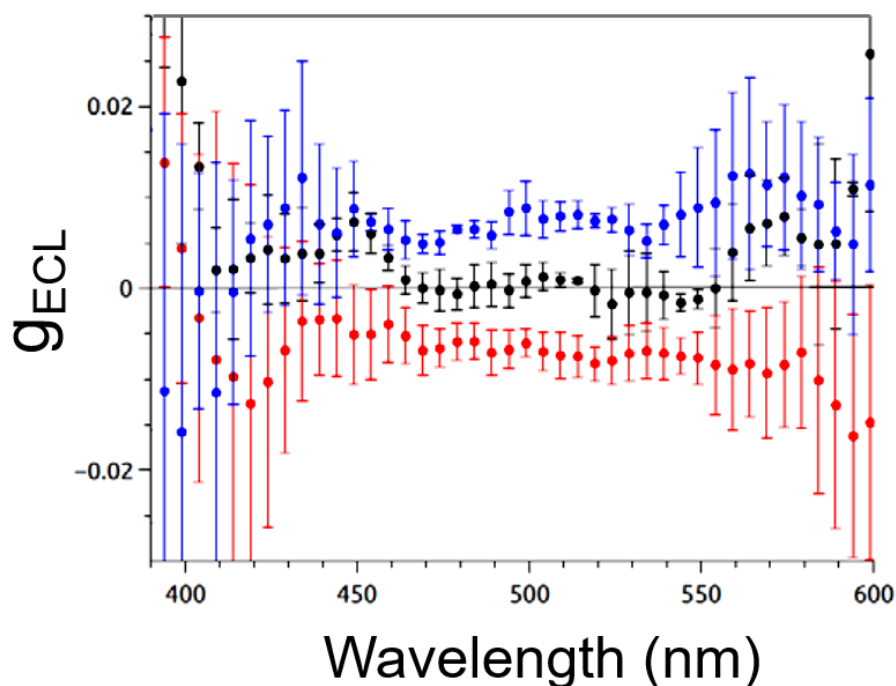


Figure 2.24 ECL dissymmetry factor of (+)-[18]-C-6-bispyrene (red points), (-)-[18]-C-6-bispyrene (blue points) and racemic mixture of [18]-C-6-bispyrene (black points). The error bars represent \pm one standard deviation and are generated over six measurements for each enantiomer and three for the racemic mixture. The errors of g_{ECL} diverge on the edges of the spectra, where total emission intensity becomes vanishing small.

As expected, the racemic mixture shows a random and small signal for ECL dissymmetry factor, with a maximum of 0.3×10^{-3} ($\pm 1.4 \times 10^{-3}$). This value will therefore represent the limit of quantitation for CP-ECL signal in this system, in order to guarantee that the CP-ECL signals measured for the two enantiomers are significant (at least around 30 times higher than the racemic mixture).⁷ The calculated luminescence dissymmetry factors reported by Lacour and coworkers⁴³ are in good agreement with the g_{ECL} values ($g_{\text{lum}} = +9.0$ and -8.8×10^{-3} for respectively (-)- and (+)-[18]-C-6-bispyrene). [18]-C-6-bispyrene enantiomers display high ECL and PL dissymmetry factors for organic compounds^{33,37,43} and this value is also one order of magnitude larger than g_{ECL} of (+)-[Ru(phen)₃](ClO₄)₂ · 6 H₂O ($+12(\pm 2) \times 10^{-4}$ at 550 nm) reported by Blok and coworkers.⁴²

2.4 Conclusions

In the first part of the chapter, the ECL properties in a series of luminophores, a spirofluorene derivative and trigonal truxene-core modified systems, were investigated according to several ECL pathways, annihilation and reductive-oxidative coreactant modes. The stabilization of the electrogenerated radicals, induced by the presence of three terminal triphenylamine units in the derivative **2**, permitted to obtain the highest ECL efficiency of the series for this system via annihilation. It was found to be more than 3 times higher than the reference system $[\text{Ru}(\text{bpy})_3]^{2+}$, while the pristine luminophore **1** showed an ECL efficiency via annihilation only 50% higher than $[\text{Ru}(\text{bpy})_3]^{2+}$. Compound **3** showed a dramatic decrease in ECL efficiency compared with both **1** and **2**, probably related to the substitution of triphenylamines by diphenylamines. The bonding between the diphenylamine that occurs through the N atom with the thiophene component probably affects the charges' stabilization. Compound **4**, composed by a modified truxene system, was not soluble enough in the experimental conditions and showed the lower ECL performances among the series. Overall, higher ECL efficiencies were found for the whole series of luminophores via coreactant ECL. Compound **2** still presented the best ECL efficiency, 4.5 times larger than $[\text{Ru}(\text{bpy})_3]^{2+}$. **1** showed an ECL efficiency of 230%, whereas for the studies with TPA as coreactant, a higher ECL efficiency of 450% was found.⁵ The delocalization of the charge between the triphenylamine and the thiophene components might permit a better stabilization of the positive charge compared to the electrogenerated anion. Compound **3** exhibited an ECL efficiency slightly lower than $[\text{Ru}(\text{bpy})_3]^{2+}$. Further theoretical calculations are necessary to deeper understand the role of each molecular component, in order to interpret the ECL experimental data and to chemically modify these systems for reaching even higher ECL performances.

The second work discussed here reported the circular polarization of the ECL emission for the organic system [18]-C-6bispyrene. It was demonstrated that the CP-ECL signal and the ECL dissymmetry factor are in good agreement with the corresponding CPL data. Therefore, it is possible to conclude that, at least for this luminophore that is characterized by high and stable ECL signal and high g_{lum} values, ECL emission can discriminate between two enantiomers. Further compounds, such as chiral lanthanide complexes with very high g_{lum} values, may be investigated in the future. But, further theoretical and experimental studies are necessary to better define the requirements for obtaining a high and significant CP-ECL signal. Soon, ECL chiral luminophores would then be employed for potential applications as extremely selective and sensitive bioprobes in bio- assays and imaging.

References

- (1) In Ceroni, P., Credi, A., Venturi, M., *Electrochemistry of Functional Supramolecular Systems*, Wiley, John & Sons, Hoboken, New Jersey, 2010.
- (2) a) Carrara, S.; Aliprandi, A.; Hogan, C. F.; De Cola, L. *Journal of the American Chemical Society* **2017**, *139*, 14605; b) Zheng, C.; Sheng, Y.; Liu, Y.; Wan, Y.; Liu, G.; Zhang, X.; Yang, M.; Kang, K.; Liu, J.; Ma, K.; Deng, S. *Analytical and Bioanalytical Chemistry* **2019**, *411*, 4797; c) Lei, Y.-M.; Zhao, M.; Wang, A.; Yu, Y.-Q.; Chai, Y.-Q.; Yuan, R.; Zhuo, Y. *Chemistry – A European Journal* **2016**, *22*, 8207; d) Zhuo, Y.; Zhao, M.; Qiu, W.-J.; Gui, G.-F.; Chai, Y.-Q.; Yuan, R. *Journal of Electroanalytical Chemistry* **2013**, *709*, 106; e) Shu, Q.; Adam, C.; Sojic, N.; Schmittl, M. *Analyst* **2013**, *138*, 4500.
- (3) Valenti, G.; Rampazzo, E.; Biavardi, E.; Villani, E.; Fracasso, G.; Marcaccio, M.; Bertani, F.; Ramarli, D.; Dalcanale, E.; Paolucci, F.; Prodi, L. *Faraday Discussions* **2015**, *185*, 299.
- (4) Pinalli, R.; Dalcanale, E. *Accounts of Chemical Research* **2013**, *46*, 399.
- (5) Li, H.; Daniel, J.; Verlhac, J.-B.; Blanchard-Desce, M.; Sojic, N. *Chemistry – A European Journal* **2016**, *22*, 12702.
- (6) Lai, R. Y.; Fleming, J. J.; Merner, B. L.; Vermeij, R. J.; Bodwell, G. J.; Bard, A. J. *The Journal of Physical Chemistry A* **2004**, *108*, 376.
- (7) Zinna, F.; Voci, S.; Arrico, L.; Brun, E.; Homberg, A.; Bouffier, L.; Funaioli, T.; Lacour, J.; Sojic, N.; Di Bari, L. *Angewandte Chemie International Edition* **2019**, *58*, 6952.
- (8) a) Bard, A. J. *Electrogenerated Chemiluminescence*; M. Dekker: New-York, 2004; b) Liu, Z.; Qi, W.; Xu, G. *Chemical Society Reviews* **2015**, *44*, 3117; c) Richter, M. M. *Chem. Rev.* **2004**, *104*, 3003; d) Debab, J. D.; Lee, S. K.; Qiao, X. X.; Pascal, R. A.; Bard, A. J. *Acta Chemica Scandinavica* **1998**, *52*, 45.
- (9) a) Fungo, F.; Wong, K.-T.; Ku, S.-Y.; Hung, Y.-Y.; Bard, A. J. *The Journal of Physical Chemistry B* **2005**, *109*, 3984; b) Omer, K. M.; Ku, S.-Y.; Wong, K.-T.; Bard, A. J. *Journal of the American Chemical Society* **2009**, *131*, 10733; c) Qi, H.; Zhang, C.; Huang, Z.; Wang, L.; Wang, W.; Bard, A. J. *Journal of the American Chemical Society* **2016**, *138*, 1947.
- (10) a) Lee, H.; Jung, H.; Kang, S.; Heo, J. H.; Im, S. H.; Park, J. *The Journal of Organic Chemistry* **2018**, *83*, 2640; b) Li, Y.; Wang, Z.; Li, X.; Xie, G.; Chen, D.; Wang, Y.-F.; Lo, C.-C.; Lien, A.; Peng, J.; Cao, Y.; Su, S.-J. *Chemistry of Materials* **2015**, *27*, 1100; c) Quinton, C.; Thiery, S.; Jeannin, O.; Tondelier, D.; Geffroy, B.; Jacques, E.; Rault-Berthelot, J.; Poriel, C. *ACS Applied Materials & Interfaces* **2017**, *9*, 6194; d) Schwartz, G.; Fehse, K.; Pfeiffer, M.; Walzer, K.; Leo, K. *Applied Physics Letters* **2006**, *89*, 083509; e) Woo, S.-J.; Kim, Y.; Kim, M.-J.; Baek, J. Y.; Kwon, S.-K.; Kim, Y.-H.; Kim, J.-J. *Chemistry of Materials* **2018**, *30*, 857; f) Wu, C. C.; Lin, Y. T.; Chiang, H. H.; Cho, T. Y.; Chen, C. W.; Wong, K. T.; Liao, Y. L.; Lee, G. H.; Peng, S. M. *Applied Physics Letters* **2002**, *81*, 577.
- (11) a) Cho, N.; Choi, H.; Kim, D.; Song, K.; Kang, M.-s.; Kang, S. O.; Ko, J. *Tetrahedron* **2009**, *65*, 6236; b) Heredia, D.; Natera, J.; Gervaldo, M.; Otero, L.; Fungo, F.; Lin, C.-Y.; Wong, K.-T. *Organic Letters* **2010**, *12*, 12; c) Jeon, N. J.; Na, H.; Jung, E. H.; Yang, T.-Y.; Lee, Y. G.; Kim, G.; Shin, H.-W.; Il Seok, S.; Lee, J.; Seo, J. *Nature Energy* **2018**, *3*, 682.
- (12) Kuehne, A. J. C.; Gather, M. C. *Chemical Reviews* **2016**, *116*, 12823.
- (13) a) Omer, K. M.; Ku, S.-Y.; Cheng, J.-Z.; Chou, S.-H.; Wong, K.-T.; Bard, A. J. *Journal of the American Chemical Society* **2011**, *133*, 5492; b) Polo, F.; Rizzo, F.; Veiga-Gutierrez, M.; De Cola, L.; Quici, S. *Journal of the American Chemical Society* **2012**, *134*, 15402.

- (14) Rashidnadi, S.; Hung, T. H.; Wong, K.-T.; Bard, A. J. *Journal of the American Chemical Society* **2008**, *130*, 634.
- (15) a) Mohsan, Z.; Kanibolotsky, A. L.; Stewart, A. J.; Inigo, A. R.; Dennany, L.; Skabara, P. J. *Journal of Materials Chemistry C* **2015**, *3*, 1166; b) Omer, K. M.; Kanibolotsky, A. L.; Skabara, P. J.; Perepichka, I. F.; Bard, A. J. *The Journal of Physical Chemistry B* **2007**, *111*, 6612; c) Moreno Oliva, M.; Casado, J.; López Navarrete, J. T.; Berridge, R.; Skabara, P. J.; Kanibolotsky, A. L.; Perepichka, I. F. *The Journal of Physical Chemistry B* **2007**, *111*, 4026; d) Dennany, L.; Mohsan, Z.; Kanibolotsky, A. L.; Skabara, P. J. *Faraday Discussions* **2014**, *174*, 357.
- (16) Rizzo, F.; Polo, F.; Bottaro, G.; Fantacci, S.; Antonello, S.; Armelao, L.; Quici, S.; Maran, F. *Journal of the American Chemical Society* **2017**, *139*, 2060.
- (17) Kudruk, S.; Villani, E.; Polo, F.; Lamping, S.; Körsngen, M.; Arlinghaus, H. F.; Paolucci, F.; Ravoo, B. J.; Valenti, G.; Rizzo, F. *Chemical Communications* **2018**, *54*, 4999.
- (18) Li, H.; Daniel, J.; Verlhac, J.-B.; Blanchard-Desce, M.; Sojic, N. *Chem. Eur. J.* **2016**, *22*, 12702.
- (19) Compton, R. G. A. B., Craig E. *Understanding Voltammetry*.
- (20) a) Oh, J.-W.; Lee, Y. O.; Kim, T. H.; Ko, K. C.; Lee, J. Y.; Kim, H.; Kim, J. S. *Angewandte Chemie International Edition* **2009**, *48*, 2522; b) Oh, J.-W.; Lee, Y. O.; Kim, T. H.; Ko, K. C.; Lee, J. Y.; Kim, H.; Kim, J. S. *Angewandte Chemie* **2009**, *121*, 2560.
- (21) Li, H.; Voci, S.; Wallabregue, A.; Adam, C.; Labrador, G. M.; Duwald, R.; Hernández Delgado, I.; Pascal, S.; Bosson, J.; Lacour, J.; Bouffier, L.; Sojic, N. *ChemElectroChem* **2017**, *4*, 1750.
- (22) a) Bard, A. J.; Faulkner, L. R. *Electrochemical methods*; Wiley: New York, 2001; b) Miao, W. *Chemical Reviews* **2008**, *108*, 2506.
- (23) Swanick, K. N.; Ladouceur, S.; Zysman-Colman, E.; Ding, Z. *Chemical Communications* **2012**, *48*, 3179.
- (24) Balzani, V. C., Paola; Juris, Alberto *Photochemistry and Photophysics: Concepts, Research and Applications*; Wiley-VCH, 2014.
- (25) Antonello, S.; Maran, F. *Journal of the American Chemical Society* **1999**, *121*, 9668.
- (26) Chandross, E. A.; Sonntag, F. I. *Journal of the American Chemical Society* **1964**, *86*, 3179.
- (27) a) Nepomnyashchii, A. B.; Ono, R. J.; Lyons, D. M.; Bielawski, C. W.; Sessler, J. L.; Bard, A. J. *Chemical Science* **2012**, *3*, 2628; b) Choi, J.-P.; Wong, K.-T.; Chen, Y.-M.; Yu, J.-K.; Chou, P.-T.; Bard, A. J. *The Journal of Physical Chemistry B* **2003**, *107*, 14407; c) Kapturkiewicz, A. *Chem. Phys.* **1992**, *166*, 259; d) Kapturkiewicz, A.; Grabowski, Z. R.; Jasny, J. *Journal of the Electroanalytical Chemistry* **1990**, *279*, 55.
- (28) Riehl, J. P.; Richardson, F. S. *Chemical Reviews* **1986**, *86*, 1.
- (29) Richardson, F. S.; Riehl, J. P. *Chemical Reviews* **1977**, *77*, 773.
- (30) In *Comprehensive Chiroptical Spectroscopy*, p 65.
- (31) a) Emeis, C. A.; Oosterhoff, L. J. *The Journal of Chemical Physics* **1971**, *54*, 4809; b) Emeis, C. A.; Oosterhoff, L. J. *Chemical Physics Letters* **1967**, *1*, 129.
- (32) Luk, C. K.; Richardson, F. S. *Journal of the American Chemical Society* **1974**, *96*, 2006.
- (33) Longhi, G.; Castiglioni, E.; Koshoubu, J.; Mazzeo, G.; Abbate, S. *Chirality* **2016**, *28*, 696.
- (34) Naito, M.; Iwahori, K.; Miura, A.; Yamane, M.; Yamashita, I. *Angewandte Chemie International Edition* **2010**, *49*, 7006.
- (35) Tohgha, U.; Deol, K. K.; Porter, A. G.; Bartko, S. G.; Choi, J. K.; Leonard, B. M.; Varga, K.; Kubelka, J.; Muller, G.; Balaz, M. *ACS Nano* **2013**, *7*, 11094.

- (36) Satrijo, A.; Meskers, S. C. J.; Swager, T. M. *Journal of the American Chemical Society* **2006**, *128*, 9030.
- (37) Zinna, F.; Di Bari, L. *Chirality* **2015**, *27*, 1.
- (38) Muller, G. *Dalton Transactions* **2009**, 9692.
- (39) Carr, R.; Evans, N. H.; Parker, D. *Chemical Society Reviews* **2012**, *41*, 7673.
- (40) Montgomery, C. P.; Murray, B. S.; New, E. J.; Pal, R.; Parker, D. *Accounts of Chemical Research* **2009**, *42*, 925.
- (41) a)Valenti, G.; Scarabino, S.; Goudeau, B.; Lesch, A.; Jović, M.; Villani, E.; Sentic, M.; Rapino, S.; Arbault, S.; Paolucci, F.; Sojic, N. *Journal of the American Chemical Society* **2017**, *139*, 16830; b)Voci, S.; Goudeau, B.; Valenti, G.; Lesch, A.; Jović, M.; Rapino, S.; Paolucci, F.; Arbault, S.; Sojic, N. *Journal of the American Chemical Society* **2018**, *140*, 14753; c)Liu, G.; Ma, C.; Jin, B.-K.; Chen, Z.; Zhu, J.-J. *Analytical Chemistry* **2018**, *90*, 4801.
- (42) Blok, P. M. L.; Cartwright, P. S.; Dekkers, H. P. J. M.; Gillard, R. D. *Journal of the Chemical Society, Chemical Communications* **1987**, 1232.
- (43) Homberg, A.; Brun, E.; Zinna, F.; Pascal, S.; Górecki, M.; Monnier, L.; Besnard, C.; Pescitelli, G.; Di Bari, L.; Lacour, J. *Chemical Science* **2018**, *9*, 7043.
- (44) a)Poggiali, D.; Homberg, A.; Lathion, T.; Piguet, C.; Lacour, J. *ACS Catalysis* **2016**, *6*, 4877; b)Vishe, M.; Hrdina, R.; Guénée, L.; Besnard, C.; Lacour, J. *Advanced Synthesis & Catalysis* **2013**, *355*, 3161; c)Zeghida, W.; Besnard, C.; Lacour, J. *Angewandte Chemie International Edition* **2010**, *49*, 7253.
- (45) a)Bachman, J. C.; Kavian, R.; Graham, D. J.; Kim, D. Y.; Noda, S.; Nocera, D. G.; Shao-Horn, Y.; Lee, S. W. *Nature Communications* **2015**, *6*, 7040; b)Dietrich, M.; Heinze, J. *Journal of the American Chemical Society* **1990**, *112*, 5142.
- (46) a)Maloy, J. T.; Bard, A. J. *Journal of the American Chemical Society* **1971**, *93*, 5968; b)Meerholz, K.; Heinze, J. *Journal of the American Chemical Society* **1989**, *111*, 2325.
- (47) Fleet, B.; Kirkbright, G. F.; Pickford, C. J. *Journal of Electroanalytical Chemistry and Interfacial Electrochemistry* **1971**, *30*, 115.
- (48) Chandross, E. A.; Sonntag, F. I. *Journal of the American Chemical Society* **1966**, *88*, 1089.
- (49) a)Valenti, G.; Bruno, C.; Rapino, S.; Fiorani, A.; Jackson, E. A.; Scott, L. T.; Paolucci, F.; Marcaccio, M. *The Journal of Physical Chemistry C* **2010**, *114*, 19467; b)Ritzert, N. L.; Truong, T.-T.; Coates, G. W.; Abruña, H. D. *The Journal of Physical Chemistry C* **2014**, *118*, 924; c)Price, J. T.; Li, M. S. M.; Brazeau, A. L.; Tao, D.; Xiang, G.; Chen, Y.; McDonald, R.; Jones, N. D.; Ding, Z. *The Journal of Physical Chemistry C* **2016**, *120*, 21778; d)Hesari, M.; Workentin, M. S.; Ding, Z. *ACS Nano* **2014**, *8*, 8543.
- (50) a)Akins, D. L.; Birke, R. L. *Chemical Physics Letters* **1974**, *29*, 428; b)Santa Cruz, T. D.; Akins, D. L.; Birke, R. L. *Journal of the American Chemical Society* **1976**, *98*, 1677.
- (51) Birks, J. B. *Aromatic Molecules*; Wiley: New York, 1970; Vol. 704.
- (52) Winnik, F. M. *Chemical Reviews* **1993**, *93*, 587.
- (53) Förster, T.; Kasper, K. *Zeitschrift für Elektrochemie, Berichte der Bunsengesellschaft für physikalische Chemie* **1955**, *59*, 976.
- (54) Antonello, S.; Musumeci, M.; Wayner, D. D. M.; Maran, F. *Journal of the American Chemical Society* **1997**, *119*, 9541.
- (55) Pavlishchuk, V. V.; Addison, A. W. *Inorganica Chimica Acta* **2000**, *298*, 97.
- (56) a)Lai, R. Y.; Fleming, J. J.; Merner, B. L.; Vermeij, R. J.; Bodwell, G. J.; Bard, A. J. *The Journal of Physical Chemistry A* **2003**, *108*, 376; b)Hoytink, G. J. *Discussions of the Faraday Society* **1968**, *45*, 14.

- (57) Sahoo, D.; Narayanaswami, V.; Kay, C. M.; Ryan, R. O. *Biochemistry* **2000**, *39*, 6594.
- (58) Bains, G.; Patel, A. B.; Narayanaswami, V. *Molecules* **2011**, *16*, 7909.
- (59) Zinna, F.; Bruhn, T.; Guido, C. A.; Ahrens, J.; Bröring, M.; Di Bari, L.; Pescitelli, G. *Chemistry – A European Journal* **2016**, *22*, 16089.
- (60) Gussakovsky, E. In *Reviews in Fluorescence 2008*; Geddes, C. D., Ed.; Springer New York: New York, NY, 2010, p 425.

III. ECL in Confined Environments

3.1 Introduction

Electrochemistry in confined environments represents electroanalysis at the ultimate limit of research current abilities. It enables measuring the response of single entities, such as cells,¹ vesicles,² molecules³, and how this latter contributes to the bulk behavior, detectable with classic electrochemical analysis.⁴ Moreover, additional information, largely unobtainable otherwise (*i.e.*, mechanistic details of catalytic processes, magnitudes of microscopic forces, macromolecular population heterogeneities), can be acquired.⁵

Alternative methods, such as spectroscopy, can be used to make single-entity and environmental-confined measurements, although electrochemistry presents many advantages. First, electrochemical processes are fundamental electron or ion transfer, from one entity to another. In addition, advances in electronics for electrochemistry as well as peculiar electrochemical methods have allowed reaching sensitivity required to perform analysis in confined environments. Finally, many fabrication techniques (*i.e.*, photolithography, focused-ion beams, reactive-ion etching, chemical vapor deposition), developed for the technology-driven semiconductor manufacturing, are currently applied to the design of electrochemical nano- and micro-devices.⁵

An important breakthrough in spatially confined electrochemistry was the development of scanned probe microscopies. In particular, scanning electrochemical microscopy (SECM), developed by Bard and coworkers in 1991,⁶ has had a critical impact for micro and nanoscale electrochemistry advances. Such technique allows the generation of controlled nano-confined

electrochemical environments by simply moving a sample electrode.⁷ As reported by Fan and Bard in 1995,³ a scanning electrochemical microscope can be used to adjust the tip-substrate distance and therefore create a generator-collector configuration between the SECM probe and the substrate that may be conductive. A metal tip electrode of nanometer dimensions was insulated in wax and approached to an electrode. A small volume of a ferrocene derivative solution could be trapped between the electrode surface and wax insulation (Fig. 3.1).

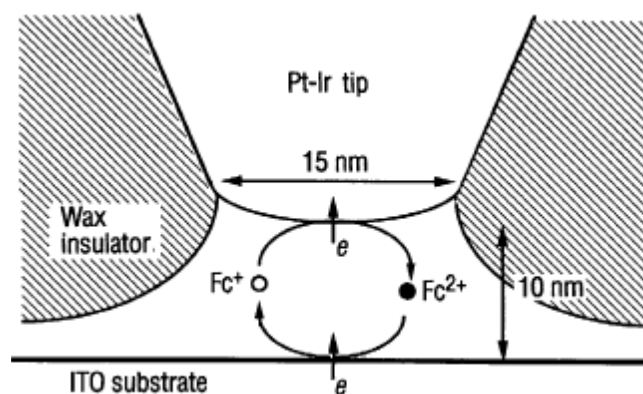


Figure 3.1 Idealized schematic illustration of the tip geometry and the tip-substrate configuration used.³

By applying an oxidizing potential at the tip electrode, the ferrocene species could be oxidized to the ferrocenium species. This latter could diffuse to the electrode surface and be reduced back, providing an oxidation-reduction cycle, called redox cycling. Such approach permitted to detect single electrochemically active molecules for the first time. SECM was recently used to detect short-lived intermediates in electrochemical reactions,⁸ neurotransmitters released from living cells⁹ and to study the catalytic properties of surfaces.¹⁰

In the positive feedback mode, SECM's ability to detect individual molecules through electron-transfer reactions is provided by the above-mentioned redox cycling phenomenon, in which the charge transferred is amplified by repeatedly reducing and oxidizing analyte molecules as they diffuse between two closely spaced electrodes.¹¹ The resulted current amplification is accompanied by significant gains in sensitivity and selectivity, while at the same time decreasing the volume of sample needed for analysis.¹¹⁻¹²

In addition, to facilitate SECM studies, nanoscale electrodes are also commonly involved in other single molecule electrochemistry areas because of their small capacitances and diffusion layers and the ability to provide a spatially-confined probe in different systems (*i.e.*, single cell studies, nanoscale electrochemical imaging). Nanoscale pipettes, obtained by filling glass

pipettes with carbon via pyrolysis of carbonaceous gases, has permitted an increase in nanoscale carbon electrodes diffusion.

In 2017, Unwin *et al.*¹³ applied a simple meniscus imaging probe of 30 nm to the direct electrochemical and topographical imaging of electrocatalytic materials. The electro-oxidation of hydrazine at the surface of electrodeposited Au nanoparticles on a glassy carbon support was investigated via voltammetric hopping mode (Fig. 3.2).

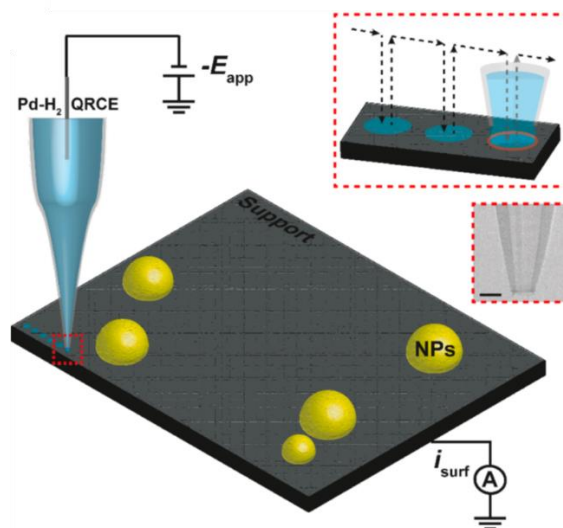


Figure 3.2 Schematic of the general procedure for voltammetric hopping mode SECM with a single-channel nanopipette probe. (Reproduced with modification from 14)

Although the wide applicability of nanoelectrodes, their reproducible fabrication remains difficult and their shape and size can mainly be electrochemically characterized, without the possibility of an independent *a priori* characterization.⁴

In the last decades, different strategies were considered, based on lithographic microfabrication techniques.^{5,14} These methods permit a great flexibility in device's design and the fabrication of multiple devices in parallel, facilitating the reproducibility requirements and the characterization. Indeed, sacrificial devices can be characterized while identical pristine devices can be retained for measurements. They can also be integrated in micro/nanofluidic components such as channels, valves and pumps.¹⁴ Figure 3.3 shows different-magnification levels of lithography-based devices.⁵

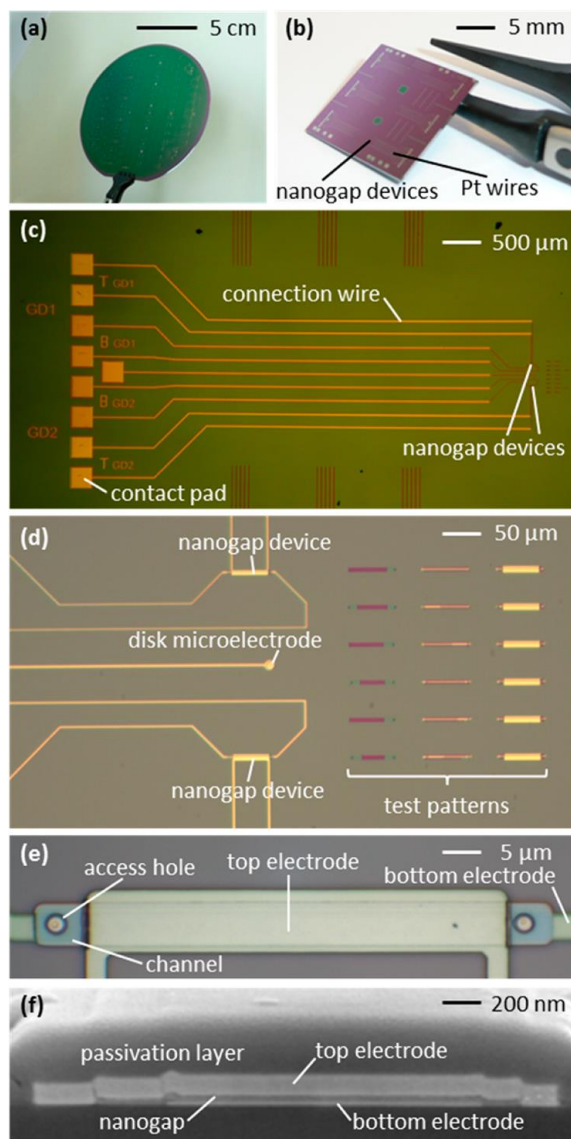


Figure 3.3 Lithography-based nanogap devices. (a) Silicon wafer with devices. (b) Silicon die cut from a wafer with 12 discrete nanogap transducers; the gray features are Pt wires. (c) Optical image showing two devices and associated wires. Contact to external instrumentation is made via the square contact pads on the left. (d) Zoomed-in view of the two devices. Also visible are an integrated microelectrode and test patterns for monitoring the fabrication process. (e) Details of a single nanogap device.¹¹ (f) Scanning electron micrograph of the cross-section of a device ($z = 30 \text{ nm}$).^{5,15}

The first electrode is positioned on a planar substrate, successively a sacrificial layer is deposited, followed by the second electrode. After removing the sacrificial layer, usually by electrochemical etching, the two working electrodes are separated by a nanogap that can be filled with solution. Different nanogap widths can be produced by simply altering the thickness of the sacrificial layer.⁷

Recently, Bohn *et al.*¹⁶ reported a variation of the photolithographic fabrication procedure that permitted the design of nanopore electrode arrays (Fig. 3.4) for the study of ion accumulation and migration effects on redox cycling.

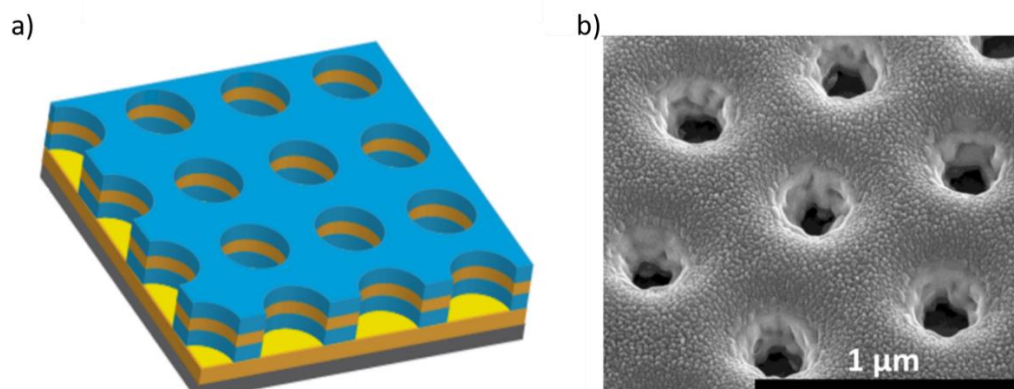


Figure 3.4 An array of ring-disk nanogap cells fabricated using lithographically defined electrodes and reactive ion etching. (Reproduced with modification from 16)

In 2014, Rassaei *et al.*¹⁷ reported a new functionality of electrochemical nanogap devices. By immobilizing tyrosinase enzyme at electrode surface inside the nanochannel, a zeptomole (10^{-21}) number of product molecules (quinone/catechol) by the enzyme reaction was detected (Fig. 3.5).

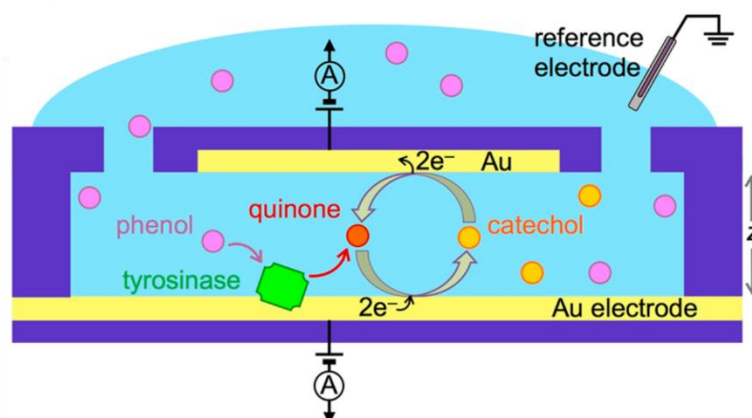


Figure 3.5 Schematic principle of operation of the electrochemical bionanofluidic device: immobilized tyrosinase enzymatically transforms inactive monophenolic substrate molecules into electrochemically active o-quinones. These molecules subsequently undergo redox cycling, yielding a highly amplified electrical current, thus enabling sensitive detection and direct signal transduction (channel height $z = 200$ nm).¹⁷

This work opens the way for small-volume biological samples analysis at single-molecule level based on the enzymatic recognition, by using the redox cycling approach in electrochemical nanofluidic devices.

Lemay and coworkers¹⁸ reported for the first time the concept of nano and micro entities collision at an electrode surface, which represents another prominent area of single entity electrochemistry.

The first investigations involved the amperometric detection of non-electroactive beads by physically hindering flux of a redox species to the electrode surface.^{4,18} Successively, electrocatalytic methods were also investigated. Recently, Zhang *et al.*¹⁹ reported the transient collision of single Pt nanoparticles (Fig. 3.6, a), for the study of their electrocatalytic effects on an inert electrode by fast-scan cyclic voltammetry.

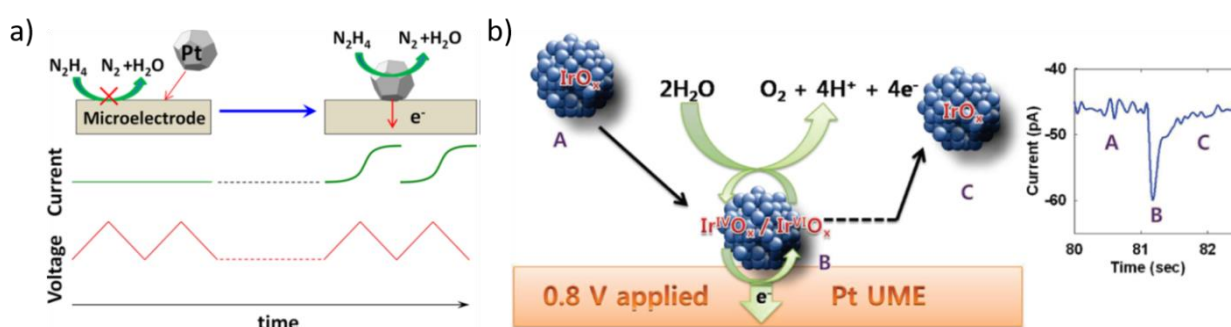


Figure 3.6 a) Fast-scan cyclic voltammetry detection of single-particle collision; b) schematic illustration of single IrO_x nanoparticles collision event and the current enhanced by electrocatalytic water oxidation. (Reproduced with modification from [19] and [20]).

In 2010, Bard and coworkers²⁰ described the electrochemical detection of single IrO_x nanoparticles at Pt ultramicroelectrodes (Fig.3.6, b). During the collisions, the nanoparticle could be observed due to the electrocatalytic phenomenon that permits to enhance the current by electrocatalytic water oxidation.

The pioneering Coulter Counter method, which permits to count particles by recording the ion current correlated with the passage of a single particle inside a restricted channel, has been extended to the characterization of cells and viruses and it is currently used in clinical and bio-diagnostics.⁴ The development of micro/nanopores offers the opportunity to investigate a variety of processes at single molecule level.²¹ The micro/nanopore position between two electrolyte solutions acts as the only connection for mass transfer.²² The successive application of an electric potential difference produces an ion current that drives individual molecule into the pore. Such event provokes a blockage current, called the volume-exclusion effect, which can be detected as ionic signal.²¹ Micro/nanopore systems have been successfully applied to single molecule studies such as molecular structure,²³ to identify DNA epigenetic modifications²⁴ and to distinguish and measure the size of individual nanoparticles.²⁵

It is possible to discriminate between biological micro/nanopores and solid-state micro/nanopores. Biological micro/nanopores present a fixed pore geometry, limiting the access to a restricted kind of molecules. In contrast to biological micro/nanopores, solid-state micro/nanopores can be used in a wide variety of experimental conditions in terms of pH, salinity, and temperature.²⁶ They are used to efficiently detect and discriminate circulating tumor cells from other blood cells.²⁷ Long and coworkers²⁸ designed recently a solid-state nanopore sensor for prostate-specific antigen (PSA) quantification as cancer biomarker, without any serum pretreatment. Selective detection was achieved by binding PSA with a single-stranded DNA probe (Fig. 3.7).

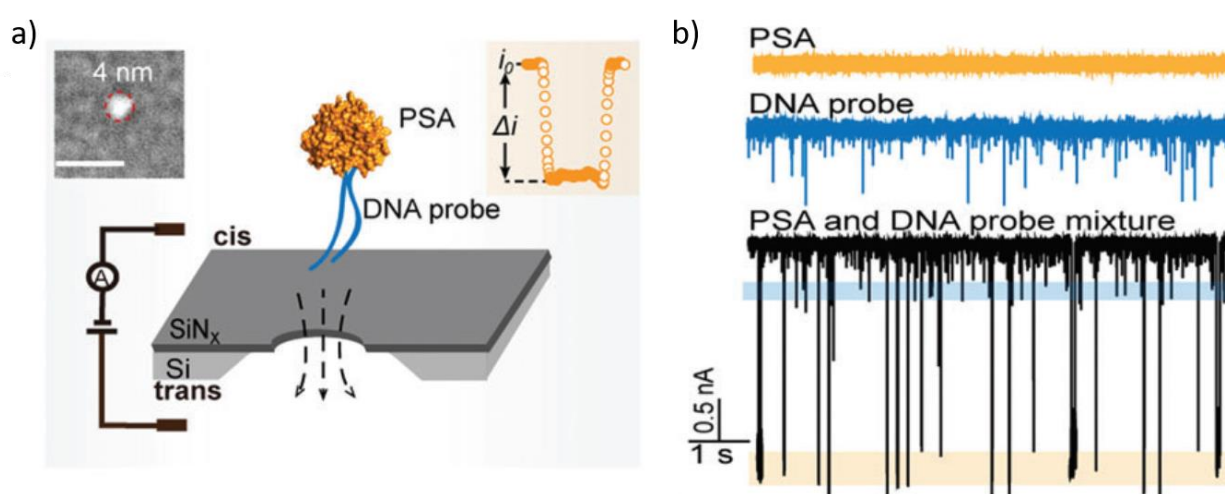


Figure 3.7 (a) Schematic representation for the detection of PSA binding with DNA probe using solid-state nanopores. The membrane with a single nanopore is positioned between two chambers of 1 M KCl (pH = 8) electrolyte solution. The two chambers are defined as cis and trans, respectively. Upper left: A TEM image of a typical 4 nm solid-state nanopore formed by controlled dielectric breakdown. Scale bar = 10 nm. Upper right: A current blockade generated by the PSA–DNA probe complex. (b) Current trace after addition of PSA alone (orange), DNA probe alone (blue), and PSA incubated with DNA probe at a molar ratio (PSA :DNA probe) of 1 : 5 (black) at a voltage of 200 mV. The final concentrations of PSA and DNA probe are 100 nM for individual experiments. The mixture contains 100 nM PSA and 500 nM DNA probe. Traces are recorded in 1 M KCl and at the applied voltage of 200 mV.²⁸

The produced PSA-DNA complex generates deep current blockades, easily distinguishable from interfering blockades and background events (Fig. 3.7, b).

A new emerging micro/nanopore sensing method confining bipolar electrochemistry processes into the pore system to detect single entity and electrochemical processes has been developed.²⁹ Bipolar electrochemistry is an interesting methodology that allows producing an asymmetric reactivity at the extremities of a conducting object, named bipolar electrode (BPE). In the most

common approach used in bipolar electrochemistry (*i.e.* “open-configuration”), a conductive object is immersed in an electrolyte solution and positioned between two feeder electrodes, which are not in physical contact with the BPE.³⁰ This wireless feature provides an additional degree of freedom, which constitutes an essential advantage in comparison to classic electrochemistry. An electric field, in a first order approximation, drops linearly across the electrolyte solution. Since the BPE is by definition equipotential, it will experience an interfacial potential difference (ΔV_{BE}) with the contacting solution. When the potential difference becomes sufficient, cathodic and anodic overpotentials on both sides of BPE are generated. This triggers reduction and oxidation reactions on the opposite sides of the BPE. In other words, a bipolar electrochemical approach induces two gradients of asymmetric electroactivity from the middle of the object to both extremities in a wireless manner. The contactless feature has been exploited to address thousands or millions of objects simultaneously with just two feeder electrodes.³¹ Other example illustrating the versatility of BPE based on its electrochemical anisotropy is the fabrication of Janus particles and self-propelled swimmers.³² The driving force of this method is the interfacial potential difference (ΔV_{BE}) between the bipolar electrode and the electrolyte solution in which it is immersed. Controlling the spatial distribution of the potential drop and its localization may allow manipulating the BPE behavior and the use of micro/nanopore represents a valid tool to explore this research line.³³ Considering the classic configuration used in bipolar electrochemistry, the polarization potential difference of the bipolar electrode (ΔV_{BE}) is directly related to the potential difference applied between the feeder electrodes (ΔV_{FE}) and to the resulting electric field strength ($\Delta V_{FE}/d$, where d is the distance between both feeder electrodes) as described by the following equation:

$$\Delta V_{BE} = \frac{\Delta V_{FE}}{d} \times L \quad (3.1)$$

with L being the length of the BPE. The potential difference ΔV_{BE} can be considered as the fraction of the applied potential that drops over the bipolar electrode. In contrast to classic electrochemistry, where the potential of the working electrode controls the faradaic reaction, the key-parameter for BPE is the distribution of the potential gradient in the electrolyte solution, more precisely the strength of the electric field, which governs the electrochemical processes. Another direct consequence of Eq. 3.1 is that for small BPE a bigger potential ΔV_{FE} is required to polarize it and induce both electrochemical reactions at its extremities. This is an inherent

physical limitation of BPE, which constitutes an important drawback for small objects. Indeed, micrometric and nanometric objects are extremely difficult to address by BPE because extremely high potentials are required (in the order of tens of kV or more),³⁴ which can provoke substantial gas evolution at the feeder electrodes. These major disadvantages generally are not mentioned or detailed in the reports of bipolar electrochemistry, even if they limit drastically the use of small BPEs. For example, 2 μm -long carbon nanotubes were modified with Au electrodeposit by applying a potential of 30 kV.^{34b} In a recent study of Albrecht and coworkers,³⁵ electrodeposition was employed for the modification of nanopore's dimensions below 10 nm. In addition, bipolar effects were quantified, with the results of a strong, localized electric field across the pore. The transformation of the electrochemical event to the optical domain is accompanied by a significant gain in signal-to-noise ratio. This allows to improve detection efficiency in single entity electrochemistry, due to the much higher energy content of a photon (for example of a wavelength of 400 nm) compared to that of an electrochemical event and to the intrinsic high spatial and temporal resolutions of optical techniques.³⁶

Different approaches have been explored, such as the use of fluorescent molecules whose fluorescence intensity varies with the redox-state, the labeling of the molecule of interest, surface enhanced raman spectroscopy (SERS, which can distinguish between different redox states), different kinds of chemiluminescence and plasmonic imaging.³⁶ Kanoufi *et al.*³⁷ combined electrochemistry in confined environments and plasmonics-based high resolution holographic microscopy for analyzing *in operando* electrochemical reactions at single nanoparticle level. The holographic setup is employed to study nanoparticles trajectory *in situ* and aggregation and adsorption phenomena. In 2008, Barbara *et al.*³⁸ applied ECL to the detection of single nanoparticles on ITO working electrode, demonstrating that ECL could be used as a tool for the detection and localization of electrochemical events in confined environments. Sub-25 nm nanoparticles of poly(9,9-dioctylfluorene-*co*-benzothiadiazole) (F8BT, Fig. 3.8, a) were immobilized on ITO working electrode and acted as ECL luminophore reacting with the coreactant TPA. Figure 3.8 (c) reports the corresponding ECL image of nanoparticles.

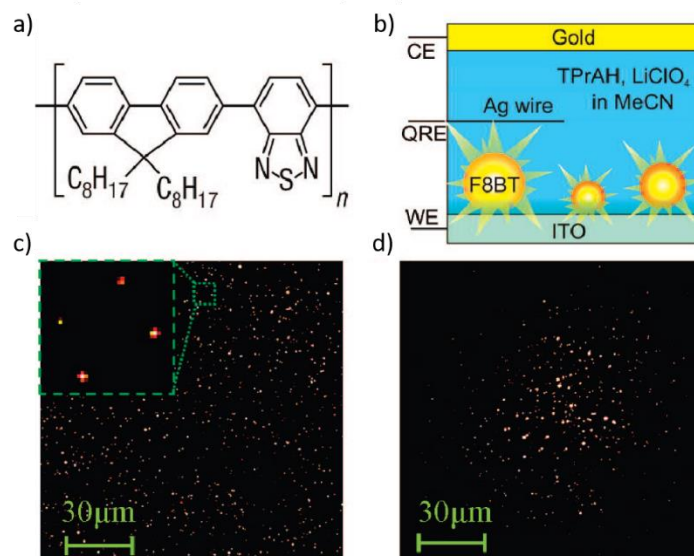


Figure 3.8 a) F8BT chemical structure; b) schematic diagram of SMSEC cell; c) wide-field ECL image; d) wide-field PL image (same area as c) with the laser beam focused on the central area of the image (inset: expanded region showing ECL from four particles). The intensity scale (0-200 counts) and integration time (0.5 s) of images c and d are the same.³⁸

The catalytic ECL amplification via coreactant pathway permitted the localization of the nanoparticles. The double nature of electrochemical and photochemical phenomenon of ECL, together with the high sensitivity, spatial and temporal resolutions should allow study of dynamic electrochemical processes at single molecule level.

This chapter is devoted to the description and discussion of two studies in which ECL is used as an analytical tool for the detection of an electrochemical phenomenon confined in nano- and micro-environments.

In the first work, performed in collaboration with Prof. Mathwig's group in Groningen University, a microfabricated transparent nanogap device was applied to the generation of stable light emission by ECL, via both annihilation and coreactant pathways.³⁹

In the second part, the synergetic actions of bipolar electrochemistry and planar micropores integrated in a microfluidic device lead to a locally enhanced polarization of a bipolar electrode. ECL is emitted in half of the micropore and reveals the asymmetric polarization in this spatial restriction. This study was made in collaboration with Dr. Bouchet-Spinelli and Dr. Ismail (University of Grenoble-Alpes) and Dr. Leichlé (LAAS-CNRS, University of Toulouse).³³

3.2 ECL by nanofluidic confinement

In the present work, the goal was to generate ECL via both annihilation and coreactant pathways in a transparent nanofluidic electrochemical device. Primarily, ECL investigations via annihilation are reported. In the second part, ECL via coreactant pathway is examined and compared to the first one.

3.2.1 Nanogap device description

Figure 3.9 shows the fabrication steps of electrochemical nanofluidic devices. The use of a transparent glass substrate altered some process parameters previously involved with opaque oxidized wafers substrates.¹¹

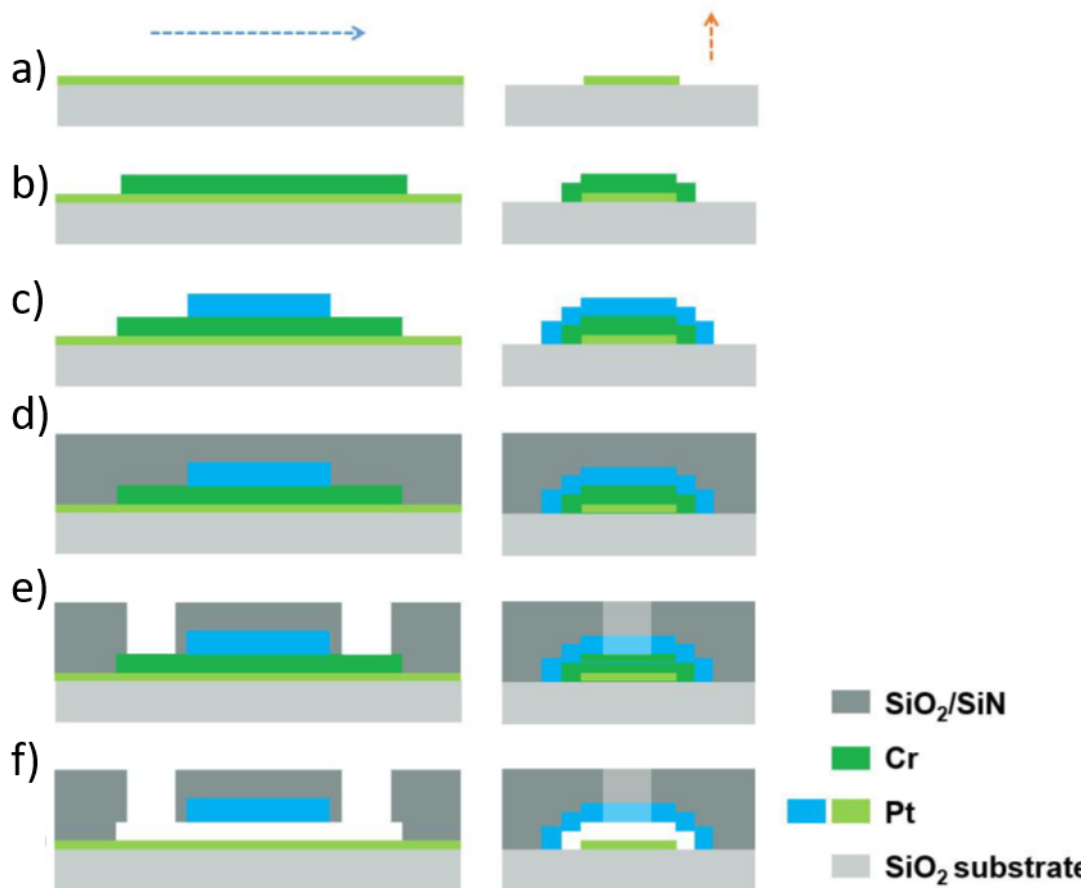


Figure 3.9 Microfabrication steps of transparent nanofluidic electrochemical transducers. a) Patterning of a 20-nm-thick Pt layer by photolithography, metal evaporation and a lift-off process. A 10-cm-wide and 700- μm -thick borosilicate wafer substrate was used. b) Photolithography, metal evaporation, and lift-off to structure the Cr layer defining the nanochannel volume. c) Photolithography, Pt evaporation and lift-off to define the top electrode. d) PECVD deposition of a $\text{SiO}_2/\text{SiN}/\text{SiO}_2$ passivation layer. e) photolithography and reactive ion etching of access holes through the passivation layer using the resist as mask. f) The wafer is diced into individual chips. Directly

before and experiment, the Cr layer is removed and the nanochannel is formed using a selective wet chemical Cr etch.

Structures comprising a thin $20\ \mu\text{m}$ Pt bottom electrode, $100\ \text{nm}$ Cr sacrificial layer (forming the nanochannel volume) and $120\ \mu\text{m}$ Pt top electrode were patterned on a $10\ \text{cm}$ borosilicate glass wafer using UV lithography, followed by evaporation deposition and lift-off. A $500\ \text{nm}$ SiO_2/SiN passivation layer, deposited using chemical vapor deposition, encased the devices. Access holes were etched through the passivation layer by reactive ion etching. Finally, the wafer was diced into individual chips. In Figure 3.10, a complete device is reported, with a $5\ \mu\text{m} \times 32\ \mu\text{m} \times 100\ \text{nm}$ channel volume, and an effective area of overlap between the electrodes of $3\ \mu\text{m} \times 20\ \mu\text{m}$.

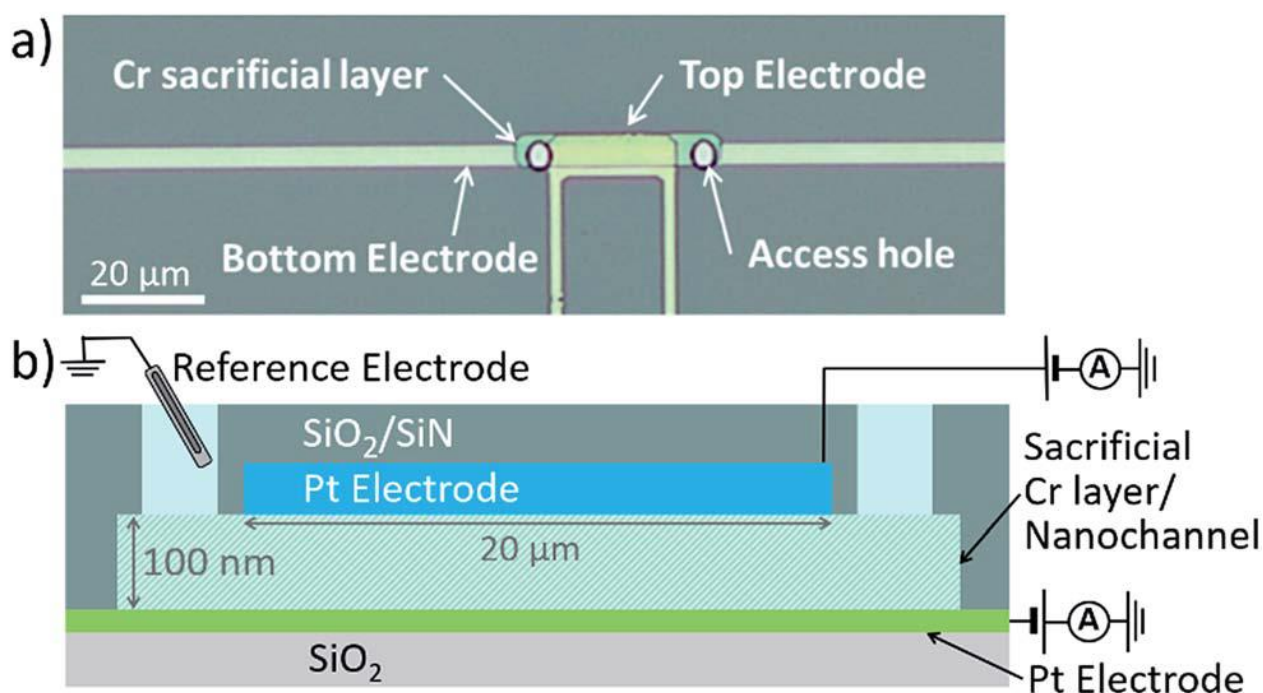


Figure 3.10 (a) Top view optical micrograph of an electrochemical nanogap device. (b) Schematic cross section of a device with access holes to reservoir and two individually addressable Pt electrodes. The sacrificial Cr layer is etched before the experiments to form the nanochannel.

Before starting the electrochemical and ECL experiments, a polydimethylsiloxane fluid reservoir was placed on top of the device, and the sacrificial layer was selectively wet-etched to form the channel. The device design and fabrication was completely developed by Prof. K. Mathwig and H. Al-Kutubi in Groningen University.

3.2.2 Enhanced annihilation ECL

As described previously, ECL light generation can follow two dominant pathways: the annihilation and the coreactant pathways. Here, the annihilation pathway inside the nanochannel is discussed. Tris(bipyridine)ruthenium(II), $[\text{Ru}(\text{bpy})_3]^{2+}$ was selected, due to its relatively high quantum yield and long-lived excited state.⁴⁰ Its annihilation pathway⁴¹ is:



The first electron transfer reactions (Eq. 3.2-3.5) for the generation of the reduced ($[\text{Ru}(\text{bpy})_3]^+$) and the oxidized ($[\text{Ru}(\text{bpy})_3]^{3+}$) forms of the luminophore were initially investigated by alternately applied an oxidizing and reducing potential to a single electrode with rapid pulses.⁴² However, this approach causes large charging currents.⁴⁰ Using two electrodes, both $[\text{Ru}(\text{bpy})_3]^+$ and $[\text{Ru}(\text{bpy})_3]^{3+}$ can be generated in close vicinity under steady-state conditions. A ring and disk electrodes setup was investigated by Maloy and Bard⁴³ to continuously generate, at ring and disk electrodes respectively, radical cations and anions of ECL luminophore under steady-state conditions. Another configuration, named generation-collection mode, allowed obtaining annihilation ECL in ambient conditions thanks to the micrometric distance between anode and cathode.⁴⁴ Scanning electrochemical microscopy (SECM) was also involved in the study of ECL processes in the annihilation mode,⁴⁵ through a controlled two-electrode approach. Bard and coworkers were able to enhance the light collection efficiency of rubrene (5,6,11,12-tetraphenyltetracene) and $[\text{Ru}(\text{bpy})_3]^{2+}$ ECL systems by using a selectively insulated ITO-transparent substrate as a microelectrode to produce the corresponding radical cations and a metallic SECM tip to produce the radical anions.^{45b} These studies have shown that annihilation occurs more efficiently at smaller inter-electrode distances, as the diffusional distance between the radical cation and the radical anion is decreased. Observation of light emission so far has been limited to a minimum inter-electrode distance of 2 μm .^{45b,46} In addition, due to the sensitivity of annihilation ECL towards impurities such as oxygen and water, those experiments were performed in drastic conditions: dried and distilled

solvents just before use, recrystallized and dried luminescent compounds and supporting electrolytes, under an inert atmosphere or in a dry box.⁴⁷ In particular, for platinum electrodes the hydrogen evolution reaction competes with the reduction potential of $[\text{Ru}(\text{bpy})_3]^{2+}$. In this context, the present work shows the possibility to observe annihilation ECL emission under ambient conditions using platinum electrodes in an electrochemical nanogap device.

3.2.2.1 Electrochemical characterization

Electrochemical measurements were performed with a bipotentiostat. Functioning simultaneously as both reference electrode and counter electrode, a Ag/AgCl/KCl (3M) was used. For all experiments, freshly etched devices were cleaned by cycling the potential of both electrodes between -0.15 V and 1.2 V *vs* Ag/AgCl in 50 mM H₂SO₄. Channels were thoroughly flushed with Milli-Q water, and subsequently with acetonitrile, which was then replaced by 10 mM of $[\text{Ru}(\text{bpy})_3](\text{PF}_6)_2$ and 0.1 M TBAPF₆ in acetonitrile (CH₃CN). This solution was used for all experiments. The first electrochemical characterization of the nanogap device was performed by disconnecting the bottom electrode (i.e., kept at a floating potential), while the top electrode was pulsed between 0 V and 2 V *vs* Ag wire. The chronoamperometric current and light intensity response (Fig. 3.11) were measured with a photomultiplier tube.

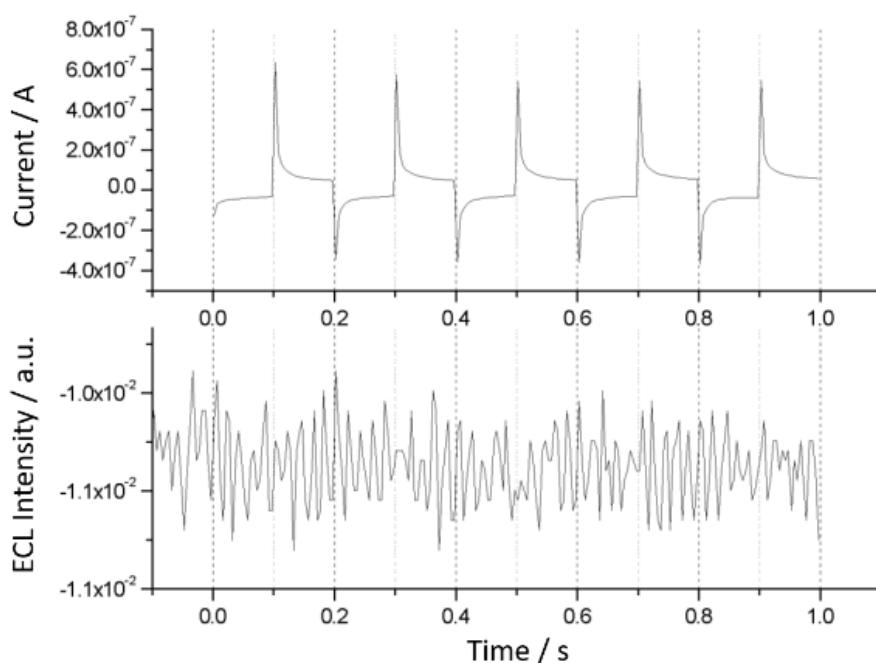


Figure 3.11 Measured chronoamperometric currents (top) and corresponding light intensity recorded with a PMT (bottom). A potential alternating between 0 V and 2 V *vs* Ag was applied to the top electrode of a nanogap device

while the bottom electrode was kept floating. A solution of 10 mM $\text{Ru}(\text{bpy})_3(\text{PF}_6)_2$ and 0.1 M TBAPF_6 in acetonitrile was used.

While pulsing a single electrode, the change in the detected light intensity is negligible compare to the background intensity. This observation demonstrates that two independently biased electrodes (at constant) potentials are necessary for the generation of ECL; indicating that light generation takes place according to the annihilation pathway shown in Eq. 3.2-3.5.

3.2.2.2 Two electrochemical modes

Two electrochemical modes were investigated in the nanofluidic channel (Fig. 3.12). In redox cycling, the top electrode is biased at an oxidizing potential, generating $[\text{Ru}(\text{bpy})_3]^{3+}$. Biasing the bottom electrode at 0 V leads to one-electron reduction of $[\text{Ru}(\text{bpy})_3]^{3+}$ and, thus, regeneration of $[\text{Ru}(\text{bpy})_3]^{2+}$.

In annihilation ECL, the same potential is imposed at the top electrode, whereas the bottom electrode is placed at a sufficiently cathodic potential to reduce $[\text{Ru}(\text{bpy})_3]^{2+}$ to $[\text{Ru}(\text{bpy})_3]^+$. The annihilation reaction (Eq. 3.4) takes place, and ECL light is emitted (Eq. 3.5). Conceptually, this process is similar to redox cycling as it involves the constant consumption and regeneration of $[\text{Ru}(\text{bpy})_3]^{2+}$. However, instead of taking place between two electrode surfaces, regeneration (annihilation) occurs homogeneously in the channel bulk, where $[\text{Ru}(\text{bpy})_3]^+$ and $[\text{Ru}(\text{bpy})_3]^{3+}$ meet.

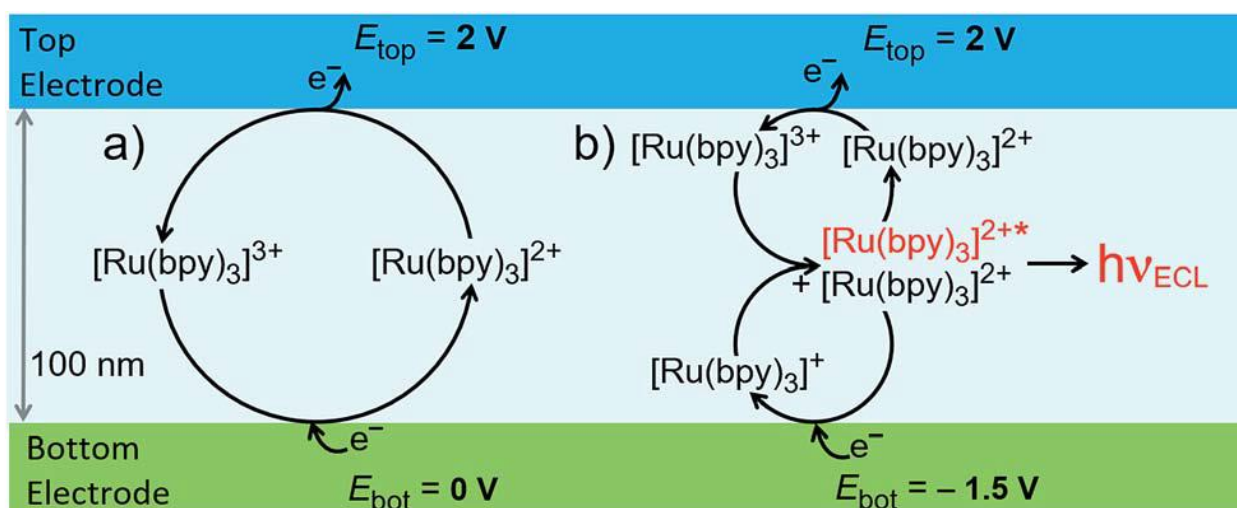


Figure 3.12 Schematic of two reaction pathways in the nanochannel: (a) redox cycling, and (b) annihilation leading to ECL emission.

In the top region, redox cycling between $[\text{Ru}(\text{bpy})_3]^{2+}$ and its oxidized form occurs, whereas the bottom region shows cycling of $[\text{Ru}(\text{bpy})_3]^{2+}$ with its reduced form. The channel is therefore effectively split, and anodic and cathodic redox cycling occur simultaneously (Fig. 3.12, b). Therefore, as diffusion time scales inversely with the length of the diffusive path, switching from redox cycling to annihilation ECL mode should result in a higher faradaic current. Figure 3.13 reports the chronoamperometric currents at both electrodes when stepping between redox cycling and annihilation ECL modes. In redox cycling mode, the oxidation and reduction currents are symmetric and constant.

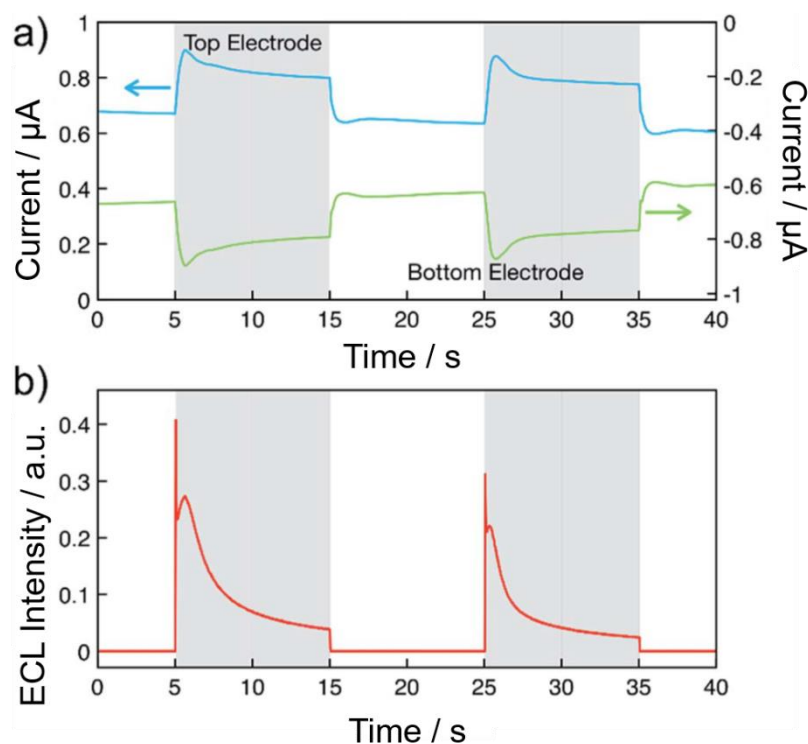


Figure 3.13 (a) Measured chronoamperometric currents at the top (blue) and bottom (green) electrodes, and (b) corresponding ECL intensity. The top electrode was maintained at 2.3 V while the bottom electrode was pulsed between 0 V and -1.5 V vs Ag, highlighted in white (redox cycling mode) and grey (annihilation ECL mode), respectively. Solution consisted of 10 mM $\text{Ru}(\text{bpy})_3(\text{PF}_6)_2$ and 0.1 M TBAPF_6 in acetonitrile.

The observed currents of $\sim 0.65 \mu\text{A}$ are in agreement with an expected analytical estimate⁴⁸ of:

$$I_{lim} = \frac{F A D c}{h} = 0.58 \mu\text{A} \quad (3.6)$$

Where F is the Faraday constant, A the active area of $3 \mu\text{m}$ by $20 \mu\text{m}$, D is the diffusion coefficient with a value of $1 \times 10^{-9} \text{m}^2 \text{s}^{-1}$, c is the concentration of $[\text{Ru}(\text{bpy})_3]^{2+}$ (10 mM), and h the channel height of 100 nm.

ECL intensity was measured simultaneously by using a photomultiplier tube. The signal was amplified by a Keithley Picoammeter before acquisition with the second input signal of

μ Autolab type II potentiostat. ECL emission was not observed in redox cycling mode (Fig. 3.13 b). Upon switching to annihilation mode, an initial transient current increase can be ascribed to adsorption of analytes onto the electrode surfaces due to the high surface-to-volume ratio of the nanogap devices.^{11,48-49} Oxidation and reduction currents are symmetric as expected for reactions (3.2-3.5). In annihilation mode, ECL emission intensity (Fig. 3.13, b) exhibits strong transient behavior before approaching a steady state. Understanding this transient behavior will require further studies, the complex transient can be partially attributed to desorption when stepping the potential as well as accumulating $[\text{Ru}(\text{bpy})_3]^{3+}$ during redox cycling. Upon switching from redox cycling to annihilation mode, an expected increase in the current is observed as the diffusive path for cycling molecules halves to 50 nm.

Concentration profiles of $[\text{Ru}(\text{bpy})_3]^{2+}$ and of its corresponding reduced and oxidized species (Fig. 3.14) were obtained by using COMSOL Multiphysics by Prof. Mathwig (Groningen University).

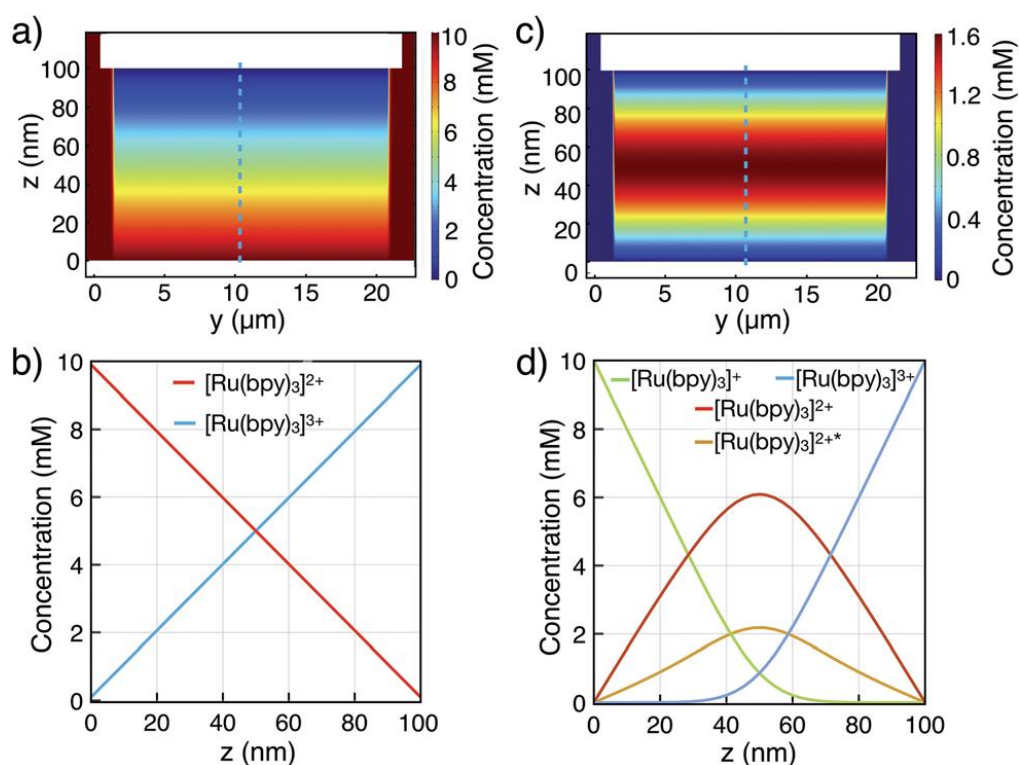


Figure 3.14 Finite element simulations of concentration profiles for a 10 mM $[\text{Ru}(\text{bpy})_3]^{2+}$ bulk concentration in the nanochannel. Two-dimensional $[\text{Ru}(\text{bpy})_3]^{2+}$ profiles in a) redox cycling mode, and c) annihilation mode. (b and d) Corresponding cross-sectional profiles in the channel center (indicated by the dashed line in both modes, respectively).

Considering the symmetry of the nanofluidic channel and the annihilation reaction (*i.e.*, double cycling redox process), ECL is emitted in the middle of the nanogap where both $[\text{Ru}(\text{bpy})_3]^{3+}$

and $[\text{Ru}(\text{bpy})_3]^+$ react to form $[\text{Ru}(\text{bpy})_3]^{2+*}$, assuming similar diffusion coefficients for $[\text{Ru}(\text{bpy})_3]^{3+}$ and $[\text{Ru}(\text{bpy})_3]^+$. The ECL emission should occur in the vertical symmetry plane of the device and be confined to the electroactive area of the nanochannel (Fig. 3.14, d). However, it is not possible to resolve this with optical microscopy due to the nanometric dimension of the inter-electrode gap.

The simulated diffusive fluxes (*i.e.*, slopes of concentration profiles) at electrode surfaces double when switching from redox cycling and annihilation. However, a ratio of only 1.2 for the steady-state redox cycling and annihilation currents is observed (Fig. 3.14, a). Understanding this low ratio requires further studies. Adsorption phenomena can play a crucial role on the electrochemical performances of nanodevices, leading to a reduced confinement effect.⁵⁰ However, in the studied system, the coupling between the nanogap and the bulk reservoir can balance such phenomenon as well as unequal diffusion coefficients in reactants.⁴⁸ The low ratio between redox cycling and annihilation modes currents can be related to electrical migration. While in macroscopic electrodes electrical migration can usually be negligible and mass transport is predominantly based on the diffusion, in such electrochemical conditions, the short distance between the two working electrodes can generate an overlapping of the electrical double layers. Therefore, diffusion cannot be considered the only contribution to mass transport and a more complex concentration profiles results.¹⁶

3.2.2.3 ECL imaging

ECL emission was produced in annihilation mode inside a nanochannel and was imaged and spatially resolved as shown in Figure 3.15 using an epifluorescence microscope (DMI6000, Leica). Photon emission was collected by an inverted 40× microscope objective and detected by an Electron Multiplying Charge Coupled Device (EM-CCD) Camera (Hamamatsu, 9100-13). Light emission from a luminophore quantity of 60 attomoles present in the active area of the device was intense enough to be recorded through the 20 nm-thick semi-transparent Pt bottom electrode, due to nanogap amplification.

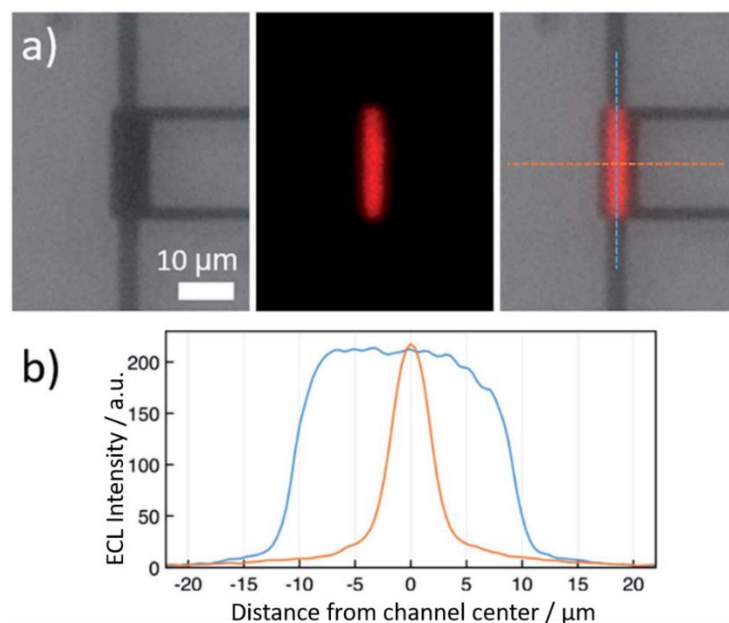


Figure 3.15 (a) From left to right: bright-field micrograph of the nanochannel, ECL emission recorded in the dark, and overlay of both images (dashed lines: direction of profiles in (b)). (b) longitudinal ECL intensity profiles (blue) and lateral (across) ECL intensity profile (orange) the center of the channel, using a solution of 10 mM $\text{Ru}(\text{bpy})_3(\text{PF}_6)_2$ and 0.1 M TBAPF_6 in acetonitrile. The top electrode was biased at 2 V, the bottom electrode at 1.5 V vs Ag.

The overlay image (Fig. 3.15, a right) shows that ECL intensity is uniform along the channel and decreases rapidly at the edges. No emission is seen from the bottom electrode area under the access holes. Furthermore, ECL emission is limited to a region narrower than the 5 μm wide channel. This indicates that emission is caused exclusively by reaction in the 3 μm \times 20 μm effective area between the electrodes. Such result was previously observed for purely electrochemical detection in a comparable nanogap device.^{15,51}

Full-width-at-half-maxima of longitudinal and lateral intensity profiles amount to 20 μm and 4.3 μm , respectively. Presumably, the optical resolution of the 40 \times objective as well as inhomogeneous transparency of Pt and glass lead to a slightly wider profile than expected. Clearly, ECL emission is confined to the active area of the nanochannel, where reactions (3.2-3.5) (Fig. 3.15, b) take place. The constant ECL intensity along the nanochannel (Fig. 3.15, b blue curve) indicates that only negligible degradation occurs. If $[\text{Ru}(\text{bpy})_3]^+$ and $[\text{Ru}(\text{bpy})_3]^{3+}$ would degrade, the intensity would be strongly attenuated in the center of the channel because the chance of encountering contaminants increases quadratically as luminophores diffuse towards the center.

3.2.3 ECL via coreactant pathway

ECL via annihilation shows an enhancement when confined in the nanochannel geometry. To further investigate the ECL reaction mechanism inside the nanochannel, the previous studied pathway and the corresponding emission profile were compared with ECL emission via coreactant in a single nanochannel and with an intermediate condition in which both ECL modes (annihilation and coreactant) may occur.

The same ECL luminophore studied in annihilation mode, $[\text{Ru}(\text{bpy})_3]^{2+}$, was selected, with TPA as coreactant. As mentioned in Chapter I, the ECL system $[\text{Ru}(\text{bpy})_3]^{2+}/\text{TPA}$ can be considered as a model system for ECL via coreactant pathway, due to the highest ECL performances and its applications in immunoassay and DNA analysis.⁵² Using a coreactant pathway, $[\text{Ru}(\text{bpy})_3]^{2+}$ can be excited by electrochemical reduction of $[\text{Ru}(\text{bpy})_3]^{2+}$ not at an electrode surface but in solution by a strongly reducing coreactant such as a TPA.⁵³

3.2.3.1 ECL analysis

Cyclic voltammogram with simultaneous detection of luminescence intensity (recorded using a PMT) was performed in the nanochannel (Fig. 3.16). The result for a coreactant mode is as expected and identical to current-time and intensity-time curves at single macroscopic or microelectrodes.

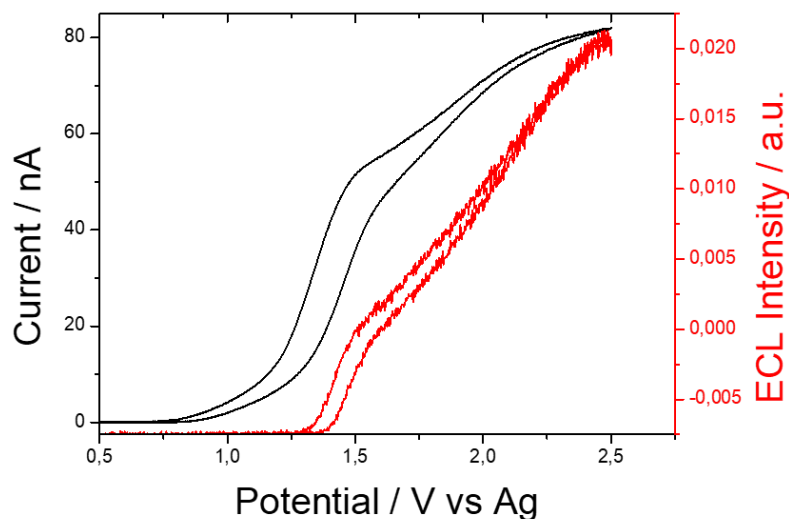


Figure 3.16 a) Cyclic voltammogram (black curve) and electrochemiluminescence (red curve) of 10 mM $\text{Ru}(\text{bpy})_3(\text{PF}_6)_2$, 100 mM TPA and 0.1 M TBAPF_6 in acetonitrile in a nanofluidic device. Scan rate = 100 mV/s.

An increase in the current starts at about 0.8 V vs Ag and it can be correlated with TPA oxidation (Fig. 3.16, black curve), which is present in excess during the analysis. The corresponding ECL photocurrent correlated with $[\text{Ru}(\text{bpy})_3]^{2+}$ emission is generated at a potential value slightly more positive, around 1.4 V vs Ag. The ECL signal appears noisy, probably because of the high sensitivity required for collecting ECL emission (-900 V were applied on the PMT, instead of -750 V, when $[\text{Ru}(\text{bpy})_3]^{2+}$ is oxidized) and to the peculiar configuration.

Figure 3.17 shows chronoamperometric currents and intensity in a nanofluidic device for an intermediate condition, in $\text{Ru}(\text{bpy})_3(\text{PF}_6)_2$ 10 mM, TPA 0.1 M, TBAPF_6 0.1 M solution in CH_3CN . Two electrochemical modes were investigated, also in presence of the coreactant TPA.

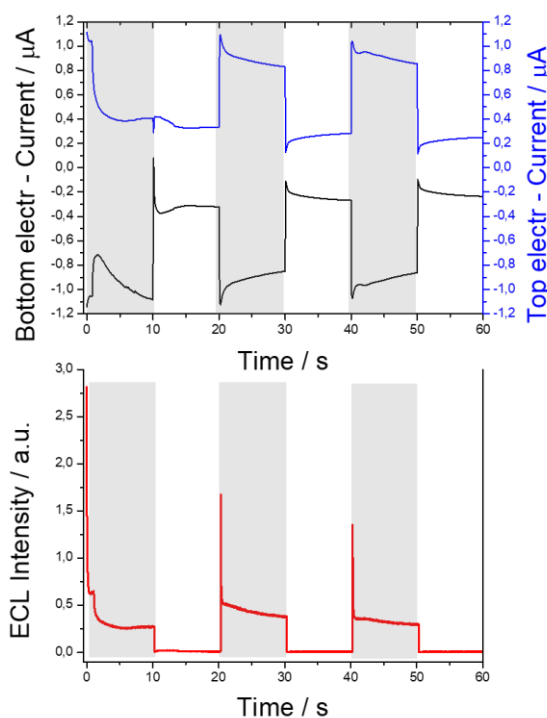


Figure 3.17 Top: Chronoamperometric current-time at the top electrode (blue) and bottom electrode (black), and, bottom: corresponding ECL intensity. The top electrode was biased at 2 V with on-off pulses at 10 s while the bottom electrode was biased constantly at -1.5 V vs Ag wire. ($\text{Ru}(\text{bpy})_3(\text{PF}_6)_2$ 10 mM, TPA 0.1 M, TBAPF_6 0.1 M in CH_3CN).

The bottom electrode was constantly biased at -1.5 V, while the top electrode was pulsed between 2 V and 0 V. In redox cycling mode, the bottom electrode was biased at -1.5 V vs Ag, while 0 V was applied to the top electrode. In these conditions, no ECL emission occurs (Fig. 3.17, bottom). Oxidation and reduction currents are symmetric as expected for a redox cycling

regime. It can be supposed that $[\text{Ru}(\text{bpy})_3]^{2+}$ is reduced to $[\text{Ru}(\text{bpy})_3]^+$ at the bottom electrode and partially regenerated at the top electrode, as the reaction is inefficient at a low top electrode potential of 0 V and only a small fraction of $[\text{Ru}(\text{bpy})_3]^+$ is oxidized there. By applying 2 V to the top electrode, ECL emission was recorded with a long transient behavior before reaching the steady state, as already observed for annihilation mode (Fig. 3.13). The complex transient can be partially attributed to desorption of products accumulated during the redox cycling mode. The presence of the coreactant TPA in solution does not permit to call this second mode “annihilation mode”. In such intermediate conditions, both ECL pathways could happen. Indeed, the presence of the coreactant TPA adds a second route to the annihilation mode already seen, as it was confirmed by ECL imaging.

3.2.3.2 ECL imaging

Imaging with spatial resolution permitted to investigate three different modes and to clarify the contribution of the two ECL pathways in the intermediate condition. ECL emission was collected by an inverted 40× microscope objective and detected by an EMCCD camera (*vide* § 3.2.2.4). In Figure 3.18 a), ECL image is shown, corresponding to the intermediate regime previously analysed (Fig. 3.17), in which a solution of luminophores and coreactants undergoes an annihilation reaction. In this case, the bottom electrode is biased at -1.5 V and the top electrode at 2 V. Faint light emission can be seen in the center of the nanochannel, as the two ECL pathways coexists, reaction is inefficient. It can be supposed that ECL via annihilation is the only contribution to the recorded emission. The presence of the coreactant TPA causes a decrease in the ECL emission inside the nanochannel that is not concomitant with an ECL emission correlated with the coreactant pathway. TPA in the nanochannel is probably converted into by-products initially after biasing, decreasing the total ECL performances.

Figure 3.18 b) shows ECL image obtained by applying 2 V and 0 V, to the bottom and the top electrodes respectively in $\text{Ru}(\text{bpy})_3(\text{PF}_6)_2$ 10 mM, TPA 0.1 M, TBAPF_6 0.1 M solution in acetonitrile in the same nanogap device. In these conditions, only ECL via coreactant pathway can occur. Light emission is limited to the access holes of the nanochannel (Fig. 3.18, b), i.e., to the electrode surface of the bottom electrode that is directly exposed to the bulk solution. The luminescence profile is here determined by lifetimes and diffusivities of participating reactants. For such a measurement of steady-state ECL, light emission is excluded from the nanochannel because the reaction is limited by a constant supply of TPA coreactant. TPA radicals are continuously generated at the electrode surface beneath the access holes as TPA constantly

diffuses to the reaction area from the bulk solution. TPA radicals cannot enter the center of the nanochannel because of the characteristic of $[\text{Ru}(\text{bpy})_3]^{2+}$ /TPA ECL mechanism (*vide* Chapter I) *i.e.*, either by reacting with the luminophore or by deprotonation. Thus, light emission is determined by the lifetime of TPA radicals, and by the distance they can diffuse during the lifetime.

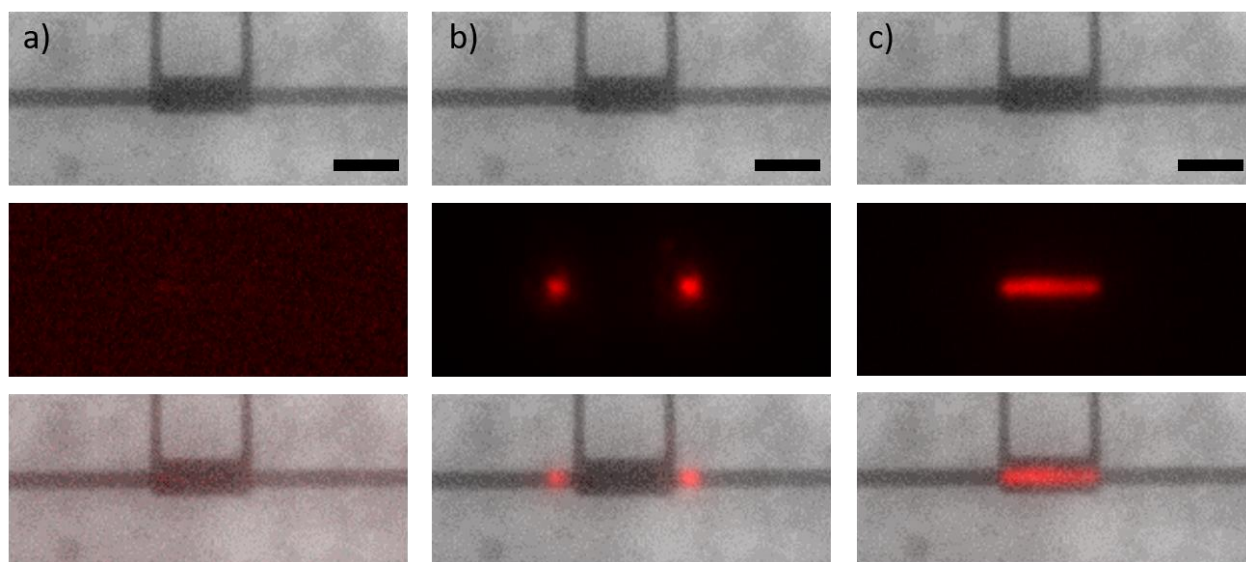


Figure 3.18 a) bright-field (top) micrograph of nanofluidic device, intermediate regime ECL image (center) and overlay (down) recording in $[\text{Ru}(\text{bpy})_3]^{2+}$ 10 mM, TPA 0.1M, TBAPF₆ 0.1 M solution in CH₃CN; Bottom electrode (WE1, -1.5 V), Top electrode (WE2, 2 V), Ag (QRE-CE); b) bright-field (top) micrograph of nanofluidic device, coreactant mode ECL image (center) and overlay (down) recording in $[\text{Ru}(\text{bpy})_3]^{2+}$ 10mM, TPA 0.1M, TBAPF₆ 0.1M solution in CH₃CN; Bottom electrode (WE1, 2 V), Top electrode (WE2, 0V), Ag (QRE-CE); c) bright-field (top) micrograph of nanofluidic device, annihilation mode ECL image (center) and overlay (down) recording in $[\text{Ru}(\text{bpy})_3]^{2+}$ 10mM, TBAPF₆ 0.1M solution in CH₃CN; Bottom electrode (WE1, -1.5 V), Top electrode (WE2, 2 V), Ag (QRE-CE). Scale bar = 10 μm .

In annihilation mode (red line, Fig. 3.18, c), ECL is limited to the volume of overlapping top and bottom electrode.³⁹ The experimental results show that nanochannels can be used to distinguish reaction pathways in a mixture of luminophores and coreactant. Table 3.1 summarizes the different potentials used to record images of Figure 3.18, depending on the three experimental ECL modes.

Table 3.1 Potentials vs Ag applied to the top and bottom electrode, respectively for recording ECL images in annihilation mode (Fig. 3.18, a), coreactant mode (Fig. 3.18, b) and annihilation mode in presence of TPA (Fig. 3.18, c).

Pt electrodes	Annihilation mode	Coreactant/TPA mode	Annihilation/TPA mode
Top	2 V	0 V	2 V
Bottom	-1.5 V	2 V	-1.5 V

In Figure 3.19, the corresponding ECL emission profiles along the nanochannel for the three different situations are compared. In the coreactant mode, light emission is limited to the access hole area and it gives the higher ECL intensity values (the three images were recorded with the same exposure time). As already discussed, in annihilation mode ECL intensity is confined inside the nanochannel. For the intermediate mode, ECL emission occurs inside the nanochannel, less efficiently than in the absence of the coreactant TPA.

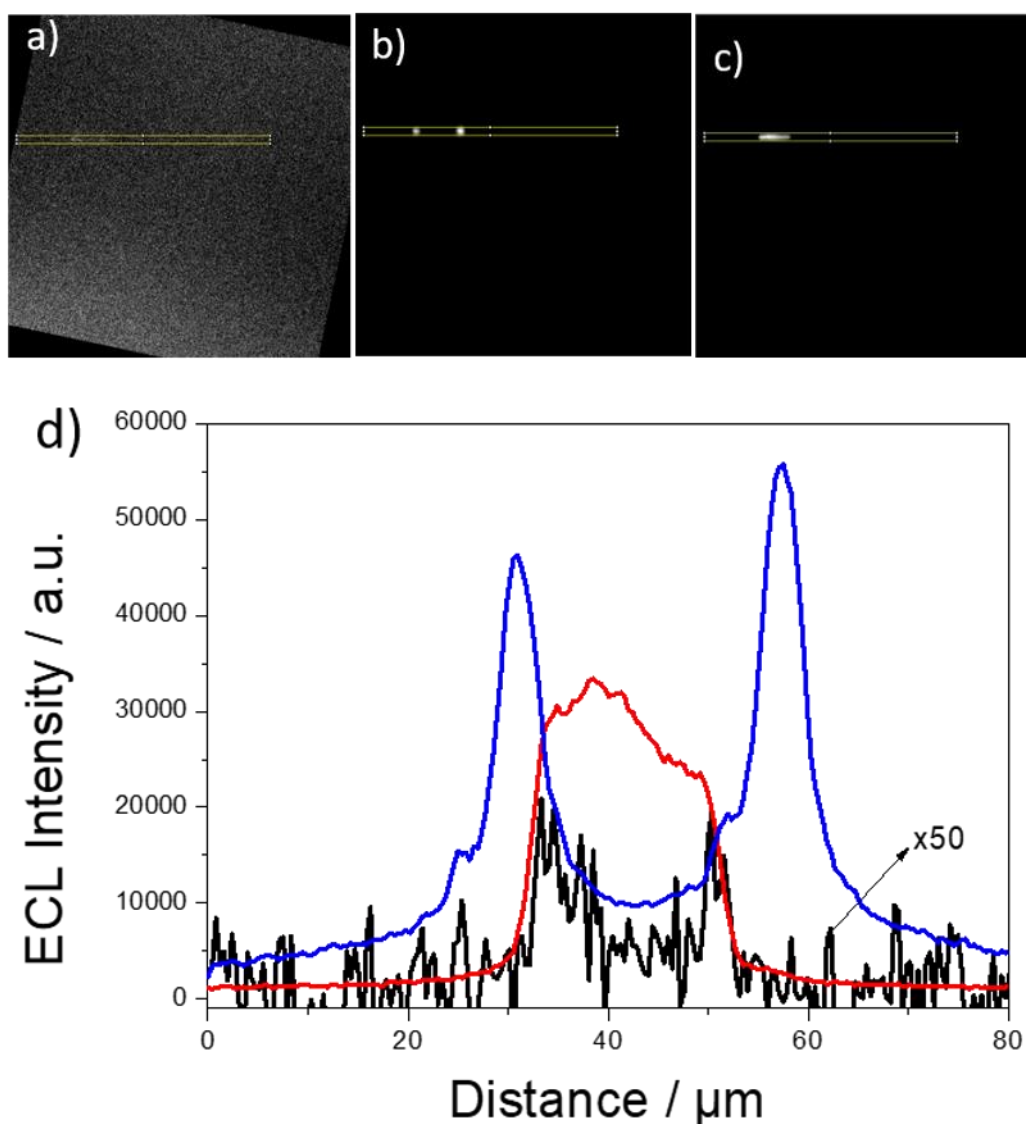


Figure 3.19 ECL emission for a) intermediate regime ($[\text{Ru}(\text{bpy})_3]^{2+}$ 10mM, TPA 0.1M, TBAPF_6 0.1M solution in CH_3CN , Bottom electrode (WE, -1.5 V), Top electrode (WE2, 2 V), Ag (QRE-CE)), b) coreactant mode ($[\text{Ru}(\text{bpy})_3]^{2+}$ 10mM, TPA 0.1M, TBAPF_6 0.1M solution in CH_3CN , Bottom electrode (WE, 2 V), Top electrode (WE2, 0 V), Ag (QRE-CE) and c) annihilation mode ($[\text{Ru}(\text{bpy})_3]^{2+}$ 10mM, TBAPF_6 0.1M solution in CH_3CN , Bottom electrode (WE, 2V), Top electrode (WE2, -1.5 V), Ag (QRE-CE)). d) Corresponding emission intensity profiles along the center of the nanochannel.

Concentration profile of $[\text{Ru}(\text{bpy})_3]^{2+*}$, corresponding to light emission intensity, (Fig. 3.20) was simulated by using COMSOL Multiphysics by Prof. Mathwig (Groningen University). Numerical simulations can give further insight into which coreactant pathway is dominant. Figure 3.20 reports a simulated emission profile for a coreactant reaction. In agreement with the experimental data, light is confined to the access holes. A numerical evaluation of both

possible coreactant mechanisms reveals that 30 % of light is contributed by $[\text{Ru}(\text{bpy})_3]^{2+}$ oxidation by TPA, and 70% by direct oxidation at the bottom electrode.

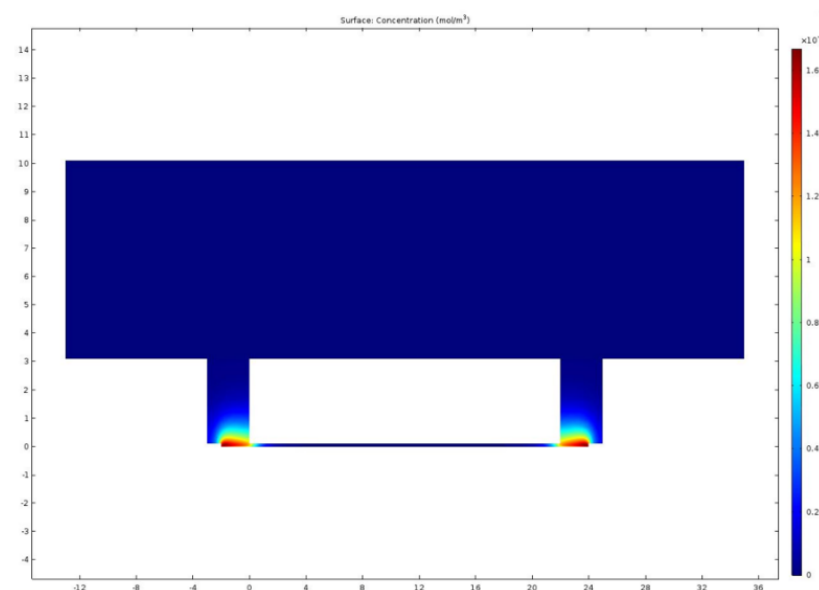


Figure 3.20 Two-dimensional finite element simulation of a cross section of a nanofluidic device. A large reservoir, access channel and a narrow nanochannel at the bottom are shown (skewed aspect ratio). Color indicates concentration of $[\text{Ru}(\text{bpy})_3]^{2+}$ luminophores corresponding to intensity of light emission ($[\text{Ru}(\text{bpy})_3]^{2+}$ 10 mM, TPA 0.1 M, TBAPF₆ 0.1 M in CH₃CN; Bottom electrode (WE1, 2V), Top electrode (WE2, 0 V), Ag (QRE-CE).

From the study of ECL at a nanometric scale, the discussion will move in the next paragraphs to the description of the ECL study at a micrometric scale, where ECL has been implemented as imaging technique for the temporal and spatial description of electrochemical processes occurring at the micropore restriction of a microfluidic system during a BPE experiments.

3.3 Enhanced bipolar electrochemistry at solid-state micropores

The coupling between BPE and ECL is a powerful approach. While BPE allows a spatial separation of two reacting poles of the bipolar electrode, ECL provides a sensitive optical detection.⁵⁴ The first application of ECL to a bipolar electrochemical system was reported in 2011 by Manz and coworkers.⁵⁵ The quantification of $[\text{Ru}(\text{bpy})_3]^{2+}$ by ECL was correlated with the indirect detection of a series of amino acids, dissolved in aqueous buffer solutions in a U-shaped Pt bipolar electrode positioned across a channel. Other studies combining ECL and BPE involved the detection of other biomolecules (*i.e.*, DNA, RNA, protein receptors, peptides, enzymatic substrates),⁵⁶ the motion of micrometric objects,⁵⁷ the recording of an optical voltammogram in the spatial domain.⁵⁸ In this work, ECL is applied as imaging technique to visualize a wireless confined polarization of a solid-state 20 μm long silicon pore integrated in a microfluidic channel.

3.3.1 Solid-State Micropore Description and Characterization

A microfluidic device integrating a single micropore and two Au feeder electrodes (Fig. 3.21) was designed and produced by top-down microfabrication steps onto *p*-type silicon substrates.

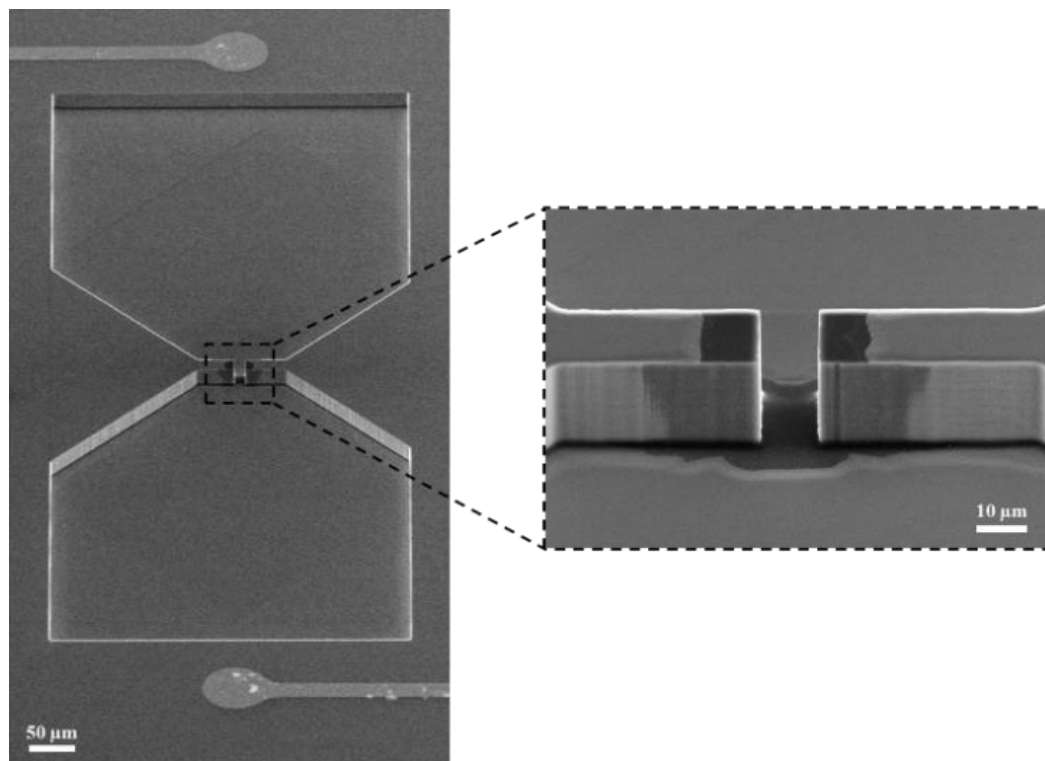


Figure 3.21 SEM images of the *p*-doped silicon microchip with the solid-state micropore and the integrated feeder Au electrodes. The deoxidized regions appear darker around the micropore. Pore dimensions: 20 μm (length) × 10 μm (width) × 20 μm (height).

The micropore patterns were transferred onto the silicon wafers by a photolithography step followed by reactive ion etching (Fig. 3.22). The dimensions of the pore were 20 μm (length) × 10 μm (width) × 20 μm (height). Both Au feeder electrodes (radius = 50 μm) were located at the extremities of the chip and separated by a center-to-center distance of 1.2 mm. These were patterned on an insulating 300-nm thick SiO₂ layer that covers the entire silicon surface at this fabrication stage. The thick SiO₂ layer also prevented electron-transfer reactions between the silicon electrode material and the redox species dissolved in solution due to the wide band gap energy of SiO₂ layer, nearly 9 eV. To form the bipolar electrode at the level of the micropore, the insulating SiO₂ layer was selectively etched only in this region with buffered hydrofluoric acid. This etching step may allow locally the electron-transfer reactions to occur in this deoxidized region, which constitutes the bipolar electrode. It appears darker on the SEM images

(Fig. 3.21) due to the difference in conductivity and accumulation of charges. At higher magnifications, it is possible to observe that the deoxidized region is located mainly within the micropore but that it also extends slightly beyond the micropore and on the top of it (Fig. 3.21).

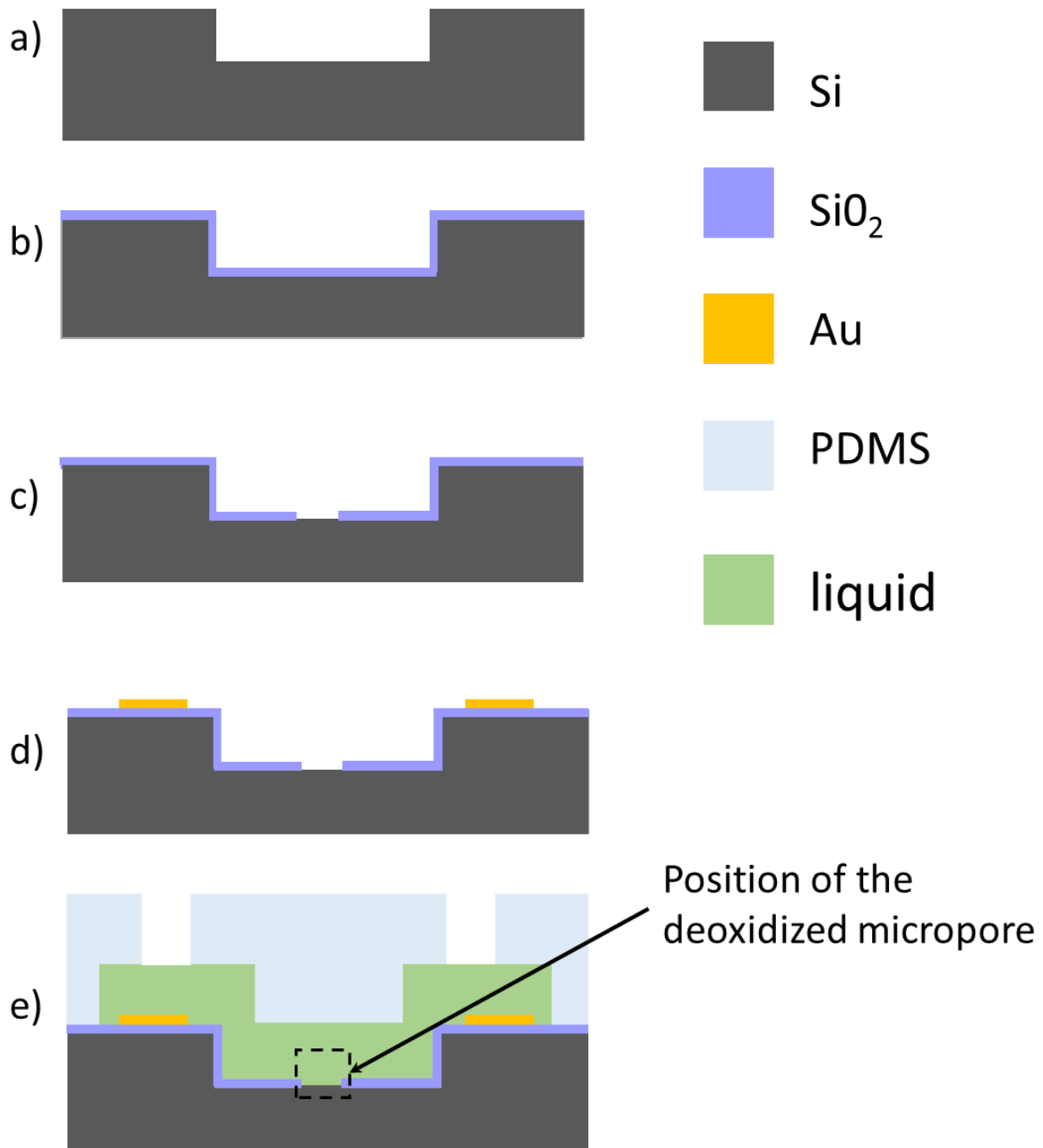


Figure 3.22 Fabrication process flow of the silicon microchip. a) Micropore fabrication onto the silicon wafer by photolithography followed by reactive ion etching. b) Dry thermal oxidation of the silicon wafer to grow 300 nm of SiO₂. c) Deoxidation of silicon by wet-etching with buffered oxide etchant. d) Patterning of metal electrodes by photolithography and wet etching techniques. . e) Enclosing the fluidic channel with a micromolded PDMS slab. f) Filling the fluidic channel with PBS solution. The scheme is not to scale.

Finally, the silicon microchip was covered with a thin PDMS mold that was specifically designed. It was aligned on top of the silicon chip (Fig. 3.22). Therefore, the oxidized region located at the top of the micropore walls was not in contact with the solution. It means that only the bottom of the micropore and the side walls can be polarized and may become electroactive. In addition, the PDMS layer is transparent and allows light transmission during ECL experiments.

The device design and fabrication was completely developed by Dr. Bouchet-Spinelli and Dr. Ismail (University of Grenoble Alpes) and Dr. Maziz and Dr. Leichlé (LAAS, Toulouse University).

3.3.2 ECL analysis

The ECL experiments were performed with a model light-emitting system consisting of $[\text{Ru}(\text{bpy})_3]^{2+}$ and TPA as the luminophore and the sacrificial coreactant, respectively. Both were dissolved in PBS solution (pH = 7.4). ECL experiments were initially performed with the *p*-type silicon substrate using cyclic voltammetry. However, the ECL signals were not stable under this conditions. This was due to the formation of an insulating SiO_2 layer grown electrochemically on the silicon that inhibits the electron-transfer reactions.⁵⁹ However, by pulsing the potential of the Au feeder electrodes, a stable ECL signal was recorded with an EMCCD camera. ECL emission was detected starting from a pulsed potential application at the Au feeder electrodes of +7 V. This polarization voltage was strong enough to induce simultaneously both redox reactions at the extremities of the micropore: oxidation of ECL reagents at the anodic pole and reduction of water at the cathodic pole (Fig. 3.23). An object of similar dimensions (i.e. a 30- μm glassy carbon beads) required a potential difference of 1 kV to trigger ECL emission, extremely higher than 7 V voltage needed for this peculiar micropore configuration.^{57c} Therefore, such an approach permits to drive the bipolar ECL reactions with a potential difference that is more than two orders of magnitude lower compared to a classic BPE setup.

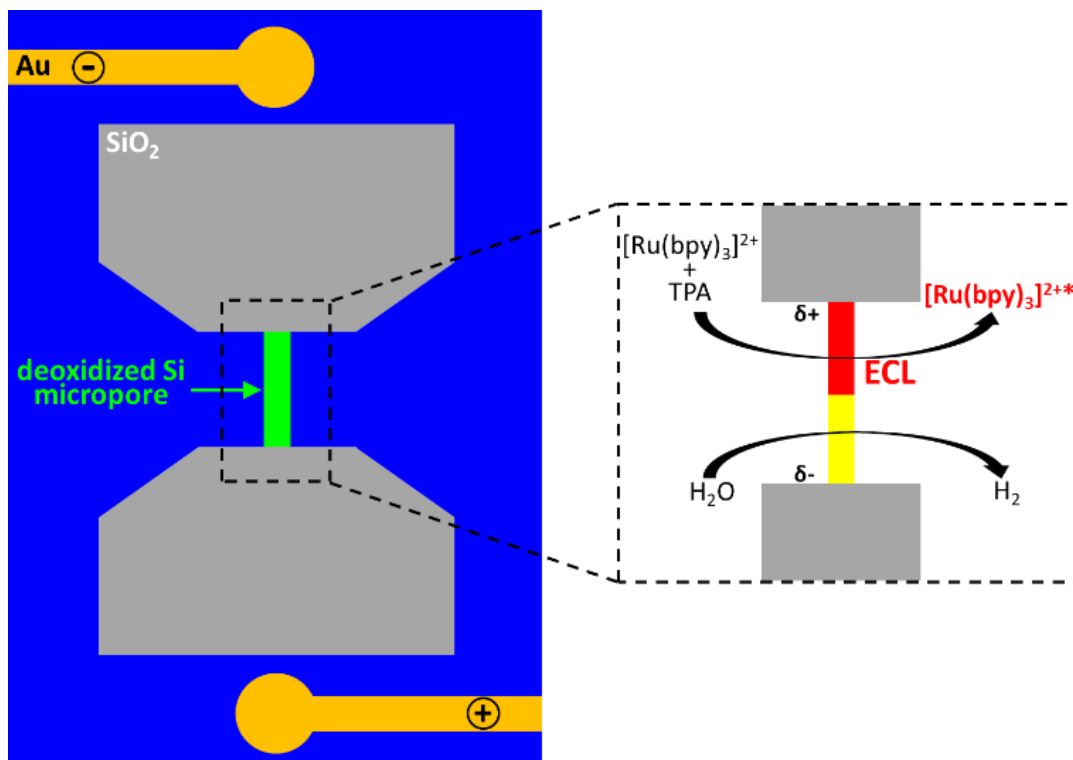


Figure 3.23 Bipolar light-emitting micropore with the asymmetric redox reactions. Left: schematic principle of the silicon micropore with the deoxidized region (green) and the Au feeder electrodes. Right: simultaneous reduction of water at the cathodically-polarized region (yellow) and oxidation of ECL reagents at the anodically-polarized region (red) leading to ECL light emission in the micropore.

By increasing progressively the potential difference, ECL raised and reached its maximum at 10 V (Fig. 3.24).

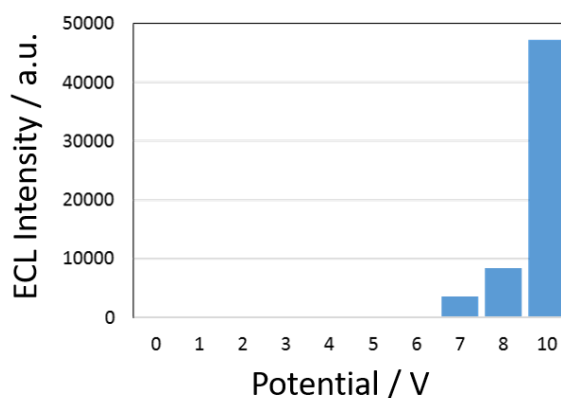


Figure 3.24 Variation of the ECL intensity generated at the level of the silicon micropore as a function of the potential applied to the Au feeder electrodes.

Higher voltages lead to a massive formation of gas bubbles at the anode and cathode feeder electrodes, which breaks the electrolytic continuity of the solution in the microfluidic chip.

Thus, a compromise value of 10 V was selected for the bias potential, which is high enough to produce strong ECL, but low enough to avoid the substantial production of gas bubbles. The optimal conditions to obtain a stable and strong ECL intensity with such deoxidized silicon chips were to pulse rapidly the potential from 0 V to 10 V for 300 ms, with a rest potential of 0 V for 100 ms (Fig. 3.25).

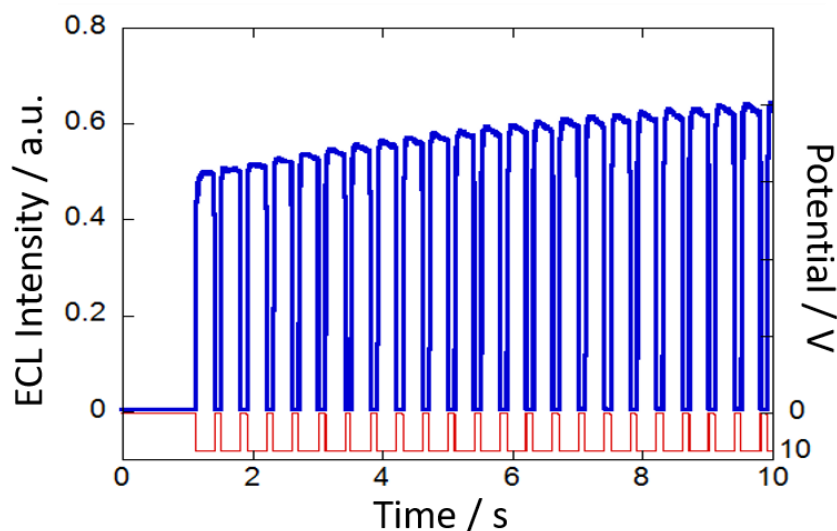


Figure 3.25 ECL intensity (blue curve) as a function of successive pulses from 0 to 10 V (red curve) applied to the Au feeder electrodes.

ECL intensity increased slightly during successive pulses. For short experiments, the passivation of the silicon surface with the generation of a SiO_2 layer is slower with the pulse technique in comparison to the voltammetric one. Such phenomenon could be directly related with a lower decay of the $[\text{Ru}(\text{bpy})_3]^{2+}$ and TPA concentrations in competition with silicon oxidation. Since silicon is not an usual electrode surface for ECL generation,⁶⁰ ECL spectra of the $[\text{Ru}(\text{bpy})_3]^{2+}$ /TPA solution with *p*-silicon and with a classic GC electrode were recorded (Fig. 3.26).

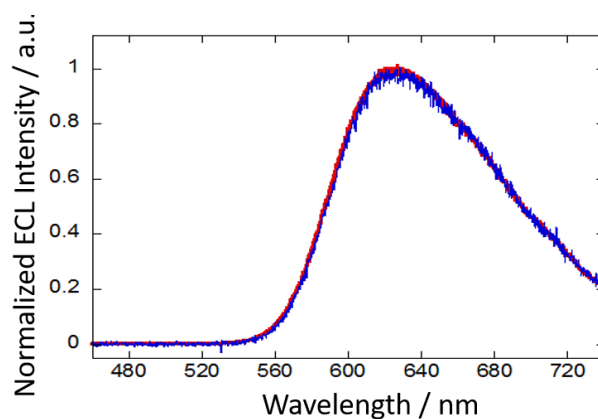


Figure 3.26 Comparison of the ECL spectra recorded on a glassy carbon electrode (red curve) and on home-made p-type Si electrode (blue curve). The composition of the PBS solution (pH 7.4) was 1 mM $[\text{Ru}(\text{bpy})_3]^{2+}$ and 50 mM TPA.

Both spectra are identical, indicating that the same MLCT (metal-to-ligand-charge-transfer) excited state $[\text{Ru}(\text{bpy})_3]^{2+*}$ was reached on both electrode materials.

3.3.3 ECL imaging

ECL imaging represents a powerful tool for the investigation of the distribution of the polarization at the level of the bipolar electrode. Indeed, the localization and the spatial extension of the ECL-emitting zone reflect the current density at the bipolar electrode and thus its local polarization.^{58,61} The channels were filled with the PBS solution containing $[\text{Ru}(\text{bpy})_3]^{2+}$ and TPA. Figure 3.27 shows the photoluminescence (PL) and ECL images of the same region of interest.

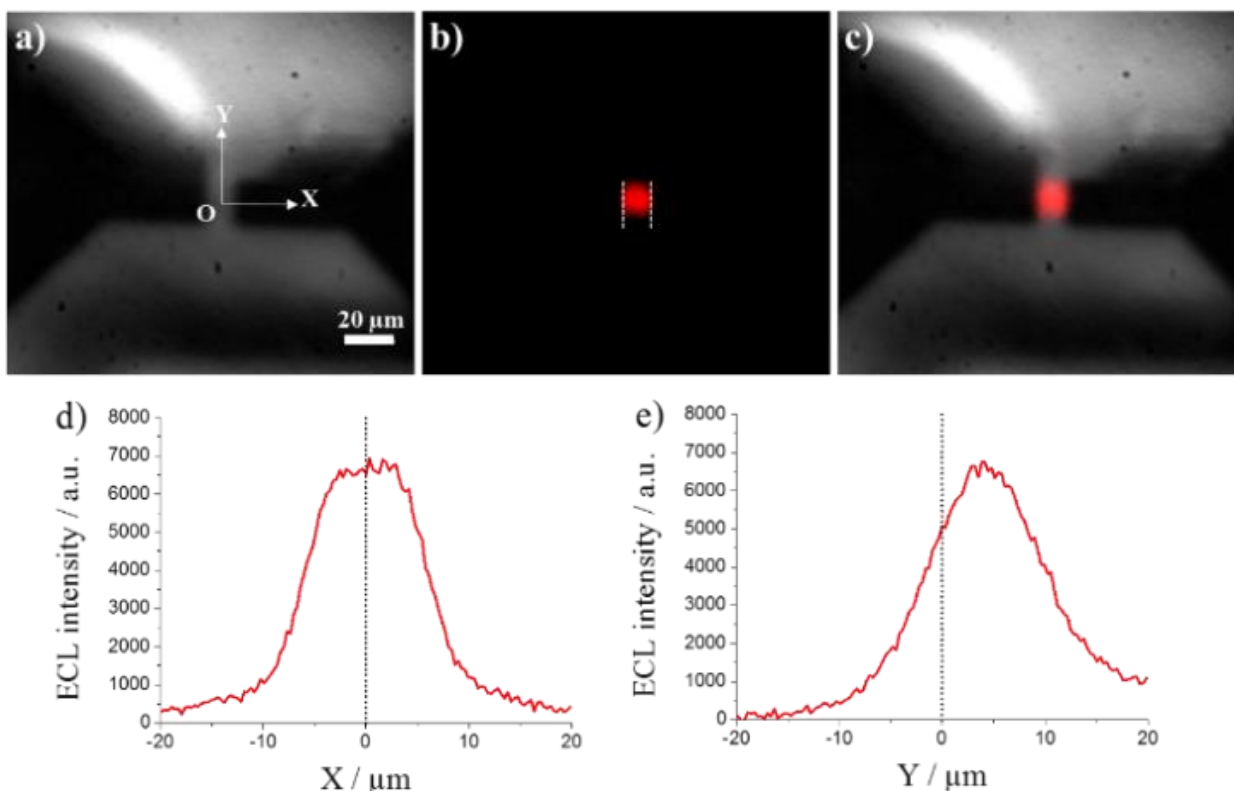


Figure 3.27 PL (a), ECL (b) and overlay (c) of both luminescence images of the same region of interest around the micropore. Both axis are represented and the origin O of the axis is defined as the center of the micropore. The dashed lines materialize the micropore walls. ECL profiles of the intensity along the X (d) and Y-axis (e) in the micropore. ECL was recorded in PBS (pH 7.4) containing 1 mM $[\text{Ru}(\text{bpy})_3]^{2+}$ and 50 mM TPA by applying potential pulses of 10 V for 0.3 s.

PL image (Fig. 3.27, a) shows, because of the PL of $[\text{Ru}(\text{bpy})_3]^{2+}$, the silicon chip with the micropore located in its middle. This PL image allows precisely defining the position of the micropore. As represented on Fig. 3.27 a), the center of the micropore was taken as the origin of both X- and Y-axis. The ECL experiment did not show any light emission before applying sufficiently high potential pulses (*i.e.*, 7 V). By imposing short pulses of 10 V, light emission from the microfabricated silicon chip was intense enough to be visible with the naked eyes and recorded through the PDMS layer with an EMCCD camera (Fig. 3.27, b). The ECL emitting region was observed and was confined in the micropore (Fig. 3.27, c).

The ECL intensity profiles extracted along both axis gave a clear picture of the electrochemical behavior in the micropore. The ECL emission is constant along X-axis (Fig. 3.27, d). Full-width-at-half-maxima of lateral (X) and longitudinal (Y) intensity profiles are 12 μm and 11 μm , respectively. The lateral 12- μm value corresponds approximately to the width of the micropore (*i.e.* 10 μm). Presumably, the optical resolution of the 50x objective coupled to the

inhomogeneous transparency of the PDMS layer as well as the contribution of the micropore walls lead to a slightly wider profile than expected. The longitudinal ECL profile shows that ECL emitting region extends over a distance of $\sim 11 \mu\text{m}$, which is almost half of the micropore length ($20 \mu\text{m}$). Furthermore, a detailed analysis of the overlay image (Fig. 3.27, c) and of the ECL profile (Fig. 3.27, e) revealed that the ECL region was not centered along the micropore. Indeed, the ECL emission occurs in the anodic part of the micropore. This corresponds to the zone in front of the feeder cathode. The deoxidized silicon is polarized anodically in this region and oxidation of both ECL reagents takes place, which leads locally to the ECL emission (Fig. 3.23). Therefore, ECL emission is confined to a region corresponding to about half of the micropore.

3.3.4 Simulations

To study the BPE behavior at the micropore level, the electrical potential distribution was calculated by numerical simulations by Dr. Pascale Pham (CEA-LETI, Minatec Campus, Grenoble).

In a classic BPE configuration (i.e. without pore), the potential varies linearly between both feeder electrodes, considering the electric double layer as negligible (Fig. 3.28, b blue curve).

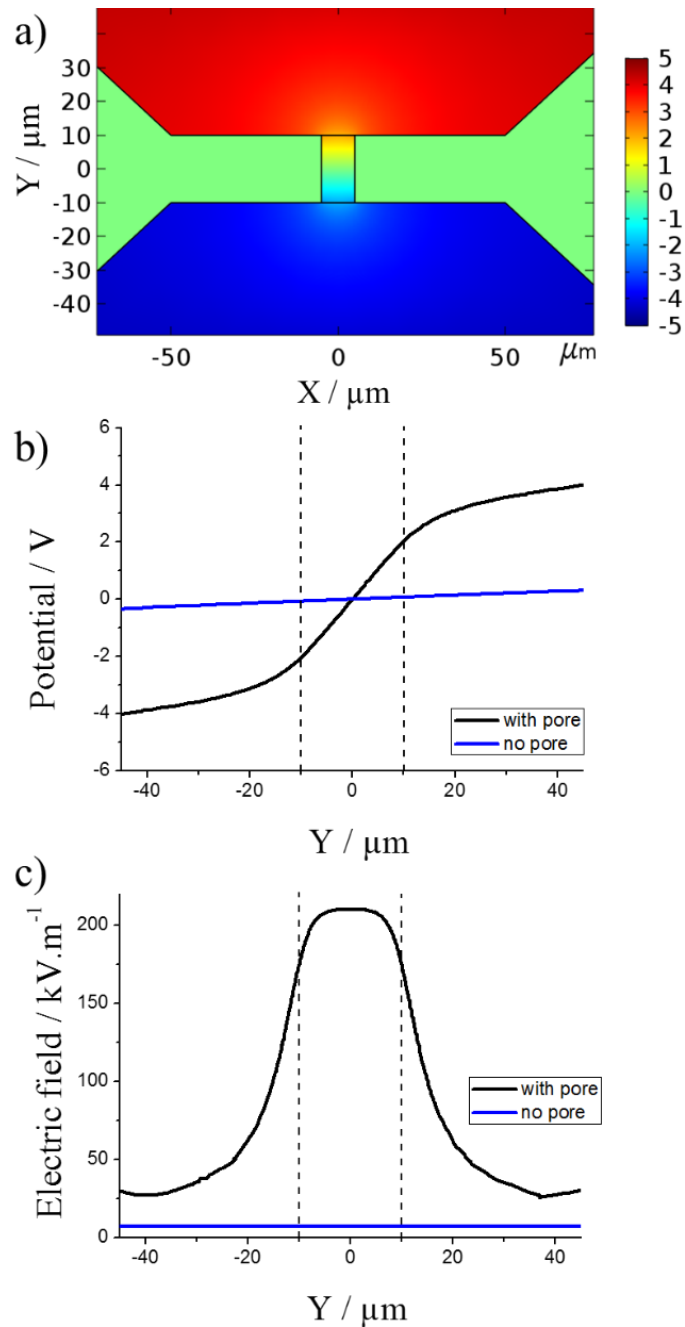


Figure 3.28 (a) Numerical simulation of the electric potential distribution around the micropore. The image was coded according to the color scale of the potential (right). Red and blue colors represent +5 V and -5 V, respectively. Corresponding (b) potential profiles and (c) norms of the electric field along the Y-axis passing in the center of the micropore (black line). Blue line represents the simulations of the microchip without micropore. Dashed lines indicate the position of the 20 μm long micropore.

In the presence of the micropore restriction, a large part of the potential drop occurs in the micropore (Fig. 3.28). A detailed analysis shows that the potential drop is 4.1 V at the level of the 20- μm -long micropore, whereas this value decreases to just 0.14 V without it (Fig. 3.28, b). The potential drop reaches 80 % at $\pm 50 \mu\text{m}$ of the micropore center due to the additional effect

of the PDMS channel restriction (Fig. 3.28, b). This highly localized potential drop in the micropore results from the combination of both the silicon micropore and the microfluidic restriction made of PDMS. A reduction of both the width and the height of the restriction (such as with nanopores) could cause a stronger effect.⁶² As previously discussed, the electric field represents the pertinent experimental parameter, which governs the electrochemical behavior of a bipolar electrode. Figure 3.28 c) displays the norm of the electric field in both configurations (*i.e.* with and without micropore) and shows that its strength is enhanced in presence of the micropore. Indeed, the electric field increases drastically at the level of the micropore reaching 208 kVm^{-1} whereas it remains at a constant value of 7 kVm^{-1} without the micropore geometry (Fig. 3.28, c and Fig. 3.29)

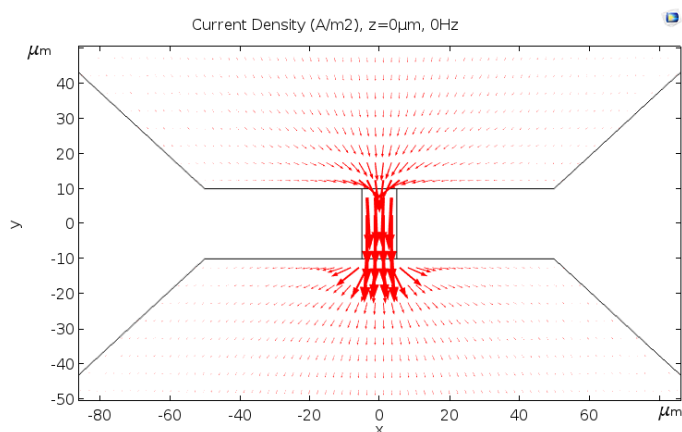


Figure 3.29 Top-view of the current density vectors in the vicinity of the micropore.

These results illustrate the nonlinear electric field distribution in case of a variable geometry of the micropore and of the PDMS microfluidic channel. The simulation shows the importance of the design of the micropore as well as of the PDMS channels to concentrate the potential drop selectively at the micropore level. Therefore, a lower bias potential is required to polarize the micropore and to trigger ECL emission locally.

3.4 Conclusions

Microfabricated nanofluidic electrochemical devices offer a highly controlled nanochannel geometry; they confine the volume of chemical reactions to the nanoscale and enable greatly amplified electrochemical detection. For the first time, ECL-emission was investigated in transparent nanofluidic devices. In annihilation reaction pathway, light emission occurred inside the nanochannel, when both electrodes were biased at appropriate potentials. Such conditions permit light emission enhancement in two ways: first, the close vicinity of the two electrodes leads to efficient annihilation reactions due to very short diffusive paths. Second, stable light

emission is achieved as the very short diffusive distances protect from degradation by contaminants. The results indicate that ECL annihilation measurements in nanodevices are possible under ambient conditions, which cannot be achieved using classical setups.

ECL annihilation pathway inside the nanochannel was then compared with ECL via coreactant pathway, by using the ECL system $[\text{Ru}(\text{bpy})_3]^{2+}/\text{TPA}$. ECL imaging highlights that in the case of ECL via coreactant, ECL emission occurs, confined to the access holes of the nanochannel. Light emission cannot reach the nanochannel, due to the limited lifetimes of coreactant electrogenerated radicals. Finally, an intermediate condition was investigated, in which a solution of luminophores and coreactants undergoes an annihilation reaction. ECL emission occurs inside the nanochannel, with an intensity lower than in the case of pure ECL annihilation. The presence of TPA limits the efficiency of ECL annihilation reactions by adding a second route and increasing the concentration of byproducts.

Thanks to the properties of exact control of an inter-electrode distance, a highly reproducible device geometry and strong confinement of analytes in the channel volume, microfabricated nanochannels permit to investigate pathways in ECL, to exploit their unique nanometric properties to develop new nanoconfined analytical systems, as multicolor ECL emission systems.³⁹

In the second investigated confined ECL system, a specific design of a solid-state 20 μm long silicon pore integrated in a microfluidic channel and of the model coreactant ECL system $[\text{Ru}(\text{bpy})_3]^{2+}/\text{TPA}$ enabled wireless polarization of micrometric deoxidized silicon electrode at much lower potentials (+7 V) than in a classic BPE setup was demonstrated. The micropore was fabricated inside silicon by microstructuring and it represents the restriction of a larger microfluidic channel. The potential drop was confined within the pore where the deoxidized silicon electrode is located. Indeed, the etched silicon walls of the micropore act as the bipolar electrodes. ECL was used as an imaging method, since the ECL intensity correlates with the current density at the bipolar electrode and thus is directly related to its local polarization. ECL imaging allowed to visualize the light distribution at the micropore level, resulting from the oxidation of the ECL reagents, $[\text{Ru}(\text{bpy})_3]^{2+}/\text{TPA}$. Such single wireless ECL micropore paves the way for the development of original analytical applications such as cell capturing coupled with ECL detection.

References

- (1) a) Leszczyszyn, D. J.; Jankowski, J. A.; Viveros, O. H.; Diliberto, E. J.; Near, J. A.; Wightman, R. M. *Journal of Biological Chemistry* **1990**, *265*, 14736; b) Finnegan, J. M.; Borges, R.; Wightman, R. M. *Neuroscience* **1996**, *71*, 833.
- (2) a) Li, X.; Dunevall, J.; Ewing, A. G. *Accounts of Chemical Research* **2016**, *49*, 2347; b) Bucher, E. S.; Wightman, R. M. *Annual Reviews of Analytical Chemistry (Palo Alto Calif)* **2015**, *8*, 239.
- (3) Fan, F.-R. F.; Bard, A. J. *Science* **1995**, *267*, 871.
- (4) Baker, L. A. *Journal of the American Chemical Society* **2018**, *140*, 15549.
- (5) Lemay, S. G.; Kang, S.; Mathwig, K.; Singh, P. S. *Accounts of Chemical Research* **2013**, *46*, 369.
- (6) Bard, A. J.; Fan, F.-R. F.; Pierce, D. T.; Unwin, P. R.; Wipf, D. O.; Zhou, F. *Science* **1991**, *254*, 68.
- (7) White, H. S.; McKelvey, K. *Current Opinion in Electrochemistry* **2018**, *7*, 48.
- (8) Kai, T.; Zhou, M.; Duan, Z.; Henkelman, G. A.; Bard, A. J. *Journal of the American Chemical Society* **2017**, *139*, 18552.
- (9) Schulte, A.; Nebel, M.; Schuhmann, W. *Annual Review of Analytical Chemistry* **2010**, *3*, 299.
- (10) a) Wang, Q.; Rodríguez-López, J.; Bard, A. J. *Journal of the American Chemical Society* **2009**, *131*, 17046; b) Bard, A. J. *Journal of the American Chemical Society* **2010**, *132*, 7559.
- (11) Kang, S.; Mathwig, K.; Lemay, S. G. *Lab on a Chip* **2012**, *12*, 1262.
- (12) a) Niwa, O.; Xu, Y.; Halsall, H. B.; Heineman, W. R. *Analytical Chemistry* **1993**, *65*, 1559; b) Kätelhön, E.; Hofmann, B.; Lemay, S. G.; Zevenbergen, M. A. G.; Offenhäusser, A.; Wolfrum, B. *Analytical Chemistry* **2010**, *82*, 8502.
- (13) Bentley, C. L.; Kang, M.; Unwin, P. R. *Journal of the American Chemical Society* **2017**, *139*, 16813.
- (14) Rassaei, L.; Singh, P. S.; Lemay, S. G. *Analytical Chemistry* **2011**, *83*, 3974.
- (15) Zevenbergen, M. A. G.; Singh, P. S.; Goluch, E. D.; Wolfrum, B. L.; Lemay, S. G. *Nano Letters* **2011**, *11*, 2881.
- (16) Ma, C.; Xu, W.; Wichert, W. R. A.; Bohn, P. W. *ACS Nano* **2016**, *10*, 3658.
- (17) Rassaei, L.; Mathwig, K.; Kang, S.; Heering, H. A.; Lemay, S. G. *ACS Nano* **2014**, *8*, 8278.
- (18) Quinn, B. M.; van't Hof, P. G.; Lemay, S. G. *Journal of the American Chemical Society* **2004**, *126*, 8360.
- (19) Guo, Z.; Percival, S. J.; Zhang, B. *Journal of the American Chemical Society* **2014**, *136*, 8879.
- (20) Kwon, S. J.; Fan, F.-R. F.; Bard, A. J. *Journal of the American Chemical Society* **2010**, *132*, 13165.
- (21) Ying, Y.-L.; Gao, R.; Hu, Y.-X.; Long, Y.-T. *Small Methods* **2018**, *2*, 1700390.
- (22) Deamer, D. W.; Branton, D. *Accounts of Chemical Research* **2002**, *35*, 817.
- (23) Kasianowicz, J. J.; Brandin, E.; Branton, D.; Deamer, D. W. *Proceedings of the National Academy of Sciences* **1996**, *93*, 13770.
- (24) Johnson, R. P.; Fleming, A. M.; Perera, R. T.; Burrows, C. J.; White, H. S. *Journal of the American Chemical Society* **2017**, *139*, 2750.
- (25) Edwards, M. A.; German, S. R.; Dick, J. E.; Bard, A. J.; White, H. S. *ACS Nano* **2015**, *9*, 12274.

- (26) Iqbal, S. M.; Akin, D.; Bashir, R. *Nature Nanotechnology* **2007**, *2*, 243.
- (27) a)Asghar, W.; Wan, Y.; Ilyas, A.; Bachoo, R.; Kim, Y.-t.; Iqbal, S. M. *Lab on a Chip* **2012**, *12*, 2345; b)Ilyas, A.; Asghar, W.; Kim, Y.-t.; Iqbal, S. M. *Biosensors and Bioelectronics* **2014**, *62*, 343.
- (28) Lin, Y.; Ying, Y.-L.; Shi, X.; Liu, S.-C.; Long, Y.-T. *Chemical Communications* **2017**, *53*, 11564.
- (29) Lin, Y.; Ying, Y.-L.; Long, Y.-T. *Current Opinion in Electrochemistry* **2018**, *7*, 172.
- (30) a)Mavr e, F.; Anand, R. K.; Laws, D. R.; Chow, K.-F.; Chang, B.-Y.; Crooks, J. A.; Crooks, R. M. *Analytical Chemistry* **2010**, *82*, 8766; b)Kostiuchenko, Z. A.; Zhang, B.; Lemay, S. G. *The Journal of Physical Chemistry C* **2016**, *120*, 22777.
- (31) a)Chow, K.-F.; Mavr e, F.; Crooks, J. A.; Chang, B.-Y.; Crooks, R. M. *Journal of American Chemical Society* **2009**, *131*, 8364; b)Sentic, M.; Arbault, S.; Bouffier, L.; Manojlovic, D.; Kuhn, A.; Sojic, N. *Chemical Science* **2015**, *6*, 4433; c)Gao, J. *Current Opinion in Electrochemistry* **2018**, *7*, 87; d)Gao, J.; Chen, S.; AlTal, F.; Hu, S.; Bouffier, L.; Wantz, G. *ACS Applied Materials & Interfaces* **2017**, *9*, 32405.
- (32) Loget, G.; Zigah, D.; Bouffier, L.; Sojic, N.; Kuhn, A. *Accounts of Chemical Research* **2013**, *46*, 2513.
- (33) Ismail, A.; Voci, S.; Pham, P.; Leroy, L.; Maziz, A.; Descamps, L.; Kuhn, A.; Mailley, P.; Livache, T.; Buhot, A.; Leichl e, T.; Bouchet-Spinelli, A.; Sojic, N. *Analytical Chemistry* **2019**.
- (34) a)Loget, G.; Roche, J.; Kuhn, A. *Advanced Materials* **2012**, *24*, 5111; b)Warakulwit, C.; Nguyen, T.; Majimel, J.; Delville, M.-H.; Lapeyre, V.; Garrigue, P.; Ravaine, V.; Limtrakul, J.; Kuhn, A. *Nano Letters* **2008**, *8*, 500.
- (35) Rutkowska, A.; Freedman, K.; Skalkowska, J.; Kim, M. J.; Edel, J. B.; Albrecht, T. *Analytical Chemistry* **2015**, *87*, 2337.
- (36) Mathwig, K.; Aartsma, T. J.; Canters, G. W.; Lemay, S. G. *Annual Review of Analytical Chemistry* **2014**, *7*, 383.
- (37) Brasiliense, V.; Berto, P.; Combellas, C.; Tessier, G.; Kanoufi, F. *Accounts of Chemical Research* **2016**, *49*, 2049.
- (38) Chang, Y.-L.; Palacios, R. E.; Fan, F.-R. F.; Bard, A. J.; Barbara, P. F. *Journal of the American Chemical Society* **2008**, *130*, 8906.
- (39) Al-Kutubi, H.; Voci, S.; Rassaei, L.; Sojic, N.; Mathwig, K. *Chemical Science* **2018**, *9*, 8946.
- (40) Bard, A. J. *Electrogenerated Chemiluminescence*; M. Dekker: New-York, 2004.
- (41) Forster, R. J.; Bertoncello, P.; Keyes, T. E. *Annual Review of Analytical Chemistry* **2009**, *2*, 359.
- (42) Santhanam, K. S. V.; Bard, A. J. *Journal of the American Chemical Society* **1965**, *87*, 139.
- (43) Maloy, J. T.; Bard, A. J. *Journal of the American Chemical Society* **1971**, *93*, 5968.
- (44) a)Bartlet, J. E.; Drew, S. M.; Wightman, R. M. *Journal of Electrochemical Society* **1992**, *139*, 70; b)Fiaccabrino, G. C.; Koudelka-hep, M.; Hsueh, Y.-T.; Collins, S. D.; Smith, R. L. *Analytical Chemistry* **1998**, *70*, 4157; c)Amatore, C.; Fosset, B.; Maness, K. M.; Wightman, R. M. *Analytical Chemistry* **1993**, *65*, 2311; d)Amatore, C.; Pebay, C.; Servant, L.; Sojic, N.; Szunerits, S.; Thouin, L. *ChemPhysChem* **2006**, *7*, 1322.
- (45) a)Fan, F.-R. F.; Cliffel, D.; Bard, A. J. *Analytical Chemistry* **1998**, *70*, 2941; b)Rodr guez-L pez, J.; Shen, M.; Nepomnyashchii, A. B.; Bard, A. J. *Journal of the American Chemical Society* **2012**, *134*, 9240.

- (46) Shen, M.; Arroyo-Currás, N.; Bard, A. J. *Analytical Chemistry* **2011**, *83*, 9082.
- (47) Kapturkiewicz, A.; Angulo, G. *Dalton Transactions* **2003**, 3907.
- (48) Mampallil, D.; Mathwig, K.; Kang, S.; Lemay, S. G. *Analytical Chemistry* **2013**, *85*, 6053.
- (49) Kätelhön, E.; Krause, K. J.; Mathwig, K.; Lemay, S. G.; Wolfrum, B. *ACS Nano* **2014**, *8*, 4924.
- (50) Bae, J. H.; Han, J.-H.; Han, D.; Chung, T. D. *Faraday Discussions* **2013**, *164*, 361.
- (51) Kang, S.; Nieuwenhuis, A. F.; Mathwig, K.; Mampallil, D.; Lemay, S. G. *ACS Nano* **2013**, *7*, 10931.
- (52) Miao, W.; Choi, J.-P.; Bard, A. J. *Journal of the American Chemical Society* **2002**, *124*, 14478.
- (53) Richter, M. M. *Chemical Reviews* **2004**, *104*, 3003.
- (54) Bouffier, L.; Manojlovic, D.; Kuhn, A.; Sojic, N. *Current Opinion in Electrochemistry* **2019**, *16*, 28.
- (55) Arora, A.; Eijkel, J. C. T.; Morf, W. E.; Manz, A. *Analytical Chemistry* **2001**, *73*, 3282.
- (56) a) Fosdick, S. E.; Knust, K. N.; Scida, K.; Crooks, R. M. *Angewandte Chemie International Edition* **2013**, *52*, 10438; b) Wu, M.-S.; Qian, G.-s.; Xu, J.-J.; Chen, H.-Y. *Analytical Chemistry* **2012**, *84*, 5407.
- (57) a) Eßmann, V.; Voci, S.; Loget, G.; Sojic, N.; Schuhmann, W.; Kuhn, A. *The Journal of Physical Chemistry Letters* **2017**, *8*, 4930; b) Sentic, M.; Arbault, S.; Goudeau, B.; Manojlovic, D.; Kuhn, A.; Bouffier, L.; Sojic, N. *Chemical Communications* **2014**, *50*, 10202; c) Sentic, M.; Loget, G.; Manojlovic, D.; Kuhn, A.; Sojic, N. *Angewandte Chemie International Edition* **2012**, *51*, 11284.
- (58) Chang, B.-Y.; Mavré, F.; Chow, K.-F.; Crooks, J. A.; Crooks, R. M. *Analytical Chemistry* **2010**, *82*, 5317.
- (59) Pliskin, W. A. *Journal of Vacuum Science and Technology* **1977**, *14*, 1064.
- (60) Valenti, G.; Fiorani, A.; Li, H.; Sojic, N.; Paolucci, F. *ChemElectroChem* **2016**, *3*, 1990.
- (61) Wood, M.; Zhang, B. *ACS Nano* **2015**, *9*, 2454.
- (62) a) Gao, R.; Ying, Y.-L.; Hu, Y.-X.; Li, Y.-J.; Long, Y.-T. *Analytical Chemistry* **2017**, *89*, 7382; b) Ying, Y.-L.; Hu, Y.-X.; Gao, R.; Yu, R.-J.; Gu, Z.; Lee, L. P.; Long, Y.-T. *Journal of the American Chemical Society* **2018**, *140*, 5385.

IV. Surface-Confined ECL Microscopy of Cellular Membranes

4.1 Introduction

The implementation of ECL as imaging technique for the detection of analytes and electrochemical processes description by optical readout has rapidly evolved from a laboratory curiosity to a powerful analytical technique featured with high sensitivity and selectivity.

Compared with fluorescence microscopy, ECL does not require photo-excitation, avoiding background from scattered light or sample auto-fluorescence. Although SECM represents the classic imaging approach for studies of spatially resolved electrochemical processes, the use of scanning electrodes limits its temporal resolution. ECL imaging is characterized by a high temporal resolution and an improved spatial resolution, still lower than the submicrometer plasmonic-based electrochemical microscopy resolution but with a higher sensitivity.¹ The first electrochemical step allows a precise control on the time and the position of the light-emitting step, as ECL emission occurs close to the electrode surface concomitantly with potential application.²

The experimental apparatus for ECL imaging is quite simple and easily adjustable. It is composed by an epifluorescence microscope, an electrical energy supply and an electron-multiplying charge-coupled device (EMCCD) for image recording.³ In the last years, the improvement in numerical aperture objectives, in light transduction pathways and recording devices has permitted the detection of luminescence coming from a limited amount of photons, as usual in ECL experiments.¹ In ECL imaging, both annihilation and coreactant pathways have been reported. However, the annihilation pathway presents important limitations related with the necessity of aprotic environment and drastic experimental conditions.⁴

The majority of signal generation systems is based on the oxidative-reduction mechanism with TPA as a sacrificial coreactant and $[\text{Ru}(\text{bpy})_3]^{2+}$ or its derivatives as a luminophore. It is due to the fact that this mechanism allows the generation of ECL in heterogeneous systems and presents high ECL performances.⁵

The first investigations on ECL imaging were conducted by Engstrom and coworkers for the study of electrodes heterogeneity and kinetics at a quantitative level.⁶ ECL was generated by using different ECL luminophores (as rubrene, $[\text{Ru}(\text{bpy})_3]^{2+}$, and 5-amino-2,3-dihydro-1,4-phthalazinedione, also called luminol) at surface-modified carbon electrodes. A submicrometer resolution was achieved. Bard⁷ and Amatore⁸ combined ECL with microscopy, for spatial resolution concentration profiles of species generated in the proximity of microelectrodes surface.

The ECL signal is linearly proportional to the concentration of both luminophore and coreactant. By attaching the luminophore to a sensing element of interest (protein, DNA, antibodies, *etc.*), ECL can be used as a robust sensing methodology. In addition, the imaging readout enables to spatially resolve the light distribution from different electrode regions.^{1,5} Recently, ECL imaging has been applied to the detection of glucose, lactate and choline by using a biosensor array.⁹ Indeed, $[\text{Ru}(\text{bpy})_3]^{2+}$ can be linked to proteins and together with luminol can be applied to ECL imaging for enzymatic activities measurements. NADH (nicotinamide adenosine dinucleotide), the reduced form of the dehydrogenase coenzyme, may generate ECL in presence of $[\text{Ru}(\text{bpy})_3]^{3+}$.¹⁰ This ECL system allows the detection of many species that are of great interest in bioanalytical chemistry, by coupling them to dehydrogenase enzymes. The ECL system luminol can rather react with hydrogen peroxide, used as coreactant, for monitoring activity of oxidases enzymes (which produce hydrogen peroxide in presence of specific substrate), oxidative stress and for detecting reactive oxygen species.¹¹ Several amplifications strategies are implemented to increase the signal-to-noise ratio in the images. For example, Yan *et al.* combined polymer dots and dual DNA amplification for the design of a protein multi-immunoassay.¹² In Figure 4.1 a, a schematic diagram shows the preparation of the probe by functionalizing the Pdots (composed by poly[(9,9-dioctylfluorenyl-2,7-diyl)-*alt*-co-(1,4-benzo-{2,1',3}-thiadiazole)]) with DNA1 and then binding a black hole quencher (BHQ)-labeled DNA2 to DNA1. The stepwise construction of the array (Fig. 4.1, b) was achieved by rolling circle amplification of oligonucleotide strands and then enzymatically cyclic release (ECR) of Pdots from the self-quenched probes, following the recognition between streptavidin and biotin-labeled antibody and biotin-labeled oligonucleotide.

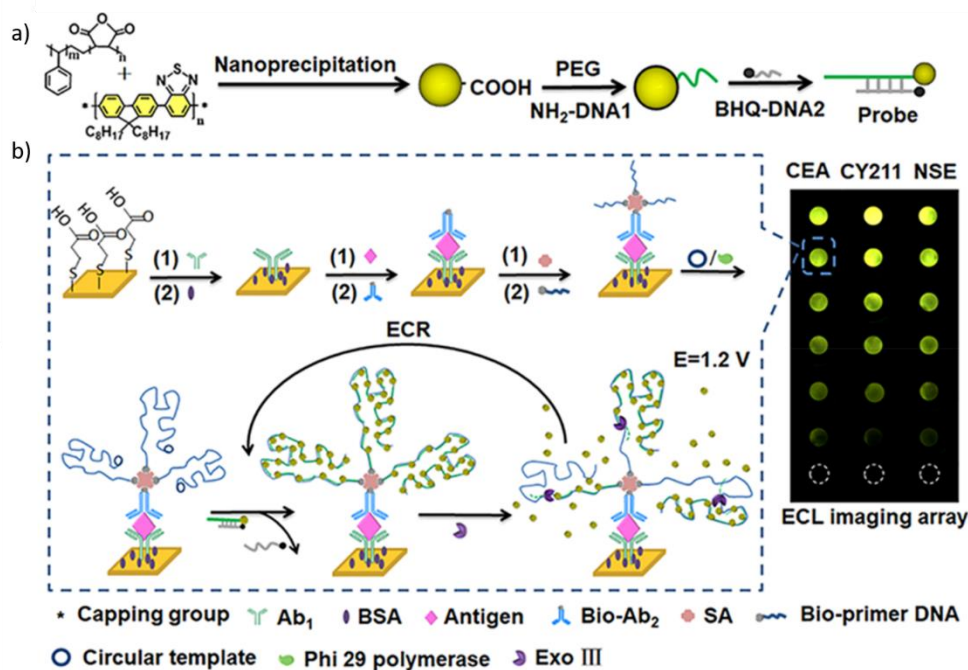


Figure 4.1 Schematic diagram of a) preparation of signal probe and b) stepwise construction of ECL imaging array and immunoassay procedure.¹²

In the last two decades, bipolar electrochemistry (BPE) approach has permitted to move from wired to wireless electrodes, which facilitates the parallel analysis of multi-electrodes and microelectrodes.¹³ The first studies combining ECL imaging and BPE used an “open” configuration.¹⁴ Thanks to ECL imaging, a current flowing in multiple bipolar electrodes is observed as light emission simultaneously. Such approach has been applied to DNA microarray sensors design and to the visualization of genotyping of various single nucleotide polymorphisms in a single run experiment.¹⁵

An alternative “closed” BPE system was successively applied to ECL imaging to prevent chemical interferences between the bipolar electrode extremity reporting the ECL cocktail and the extremity with the target containing solution.¹ In such “closed” configuration, a stronger ECL signal was found than in the “open” configuration.¹⁶ BPE offers the possibility to design swimmers, whose mechanical motion can be observe by ECL imaging. In 2014, Sentic *et al.* reported ECL swimmers for the detection of local glucose concentration by combining luminophore and enzymatically-produced NADH oxidations.¹⁷ As reported in Figure 4.2, a glassy carbon bead was positioned inside a vertical capillary. By application of an adequate electric field, the bipolar swimmer was polarized. At the cathodic extremity of the bead facing the feeder electrode, hydrogen evolution reaction permitted the bead propulsion along the capillary. Only in presence of glucose, [Ru(bpy)₃]²⁺ could react with the generated NADH, at

the anodic pole of the polarized bead and emit ECL, revealing the mechanical motion and, by ECL intensity quantification, glucose concentration.

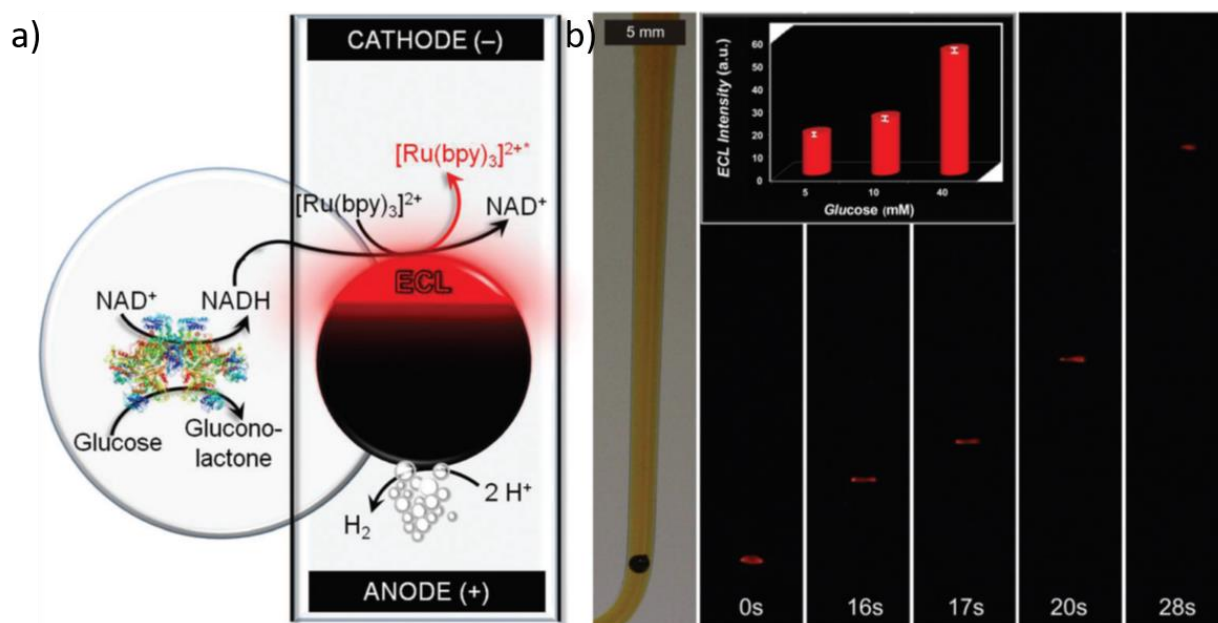


Figure 4.2 a) Illustration of enzyme-driven ECL observed on a bipolar swimmer. Glucose is oxidized by glucose dehydrogenase (GDH) with NAD^+ as a co-factor. The enzymatically-produced NADH behaves as an in situ coreactant for the ECL generation. b) ECL sensing and reporting of glucose concentration during the swimmer motion. Series of optical images showing a GC bead emitting ECL at different times during its motion. The GC bead is positioned in a U-shaped cell, filled with 100 mM PBS solution (pH 7.4) containing 10 U mL⁻¹ GDH, 1.5 mM $[\text{Ru}(\text{bpy})_3]^{2+}$, 10 mM NAD^+ , 40 mM glucose and a few drops of surfactant. Applied electric field: 23 Vcm^{-1} . The left image is recorded under white light whereas the other images were taken in the dark. Inset: plot showing the dependence of the ECL signal on the glucose concentration.¹⁷

Combination of single particle electrochemistry with optical techniques enables to visualize multiple electrochemical signals in parallel. Thanks to the high signal-to-noise ratio, ECL is improving as a transduction technique for single micro/nano-particles characterization.⁵ Bard et al. reported for the first time single particle collision observation by ECL. An enhancement in ECL intensity was correlated with the collision of individual Pt nanoparticles on an indium tin oxide (ITO) film.¹⁸ ECL from carbon-based nanoparticles (made of graphene oxide and graphite) were also successively studied by the same group.¹⁹ Willets *et al.* showed a similar approach for the visualization of gold nanowires on ITO electrodes. ECL emission was imaged at the level of the single nanowire electrode, without the need of extrinsic illumination or scanning electrochemical probe.²⁰ In 2015, Pan *et al.* reported the visualization of local redox activities of single Au nanoparticles size from 30 to 300 nm by ECL microscopy.²¹

Ma *et al.*^{3b} have shown the stochastic collision electrochemistry of single nano-emitters. By using a technique combining ECL microscopy with photoluminescence and SEM images they were able to trace the three dimensional trajectory and spatially distinguish simultaneous collision events in multiple nanoparticles.^{3b} Single nanoparticle collisions (Fig. 4.3, a and b) were recorded by injection of $[\text{Ru}(\text{bpy})_3]^{2+}$ - doping silica nanoparticles (Ru-DSNs) into the electrolyte solution containing TPA and glassy carbon (GC) bare electrode. Two discrete ECL signals could be distinguished: a “spike”, that is, an elastic collision (Fig. 4.3, a) and a “staircase”, sticking collision (Fig. 4.3, b).

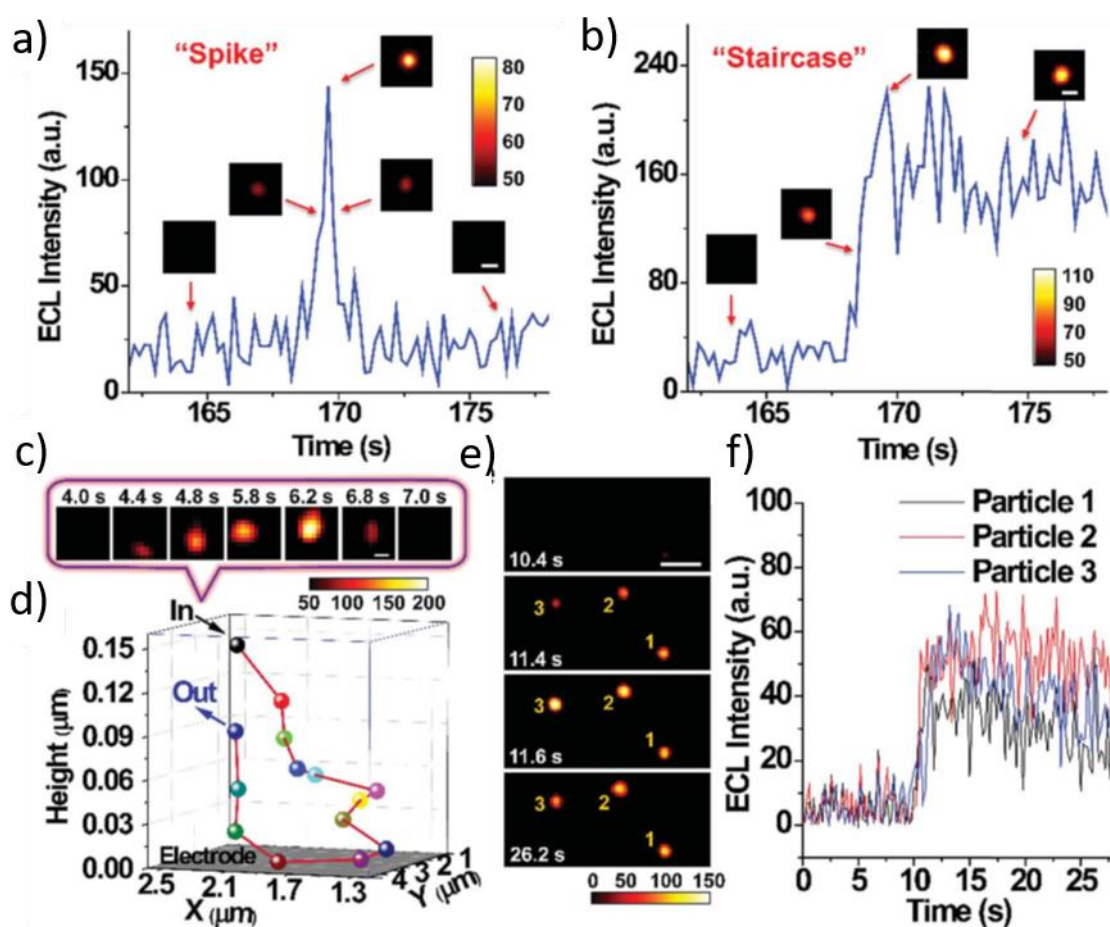


Figure 4.3 Single ECL spike (a) and staircase (b) signals during the collisions process. Insets, ECL snapshots of individual nanoparticles during a typical collision process. Constant potential: 1.4 V. Scale bars (white), 2 μm . Exposure time: 0.2 s. (c) ECL snapshots of individual nanoparticle during an elastic collision with Brownian motion. Scale bars (white), 1 μm . Exposure time: 0.2 s. (d) Three-dimensional collision trajectory of single nanoparticle in (c). (e) ECL snapshots of three RuDSNs colliding with the electrode simultaneously. Scale bars (white), 5 μm . Exposure time: 0.2 s. (f) ECL intensity vs. time curves of three RuDSNs in (e).^{3b}

Horizontal motions of the spot (Fig. 4.3, c) accompanies the variation of ECL intensity during collision, revealing Brownian motion of single Ru-DSN in all direction. In addition, three-dimensional spatial position of the Ru-DSN during the collision was calculated (Fig. 4.3, d).

ECL microscopy is a potential transduction technique for high throughput and spatial/temporal analysis at single cell level. Being able to provide information associated with cellular heterogeneity is fundamental for early diagnosis in medicine and for fundamental issues in biology.

Fluorescence microscopy, especially confocal laser fluorescence microscopy, total internal fluorescence microscopy (TIRF) and single molecule microscopies, are widely used to image specific proteins localization and various activities (such as membrane fusion, channel activities, *etc.*).²² However, autofluorescence of the sample is an intrinsic limitation of such techniques that can be avoided by using methods based on other physical principles. For example, methods based on micro/nano electrodes²³ or on SECM²⁴ have been applied to the study of complex biological processes. In particular, SECM is temporally limited by the requirement to scan the sample in order to reconstruct an image of the “electrochemical” activity or topography of the cells. Zu *et al.* reported a near-field scanning optical microscopy (NSOM) with an ECL light source produced at a nanoelectrode tip.⁷ This ECL nanoprobe was scanned over the substrate using the shear force mode.

ECL bioimaging has focused on two areas, first on the qualitative and quantitative detection of biomolecules inside the cell and second on the visualization of cellular surface structures. The ECL system composed by luminol as luminophore and hydrogen peroxide as coreactant is very useful in ECL bioimaging applications. ECL emission is correlated with the amount of hydrogen peroxide, giving important information in the context of detection of reactive oxygen species and oxidative stress. Moreover, it allows monitoring the enzymatic activity of oxidases, which generate hydrogen peroxide in presence of their substrate. Ma *et al.* reported luminol ECL applied to the analysis of active cholesterol at single mammalian cells membrane.²⁵ Successively, total (membrane and intracellular) cholesterol at single cells was imaged with ECL from luminol and hydrogen peroxide.²⁶ A g-C₃N₄ nanosheet modified microwell array provided an enhanced ECL emission and sensitivity, by catalyzing the decomposition of hydrogen peroxide. Individual cells were positioned at g-C₃N₄ nanosheets modified with Au NPs/ITO regions in the cell-sized microwells (Fig. 4.4, a). Cholesterol oxidase was introduced and reacted with plasma membrane cholesterol to generate hydrogen peroxide induced ECL for membrane cholesterol quantification. Triton X-100 was then applied to break cellular membrane to permit the quantification of intracellular cholesterol too. Figure 4.4 b) and c)

report respectively an example of ECL image of the microwells for membrane cholesterol detection and the correlation between ECL intensity and hydrogen peroxide concentration.

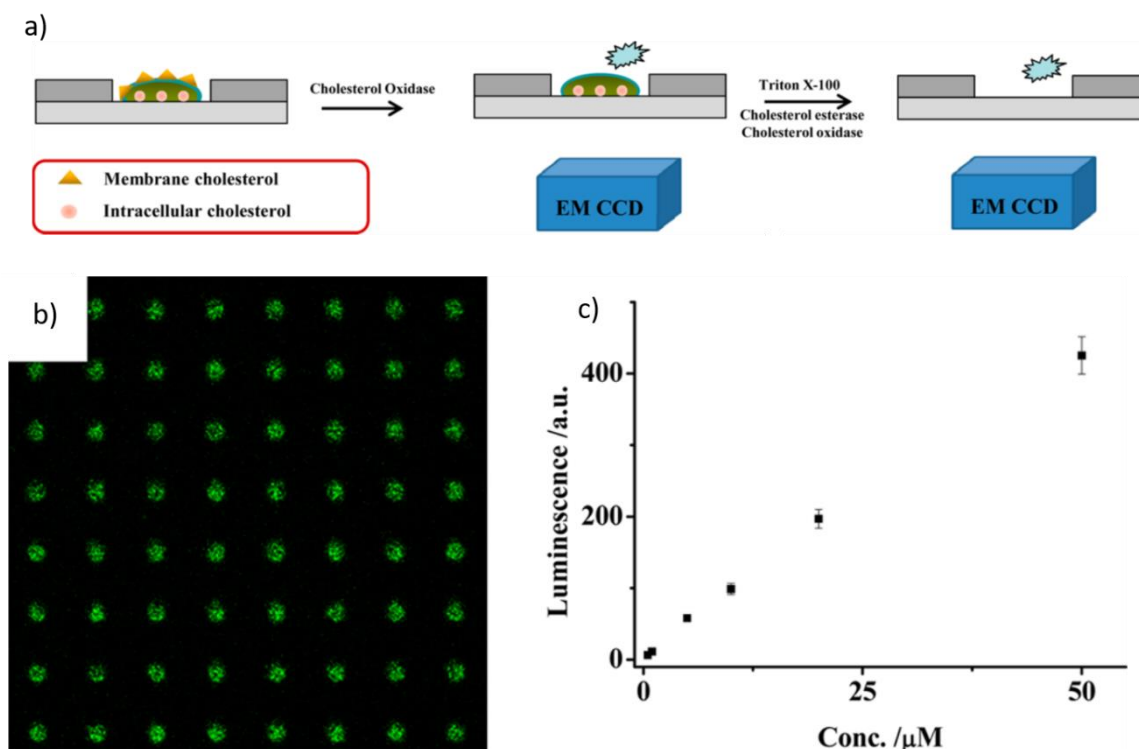


Figure 4.4 a) Process for the analysis of membrane and intracellular cholesterol at single cells; b) typical luminescence image of 500 nM hydrogen peroxide at g-C₃N₄ nanosheet modified Au NPs/ITO regions in cell sized microwells. The luminescence intensity was the luminescence ratio before and after the addition of hydrogen peroxide. The solution was 10 mM PBS with 200 μM L012; (c) the correlation of luminescence intensity with the concentrations of hydrogen peroxide. The error bar presented the standard deviation measured from 64 microwells on the ITO slide.²⁶

In collaboration with Paolucci's group, our group reported recently for the first time a spatially resolved ECL imaging of single cells.²⁷ A first cell line, CHO (Chinese Hamster Ovary) cells, was labeled with [Ru(bpy)₃]²⁺ by a biotin-streptavidin link and the corresponding ECL imaging at single cell level was reported. By contrast with fluorescence microscopy, ECL emission was observed only at cell borders. After this first proof of concept, a second cell line, MCF10A cells, was used to investigate a potential disposable analytical device, composed of CNTs (carbon nanotubes) as electrodic material and PET (polyethylene) as substrate and fabricated by inkjet-printed technique. MCF10A cells were grown on such support and labeled with [Ru(bpy)₃]²⁺ by immunohistochemistry approach for the detection of EGFR (epidermal growth factor receptor), overexpressed on the surface of several cancer cells. As for CHO cells, ECL emission was located at cell borders. Experimental data were supported by steady-state

simulations that confirm the confinement of ECL emission to a restricted region in proximity of cell/electrode border.

To overcome the negative effect of the steric hindrance and the insulation from cells, Liu and coworkers proposed the use of a chitosan film modified electrode.²⁸ The ECL luminophore L012 (8-amino-5-chloro-7-phenylpyrido[3,4-*d*]-pyridazine-1,4(2*H*,3*H*)-dione), a luminol analogue, could diffuse through a chitosan film and react with H₂O₂ released by cells, emitting ECL light (Fig. 4.5).

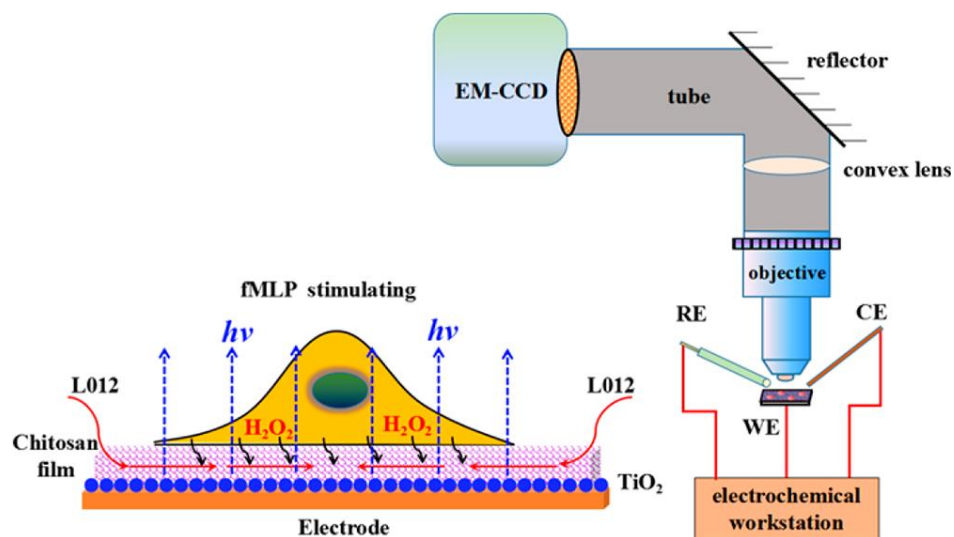


Figure 4.5 Setup and strategy for the ECL imaging of cells.²⁸

However, expanding the space between the cells and the electrode could hinder the diffusion of the electrogenerated species. A simpler method to increase the accessibility of the electrochemically generated radicals, without adding electrode modification steps, consists in a permeabilization step after cells fixation, as reported later in this chapter.²⁹

An ECL signal amplification strategy was developed, by combining BPE and functional nanoprobe of heterogeneous [Ru(bpy)₃]²⁺@SiO₂/Au nanoparticles for visual immunoassay of prostate specific antigen (PSA) at single LNCaP cells.³⁰ Such silica NPs could immobilize a large amount of [Ru(bpy)₃]²⁺ molecules and the Au NPs decorated on the surface of [Ru(bpy)₃]²⁺@SiO₂ NPs increased the amount of loaded antibody so that the ECL signal was amplified.

Here, we are reporting the development of surface-confined ECL microscopy, which efficiently images the entire cell basal membrane including its passive transport properties.

A second part of this work is devoted to widen the applicability of the above ECL microscopy by using innovative electrode supports.³¹

4.2 Development of ECL microscopy of cellular membranes

To proof ECL microscopy principles and its applicability to biological systems, ECL was applied to the visualization of single cells and to investigate the transport properties through cellular membrane.

4.2.1 Cellular membrane labeling procedure

Mammalian Chinese Hamster Ovary (CHO) cells were grown on the surface of glassy carbon (GC) electrodes. Carbon-based materials are characterized by a relatively faster kinetics for the amine oxidation than noble metal electrodes. Such a characteristic allows a very efficient ECL generation at the electrode surface.³² After 48h in cells incubator, CHO cells were incubated with biotin X that reacts with primary amino groups of cell surface proteins. Biotinylation is a method classically used in biology to label specifically extracellular proteins remained unlabeled.³³ Streptavidin-modified $[\text{Ru}(\text{bpy})_3]^{2+}$ labels (noted SA_v@Ru) were then attached to the biotinylated proteins of cellular membrane.³⁴

4.2.2 Single cell ECL imaging: proof of concept

Photoluminescence (PL) image (Fig. 4.6, a) was obtained by exciting the sample with an external light source. The PL emission confirms that the cellular membrane was completely labeled by SA_v@Ru.

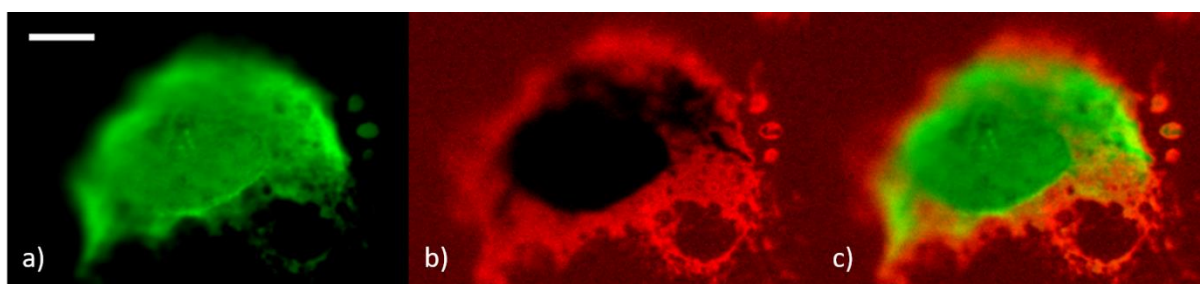


Figure 4.6 PL a), ECL b) and overlay of both luminescence signals c) of CHO cells labeled with SA_v@Ru. Cells were grown on GC electrodes. SA_v@Ru labels were attached to the biotinylated proteins of the cellular membrane. Both PL and ECL images were recorded in the reflection configuration on the same region of interest in the ECL focal plane. ECL was generated in PBS (pH = 7.4) containing 100 mM TPA by applying 1.4V vs Ag/AgCl/KCl 3M. Scale bar: 10 μm .

After switching off the excitation light source and by applying 1.4 V vs Ag/AgCl in presence of TPA, the $[\text{Ru}(\text{bpy})_3]^{2+}$ labels react with the electrogenerated TPA radicals. The potential

value was related with a strong and stable ECL signal on labeled cells, as found by cyclic voltammetry analysis (Fig. 4.7) and related ECL intensity, recorded with a photomultiplier tube. In Figure 4.7 a cyclic voltammogram (black curve) and ECL intensity (blue curve) is reported for CHO cells labeled with $[\text{Ru}(\text{bpy})_3]^{2+}$ by biotin-streptavidin link, in PBS 0.1 M (pH = 7.4) and TPA 0.1 M. The analysis was focused on the oxidation potential region, where the oxidation-reductive ECL mechanism of $[\text{Ru}(\text{bpy})_3]^{2+}/\text{TPA}$ occurs. The cyclic voltammogram is dominated by a single irreversible oxidation, with a potential peak of 1.25 V (*vs* Ag/AgCl) due to TPA oxidation. As expected, oxidation of $[\text{Ru}(\text{bpy})_3]^{2+}$ is not observable, due to the immobilization of $[\text{Ru}(\text{bpy})_3]^{2+}$ on the surface of cellular membranes and to the excess of TPA concentration (*vide* § 4.2.3). The corresponding ECL intensity (Fig. 4.7, blue curve) starts just after TPA oxidation peak, at about 0.85 V, with a maximum at 1.35 V (*vs* Ag/AgCl).

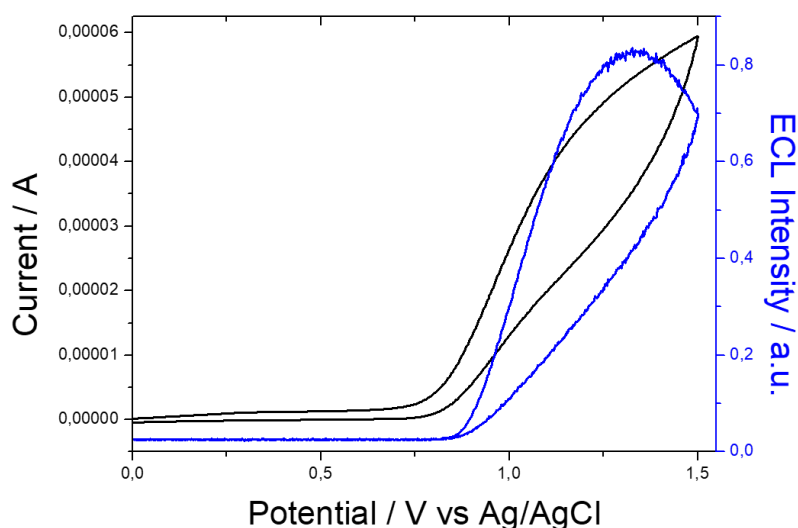


Figure 4.7 Voltammetric (black curve) and ECL (blue curve) signals recorded in PBS (pH = 7.4) containing 100 mM TPA on a GC disk (d = 3 mm) electrode where cells labeled with **SA@Ru** were grown. Scan rate = 0.1 Vs⁻¹

The corresponding ECL image (Fig. 4.6, b) reveals that light emission is now restricted to the external cell borders.²⁷ The reason of such a different spatial distribution between PL and ECL emissions has to be found in the predominant mechanism in this peculiar ECL configuration, called heterogeneous ECL. In the case of heterogeneous ECL, the luminophore is immobilized as a label and cannot be directly oxidized at the electrode surface. A mapping of ECL reactivity and of the emission spatial distribution was reported by Sentic *et al.* By using an immunoassay approach, they labeled polystyrene microbeads surface with $[\text{Ru}(\text{bpy})_3]^{2+}$ and performed an ECL imaging analysis in top and lateral beads view. They could experimentally demonstrate and confirm by computational calculations that the maximum ECL emission occurs in the

micrometric region, where concentration of TPA radicals are locally the highest. By lateral view analysis, they could also observed that only the luminophores located within 2-3 μm region close to the electrode contribute to the ECL signal.

The experimental observations can be confirmed by the intensities profiles of a selected region of interest of the images of Figure 4.6, as reported in Figure 4.8.

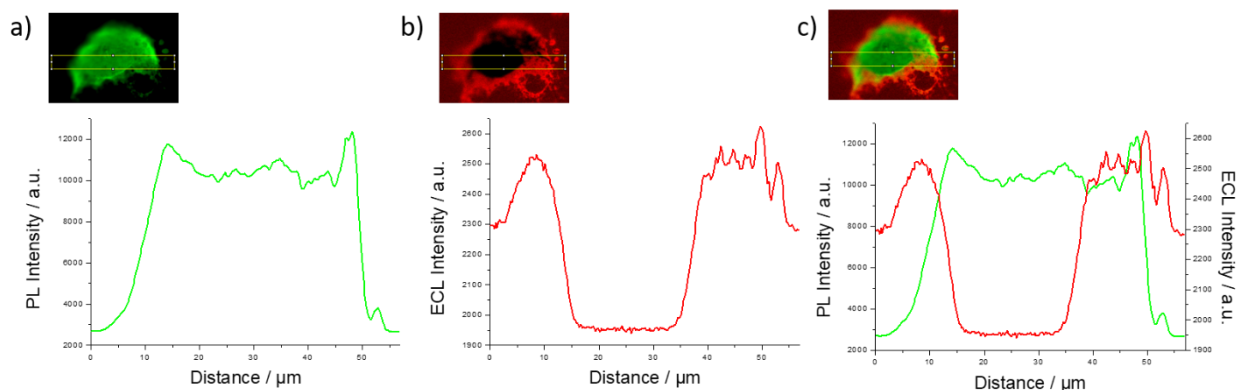
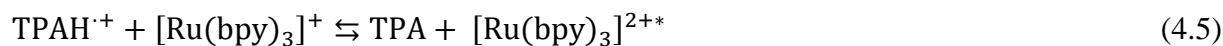


Figure 4.8 PL a) intensity profile, ECL intensity profile b) and overlay of both profiles c) of CHO cells labeled with SA_v@Ru (corresponding images reported in Fig. 4.1), in PBS (pH = 7.4) containing 100mM TPA by applying 1.4 V vs Ag/AgCl/KCl 3M. The images represent the selected region of interest for each image.

While PL intensity (Fig. 4.8, a) presents a maximum in the central part of the cell, ECL intensity (Fig. 4.8, b) is maximal at the cell contour.

4.2.3 $[\text{Ru}(\text{bpy})_3]^{2+}$ / TPA mechanisms

The study of $[\text{Ru}(\text{bpy})_3]^{2+}$ / TPA ECL mechanism is of fundamental importance for the clarification of the experimental results in ECL microscopy. The system follows the oxidative-reductive coreactant pathway, where the oxidation of TPA generates a strong reductant species reacting with the luminophore. TPA oxidation can directly occur at the electrode surface, as reported in Figure 4.9. In these cases, ECL can be generated by reaction of TPA electrogenerated radical with $[\text{Ru}(\text{bpy})_3]^{3+}$ (Fig. 4.9, a) or with $[\text{Ru}(\text{bpy})_3]^{2+}$ (Fig. 4.9, b).



After TPA oxidation to the corresponding radical cation, the latter undergoes deprotonation to a strong reducing species. The generated TPA^\cdot ($E^0 = -1.5 \text{ V vs NHE}$)^{2b,38} can indeed reduce $[\text{Ru}(\text{bpy})_3]^{2+}$ to $[\text{Ru}(\text{bpy})_3]^+$. The radical cation $\text{TPAH}^{\cdot+}$ ($E^0 = +1.1 \text{ V vs NHE}$)^{2b,38} oxidizes $[\text{Ru}(\text{bpy})_3]^+$ with the generation of the excited state $[\text{Ru}(\text{bpy})_3]^{2+*}$, which radiatively deactivate emitting the ECL signal. Such mechanism was verified by ECL-SECM and cyclic voltammetry experiments and supported by cyclic voltammetry simulations. TPA^\cdot evidence and stability were also demonstrated by electron spin resonance. The key kinetic parameter of the proposed mechanism is the rate constant of TPA^\cdot deprotonation, leading to a half-time of about 0.24 ms.^{35,37} Taking into account the overall mechanistic scheme for TPA (Eq. 4.1-4.6), simulations in bulk configuration have shown that maximum ECL intensity occurs at 0.5 μm from the electrode surface and then decays exponentially until 1 μm .^{27,35,37} The extension of this ECL layer might even be smaller within or in the cell-electrode interspace in comparison to the bulk situation.

Consequently, the immobilized ECL luminophores, located at a distance exceeding few micrometers from the electrode surface, cannot be reached by both coreactant radicals. ECL emission is limited by the access of the electrogenerated radicals to the label sites and lies in proximity of the cell borders.

4.2.4 Single cell ECL imaging: permeabilization step

In the pioneering work of Bondarenko *et al.*²⁹, for the first time the target of specific intracellular biomarkers by SECM was possible for adherent cells by a fixation-permeabilization approach. Fixation is a classic biological method, which blocks cell biological activity and dynamic variability preserving at the same time the cellular structure as well as biomolecules from metabolic processes in their original spatial location inside the cells. This approach permits to investigate cells activity as well as the localization of biomarkers without

the occurring of cell variability due to metabolic processes, experimental restrictions (such as measurements time) and morphological changes. However, the detection of intracellular markers is limited by cellular membrane, which acts in several cases as a pure insulator. By adding a permeabilization step, after fixation, cellular membrane allows diffusion without releasing of intracellular content (as it would happen for living and permeabilized cells).²⁹ Permeabilization – a standard biological procedure - occurs by adding a specific surfactant, such as saponin, digitonin, Tween 20 and Triton X-100, or an organic solvent (methanol and acetone) to cells after fixation.³⁹ In this way, the lipid bilayers of cellular membrane can be partially perforated, allowing diffusion across cellular membrane. Such fixation-permeabilization approach was applied to single cell ECL imaging for an enhancement of TPA accessibility through the cellular membrane.

The PL image in Figure 4.11 (a) shows that all the cellular membrane of a permeabilized cell was labeled with SAv@Ru. When applying 1.4 V vs Ag/AgCl the corresponding ECL image was recorded (Fig. 4.11, b).

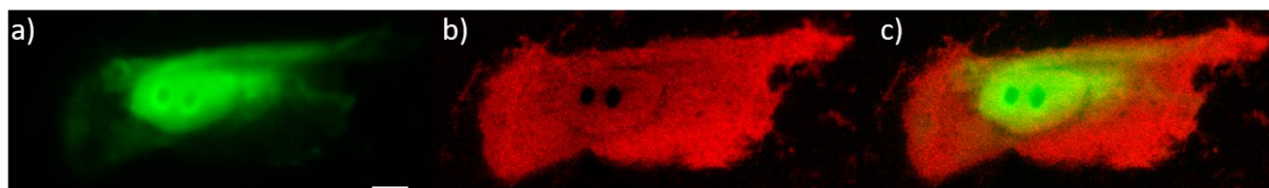


Figure 4.11 PL a), ECL b) and overlay of both luminescence signals c) of CHO cells permeabilized and then labeled with SAv@Ru. Cells were grown on GC electrodes. SAv@Ru labels were attached to the biotinylated proteins of the cellular membrane. Both PL and ECL images were recorded in the reflection configuration on the

same region of interest in the ECL focal plane. ECL was generated in PBS (pH = 7.4) containing 100mM TPA by applying 1.4V vs Ag/AgCl/KCl 3M. Scale bar: 10 μ m.

It is clearly observable that ECL emission occurs now at the whole cell membrane facing the electrode and not only from the cell borders. The corresponding intensity profiles (Fig. 4.12) for a selected region of interest of cell reported in Fig. 4.11 confirm experimental observations.

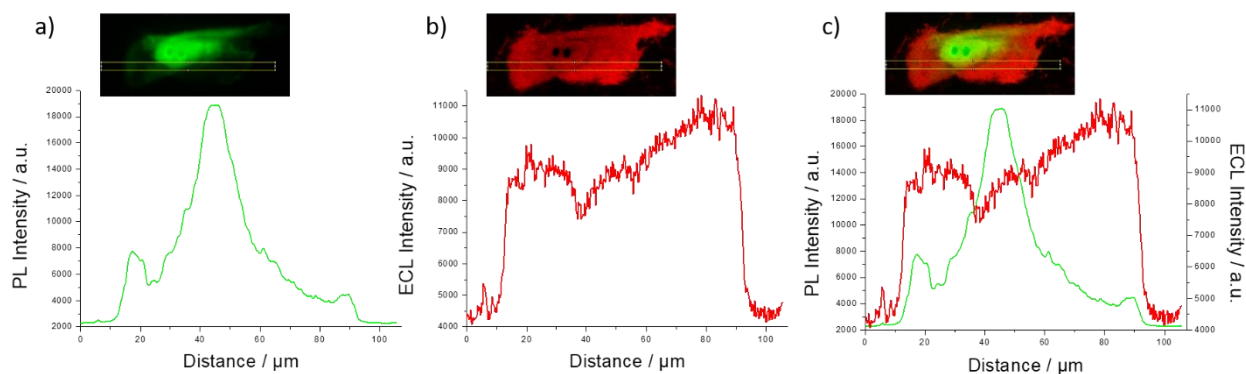


Figure 4.12 PL a) intensity profile, ECL intensity profile b) and overlay of both profiles c) of CHO cells permeabilized and then labeled with SAV@Ru (corresponding images reported in Fig?), in PBS (pH = 7.4) containing 100mM TPA by applying 1.4 V vs Ag/AgCl/KCl 3M. The images represent the selected region of interest for each image.

The ECL intensity profile shows a more homogeneous distribution of the ECL emission not only at cell borders, but also in the central region of the basal cell membrane. Such a significant result proves unambiguously that TPA diffusion through membranes, at least through the plasma membrane, is essential for reaching the electrode surface and obtain a global imaging of the cell.

In Figure 4.13, a schematic representation presents the difference in the ECL emission localization, occurring during ECL imaging single SAV@Ru-labeled cell between not permeabilized and permeabilized cells.

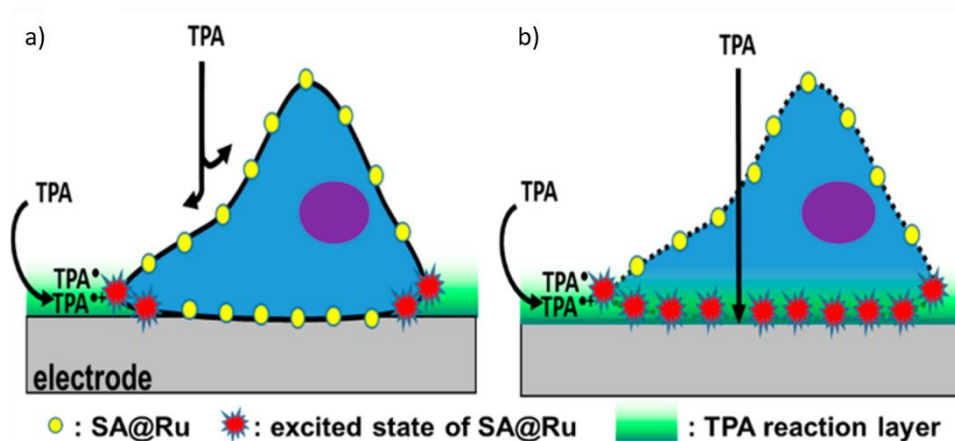


Figure 4.13 Representation of the influence of the membrane permeabilization step on the ECL responses of fixed a) and also permeabilized b) cells. It illustrates the effects of the permeabilization step on the TPA diffusion through the cell membrane and on the resulting localization of the ECL-emitting regions.³¹

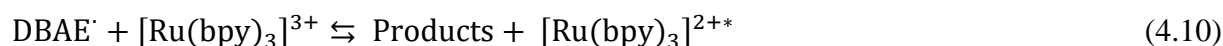
While in not permeabilized SA_v@Ru labeled cells TPA can only be electrochemically oxidized and diffuse in correspondence of cell contours, permeabilization procedure allows TPA to reach a wider part of the interface between cell and electrode.

In Figure 4.11 b), a detailed observation shows that ECL light is also detected in the nucleus region. Even the nucleus membrane has become permeable to TPA following this procedure. However, two nucleoli clearly visible inside the nucleus remain dark. They have not been permeabilized and block the TPA diffusion from the bulk to the electrode surface. Thus, diffusion of TPA through the membranes governs the location of the ECL-emitting regions within the cell as well as the proximity to the electrode surface. Consequently, such ECL microscopy does not reflect only the spatial distribution of the labels and the structure of the plasma membrane but reveals also the passive transport properties. Therefore, ECL microscopy may allow investigating the transport and trafficking across the cell membranes.

4.2.5 [Ru(bpy)₃]²⁺/DBAE ECL system for single cell ECL imaging

TPA represents the most widely-used ECL coreactant, in particular for [Ru(bpy)₃]²⁺ as luminophore. However, TPA is highly toxic, volatile, basic (high quantity of acid are necessary to reach a neutral pH value), and the ECL intensity of [Ru(bpy)₃]²⁺/TPA system is strongly affected by the electrodic material.⁴⁰ Alternative coreactants are therefore under investigation, in particular other tertiary amines, whose electrogenerated radicals are more stable than the secondary amines', primary amines' and other coreactants' ones. An environmentally friendly tertiary amine, 2-(dibutylamino)ethanol (DBAE) was tested as alternative coreactant.⁴¹

$[\text{Ru}(\text{bpy})_3]^{2+}/\text{DBAE}$ allows to reach between 10 and 100 times higher ECL intensities than $[\text{Ru}(\text{bpy})_3]^{2+}/\text{TPA}$ at Au and Pt electrodes (for 25 mM of each coreactant in solution).^{2b,42} As reported by Xu *et al.*⁴⁰, the ECL system $[\text{Ru}(\text{bpy})_3]^{2+}/\text{DBAE}$ provides ECL intensities close to $[\text{Ru}(\text{bpy})_3]^{2+}/\text{TPA}$ for concentrations of $[\text{Ru}(\text{bpy})_3]^{2+}$ of about 1 mM. By contrast, an increase of 10 times in ECL intensity is revealed for DBAE system in comparison to TPA when the concentration of $[\text{Ru}(\text{bpy})_3]^{2+}$ is 1 μM at Au and Pt electrodes. The direct oxidation of the coreactant is important for low $[\text{Ru}(\text{bpy})_3]^{2+}$ concentrations conditions, while the electrocatalytic oxidation of the coreactant via $[\text{Ru}(\text{bpy})_3]^{2+}$ is predominant at higher $[\text{Ru}(\text{bpy})_3]^{2+}$ concentrations. ECL intensity for $[\text{Ru}(\text{bpy})_3]^{2+}/\text{DBAE}$ increases rapidly with increasing concentration up to 20 mM, then it decreases slowly upon further increasing its concentration, probably due to collateral reactions.⁴⁰ DBAE presents a chemical structure similar to TPA and as tertiary amine it can be supposed that the ECL mechanism (4.7-4.11) would be close to TPA mechanism for ECL generation with dissolved $[\text{Ru}(\text{bpy})_3]^{2+}$ as luminophore:



The short-lived DBAE radical cation, $\text{DBAE}^{\cdot+}$ deprotonates generating the strong reductant species DBAE^{\cdot} . This latter can reduce $[\text{Ru}(\text{bpy})_3]^{3+}$ to $[\text{Ru}(\text{bpy})_3]^{2+*}$ that can radiatively deactivate by light emission.⁴²

Figure 4.14 reports PL (Fig. 4.14, a), ECL (Fig. 4.14, b) and their overlay image (Fig. 4.14, c) for CHO cells whose cellular membrane was labeled with $[\text{Ru}(\text{bpy})_3]^{2+}$ (*vide* § 4.2.1). PL image shows the distribution of the ECL luminophore on the whole cellular membrane. By switching off the excitation light source and by applying 1.2 V *vs* Ag/AgCl in presence of 20 mM of

DBAE (in PBS 0.1 M, pH = 7.4), ECL image was recorded (Fig. 4.14, b). ECL intensity was below the detection limit and any part of the basal membrane of the cells was visible.

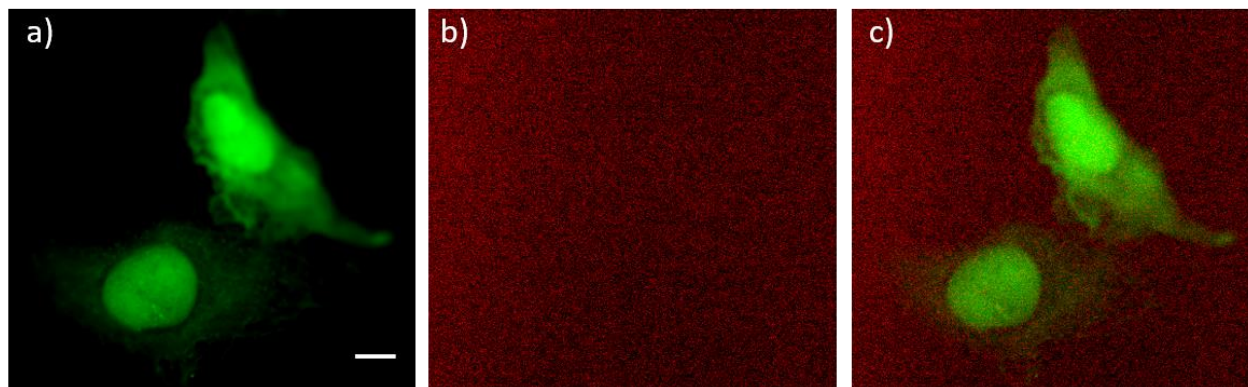


Figure 4.14 PL (a), ECL (b) and overlay of both luminescence c) images of CHO cells that were labeled with SAv@Ru. Cells were grown on GC electrodes. SAv@Ru labels were attached to the biotinylated proteins of the cellular membrane. Both PL and ECL images were recorded in the reflection configuration on the same regions of interest in the ECL focal plane. ECL was generated in PBS (pH = 7.4) containing 20 mM DBAE by applying 1.2 V. Scale bar: 10 μ m.

These results are in good agreement with a previous work based on ECL imaging of [Ru(bpy)₃]²⁺-labeled polystyrene micrometric beads.⁴³ The ECL intensity associated with [Ru(bpy)₃]²⁺ / DBAE system was found to be seven times lower than for [Ru(bpy)₃]²⁺/TPA, as [Ru(bpy)₃]²⁺ is immobilized as label on the surface of the micrometric bead. In the case of heterogeneous ECL, DBAE electrogenerated radicals must diffuse in solution and react with the ECL luminophores positioned on the bead surface to generate ECL emission. Such a behavior underlines the difference in the radicals' stability and lifetimes for DBAE and TPA. The different behavior of DBAE in comparison of TPA might be attributed to the intervention of a very unstable intermediate and/or to the inadequate potential of the DBAE^{•+} radical, which is unable to populate the excited state by reaction with [Ru(bpy)₃]²⁺ (4.5).⁴³ The negative ECL results obtained by using DBAE supports the proposed mechanism (*vide* § 4.2.3) for heterogeneous ECL. The diffusion and stability of the coreactant electrogenerated radicals governs the ECL emission in these peculiar experimental conditions.

4.2.6 Comparison between fluorescence and ECL microscopies

To better understand the surface-confinement feature of ECL microscopy and its differences with wide-field fluorescence microscopy, it can be useful to analyze and compare both PL and ECL images in different focal planes (Fig. 4.15).

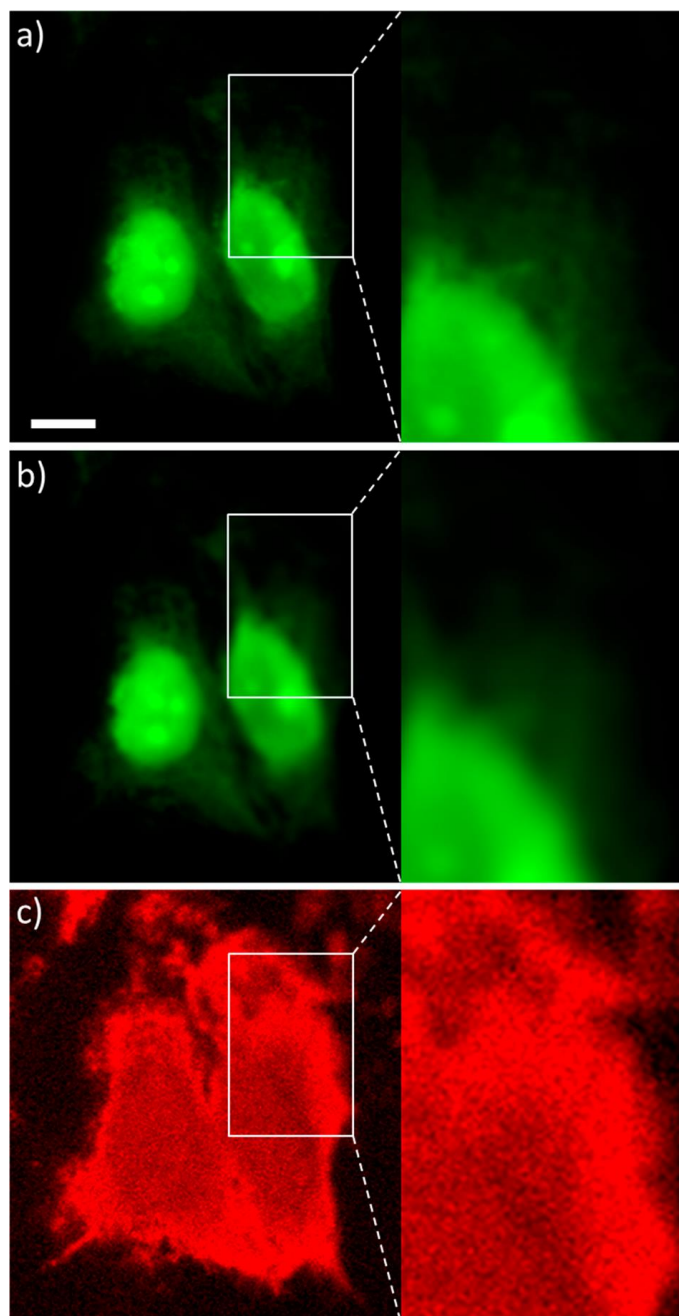


Figure 4.15 PL images of the same CHO cells focused in the focal PL a) or ECL b) planes at different magnifications. c) ECL images of the same region of interest recorded with the objective focused in the ECL focal plane (*i.e.*, similar to b). Cells were grown on GC electrodes, fixed and then treated with Triton X-100 for 10 min. SAV@Ru labels were attached to the biotinylated proteins of the cellular membrane. Both PL and ECL images were recorded in the reflection configuration. ECL was generated in PBS (pH = 7.4) containing 100mM TPA by applying 1.4V vs Ag/AgCl/KCl 3 M. Scale bar: 10 μ m.

When considering resolution in optical microscopy, in addition to the lateral resolution, the main characteristic is the vertical resolution.⁴⁴

For instance, in wide-field fluorescence microscopy, the excitation wavelength provokes the entire object to fluoresce, and in usual conditions, more than 90 % of the collected fluorescence signal is out of focus emission, which can completely mask the in-focus details.^{44a} Vertical resolution is determined by the depth of field so that a thin section of the cell can be imaged.⁴⁴ The depth of field may be defined as the distance from the nearest object plane in focus to that of the farthest plane also simultaneously in focus.⁴⁵ Figure 4.15 shows PL and ECL images of the same region of interest presenting two adherent cells on the GC electrode. These images have been recorded with a high numerical aperture (NA = 1.2) 63x objective in different focal planes. The depth of field of the objective is about 680 nm. By adjusting the focus in the PL mode (Fig. 4.15, a), the cell and nucleus membranes are clearly imaged as well as the pseudopods. After switching off the excitation light source, the ECL image was recorded by applying 1.4 V vs Ag/AgCl to the electrode in presence of TPA. In this PL focal plane, the resulting ECL image appeared blurry, out of focus (Fig. 4.16).

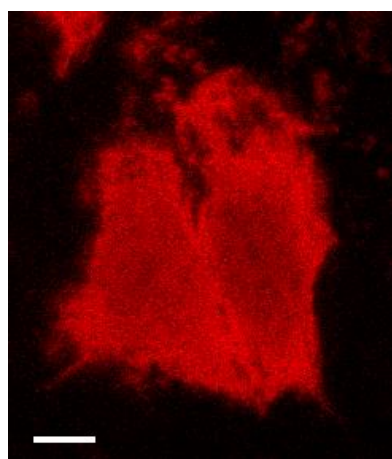


Figure 4.16 ECL images of the same CHO cells (Figure 4.6) focused in the focal PL plane. Cells were grown on GC electrodes and then treated with Triton X-100 for 10 min. SAv@Ru labels were attached to the biotinylated proteins of the cellular membrane. ECL image was recorded in the reflection configuration. ECL was generated in PBS (pH = 7.4) containing 100 mM TPA. Scale bar: 10 μ m.

Well-defined ECL imaging of the cell (Fig. 4.15, c), of its plasma membrane, was obtained when moving the focal plane of the objective 1.2 μ m below the previous PL focus, *i.e.*, closer to the electrode surface. By recording PL image in this adequate focal plane for ECL, PL image of the cells appeared blurry, not well-defined (Fig. 4.15, b). It means that the focal PL and ECL planes are distinct and not located at the same distance from the electrode surface.

The mean average distance between PL and ECL focal planes has been evaluated as 1.2 ± 0.4 μm ($n > 30$ CHO cells). In other words, the ECL focal plane is located 1.2 ± 0.4 μm closer to the electrode surface in comparison to the PL focal plane. This conclusion appears fully logic since PL is acquired in far-field mode and provides a whole cell image of all SAv@Ru labels present on membranes from the apical (top) to the basal (down) planes of the cell. Otherwise, ECL emission only occurs from SAv@Ru labels reacting with TPA electrogenerated radicals, meaning in the TPA reaction layer (Fig. 4.13, b) between the electrode surface and basal cell membranes.

AFM images performed on CHO cells (70 % confluent) are reported in Figure 4.17, for a better understanding of CHO cells topology. Typical dimensions of the cells were about 30-70 μm , as in usual culture conditions. Characteristic brighter regions corresponding to thicker parts in the central region of the cells (Fig. 4.17, a) are attributed to the nucleus areas. The zones surrounding the nuclei correspond to the cytoplasm, which becomes progressively thinner at the pseudopods ensuring the adhesion on the surface. Figure 4.17 b) represents two typical cells' profiles. Nuclei regions appeared about 1.5-2 μm in height whereas cell borders are about 1 μm . These AFM results are in good agreement with similar topographic studies performed on CHO cells.⁴⁶ It is possible to estimate that PL focal plane is in the middle of the cell (as schematic represented in Fig. 4.17, b).

Considering that ECL focal plane is 1.2 ± 0.4 μm below PL focal plane, ECL is truly emitted from a cell zone in the immediate vicinity of the electrode surface. It means in the TPA reaction layer. ECL emission is confined to the basal cell membrane.

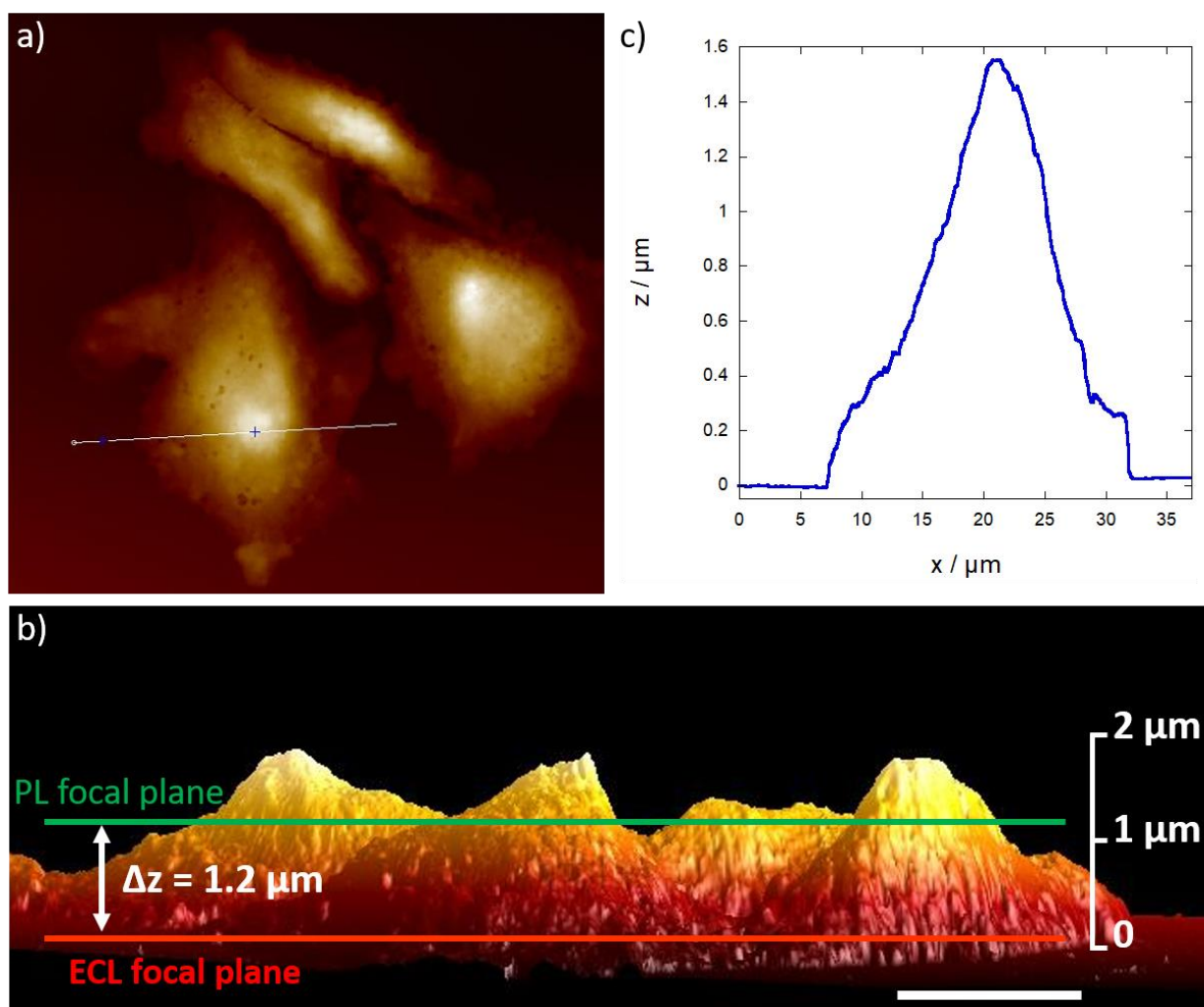


Figure 4.17 Top a) and c) side views of AFM images of CHO cells grown on a GC surface. The bright regions correspond to the nuclei region. b) Cross-section profile of two adjacent cells along the white line materialized on a). On the side view, both mean PL (green) and ECL (red) focal planes are schematically represented. Scale bars: 10 μm .

Previous studies, based on surface plasmon resonance (SPR) and TIRF microscopies, reported a distance of about 100-150 nm between the plasma membrane and the substrate (such as the electrode), via the formation of extracellular matrices-integrin-cytoskeleton linkages.⁴⁷ Therefore, since the cellular membrane is SAv@Ru labeled, ECL emission is intrinsically confined close to the electrode surface and occurs at the level of the basal cell membrane. Consequently, single cell ECL imaging offers a near-field resolution of biological structures at distance close to the emission wavelength of $[\text{Ru}(\text{bpy})_3]^{2+}$ (615 nm). This is emphasized by the overlay between PL and ECL intensities profiles of Figure 4.11 c), which shows that ECL allows the imaging of a significantly larger spatial extension of the cell borders. The parts of

the plasma membrane that reside closer to the electrode surface generates a stronger ECL intensity whereas they remain dark in PL. ECL microscopy permits an extended and a higher resolved imaging of the basal cell membrane and of the cell contours. The contrast is indeed much improved in comparison to PL images. Therefore, different and complementary information are provided by classic wide-field fluorescence microscopy and ECL microscopy. In fact, fluorescence microscopy presents important limitations. First, the (x, y) resolution limit is near $0.2 \mu\text{m}$,⁴⁸ from the diffraction limit calculation:

$$r = \lambda / 2NA \quad (4.12)$$

where r defines the resolution of the imaging system, λ (nm) is the wavelength of the light (*i.e.*, fluorescence emission), NA is the numerical aperture of the objective. Consequently, the standard far-field fluorescence microscopy does not permit to distinguish for example individual proteins complexes.

Far-field and confocal microscopy can greatly enhance resolution, but those techniques are still limited by respectively out-of-focus light and strong and rapid photobleaching. In particular, out-of-focus fluorescence provokes an increase in background noise and decreases the spatial resolution related with the intensity of the true signal.^{22a} In recent years, a number of “super-resolution microscopies” has been developed, including TIRF microscopy, stimulated emission depletion (STED), stochastic optical resolution microscopy (STORM), and photoactivated localization microscopy (PALM). In particular, the development of TIRF microscopy has effectively eliminated out-of-focus fluorescence, thanks to its near-field nature. The surface-confinement of ECL microscopy can be conceptually associated with TIRF microscopy. This latter can reach a resolution beyond the diffraction limit. When the incident light is reflected at the interface between two transparent media with a different refractive index, evanescent waves occur.⁴⁹ As for ECL microscopy, TIRF is characterized by a limited extension in height (z) of the probed space, due to the non-propagating properties of the evanescent electromagnetic field. Indeed, the evanescent wave decays exponentially into the sample within few hundreds of nanometers, typically about 300 nm, from the surface. Thus, only the fluorophores located in this space are photoexcited and may contribute to the fluorescence signal.³¹ The finite ECL

reaction layer, which results from the reactivity of the TPA radicals, provides the surface-confinement feature for generation and observation of ECL luminophores.

4.3 Towards disposable device-based analysis

As already mentioned, GC electrodes represent widely used electrodic material for ECL generation in aqueous environment, in particular with the system $[\text{Ru}(\text{bpy})_3]^{2+}$ / TPA. Although GC electrodes show a fast kinetic for coreactant oxidation and a high overpotential for water oxidation in comparison with noble metals- based electrodes due to its greater inertness,⁵⁰ surface properties and activity of such electrodes can drastically be modified during experiments. Moreover, GC electrodes can hardly be considered as good candidate for ECL microscopy applications in biodiagnostic and in high-resolution cells imaging. The use is indeed limited to the reflection configuration and requires several preparation steps before measurements. Ideal electrode materials for ECL microscopy should present a high electrical conductivity, an excellent electrochemical stability and high optical transparency. This latter property permits to collect light emitted through the electrode material, avoiding solution's scattering phenomenon and inner filter effects.

4.3.1 Transparent electrodes for applications in microscopy

Glass/metal oxide electrodes, such as indium-doped tin oxide (ITO) and fluorine-doped tin oxide (FTO), are currently the standard materials for transparent electrodes.³² ITO-base electrode was recently used for the detection of cholesterol at cellular membrane by ECL analysis with luminol as luminophore.²⁵ Indeed, for luminol ECL, the low oxidation efficiency favors the formation of chemiluminescent products rather than more oxidized byproducts.

ITO and FTO-based electrodes paved the way for the implementation of ECL as imaging technique for the visualization of single objects, such as microbeads,⁵¹ fingerprints⁵² and cells.⁵³ But the rather limited stability of these oxides restricts the electrochemical potential window, and their low efficiency for TPA oxidation leads to very low ECL intensity for the ECL system $[\text{Ru}(\text{bpy})_3]^{2+}$ / TPA compared to carbon-based materials.

Carbon-based materials, such as graphene and carbon nanotubes, have recently been emerged as higher efficient transparent electrodes in comparison of ITO and FTO electrodes.^{32,54} However, graphene and CNTs are not freestanding and must be deposited on an inert support, like glass or polyethylene terephthalate (PET).

4.3.2 CNTs-based inkjet-printed electrodes

In the last years, in Ecole Polytechnique Fédérale de Lausanne a CNT-based transparent electrode has been developed by inkjet-printing technique on polyethylene terephthalate (PET). The inkjet-printing technology permits the deposition of a material by ejection of picoliter droplets from up to several hundred parallel nozzles. It is a digital, mask-less and contact-less technique, which approaches progressively the industrial production level at reasonable costs for thin layer materials.^{27,55}

The optical properties of the device were tested in reflection and in transmission mode. Figure 4.18 shows the PL images for polystyrene 12- μm beads deposited on the surface of CNTs electrodic material of the device for Figure 4.18 a) and b) and on a microscope glass coverslip for Figure 4.18 c). The beads were labeled with $[\text{Ru}(\text{bpy})_3]^{2+}$ by a biotin-streptavidin link.⁴³ All PL images show that the whole surface of the beads was labeled with $[\text{Ru}(\text{bpy})_3]^{2+}$. However, while in reflection mode the CNTs inkjet-printed electrodes permits to record well-resolved PL image, in transmission configuration, the PET layer induces some optical distortions probably related to the different refractive index of PET (Fig. 4.18, b).³¹ By contrast, PL image could be easily recorded in a microscope glass coverslip in transmission mode.

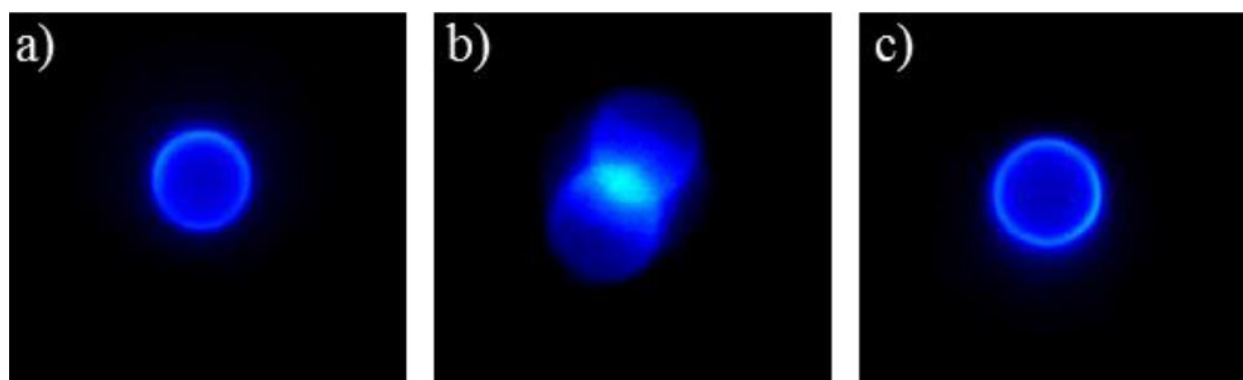


Figure 4.18 PL images of $[\text{Ru}(\text{bpy})_3]^{2+}$ -labeled polystyrene 12- μm beads deposited on (a-b) polyethylene terephthalate sheets or (c) on the microscope glass coverslips. They were imaged (a) in reflection configuration or (b-c) in transmission configuration with an epifluorescence microscope.

In a recent work, such electrodic system was applied for the first time to single cell ECL imaging, for the detection and visualization of the epidermal growth factor receptor in MCF10A cells, in reflection configuration.²⁷ In collaboration with Dr. Lesch (Ecole Polytechnique Fédérale de Lausanne), CNT-based transparent electrode was modified and a classic microscope glass coverslip (0.13-0.16 mm thickness) replaced PET as substrate. Such glass

coverslips are ideal for biologists and for researchers working with microscopy because it is a standard object in these fields. Such modified device allowed to work in reflection and in transmission modes (Fig. 4.18, c) and Fig. 4.19).

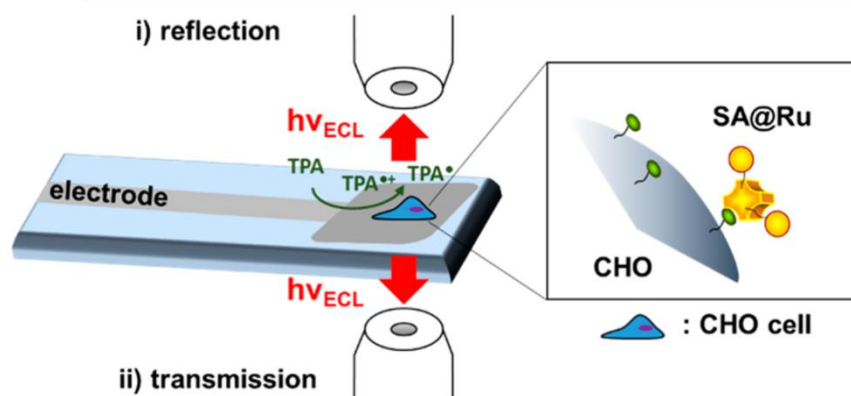


Figure 4.19 Schematic representation of the two configuration for surface-confined ECL microscopy: i) in reflection configuration with the GC electrode; ii) in transmission configuration through the transparent CNT inkjet-printed electrode.

An inkjet-printed Ag pattern served as electrical connection for the printed CNT layer on the glass coverslip (“CNT/glass”, Fig. 4.20, a).

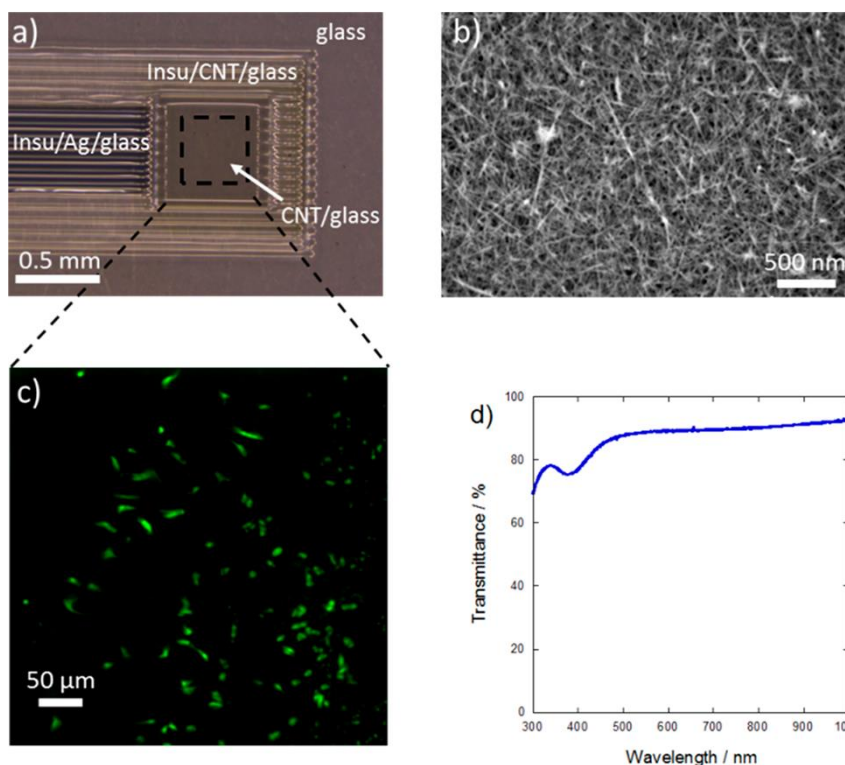


Figure 4.20 a) Photograph of the inkjet-printed CNT electrodes on the microscope glass coverslips. b) SEM of the CNT electrode surface. c) PL images of the CHO cells grown on the inkjet-printed CNT electrodes. d) Transmission curve of the inkjet-printed CNT electrodes.

An inkjet-printed insulation layer (“Insu/CNT/glass”) defined precisely the stand-alone CNT working electrode area and protected the Ag from the solution (“Insu/Ag/glass”). The SEM image shows a uniform surface coverage of the glass substrate by the CNTs (Fig. 4.20, b). The oxidation of TPA occurs efficiently on such CNT electrode surfaces, giving an ECL activity one order of magnitude higher compared with the standard transparent ITO electrode.⁵⁶ The CNT-printed electrodes were quasi-transparent allowing about 90 % of transmission (Fig. 4.20, d) at $[\text{Ru}(\text{bpy})_3]^{2+}$ emission wavelength (615 nm). CHO cells were cultured on the inkjet-printed CNT electrodes as illustrated by the PL image (Fig. 4.20, c). CNT’s biocompatibility was already attested by its use as scaffold for cells’ proliferation⁵⁷ and in living cells fluorescence imaging.⁵⁸ Cells viability on this specific CNT system was comparable to a glass substrate, as reported previously.²⁷

4.3.3 CNTs inkjet-printed electrodes: application to ECL microscopy

In Figure 4.21, PL and ECL images of SAV@Ru-labeled and permeabilized CHO cells are reported.

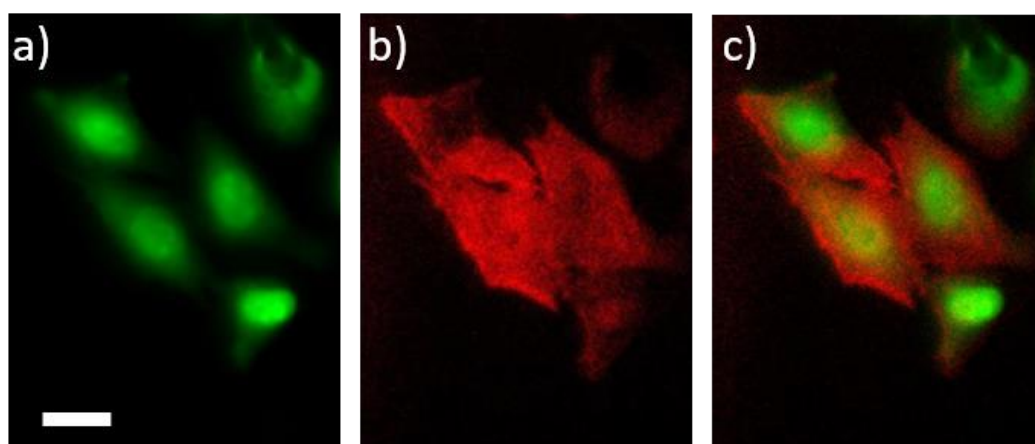


Figure 4.21 PL a), ECL b) and overlay of both luminescence images c) of CHO cells that were obtained in the transmission configuration through the CNT inkjet-printed electrode. Cells adherently grown on the CNT electrodes were permeabilized and labeled with Sav@Ru. PL and ECL images were both recorded on the same region of interest in the ECL focal plane. ECL was generated in PBS (pH = 7.4) containing 100 mM TPA by applying 1.4 V vs Ag/AgCl/KCl 3M. Scale bar: 20 μm .

Figure 4.21 a) shows PL image in the transmission configuration (Fig. 4.19, ii) through the CNT layer. Cells appeared relatively separated when observed in the PL mode. Then, the same region of interest was recorded in ECL with the transmission configuration (Fig. 4.21, b).

Due to the peculiar surface-confinement of heterogeneous ECL, ECL light is generated at the level of the basal membrane, transmitted through the CNT layer and the coverslip, and collected by the microscope objective. The permeabilization procedure allows the visualization of the entire cell area by ECL microscopy. As a result, they appear much closer than in PL (Fig. 4.21, a), similarly to images recorded in the reflection configuration with GC electrodes. The regions of the labeled membrane located in the immediate vicinity of the electrode surface are clearly visible in ECL, whereas they are not distinguished in PL.

ECL microscopy allows observing membrane details, which are difficult to resolve by classic PL microscopy. This approach demonstrates the potential diagnostic applications of ECL single cell imaging by selecting a disposable device.

4.4 Conclusions

A surface-confined microscopy, based on ECL, was developed and applied to image plasma membranes at single cell. By comparing PL, ECL and AFM images of the cells, it was demonstrated that, in contrast with classic fluorescence microscopy, the ECL emission is restricted to the immediate vicinity of the electrode surface. Thus, only the basal membrane generates ECL light and ECL microscopy reveals details that are hardly resolved by classic far-field fluorescence microscopy. The limited extension of the ECL emitting region results from the ECL mechanism and the short lifetimes of the coreactant radicals.

Conceptually, this sub-wavelength vertical resolution is reminiscent of TIRF microscopy with a restricted propagation depth of ECL reactants mimicking the exponential decay of the evanescent wave. By using other coreactants presenting different radical lifetimes, the extension of the ECL emitting could be modulated, allowing to image different heights in substrates or in cells by ECL. Moreover, the replacement of the toxic TPA with other coreactants, in particular with biomolecules, would allow the analysis of living cells.

Since ECL emission requires the oxidation of the coreactant at the electrode surface, the reported ECL microscopy is a dynamic technique. It does not only visualize the plasma membrane structures, but it also reflects their passive transport properties. The presented strategy may allow investigating the transport and trafficking properties through cellular membranes, *i.e.* by modulation of the permeabilization degree.

Finally, ECL microscopy is performed for the first time in both reflection and transmission configurations owing to disposable transparent CNT-based electrodes inkjet-printed on standard glass coverslips for microscopy. Therefore, such approach using standard biological

objects expands the possibilities of ECL to diverse microscopy fields by imaging globally the dynamics of biological entities. The presented surface-confined ECL microscopy offers exciting potential opportunities to study the dynamic properties of the cell membranes and promising applications in ultrasensitive cell imaging assays. A new approach is already being investigated in which CHO cells are grown on GC electrode surface and fixed without successive labeling step. The ECL microscopy experiment is performed by using a solution of 0.1 M of TPA, 10 μ M of $[\text{Ru}(\text{bpy})_3]^{2+}$ in PBS 0.1 M (pH = 7.4). The “negative ECL” images of CHO cells resulting from this approach may be able to reveal the passive transport properties of cellular membranes in an alternative way.

Future perspectives can be the labeling of specific proteins on cellular membrane or inside the cell. For example, actin represents the most abundant protein in most eukaryotic cells, with important functions in cytoskeleton and cells motility.⁵⁹ The interaction between an adherent cell and the support is strongly affected by actin. Unfortunately, many mechanisms in actin activities and dysfunctions related with different pathologies are still under investigation. In this context, the application of surface-confined ECL microscopy to actin-labeled cells may provide new important information.

In addition to the investigation of different coreactants and different cellular regions, the use of new luminophores will permit to expand ECL microscopy of labeled cells to multiplex assay systems. Iridium complexes represent interesting candidates thanks to the possibility of easily tuning the emission wavelength, for the high ECL efficiencies and for the possibility to work in aqueous environment.⁶⁰

References

- (1) Zhang, J.; Arbault, S.; Sojic, N.; Jiang, D. *Annual Review of Analytical Chemistry* **2019**, *12*, null.
- (2) a)Hu, L.; Xu, G. *Chemical Society Reviews* **2010**, *39*, 3275; b)Miao, W. *Chem. Rev.* **2008**, *108*, 2506.
- (3) a)Jiang, G.; Liu, X.; Wang, Y.; Ruan, S.; Qi, H.; Yang, Y.; Zhou, Q.; Zhang, C. *Analytical Sciences* **2016**, *32*, 1023; b)Ma, C.; Wu, W.; Li, L.; Wu, S.; Zhang, J.; Chen, Z.; Zhu, J.-J. *Chemical Science* **2018**, *9*, 6167.
- (4) Al-Kutubi, H.; Voci, S.; Rassaei, L.; Sojic, N.; Mathwig, K. *Chemical Science* **2018**, *9*, 8946.
- (5) Zanut, A.; Fiorani, A.; Rebecani, S.; Kesarkar, S.; Valenti, G. *Analytical and Bioanalytical Chemistry* **2019**.
- (6) a)Engstrom, R. C.; Johnson, K. W.; DesJarlais, S. *Analytical Chemistry* **1987**, *59*, 670; b)Engstrom, R. C.; Pharr, C. M.; Koppang, M. D. *Journal of Electroanalytical Chemistry* **1987**, *221*, 251; c)Engstrom, R. C.; Small, B.; Kattan, L. *Analytical Chemistry* **1992**, *64*, 241; d)Pharr, C. M.; Engstrom, R. C.; Klancke, J.; Unzelman, P. L. *Electroanalysis* **1990**, *2*, 217.
- (7) Zu, Y.; Ding, Z.; Zhou, J.; Lee, Y.; Bard, A. J. *Analytical Chemistry* **2001**, *73*, 2153.
- (8) Amatore, C.; Pebay, C.; Servant, L.; Sojic, N.; Szunerits, S.; Thouin, L. *ChemPhysChem* **2006**, *7*, 1322.
- (9) Zhou, Z.; Xu, L.; Wu, S.; Su, B. *Analyst* **2014**, *139*, 4934.
- (10) Milutinovic, M.; Sallard, S.; Manojlovic, D.; Mano, N.; Sojic, N. *Bioelectrochemistry* **2011**, *82*, 63.
- (11) a)Zhao, H.-F.; Liang, R.-P.; Wang, J.-W.; Qiu, J.-D. *Chemical Communications* **2015**, *51*, 12669; b)Cao, Y.; Yuan, R.; Chai, Y.; Mao, L.; Niu, H.; Liu, H.; Zhuo, Y. *Biosensors and Bioelectronics* **2012**, *31*, 305.
- (12) Wang, N.; Feng, Y.; Wang, Y.; Ju, H.; Yan, F. *Analytical Chemistry* **2018**, *90*, 7708.
- (13) Chow, K.-F.; Mavr e, F.; Crooks, J. A.; Chang, B.-Y.; Crooks, R. M. *Journal of American Chemical Society* **2009**, *131*, 8364.
- (14) Arora, A.; Eijkel, J. C. T.; Morf, W. E.; Manz, A. *Analytical Chemistry* **2001**, *73*, 3282.
- (15) a)Khoshfetrat, S. M.; Ranjbari, M.; Shayan, M.; Mehrgardi, M. A.; Kiani, A. *Analytical Chemistry* **2015**, *87*, 8123; b)Chow, K.-F.; Mavr e, F.; Crooks, R. M. *Journal of the American Chemical Society* **2008**, *130*, 7544.
- (16) Chang, B.-Y.; Chow, K.-F.; Crooks, J. A.; Mavr e, F.; Crooks, R. M. *Analyst* **2012**, *137*, 2827.
- (17) Sentic, M.; Arbault, S.; Goudeau, B.; Manojlovic, D.; Kuhn, A.; Bouffier, L.; Sojic, N. *Chemical Communications* **2014**, *50*, 10202.
- (18) Fan, F.-R. F.; Bard, A. J. *Nano Letters* **2008**, *8*, 1746.
- (19) Fan, F.-R. F.; Park, S.; Zhu, Y.; Ruoff, R. S.; Bard, A. J. *Journal of the American Chemical Society* **2009**, *131*, 937.
- (20) Wilson, A. J.; Marchuk, K.; Willets, K. A. *Nano Letters* **2015**, *15*, 6110.
- (21) Pan, S.; Liu, J.; Hill, C. M. *The Journal of Physical Chemistry C* **2015**, *119*, 27095.
- (22) a)Zheng, X. T.; Li, C. M. *Chemical Society Reviews* **2012**, *41*, 2061; b)Stone, M. B.; Shelby, S. A.; Veatch, S. L. *Chemical Reviews* **2017**, *117*, 7457.
- (23) a)Wightman, R. M.; Jankowski, J. A.; Kennedy, R. T.; Kawagoe, K. T.; Schroeder, T. J.; Leszczyszyn, D. J.; Near, J. A.; Diliberto, E., Jr.; Viveros, O. H. *Proceedings*

- of the National Academy of Sciences of U.S.A. **1991**, 88, 10754; b)Amatore, C.; Bouret, Y.; Travis, E. R.; Wightman, R. M. *Angewandte Chemie International Edition* **2000**, 39, 1952;
- c)Amatore, C.; Arbault, S.; Guille, M.; Lemaître, F. *Chemical Reviews* **2008**, 108, 2585; d)Zhao, X.; Diakowski, P. M.; Ding, Z. *Analytical Chemistry* **2010**, 82, 8371.
- (24) a)Clausmeyer, J.; Schuhmann, W. *Trends of Analytical Chemistry* **2016**, 79, 46; b)Salamifar, S. E.; Lai, R. Y. *Analytical Chemistry* **2013**, 85, 9417.
- (25) Ma, G.; Zhou, J.; Tian, C.; Jiang, D.; Fang, D.; Chen, H. *Analytical Chemistry* **2013**, 85, 3912.
- (26) Xu, J.; Jiang, D.; Qin, Y.; Xia, J.; Jiang, D.; Chen, H.-Y. *Analytical Chemistry* **2017**, 89, 2216.
- (27) Valenti, G.; Scarabino, S.; Goudeau, B.; Lesch, A.; Jović, M.; Villani, E.; Sentic, M.; Rapino, S.; Arbault, S.; Paolucci, F.; Sojic, N. *Journal of the American Chemical Society* **2017**, 139, 16830.
- (28) Liu, G.; Ma, C.; Jin, B.-K.; Chen, Z.; Zhu, J.-J. *Analytical Chemistry* **2018**, 90, 4801.
- (29) Bondarenko, A.; Lin, T.-E.; Stupar, P.; Lesch, A.; Cortés-Salazar, F.; Girault, H. H.; Pick, H. *Analytical Chemistry* **2016**, 88, 11436.
- (30) Cao, J.-T.; Wang, Y.-L.; Zhang, J.-J.; Dong, Y.-X.; Liu, F.-R.; Ren, S.-W.; Liu, Y.-M. *Analytical Chemistry* **2018**.
- (31) Voci, S.; Goudeau, B.; Valenti, G.; Lesch, A.; Jović, M.; Rapino, S.; Paolucci, F.; Arbault, S.; Sojic, N. *Journal of the American Chemical Society* **2018**, 140, 14753.
- (32) Valenti, G.; Fiorani, A.; Li, H.; Sojic, N.; Paolucci, F. *ChemElectroChem* **2016**, 3, 1990.
- (33) Howarth, M.; Ting, A. Y. *Nature protocols* **2008**, 3, 534.
- (34) Zhou, X.; Zhu, D.; Liao, Y.; Liu, W.; Liu, H.; Ma, Z.; Xing, D. *Nature Protocols* **2014**, 9, 1146.
- (35) Miao, W.; Choi, J.-P.; Bard, A. J. *Journal of the American Chemical Society* **2002**, 124, 14478.
- (36) Zu, Y.; Bard, A. J. *Analytical Chemistry* **2000**, 72, 3223.
- (37) Sentic, M.; Milutinovic, M.; Kanoufi, F.; Manojlovic, D.; Arbault, S.; Sojic, N. *Chemical Science* **2014**, 5, 2568.
- (38) Lai, R. Y.; Bard, A. J. *The Journal of Physical Chemistry A* **2003**, 107, 3335.
- (39) Jamur, M. C.; Oliver, C. In *Immunocytochemical Methods and Protocols*; Oliver, C., Jamur, M. C., Eds.; Humana Press: Totowa, NJ, 2010, p 63.
- (40) Liu, X.; Shi, L.; Niu, W.; Li, H.; Xu, G. *Angewandte Chemie* **2007**, 119, 425.
- (41) Liu, X.; Shi, L.; Niu, W.; Li, H.; Xu, G. *Angewandte Chemie International Edition* **2007**, 46, 421.
- (42) Xue, L.; Guo, L.; Qiu, B.; Lin, Z.; Chen, G. *Electrochemistry Communications* **2009**, 11, 1579.
- (43) Sentic, M.; Milutinovic, M.; Kanoufi, F.; Manojlovic, D.; Arbault, S.; Sojic, N. *Chemical Science* **2014**, 5, 2568.
- (44) a)Conchello, J.-A.; Lichtman, J. W. *Nature Methods* **2005**, 2, 920; b)Agard, D. A. *Annual Reviews of Biophysics and Bioengineering* **1984**, 13, 191.
- (45) Keller, H. E. In *Handbook of Biological Confocal Microscopy*; Pawley, J., Ed.; Plenum Press: New York, 1995; Vol. 145-161.
- (46) Puntheeranurak, T.; Wildling, L.; Gruber, H. J.; Kinne, R. K. H.; Hinterdorfer, P. *Journal of Cell Science* **2006**, 119, 2960.
- (47) a)Giebel, K. F.; Bechinger, C.; Herminghaus, S.; Riedel, M.; Leiderer, P.; Weiland, U.; Bastmeyer, M. *Biophysical Journal* **1999**, 76, 509; b)Wang, W.; Wang, S.; Liu, Q.; Wu, J.; Tao, N. *Langmuir* **2012**, 28, 13373.

- (48) Kudalkar, E. M.; Davis, T. N.; Asbury, C. L. *Cold Spring Harbor Protocols* **2016**, 2016, pdb.top077800.
- (49) Dürig, U.; Pohl, D. W.; Rohner, F. *Journal of Applied Physics* **1986**, 59, 3318.
- (50) Zu, Y.; Bard, A. J. *Analytical Chemistry* **2000**, 72, 3223.
- (51) Dolci, L. S.; Zandarini, S.; Ciana, L. D.; Paolucci, F.; Roda, A. *Analytical Chemistry* **2009**, 81, 6234.
- (52) Xu, L.; Li, Y.; Wu, S.; Liu, X.; Su, B. *Angewandte Chemie International Edition* **2012**, 51, 8068.
- (53) Zhou, J.; Ma, G.; Chen, Y.; Fang, D.; Jiang, D.; Chen, H.-y. *Analytical Chemistry* **2015**, 87, 8138.
- (54) a) Ritzert, N. L.; Li, W.; Tan, C.; Rodríguez-Calero, G. G.; Rodríguez-López, J.; Hernández-Burgos, K.; Conte, S.; Parks, J. J.; Ralph, D. C.; Abruña, H. D. *Faraday Discussions* **2014**, 172, 27; b) Zamolo, V. A.; Valenti, G.; Venturelli, E.; Chaloin, O.; Marcaccio, M.; Boscolo, S.; Castagnola, V.; Sosa, S.; Berti, F.; Fontanive, G.; Poli, M.; Tubaro, A.; Bianco, A.; Paolucci, F.; Prato, M. *ACS Nano* **2012**, 6, 7989; c) Deng, S.; Lei, J.; Huang, Y.; Cheng, Y.; Ju, H. *Analytical Chemistry* **2013**, 85, 5390; d) Su, Y.; Lv, Y. *RSC Advances* **2014**, 4, 29324.
- (55) Jović, M.; Zhu, Y.; Lesch, A.; Bondarenko, A.; Cortés-Salazar, F.; Gumy, F.; Girault, H. H. *Journal of Electroanalytical Chemistry* **2017**, 786, 69.
- (56) Valenti, G.; Zangheri, M.; Sansaloni, S. E.; Mirasoli, M.; Penicaud, A.; Roda, A.; Paolucci, F. *Chemistry - A European Journal* **2015**, 21, 12640.
- (57) Zanello, L. P.; Zhao, B.; Hu, H.; Haddon, R. C. *Nano Letters* **2006**, 6, 562.
- (58) Chen, X.; Tam, U. C.; Czapinski, J. L.; Lee, G. S.; Rabuka, D.; Zettl, A.; Bertozzi, C. R. *Journal of the American Chemical Society* **2006**, 128, 6292.
- (59) Dominguez, R.; Holmes, K. C. *Annual Review of Biophysics* **2011**, 40, 169.
- (60) Guo, W.; Ding, H.; Gu, C.; Liu, Y.; Jiang, X.; Su, B.; Shao, Y. *Journal of the American Chemical Society* **2018**, 140, 15904.

Experimental section

1. Chapter II – Supramolecular ECL

1.2 ECL study of trigonal truxene-core spirofluorene dyes

1.2.2 Materials

Anhydrous DMF (Sigma-Aldrich, 99.8 %) was used as received. TBAPF₆ (≥ 99%) and benzoyl peroxide were purchased from Sigma Aldrich and used without further purification.

1.2.2 Electrochemical characterization

The working electrode was a homemade glassy carbon (GC) disk electrode (3 mm diameter, Tokai GC-20) connected to a copper wire with silver epoxy and sealed in a PEEK body. The electrode was polished with a 0.25 μm diamond paste (Struer) and electrochemically activated in the background solution by means of several voltammetric cycles at 0.5 Vs⁻¹ between the anodic and the cathodic solvent/electrolyte discharges, until the expected quality features were attained.¹ A platinum wire served as the counter electrode and a silver wire, separated from the main electrolytic compartment by a Vycor® frit, was used as a quasi-reference electrode. At the end of each experiment, its potential was calibrated against the ferricenium/ferrocene couple (Fc/Fc⁺), used as an internal redox standard. In DMF/0.1 M TBAP₆, ferricenium/ferrocene has

a formal potential of 0.464 V against the KCl saturated calomel electrode (SCE);^{1b} all potentials were given against SCE. The cyclic voltammetry (CV) experiments were carried out in DMF/0.1 M TBAPF₆, using a 1 mM concentration for the electroactive compound (2.5×10^{-5} M for **4**). The CV and ECL experiments were conducted at 25 °C under an Ar atmosphere using a cell consisting of a purposely-modified quartz cuvette. A CHI 760E Electrochemical Workstation (CH Instruments) was used. For the CV experiments, the feedback correction was employed to minimize the ohmic drop between the working and the reference electrodes. The formal potential (E°) values (or, for evidently multi-electron waves, apparent E° values) were obtained as the average between the cathodic and anodic peak potentials.

1.2.3 Electrochemiluminescence

ECL emission was collected with a Hamamatsu R5070 photomultiplier tube with a Hamamatsu C9525 high-voltage power supply. The PMT detector was held at -750 V and placed at a defined distance of few millimeters from the working electrode. The output signal was amplified by a Keithley 6485 Picoammeter, then it was acquired *via* the second input channel of the μ Autolab type III potentiostat. ECL spectra were recorded with a Princeton Instruments Acton SpectraPro 2300i after the CCD camera, cooled to -110 °C with liquid N₂. The optical fiber connected to the device was located at a defined distance of few millimeters from the working electrode.

1.3 Circularly polarization of ECL from a chiral bis-pyrene organic macrocycle

1.3.1 Materials

[18]-C-6bispyrene was synthesized and characterized according to the published procedure.² All reactions involving air sensitive compounds were carried out under N₂. All the reagents and solvents were purchased from commercial sources and employed without any further purification. Acetonitrile was stored under argon on activated molecular sieves. [18]-C-6bispyrene was obtained in enantiopure forms as reported in the literature.³

1.3.2 Electrochemical and ECL characterization

Voltammetric experiments were performed with a PGSTAT30 Autolab potentiostat connected to a conventional three-electrodes cell, consisting in a silver wire pseudo-reference electrode, a platinum wire auxiliary electrode, and a GC disk ($d = 3$ mm) working electrode. Prior to measurements, GC disks were polished with alumina slurry of different size, rinsed thoroughly

with Milli-Q water between each polishing step, and sonicated in water and ethanol respectively, followed by a final rinse with acetonitrile and dried with N₂ stream. Voltammograms of ferrocene were also recorded in the same experimental conditions before and after the electrochemical characterization of [18]-C-6bispyrene. The ferrocene/ferrocenium (Fc/Fc⁺) redox couple shows an oxidation potential value of 0.44 V *vs* Ag. ECL intensity was measured using a Hamamatsu photomultiplier tube (PMT) R5070A with a Hamamatsu C9525 high voltage power supply. The PMT detector was held at -750 V and placed at a constant distance of 5 mm in front of the working electrode. The output signal was amplified by a Keithley 6485 Picoammeter, before acquisition via the second input channel of the PGSTAT30 Autolab potentiostat. All these experiments were performed on racemic [18]-C-6bispyrene.

1.3.3 CP-ECL measurements

Experiments were performed with a μ -Autolab potentiostat connected to a transparent home-built three-electrodes cell, consisting of a purposely-modified quartz cuvette, a silver wire pseudo-reference electrode, a platinum-wire auxiliary electrode. The working electrode was a homemade GC disk electrode (3 mm diameter, Tokai GC-20) connected to a copper wire with silver epoxy and sealed in a PEEK body. A constant potential of -2.45 V *vs* Ag was applied to generate the ECL emission. The CP-ECL experiments were performed on a solution of 0.7 mM of [18]-C-6bispyrene, 10 mM BPO and 0.1 M of TBAPF₆ in acetonitrile. Before recording the spectra the samples were sonicated for 10 minutes and then N₂ was inflated inside the cell to remove dioxygen. The measurements were carried out by maintaining a small flux of nitrogen on the top of the solution. CP-ECL spectra were recorded using a home-built spectrofluoropolarimeter.⁴ The following parameters were used: scan-speed 2 nm/sec, integration time 4 sec, slit width 4 mm, PMT-voltage 800 V. In order to increase the signal-to-noise ratio, the spectra were recorded 6 times for each enantiomer and were averaged. CP-ECL spectra were normalized on the maximum of the corresponding ECL emission profile. ECL dissymmetry factors (g_{ECL}) were calculated, according to the definition (*vide* Eq. 2.27).

2. Chapter III – ECL in confined environments

2.1 ECL by nanofluidic confinement

2.1.1 Materials

Tris(2,2'-bipyridine)ruthenium(II) hexafluorophosphate ($\text{Ru}(\text{bpy})_3(\text{PF}_6)_2$), sulfuric acid, TPA and the supporting electrolyte tetrabutylammonium hexafluorophosphate (TBAPF_6) were purchased from Sigma-Aldrich, chromium etchant (Selectipur) from BASF. All solutions were prepared using Milli-Q water (resistivity = 18 M Ω cm) or HPLC-grade acetonitrile (Sigma-Aldrich).

2.1.2 Device fabrication

The fabrication of the electrochemical nanofluidic device was executed in Delft University of Technology and completed in Groningen University.⁵

2.1.3 Electrochemical and ECL characterizations

Voltammograms were performed with a PGSTAT30 Autolab potentiostat connected to a conventional three-electrodes cell, consisting of a silver wire pseudo-reference electrode, a platinum-wire auxiliary electrode, and a GC disk ($d = 3$ mm) working electrode. Prior to measurements, GC disks were polished with alumina slurry of different size, rinsed thoroughly with Milli-Q water between each polishing step, and sonicated in water and ethanol respectively, followed by a final rinse with acetonitrile and dried with N₂ stream. ECL intensity was measured using a Hamamatsu photomultiplier tube (PMT) R5070A with a Hamamatsu C9525 high voltage power supply. The PMT detector was held at -750 V and placed at a constant distance of 5 mm in front of the working electrode. The output signal was amplified by a Keithley 6485 Picoammeter, before acquisition via the second input channel of the PGSTAT30 Autolab potentiostat.

2.1.4 ECL Imaging

ECL images were recorded using an epifluorescence Leica (DMI6000, Leica Microsystems) microscope equipped with an EM-CCD 9100-13 camera from Hamamatsu, with an inverted 40 \times microscope objective from Leica (40 \times /0.6, 3.3 mm). All experiments were performed at ambient temperature (25 °C). The images were treated using ImageJ software.

2.2 Enhanced bipolar electrochemistry at solid-state micropores

2.2.1 Materials

Su-8 2075 was purchased from Microchem (Westborough, MA). All other chemicals were obtained from Sigma Aldrich. Tris(2,2'-bipyridil)-dichlororuthenium(II) hexahydrate (1 mM) and TPA (50 mM) were prepared in phosphate buffer solution (0.1 M, pH 7.4). The conductivity of the solution was 13.9 mS cm^{-1} .

2.2.2 Fabrication of silicon with integrated micropore

The micropore chips were fabricated in the group LAAS-CNRS, in Toulouse University.⁶

2.2.3 Electrochemical and ECL characterization

Voltammetric and ECL experiments were performed with a PGSTAT30 Autolab potentiostat connected to a conventional three-electrodes cell. ECL intensity was measured using a Hamamatsu photomultiplier tube (PMT) R5070A with a Hamamatsu C9525 high voltage power supply. The output signal was amplified by a Keithley 6485 Picoammeter before acquisition via the second input channel of the PGSTAT30 Autolab potentiostat. ECL spectra were recorded using a Princeton Instruments Acton SpectraPro 2300i. The cell is built with a glass slide at the bottom in order to record the ECL signal. The optical fiber connected to the device was placed close to this glass slide in front of the working electrode. The potential was controlled by a potentiostat (μ -Autolab type III), the reference and counter electrodes were a Ag/AgCl wire and a platinum wire, respectively. Potential pulses of 10 V for 300 ms separated by a delay of 100 ms were applied for 10 s using a power supply DG1032 from Rigol.

2.2.4 Imaging

ECL images were recorded using an epifluorescence Leica (DMI6000, Leica Microsystems) microscope equipped with an EM-CCD 9100–13 camera from Hamamatsu, with an inverted 50 \times microscope objective from Leica (50 \times /0.55, 8 mm). All experiments were performed at ambient temperature (25 °C). Exposure time of the CCD camera was synchronized with the potential application for 10 s. The images were treated using ImageJ software. The SEM images were obtained with a FEI Helios 600i SEM instruments.

3. Chapter IV - Surface-Confined ECL Microscopy of Cellular Membranes

3.1 Materials

TPA, 2-(dibutylamino)ethanol (DBAE), phosphate buffered saline (PBS) solution (pH 7.4), streptavidin from *Streptomyces avidinii*, bis(2,2'-bipyridine)-4'-methyl-4-carboxybipyridine-ruthenium N-succinimidyl ester bis-(hexafluorophosphate) [Ru(bpy)₂(mcbpy-O-Su-ester)(PF₆)₂] and paraformaldehyde (PFA) were from Sigma-Aldrich and used without any further purification. Triton X-100 was from Acros Organic. Iscove's modified Dulbecco's medium, fetal bovine serum, PBS 1×, trypsin and penicillin/streptomycin 100 U/mL were from Gibco. Biotin X was from Fisher Scientific. DMSO was from Invitrogen. Phosphate buffer solution (PBS) 0.1 M (pH = 7.4) was obtained by mixing 0.1 M of sodium phosphate monobasic monohydrate (NaH₂PO₄·H₂O) and 0.1 M sodium phosphate dibasic heptahydrate (Na₂HPO₄·7H₂O), both from Sigma-Aldrich and used as received.

3.2 Cell culture, labeling and permeabilization

CHO-K1 cells were from Public Health England (HPA) Culture Collections and supplied by Sigma Aldrich (85051005). Iscove's modified Dulbecco's medium (IMDM) supplemented with 10% fetal bovine serum and penicillin/streptomycin 100 U/mL were used to grow cells in an incubator. CHO-K1 cells were trypsinized, plated on GC electrode or in a Petri dish containing CNT electrode and incubated 48 h with culture medium at 37 °C, 5% CO₂. A solution of 100 μL of ruthenium complex (10 mg/mL) in anhydrous DMSO, 100 μL of streptavidin (1 mg/mL in PBS), and 800 μL PBS was prepared. The solution was vortexed for 4 h at 4 °C and dialyzed overnight under stirring at 4 °C. Before ECL experiment, CHO-K1 cells were fixed 10 min with PFA 4%, permeabilized 10 min with Triton X-100 0.1%, labeled with biotin X 11 μM and streptavidin-ruthenium complex solution SA@Ru (0.1 mg/mL).

3.3 ECL analysis

The ECL/PL microscopies were performed in a PTFE (Teflon) homemade electrochemical cell. The ECL imaging cell was used in a three-electrodes configuration, in which GC or CNT electrodes acted as working electrode, Ag/AgCl (KCl, 3M) as reference electrode and a Pt wire as counter electrode. For ECL experiments, the potential applied to the working electrode was 1.4 V vs Ag/AgCl (KCl, 3M).

3.4 Imaging

For microscopic imaging, an epifluorescence microscope from Leica (DMI6000, Leica Microsystems) equipped with ultrasensitive Electron-Multiplying Charge Coupled Device camera (EM-CCD 9100–13 from Hamamatsu, Hamamatsu Japan) was used with an inverted 63× microscope objective from Leica (63×/1.2, 0.2 mm). The integrated system also included a potentiostat from AUTOLAB (μ AUTOLAB, type II) suitable to provide the required potential to generate ECL.

3.5 Atomic force microscopy

AFM experiments were performed with a Veeco MultiMode 8.

References

- (1) a) Belèn Meneses, A.; Antonello, S.; Arévalo, M. C.; Maran, F. *Electroanalysis* **2006**, *18*, 363; b) Antonello, S.; Musumeci, M.; Wayner, D. D. M.; Maran, F. *Journal of the American Chemical Society* **1997**, *119*, 9541.
- (2) a) Jarolímová, Z.; Vishe, M.; Lacour, J.; Bakker, E. *Chemical Science* **2016**, *7*, 525; b) Poggiali, D.; Homberg, A.; Lathion, T.; Piguët, C.; Lacour, J. *ACS Catalysis* **2016**, *6*, 4877; c) Vishe, M.; Hrdina, R.; Poblador-Bahamonde, A. I.; Besnard, C.; Guénée, L.; Bürgi, T.; Lacour, J. *Chemical Science* **2015**, *6*, 4923.
- (3) Homberg, A.; Brun, E.; Zinna, F.; Pascal, S.; Górecki, M.; Monnier, L.; Besnard, C.; Pescitelli, G.; Di Bari, L.; Lacour, J. *Chemical Science* **2018**, *9*, 7043.
- (4) Zinna, F.; Bruhn, T.; Guido, C. A.; Ahrens, J.; Bröring, M.; Di Bari, L.; Pescitelli, G. *Chemistry – A European Journal* **2016**, *22*, 16089.
- (5) Al-Kutubi, H.; Voci, S.; Rassaei, L.; Sojic, N.; Mathwig, K. *Chemical Science* **2018**, *9*, 8946.
- (6) Ismail, A.; Voci, S.; Pham, P.; Leroy, L.; Maziz, A.; Descamps, L.; Kuhn, A.; Mailley, P.; Livache, T.; Buhot, A.; Leichlé, T.; Bouchet-Spinelli, A.; Sojic, N. *Analytical Chemistry* **2019**.

Conclusions and Perspectives

This PhD project focused on the study of new ECL luminophores, of innovative ECL properties, on the use of ECL as tool for the spatial and temporal localization of chemical and physical phenomena and on the preliminary steps of a new ECL microscopy.

In the first part of chapter II, a spirofluorene derivative and its trigonal truxene-core modified analogues were investigated. It was demonstrated that the stability of the radical anions and cations was enough to obtain high ECL intensity via annihilation for compounds **1** and **2**. In particular, compound **2** showed the best ECL efficiency value of 314 %, relatively to $[\text{Ru}(\text{bpy})_3]^{2+}$, while ECL efficiency for compound **1** was estimated as 159 %. The substitution of triphenylamine with diphenylamine in compound **3** probably decreased the stability of the electrogenerated radicals, with a consequence in its ECL performances. ECL of these systems was also investigated in reductive-oxidative coreactant pathway, by employing BPO as coreactant. Compound **2** still reached the best ECL performances, with an ECL intensity 4.5 times higher than $[\text{Ru}(\text{bpy})_3]^{2+}$. A higher ECL efficiency compared with ECL in annihilation mode was also obtained for **1**, with a value of 230 %. ECL spectra for the series of luminophores were also recorded and were found in good agreement with PL spectra. Theoretical calculations are necessary to clarify the role of the functional groups in the electrochemical and ECL properties of the dyes. The second part of chapter II discussed the first observation of CP-ECL from two enantiomers of a purely organic molecule. After testing the electrochemical properties of the supramolecular system, BPO was chosen as sacrificial coreactant. It was observed that ECL occurred only when both the luminophore and the coreactant were reduced. The more

probable ECL mechanism consisted in the heterogeneous reduction of [18]-C-6bispyrene and BPO, or the homogeneous reduction of BPO by the luminophore monoanion. The reduced BPO generates a benzoate anion and a benzoate radical, which reacts with the reduced form of the supramolecular system for the generation of the excimer. The stable and strong ECL intensity, associated with the generation of the excimer and caused by the peculiar configuration of the supramolecular system, allowed the recording of the CP-ECL signal. ECL dissymmetry factors of $+8.4 \times 10^{-3}$ and -7.3×10^{-3} were obtained, well comparable for sign and values to the CPL previously published results. A new observable in ECL measurements in chiral systems and environments, that is its degree of polarization, has been added. Further studies are needed to define the requirements for obtaining a significant CP-ECL signal, in terms of dissymmetry factor and ECL stability and intensity. In the future, lanthanide complexes, giving the highest CPL signals, could be employed as labels and probes for ECL bioassays and bioimaging.

The first part of chapter III is devoted to the discussion of ECL in an electrochemical nanofluidic device. $[\text{Ru}(\text{bpy})_3]^{2+}$ has been employed as ECL luminophore. By independently biasing two Pt electrodes positioned at the top and bottom of a 100 nm-channel, an enhancement in ECL annihilation was observed and it was possible to detect ECL light from 60 attomoles of $[\text{Ru}(\text{bpy})_3]^{2+}$. ECL imaging of the nanochannel confirmed that ECL emission was confined inside the nanochannel. The ECL system $[\text{Ru}(\text{bpy})_3]^{2+}/\text{TPA}$ was also utilized and ECL emission was detected only at the access holes of the nanodevice, as expected by the limited lifetimes of the electrogenerated radicals of TPA. An intermediate mode, in which annihilation was performed in presence of TPA, was associated with a weak ECL emission into the nanochannel. This study represents the basis of potential analytical devices in which ECL imaging can be implemented for detection of analytes at very low concentrations by nanogap amplification. In the second part of the chapter, the specific design of a microfluidic device integrating a 20 μm -long pore and two Au feeder electrodes permitted to obtain an asymmetric polarization of the bipolar electrode (corresponding to the micropore) at a voltage at least one hundred times lower than the value required in a classic configuration. The polarization of the bipolar electrode was combined with the emission of the ECL standard model system $[\text{Ru}(\text{bpy})_3]^{2+}/\text{TPA}$. Starting at a voltage of +7 V, the ECL emission of $[\text{Ru}(\text{bpy})_3]^{2+}$ was detected. ECL imaging experiments confirmed that ECL occurs in the anodic extreme of the micropore. Therefore, ECL was applied as imaging tool for the demonstration of the enhancement of BPE performances of a micropore configuration. By capturing specific species, even cells or bacteria, into the micropore surface, new original ECL analytical applications could be developed.

Chapter IV was devoted to the description of the main project of this PhD work, involving the development of ECL based microscopy. The surface confinement of ECL microscopy was demonstrated by imaging of the $[\text{Ru}(\text{bpy})_3]^{2+}$ -labeled cellular membrane of CHO cells. Indeed, a focus of 1.2 μm closer to the electrode surface was estimated for ECL compared to PL. While PL images of the cellular membrane showed the emission of the whole cellular membrane, ECL emission was confined to the cell borders, due to the peculiar ECL mechanism and the limited access of the electrogenerated radicals to the luminophores located in the central part of the basal membrane. The accessibility of TPA beyond cellular borders in the central region of the basal cellular membrane was obtained by adding a permeabilization step. For permeabilized cells, the ECL emission of the entire basal cellular membrane was achieved. From the proof of concept, another step towards potential diagnostic applications was moved by employing CNT inkjet-printed electrodes with a coverslip as substrate as working electrode instead of GC. In this way, cells could be imaged not only in reflection but also in transmission mode. Future perspectives will be the research of less toxic ECL coreactant in order to move to the study of living cells. The investigation of new ECL luminophores will also permit to tune the ECL emission, and finally to perform colocalization studies via ECL. A more specific labelling system, for the detection of proteins or other biomolecules into the cells, could be investigated using antibodies labelled with ECL luminophores.

Acknowledgements

I would like to thank my supervisor Prof. Neso Sojic for all the opportunities of learning and growing as a student and as a person that he gave me and for his constant support, far beyond the basic duty of a supervision. He was always extremely available for any scientific discussion and I felt always free to ask questions and express my ideas. However, his most important lessons were not just made in words but with his constant example of hard working, perseverance and great humility.

I am very grateful to Dr. Stéphane Arbault and Dr. Laurent Bouffier for the advices and the scientific support in my different PhD projects, and for the kindness that they demonstrated to me.

I would like to warmly thank as well Prof. Valérie Ravaine and Prof. Alexander Kuhn for their kindness and their scientific advices during my PhD.

A special thank is addressed to Dr. Bertrand Goudeau. He transferred to me a lot of knowledge with extreme generosity and humanity, he installed in me the desire to knowing more and more and he showed me what good research means. I cannot think about a more precious gift to receive. Thank you for all.

Thanks to Aline Simon-Lalande for all her competent and kind help, her warmth and all the advices.

I am very grateful to Dr. Stéphane Reculosa, Dr. Dodzi Zigah, Dr. Adeline Perro-Marre, Patrick Garrigue, Véronique Lapeyre and Cécile Allilaire for their help during all my time in NSysA.

I would like to thank all the members of the commission, Dr. Elodie Anxolabéhère-Mallart, Prof. Fabian Miomandre, Dr. Frédéric Kanoufi, and Prof. Francesco Paolucci for spending their time and competences for the examination of my work.

Thanks to Prof. Jérôme Lacour, Dr. Simon Pascal, Prof. Klaus Mathwig, Dr. Federico Polo, Dr. Aurèlie Bouchet-Spinelli, Prof. Lorenzo Di Bari, Dr. Abdulghani Ismail, Dr. Andreas Lesch, Prof. Wolfgang Schuhmann, Dr. Vera Eßmann, Dr. Gabriel Loget, Dr. Tiziana Funaioli Lorenzo Arrico, Hanan Al-Kutubi and Dr. Francesco Zinna for collaborating with our group and me during my PhD.

A special thanks to the group of molecular electrochemistry of Bologna University, in particular Prof. Francesco Paolucci, Dr. Giovanni Valenti, Prof. Stefania Rapino and Dr. Matteo Iurlo not

only for our collaboration during my PhD but also for their support and for all the knowledge that they transferred me and are always extremely important and useful for me.

Thanks a lot to Camille Colin that shared with me all the joys and the hardest moments of our PhDs.

I am extremely grateful to Dr. Cristina Carucci, Alice Dauphin and Dr. Priyanka Dutta for their friendship and their huge support. I felt more confident, always in good company and a richer person thanks to you.

A special thanks to Dr. Pauline Lefrançois, Dr. Emanuel Suraniti, Dr. Gerardo Salinas, Laura Adam, Sunpet Assavapanumat, Dr. Elena Villani, Dr. Bahvana Gupta and Jing Yu for their friendliness and all their help and suggestions.

Thanks so much to all the colleagues that I had the chance to meet during my PhD, you cannot know how much your simple smiling to me and your advices helped me every day, in particular Dr. Yuliia Maliytska, Dr. Lin Zhang, Dr. Maciej Mierzwa, Yuanhao Ding, Dr. H  l  ne Labie, Dr. Serena Arnaboldi, Dr. Haidong Li, Dr. Eliana Farias, Paul Chassagne, Dr. Maria Combres, Roberto Maria Hormigos, Dr. Ambrose Melvin, Sopon Butcha, Dr. Marcin Dabrowski, Bruno Silva, Dr. Aleksandar Karajic, Abdelmounaim Akchach, Samuel Guilbault, Aoy.

I would like to thank my closest friends, Anita and Alessandra, as well as Dr. Stefano Lorenzi that could find the time to help me even at thousands kilometers of distance.

Finally, I would like to thank my mother, Marilena, my sister, Diana, my grandparents, Antonino and Marisa, my nephew, Leonardo, the rest of my family and Lorenzo for all their love and support and for believing in my intuitions and choices. Grazie di tutto.

This work is dedicated to Vincenzo Voci, Giuseppe Voci, and Lorenzo Pucillowski.